Slip patterns on heterogeneous frictional interfaces

Thesis by

Kavya Sudhir

In Partial Fulfillment of the Requirements for the
Degree of
Doctor of Philosophy in Mechanical Engineering

CALIFORNIA INSTITUTE OF TECHNOLOGY
Pasadena, California

2022
Defended Dec 7, 2021

Kavya Sudhir
ORCID: 0000-0001-6673-0979

ACKNOWLEDGEMENTS

It gives me great pleasure to thank the many people who made my PhD journey and this thesis possible.

First, I would like to express my gratitude to my advisor, Nadia Lapusta, for her guidance, kind support and mentorship —both in matters of research and life— through these past 6 years. The amount of positivity and encouragement Nadia radiates is unreal; I would go into a research meeting worried and filled with doubts, and emerge with new-found motivation and energy every single time. Nadia's way of quickly examining sprawling research papers/presentations and immediately zeroing-in on the crux of the matter is something I deeply admire and hope to try and replicate in my professional career. I am eternally grateful to Nadia for giving me the time and freedom to examine different career prospects during my final year and supporting me in myriad ways in these pursuits. Thank you for always being in our corner, Nadia.

I would also like to thank the other members of my thesis committee; Kaushik Bhattacharya, José Andrade and Jean-Philippe Avouac. Thank you Kaushik for being the chair of my committee, for always being approachable and considerate to graduate students. Thank you José for being on my committee, and your gracious support and encouragement all the way from my candidacy days to thesis defense. Thank you Jean-Philippe for spending the time and effort to look through my thesis and suggest improvements; I am very grateful, and in awe of your drive for lifelong learning.

While on the topic of mentorship, I also wish to thank my undergraduate mentors, Shankar J. Subramanian for his invaluable mentorship and guidance at a crucial point in my journey as a student; and Upendra Natarajan, for convincing me to aim high and apply to Caltech.

I would like to thank the members of the Lapusta group, who made my research life richer. Thank you to Natalie Schaal, for all the invaluable guidance and counsel she gave me as an early graduate student. Thank you to Yen-Yu Lin and Valere Lambert for their selfless aid whenever any research-related hiccup arose. Thank you to the other members of Nadia's group during my time at Caltech: Stacy, Ollie, Stephen, Semechah, Vito, Marcello, Taeho, Shengduo, for their constructive criticism and support during the different presentations and meetings.

I would like to extend my heartfelt gratitude other members in the MCE department and the broader Caltech community who made my time at Caltech that much more special. As an international student in an unknown country, the warmth extended to me by the different community members immediately eased my transition. Thank you to the different MCE staff for all that they did and continue to do for the students, especially Carolina Oseguera. Thank you to Daniel and Laura at the International Students Program (ISP) for their empathy and kindness in helping us navigate our immigration woes. The ISP orientation in my first quarter at Caltech gave me so many close friends and acquaintances, it really set the tone for the rest of my time here.

I am indebted to all the wonderful friends I made at Caltech, who made this a second home for me. My close-knit friend group of women batchmates in MCE/GALCIT: Tori, Ying Shi, Erika and Becky, made my PhD life infinitely more enjoyable and fulfilling, and I hope to cherish and maintain our friendship for life. Thank you to my other MCE/GALCIT friends; Valere, Danilo, Tomo, Joel, GG, Sharan, Philippos, Jin, Jagannadh and many others, for your company and the many conversations. I also made numerous friends in the international student community, specifically in the South-Asian community. Thank you to Akshata for being there for me from Day 1, and dispeling any and all specks of homesickness. Thank you Saberi, Siddharth, Prachi, Srikanth, Gautam, Anupama, Vidya, Ishan, Jenish, Utkarsh and many others, for all the fun times at OASIS cultural events and the memories.

Finally, I would like to thank the most important people in my life: my husband, Vashist and my parents, Sudhir and Beena.

Being the spouse/partner of an anxious PhD candidate is an unnerving task indeed, I would not wish it on my enemy. My husband supported me through the hardest, grimiest parts of it all, encouraging me during my lows and helping me keep faith and good humor. I would not have been able to come out the other side without his unwavering care and support, and I am eternally thankful for his love and presence in my life.

Being an only child, I was always extremely close to my parents; it was and continues to be a constant struggle to be so far apart from them. It took immense sacrifice and courage on my parents' side to let me pursue my dreams on the other side of the planet. Throughout the last 6 years, they have been my biggest cheerleaders and support system, over innumerable video calls. I am truly blessed to have my parents and dedicate this thesis and all my life's successes to them.

ABSTRACT

Understanding the implications of heterogeneity on frictional interfaces for the resulting slip patterns is a challenging, highly nonlinear, and dynamic problem with special relevance to earthquake source processes. Natural fault surfaces are rarely homogeneous and host a spectrum of slip behaviors in response to slow tectonic loading where slow steady slip and earthquake ruptures are just the end members. Understanding how heterogeneous frictional properties translate into different slip patterns would enable us to constrain the heterogeneity of natural faults and get an insight into processes that are difficult to observe in the field such as earthquake nucleation, with important implications for the assessment of seismic hazard.

In this thesis, we advance our understanding of fault heterogeneity and its effects by conducting numerical simulations of long-term slip histories on heterogeneous frictional interfaces. We first focus on how irregular fault geometry affects the variability in repeating sequences by investigating a specific example of the SF-LA repeaters in the Parkfield segment of the San Andreas Fault (SAF) in California. We then investigate the effect of increasing heterogeneity in the effective normal stress on earthquake nucleation processes, complexity of earthquake sequences, and features of larger-scale ruptures. In both cases, we incorporate the heterogeneity in physical properties into 2D planar faults governed by rate-and-state friction and embedded into 3D homogeneous elastic bulk. Fully dynamic simulations are used to numerically solve the resulting elastodynamic problems with friction as a nonlinear boundary condition.

Our models reproduce many observations about SF-LA repeating sequences, including their mean moment, mean recurrence times, stress drops, the observed non-trivial scaling between the seismic moment and recurrence times of the repeaters, the ranges of variability in moment and recurrence time, and the ranges of triggering times between the two sequences. Multiple models produce slip behaviors comparable to observations, indicating that the models cannot be uniquely constrained based on available observations. We also study how small-scale features of heterogeneity affect model response. We find that smoothing the distribution over scales smaller than governing length scales in the problem, such as the nucleation size in our case, changes the specific evolution of slip, but preserves its key characteristics, such as the range of event variability and triggering times between events. However, smoothing the distribution on larger scales modifies the response qualitatively.

Our study of the earthquake initiation processes on interfaces with normal stress heterogeneity reveals that systematic increase in heterogeneity induces a continuum of behaviors, ranging from purely fault-spanning events to persistent foreshock-like events interspersed between fault-spanning mainshocks. In models with strong heterogeneity, most smaller-scale and larger-scale events initiate from scales much smaller than the nucleation size estimates calculated for uniform interfaces with equivalent average properties. While the variations in normal stress induce inversely proportional variations in the instability length scale often called nucleation size, we find that the nucleation-size variations by themselves are insufficient to cause such behavior, and that the associated strong heterogeneity in frictional strength is also required. In models with uniform friction strength but the same nucleation-size variation, the nucleation processes of larger-scale events are similar to those on uniform interfaces, with an addition of multiple triggered small-scale earthquakes. Our simulations show that several hypothesized scenarios of earthquake nucleation and foreshocks on natural faults may be viable and reflect different types and levels of heterogeneity on different faults the effects of which, in addition, vary as fault conditions evolve. For example, even with strong fault heterogeneity, some large-scale events have foreshocks and some do not, in the same simulation.

The increasing fault heterogeneity generally leads to increasing complexity of the resulting earthquake sequences and moment-rate release (also called source-time function) of large-scale, fault-spanning events, as intuitively expected, although with some saturation at the higher heterogeneity levels. We find that, in the presence of significant normal-stress heterogeneity, source-time functions of many larger-scale events exhibit prolonged seismic initiation phases, similar to some observations, as the events nucleate from the heterogeneity scale and re-rupture the areas pre-slipped quasi-statically and in foreshocks. The source-time functions also reveal that larger-scale events in our models—that are arrested by velocity-strengthening barriers—have a more abrupt arrest phase than natural earthquakes, which places constraints on rupture-arresting mechanisms that should be used in modeling. The initial moment rates are similar for events of different eventual sizes on interfaces with strong heterogeneity, implying that, in those cases, large events are just small events that ran away.

TABLE OF CONTENTS

Acknowledgements . . . iii
Abstract . . . v
Table of Contents . . . vii
List of Illustrations . . . ix
List of Tables . . . xxvi
Chapter I: Introduction . . . 1
1.1 Motivation . . . 1
1.2 Modeling variability and interaction of repeating earthquake sequences on heterogeneous faults . . . 2
1.3 Nucleation processes on interfaces with heterogeneous normal stress 7
1.4 Effect of heterogeneous fault property distributions on complexity of sequences and evolution of dynamic ruptures . . . 11
Chapter II: Modeling variability and interaction of repeating earthquake sequences on rate-and-state faults: realistic shapes of source patches vs. properties of the creeping region . . . 16
2.1 Methodology . . . 16
Fault friction . . . 16
Fault model . . . 17
Generation of heterogeneous property distributions . . . 21
2.2 Models studied . . . 23
2.3 Response of a representative two-patch model . . . 24
2.4 Single-Patch Studies . . . 26
Effect of shape and size of the source . . . 26
Effect of properties in the VS region . . . 32
2.5 Double-Patch Studies . . . 32
Effect of shape of the source patches . . . 33
Effect of perturbing sub-critical patches . . . 38
Effect of VS properties . . . 38
Matching the observed variability . . . 44
2.6 Effect of small-scale heterogeneity on slip behavior . . . 44
2.7 Conclusions . . . 54
Chapter III: Nucleation processes on interfaces with heterogeneous normal stress . . . 57
3.1 Model description and methodology . . . 57
Heterogeneity in normal stress . . . 57
Fault Model . . . 61
3.2 Qualitative similarity between models with uniform and fractal normal stress . . . 63

3.3 Qualitatively different outcomes in models with stronger heterogeneity: smaller-scale events and asperity-driven nucleation 68
3.4 Cases with ten-fold variations in nucleation sizes achieved through combined variations in normal stress and rate-and-state characteristic slip 75
3.5 Conclusions 81
Chapter IV: Effect of heterogeneous fault property distributions on complexity of sequences and evolution of dynamic ruptures 84
4.1 Complexity in earthquake sequences with increasing heterogeneity . 84
Size distributions of dynamic events 84
Nearly heterogeneity- and magnitude-invariant static stress drops in our models 92
4.2 Effect of heterogeneity on progression of dynamic ruptures 96
Recurrence time of larger-scale events 96
Source-time functions 100
Identifying dynamic events: slip-velocity threshold and variability of events within the same model 128
4.3 Conclusions 137
Chapter V: Conclusions and Future Work 139
Bibliography 143

LIST OF ILLUSTRATIONS

Number *Page*

1.1 Repeating sequences from several tectonic regions are neither time- nor slip-predictable (adapted from Rubinstein et al., 2012). (Left) The recurrence time interval between events vs. the seismic moment of the preceding event, normalized by the mean recurrence interval and mean seismic moment, respectively. If the recurrence interval increases predictably with the moment of the preceding event, then it would fall onto the pink strip. (Right) The seismic moment of events vs. the recurrence interval preceding the event, normalized by the mean seismic moment and recurrence interval, respectively. If the seismic moment (and hence slip) increases predictably with the time since the previous event, then it would fall onto the pink strip. 4

1.2 a. Time progression of moment magnitudes of SF-LA repeater sequences, before the 2004 M6 Parkfield earthquake. The LA events (blue bars) consistently happen soon after the SF events (red bars), indicating a strong interaction between the two sequences, with inter-event times spanning from seconds to months. (Data from Waldhauser and Schaff (2008)) b. Triggering times for the 7 SF-LA event pairs before 2004, plotted on a log-scale normalized with respect to the mean recurrence time of SF sequence. The triggering times range from seconds to months. c. Testing time predictability and slip predictability for 6 recurrence periods of SF and LA sequences before the 2004 M6 earthquake. The axes are normalized with respect to the mean quantities. The red and blue rectangles bound the variability of SF and LA events, respectively. 5

1.3 (Left) Schematic of a typical boxplot, indicating the median, inter-quartile range, the first (Q1) and second (Q3) quartiles bounding the middle 25% of data, with the maximum and minimum non-outlier values in the data set indicated by the whiskers. (Right) Box plots constructed for normalized seismic moment and recurrence times of SF and LA repeaters show the variability to be higher in the LA repeaters. 6

1.4 Schematics of slip evolution on the lab fault (from McLaskey and Kilgore, 2013). Slow earthquake nucleation (blue) that eventually grows into dynamic rupture (shaded blue) triggers microseismicity (circles). Presumably, similar processes occur during foreshock sequences on real faults, just on a different scale. 10
1.5 A representative set of velocity seismograms used in the analysis of Ellsworth and Beroza (1995) where the reluctant initial phase, dubbed "seismic nucleation" is observed (Reproduced with permission from Ellsworth and Beroza (1995)). 14
1.6 a. Median STFs of events in physical scale. b. Median STFs of events in normalized scales (Reproduced with permission from Meier et al. (2017)). 15
2.1 A model of a planar fault interface embedded between two isotropic, linear elastic half-spaces, which are pre-stressed and being sheared. The loading with the applied slip velocity V_{pl} outside of the frictional region simulates a case where long-term relative plate velocity of V_{pl} is driving the fault motion, resulting in slip with such slip rate everywhere on the fault except in the frictional region. The spectral approach used in the numerical simulations of the problem periodically repeat the fault domain of the frictional region and the surrounding loading region, with the repeat intervals of λ_x and λ_z, respectively. 18

2.2 a. Representative model domain used in the simulations, normalized by the estimate of the nucleation size for the VW region (yellow), h^*. The domain of interest containing the heterogeneous property distribution is surrounded by load-transmitting VS region (blue), around which steady slip at V_{load} is applied (green) to simulate the steady creep of the larger surrounding region. b. (Left) A realization of the random field with two dominant areas that can serve as the source patches for the SF and LA sequences. The random field is characterized by the Hurst constant, H, that determines the spectral decay at high frequencies and a_{max}, which modulates the largest feature sizes; we choose H = 1 (self-similar). a_{max} = 64 is chosen to obtain the feature sizes comparable to h^*, given the computational restriction on the overall size of the heterogeneous domain (set to $4h^*$). (Right) Power spectral density of the fractal field. The dashed blue line indicates the corner wave number, k_c, beyond which the spectrum shows power law decay. 19

2.3 (a) Heterogeneous distribution of VW (yellow) and VS (blue) frictional properties obtained from the random field in Figure 4. (b) The distribution with only two main irregular patches and all other perturbing features removed. (c-d) Constructing analogous fault model with circular patches by fixing centroids of the two main patches and conserving their areas. (e) Fault model with circular patches of smaller radii that has similar moment magnitudes to the model with irregular patches from (a-b). (f) Fault model with circular patches and smaller perturbing patches from (a). 22

2.4 Slip velocity snapshots from the representative model F1p-D. The top row illustrates a typical triggering sequence where the post-seismic slip from the left-patch event triggers an event in the right patch. The middle row shows the subsequent interseismic period, marked by aseismic transients. The third row indicates the following triggering sequence in which the left patch event triggers the right patch yet again, albeit with a shorter triggering time and at a different location. 26

2.5 a. Single-patch models with different patch sizes: (top row, left to right) C1n-S Scaled down 20 %, C1n-S, C1n-S Scaled up 20%, (bottom row, left to right) F1n-S Scaled down 20%, F1n-S, F1n-S Scaled up 20% b. Comparison of moment and recurrence time of a single circular patch model (C1n-S) with a single fractal patch model (F1n-S). C1n-S has a lower mean recurrence time but higher mean seismic moment, implying that a complete analogy in properties between the two patch shapes might be difficult to produce. 28

2.6 Box plots of the single-patch models comparing their seismic moment and recurrence time. The variability of moment and recurrence time generally increases with the coupled effect of a complex patch shape and increased patch size. Models with less strengthening region around the patches have larger variability (C3n-S and F3n-S vs. C1n-S and F1n-S). 29

2.7 Slip velocity snapshots from the model F1n-S (with patch size larger by 25%) for two different dynamic events (top and bottom rows) illustrating the effect that the patch shape has on the nucleation and propagation of dynamic rupture. For a large patch with complex shape, patch can be ruptured differently—and with different area covered—in subsequent events. 30

2.8 a. Scaling between the recurrence time of events in each repeating sequence T_{rec} vs. their seismic moment M_o for single-patch circular models (circular markers), single patch fractal models (diamond markers), and left and right patch events from the base model (F1p-D) (star markers). b. The scaling with the line fit for the mean recurrence times of each model. Results match the scaling observed for repeaters of the creeping section next to Parkfield (black line), approximated by the expression $T_{rec} \approx 7 \times 10^4 {M_o}^{0.17}$ (Chen and Lapusta, 2009). The theoretical scaling relation for the constant stress drops of 20 MPa is shown by the red line for comparison. 31

2.9 Comparing the time-predictability plots of models with single and double fractal patches (F1n-S and F1n-D) shows the increase in variability of slip behavior due to interaction between the patches. 32

2.10 Fault models C1n-D, C1p-D, F1n-D, F1p-D for the double-patch simulations. 34

2.11 Slip-time predictability plots for the double-patch models. The data points in the case of the circular-patch model (C1n-D) are clustered, whereas the addition of sub-critical perturbing patches increases the spread of data points (C1p-D). The fractal source shape (F1n-D) significantly increases the scatter, which is further enhanced by addition of perturbing patches (F1p-D). The red and blue rectangles bounding the time- and slip-predictability data points of the SF-LA event pairs are superposed for comparison to models. 35

2.12 Comparison of moment and recurrence time box plots from the left-patch events in double-patch simulations. A substantial increase in variability is introduced by the fractal patch shape (F1n-D), with further, more subtle increase in variability with addition of perturbing patches (C1p-D, F1p-D). 36

2.13 Triggering times in double-patch models. In the case of the circular-patch model (C1n-D), the lower triggering times are absent, with the addition of sub-critical perturbing patches increasing the range of triggering times, though still not to the extent of realistic behavior (C1p-D). The fractal source shapes (F1n-D) give rise to a wide range of triggering times comparable to the observations, which persist with addition of perturbing patches (F1p-D). 37

2.14 Time-predictability and slip-predictability plots for double-patch models with decreasing velocity strengthening in the region surrounding the patches (C1n-D, C2n-D, and C3n-D). The variability of seismic moments and recurrence times is similar, slightly increasing with the reduction in the strengthening. 39

2.15 a. Box plots visualizing the variation in moment and recurrence time with varying VS properties. b. Triggering times of left and right patches for models with circular patches, C1n-D, C2n-D, C3n-D. The red points indicate inter-event times in which the bigger, left patch is triggering the smaller, right patch. The model with the reduced strengthening of the surrounding medium has response comparable to observations, with a range of triggering times. 40

2.16 Slip velocity history at the centers of left (red) and right (blue) patches in model C3n-D. The history shows the behavior alternating between periods in which event in one patch triggers an event in the other patch nearly instantaneously compared to the average recurrence time of each sequence (e.g. during 15-20 time units) and periods in which the left and right patch events occur more spaced out in time, with their interevent time being a large fraction of the average recurrence time (e.g. during 10-15 time units). 42

2.17 Two types of interaction between patches observed in C3n-D model. Time t is the simulated time since an event in the left patch as shown in the left-most panel. Time t' refers to the simulated time normalized with respect to mean recurrence time of left patch events ($T_{rec,L}$). (Top row) The postseismic front from a left-patch event triggers an aseismic transient in the right patch, with the nucleation of the next seismic event there occurring in 1.1 years or 0.4 of the recurrence interval. b. The postseismic front from a left-patch event triggers a dynamic event in the right patch within seconds or nearly instantaneously compared to the recurrence period, owing to the favorable state of stress in the right patch. 43

2.18 a. Removing small-scale heterogeneity by thresholding the power spectral density of the underlying fractal distribution. b. The property distributions for $a_{min} = 1$ and $a_{min} = 4$ appear visually identical to the observer, whereas the resulting slip behavior exhibits visible differences. 46

2.19 Models obtained by smoothing of the patch shapes by eliminating high-frequency contributions. The fractal features gradually disappear, and the separate patches coalesce to form a single area for some models. At $a_{min} = 63$, the patches present as relatively simple shapes, with the power-law decay completely removed from the spectra (Figure 2.18). Note that $a_{min} = 32$ still preserves heterogeneous features at the scale of the nucleation size, with larger values of a_{min} resulting in significant modifications of the shape at that scale. 48

2.20 Slip predictability in models with increasingly smoother distributions. The variability exhibited is similar in models with small enough features removed, for a_{min}=1 to 32. Beyond that, as the fractal features get wiped off, the data points in the predictability plots become increasingly clustered. See also Figure 2.22 for more quantitative measure. 49

2.21 Triggering times are compared across models subjected to smoothing of fractal features. The range of triggering times is similar in models with small enough features removed, for a_{min} = 1 to 32. The shorter triggering times vanish, diverging from the field observations, as the distribution is smoothed further. 50

2.22 Box plots comparing variability in gradually smoothed distributions. The variability is most similar in the models with small enough features removed, for a_{min} = 1 to 32, have most similar. Beyond that, the variability first increases and then decreases. 51

2.23 a. Comparison between the circular patch model (C1n-D) and the most smoothed fractal patch model (F1n-D, a_{min}=63). b. The slip predictability plots show more variability for F1n-D (a_{min}=63) compared to C1n-D. c. The left-patch box plots of models C1n-D and F1n-D (a_{min}=63). The variability is again larger for the fractal patch model. d. The slight complexity in shape produces more variable triggering times, though not broad enough compared to the natural sequences. 52

3.1 2D and 3D views of several normal stress distributions studied in this work. a. Uniform normal stress ($\sigma_{max}/\sigma_{uni}$=1). b. Fractal normal stress ($\sigma_{max}/\sigma_{uni}$ = 1.6). c. Modified fractal normal stress ($\sigma_{max}/\sigma_{uni}$ = 5). d. Modified fractal normal stress ($\sigma_{max}/\sigma_{uni}$ = 10). 59

3.2 A realization of the random field with multiple source patches. The fractal field is characterized by the Hurst constant H that determines the spectral decay at high frequencies and parameter k_c that modulates the sizes of the largest features. We choose H = 1 (self-similar distribution) and k_c = 0.14 such that there are multiple similarly-sized high-normal-stress patches within the field. 60

3.3 Representative model domain used in the simulations, normalized with respect to h^*_{uni}, the nucleation size estimate corresponding to σ_{uni}. 61

3.4 Slip velocity snapshots for a typical dynamic rupture event from models with $\sigma_{max}/\sigma_{uni} = 1$ (left) and $\sigma_{max}/\sigma_{uni} = 1.6$ (right). The events are similar in that they span the entire VW region and nucleate from a similar scale comparable to the nucleation size estimate for the model with uniform normal stress. The fractal distribution results in slightly smaller nucleation size and more complex slip pattern for each event. 65

3.5 (Top) Evolution of the maximum slip velocity over the fault for the models with the uniform (blue line), fractal (red line), and modified fractal normal stress with $\sigma_{max}/\sigma_{uni} = 10$ (yellow line). The maximum slip velocity is normalized with respect to the dynamic velocity threshold (V_{dyn}). The time is normalized with respect to the mean recurrence time of events in the model with uniform normal stress. Each vertical line signifies dynamic rupture, as slip rates become much larger than the dynamic threshold (upper dashed line). Flat sections correspond to the loading plate rate. The uniform and fractal cases result in comparable sequences of events, with quasi-periodic model-spanning events in both cases, although the recurrence interval is slightly shorter in the fractal case. The modified fractal case with stronger normal stress heterogeneity exhibits more complex events, with smaller events appearing in between larger events. (Bottom plot) Slip velocity history at the middle of the VW fault region in the uniform normal stress model. Dynamic events are separated by inter-event periods of essentially locked interface, with slip rates several orders of magnitude lower than the loading plate rate (lower dashed line). 66

3.6 Slip velocity snapshots of a typical event nucleation on (a) an interface with uniform normal stress, (b) interface with fractal normal stress, and (c) interface with stronger normal stress heterogeneity of $\sigma_{max}/\sigma_{uni} = 5$. To facilitate the comparison, the size of each panel is the same, $2h^*_{uni}$ by $1.5h^*_{uni}$. The actual simulated nucleation size, h^*_{sim}, is similar to h^*_{uni} in the homogenous case, as expected. h^*_{sim} is measured by the approximate size of the (bright-orange-to-red) area that slips with velocities higher than $0.1V_{dyn}$ when the maximum slip velocity at any point on the fault matches the dynamic velocity threshold V_{dyn}. In the fractal stress case, the event nucleates similarly, from a slightly more irregular patch. The h^*_{sim} is slightly smaller but comparable to h^*_{uni}. In the model with stronger normal stress heterogeneity, model-spanning earthquakes initiate from scales much smaller than the nucleation size estimates calculated based on average properties. The nucleation behavior is governed by the smaller-scale nucleation size based on the local normal stress peaks, i.e. by the length scale of the heterogeneity, rather than h^*_{uni}. 67

3.7 Slip velocity snapshots from two consecutive model-spanning events from the model with $\sigma_{max}/\sigma_{uni} = 5$. There are no smaller-scale events in between. The larger-scale events are nucleating from the asperity scale much smaller than the mean nucleation size estimate. . 71

3.8 Slip velocity snapshots from the model with $\sigma_{max}/\sigma_{uni} = 10$. Small-scale events (panels S1-S2, S5-S6, S8-S9) precede the larger-scale event (S12-S14) and the larger-scale event also nucleates from scales much smaller than h^*_{mean}. The time difference between snapshots S7 and S8 is 6644 normalized time units and the time difference between snapshots S11 and S12 is 47 normalized time units, where 1 unit corresponds to the time for the shear wave to propagate through the length of the fault and hence 1 unit is comparable to the duration of a large-scale event. Hence these events are separated by long enough times to be considered separate events, but short enough times in comparison to the average recurrence time of the large-scale events for the smaller events to be considered a foreshock. 72

3.9 Slip velocity snapshots of typical dynamic event nucleation zones on an interface with modified fractal normal stress and $\sigma_{max}/\sigma_{uni} = 10$ (Figure 3.1d), for small-scale events (top row) and a larger-scale event (bottom row). Both small and large events tend nucleate from scales much smaller than the mean nucleation size and close to the asperity—or heterogeneity—scale, although some large events nucleate differently (Figure 3.10). 73

3.10 Slip velocity snapshots from the model with $\sigma_{max}/\sigma_{uni} = 10$ showing a case of a larger-scale event nucleating from a slipping zone comparable in size to h^*_{uni} (S12). The larger-scale event is still preceded by three small-scale foreshock-like events, separated from the larger-scale event by 4, 4 + 490 = 494, and 494 + 197 = 691 time units (snapshots S9-S10, S6-S7, and S2-S3, respectively). 74

3.11 Models with ten-fold variations in nucleation sizes achieved through combined variations in normal stress and rate-and-state characteristic slip D_{RS}, illustrated by property distributions along the mid-depth of the fault. (a) Distributions of the normal stress and D_{RS} for the case of modified fractal normal stress distribution with $\sigma_{max}/\sigma_{uni} = 10$ considered in the previous section; D_{RS} is uniform in this case. (b) The corresponding distribution of the nucleation size estimate. (c) The case of a fractal normal stress with $\sigma_{max}/\sigma_{uni} = 1.6$ and modified D_{RS} that result in the same distribution of the nucleation size estimate as in (b). (d) The case of uniform normal stress with $\sigma_{max}/\sigma_{uni} = 1$ and modified D_{RS} that result in the same distribution of the nucleation size estimate as in (b). 77

3.12 Slip velocity snapshots from the model M1 with the same distribution of the nucleation size estimate as for the modified fractal normal stress $\sigma_{max}/\sigma_{uni} = 10$ (and hence with $h^*_{uni}/h^*_{min} = 10$ but achieved through a fractal distribution of normal stress with $\sigma_{max}/\sigma_{uni} = 1.6$ and variations in D_{RS}); the snapshots continue in Figure 3.13. The patches of the low nucleation size produce multiple small-scale foreshock-like events, some of which repeat in the same locations. These foreshocks appear to be triggered by the quasi-static nucleation of the subsequent larger-scale event that nucleates from the larger scale comparable to the mean nucleation size. 78

3.13 Slip velocity snapshots from the model M1 with the same distribution of the nucleation size estimate as for the modified fractal normal stress $\sigma_{max}/\sigma_{uni} = 10$ (and hence with $h^*_{uni}/h^*_{min} = 10$ but achieved through a fractal distribution of normal stress with $\sigma_{max}/\sigma_{uni} = 1.6$ and variations in D_{RS}); continued from Figure 3.12. The patches of the low nucleation size produce multiple small-scale foreshock-like events, some of which repeat in the same locations. These foreshocks appear to be triggered by the quasi-static nucleation of the subsequent larger-scale event that nucleates from the larger scale comparable to the mean nucleation size. 79

3.14 Slip velocity snapshots from the model M2 with the same distribution of the nucleation size estimate as for the modified fractal normal stress $\sigma_{max}/\sigma_{uni} = 10$ (and hence with $h^*_{uni}/h^*_{min} = 10$ but achieved through uniform normal stress with $\sigma_{max}/\sigma_{uni} = 1$ and variations in D_{RS}). As for model M1, the patches of the low nucleation size produce multiple small-scale foreshock-like events, some of which repeat in the same locations. These foreshocks appear to be triggered by the quasi-static nucleation of the subsequent larger-scale event that nucleates from the larger scale comparable to the mean nucleation size. 80

4.1 Distribution of event sizes across the models with heterogeneous normal stress. The seismic moments on the horizontal axis are normalized with respect to the mean moment of events from the uniform normal stress model. The fraction of the events in a given moment range is plotted on the vertical axis. Increasing heterogeneity generally leads to increasing complexity in the sizes of larger events and appearance of significantly smaller events. 86

4.2 Distribution of event sizes across the models with heterogeneous normal stress. The seismic moments on the horizontal axis is normalized with respect to the mean moment of events from the uniform normal stress model and plotted in the logarithmic scale. The fraction of events in a given log-normalized moment range is plotted on the vertical axis. The moments plotted in log scale elucidate the richer size distribution, with more sizes represented, with increasing heterogeneity. 87

4.3 Distribution of event sizes across models with the same distribution of the nucleation size estimate as for the modified fractal normal stress $\sigma_{max}/\sigma_{uni} = 10$ (and hence with $h^*_{uni}/h^*_{min} = 10$). The seismic moments on the horizontal axis are normalized with respect to the mean moment of events from the model with uniform normal stress and D_{RS}. The fraction of the events in a given moment range is plotted on the vertical axis. (Top) Results for the modified fractal distribution with $\sigma_{max}/\sigma_{uni} = 10$ and uniform D_{RS}. (Bottom left) Results for uniform normal stress and modified D_{RS}. (Bottom right) Results for a fractal distribution of normal stress with $\sigma_{max}/\sigma_{uni} = 1.6$ and modified D_{RS}. Strong heterogeneity in normal stress results in more significant variation in sizes of the larger events while the heterogeneity in D_{RS} generates a large fraction of small-scale events. 88

4.4 Distribution of event sizes across models with the same distribution of the nucleation size estimate as for the modified fractal normal stress $\sigma_{max}/\sigma_{uni} = 10$ (and hence with $h^*_{uni}/h^*_{min} = 10$). The seismic moments on the horizontal axis are normalized with respect to the mean moment of events from the uniform normal stress model and plotted in the logarithmic scale. The fraction of the events in a given log-normalized moment range is plotted on the vertical axis. (Top) Results for the modified fractal distribution with $\sigma_{max}/\sigma_{uni} = 10$ and uniform D_{RS}. (Bottom left) Results for uniform normal stress and modified D_{RS}. (Bottom right) Results for a fractal distribution of normal stress with $\sigma_{max}/\sigma_{uni} = 1.6$ and modified D_{RS}. Strong normal stress heterogeneity results in a more significant variation of larger-scale events and some intermediate events. Cases with the modifying D_{RS} distribution generate a larger number of much smaller events and no intermediate events. 89

4.5 Cumulative distributions of event sizes representing all events occurring above each log normalized moment range plotted in log scale for models with normal-stress heterogeneity. b-values of the Gutenberg-Richter scaling law are calculated for each model for the moment range $\log_{10}(\mathrm{M_o}/\bar{\mathrm{M}}_{\mathrm{o,uniform}}) \in [-2.5, 0]$). The b-values first systematically increase with increasing heterogeneity until $\sigma_{max}/\sigma_{uni} = 8$ and then stay in the range of $0.35 - 0.55$ after. 90

4.6 Cumulative distribution of event sizes representing all events occurring above each log normalized moment range, plotted in log scale, for models with the same distribution of the nucleation size estimate as for the modified fractal normal stress with the largest heterogeneity $\sigma_{max}/\sigma_{uni} = 10$ (and hence with $h^*_{min}/h^*_{uni} = 0.1$). b-values are close to 0 for the models with modified D_{RS} distribution in the event size range $\log_{10}(\mathrm{M_o}/\bar{\mathrm{M}}_{\mathrm{o,uniform}}) \in [-2.5, 0]$, reflecting the absence of intermediate-scale events and lack of variation in the larger-scale event sizes. For the models with modified D_{RS} distribution, b-values are also calculated in the range $\log_{10}(\mathrm{M_o}/\bar{\mathrm{M}}_{\mathrm{o,uniform}}) \in [-6, -3]$, denoted by b^*. 91

4.7 Static (shear) stress drops across different models with increasing heterogeneity in normal stress. The stress drops of larger-scale events are indicated by bigger red circles and those of other events by smaller circles. The larger-scale event stress drops are nearly the same with increasing normal stress heterogeneity. The median stress drops at each heterogeneity level are indicated by blue diamonds, and have a nominally increasing trend. 94

4.8 Variation of stress drops for models with uniform normal stress, fractal normal stress, and three models with the same distribution of the nucleation size estimate as for the modified fractal normal stress with the largest heterogeneity $\sigma_{max}/\sigma_{uni} = 10$. The stress drops of larger-scale events are indicated by bigger red circles and those of other events by smaller circles. The median stress drops at each heterogeneity level are indicated by blue diamonds. The models with modified D_{RS} distributions have median stress drops below $\Delta\tau_{uni}$. . . 95

4.9 Variation of stress drops with event sizes for several models. 96

4.10 Variation of larger-scale-event recurrence time with increasing normal stress heterogeneity levels, visualized by box plots. The median recurrence time at each heterogeneity level is indicated by the red line. The recurrence times are normalized with respect to the recurrence time of events in the uniform normal stress model. The larger-scale-event recurrence times remain more or less comparable with increasing normal-stress heterogeneity. 98

4.11 Variation of larger-scale-event recurrence time, visualized by box plots, for the models with uniform normal stress, fractal normal stress, and models preserving the local nucleation size distribution with $h^*_{min}/h^*_{uni} = 0.1$, in different ways. The median larger-scale-event recurrence time for each model is indicated by the red line. The recurrence times are normalized with respect to the recurrence time of events in the uniform normal stress model. The larger-scale-event recurrence times in the models with modified D_{RS} distributions have less variation. 99

4.12 STFs from the uniform fault model, $\sigma_{\max}/\sigma_{\text{uni}} = 1$. a. STF using slip-velocity threshold for event identification. Time is normalized by the time for the shear wave to traverse the length of the VW fault region. Moment rate is normalized by the peak moment rate of the uniform fault model. b. STF using moment-rate threshold for event identification c. STF using moment rate threshold for event identification with a different normalization: time is normalized by each rupture duration and moment rate is normalized such that the area integrates to unity. 102

4.13 STFs from the fractal normal-stress model with $\sigma_{\max}/\sigma_{\text{uni}} = 1.6$. Same plotting conventions as Figure 4.12. 103

4.14 Comparison of typical events in the models with uniform ($\sigma_{\max}/\sigma_{\text{uni}} = 1$) and fractal ($\sigma_{\max}/\sigma_{\text{uni}} = 1.6$) normal-stress distributions. (Top) STFs. (Bottom) Slip-rate snapshots. The differences in the shape of STF and peak moment rates reached is affected by where the event nucleates and rupture directivity. 104

4.15 Comparison of typical events in the model with uniform normal stress and reduced D_{RS} and in the model with the fractal normal stress ($\sigma_{\max}/\sigma_{\text{uni}} = 1.6$). The event in the uniform model with lower D_{RS}—and hence lower nucleation size—nucleates closer to the edge, becoming more similar to the fractal case. 105

4.16 STFs from $\sigma_{\max}/\sigma_{\text{uni}} = 3$ model. Same plotting conventions as Figure 4.12. 107

4.17 STFs from $\sigma_{\max}/\sigma_{\text{uni}} = 4$ model. Same plotting conventions as Figure 4.12. 108

4.18 STFs from $\sigma_{\max}/\sigma_{\text{uni}} = 5$ model. Same plotting conventions as Figure 4.12. 109

4.19 STFs from $\sigma_{\max}/\sigma_{\text{uni}} = 6$ model. Same plotting conventions as Figure 4.12. 110
4.20 STFs from $\sigma_{\max}/\sigma_{\text{uni}} = 7$ model. Same plotting conventions as Figure 4.12. 111
4.21 STFs from $\sigma_{\max}/\sigma_{\text{uni}} = 8$ model. Same plotting conventions as Figure 4.12. 112
4.22 STFs from $\sigma_{\max}/\sigma_{\text{uni}} = 9$ model. Same plotting conventions as Figure 4.12. 113
4.23 STFs from $\sigma_{\max}/\sigma_{\text{uni}} = 10$ model. Same plotting conventions as Figure 4.12. 114
4.24 STFs from $\sigma_{\max}/\sigma_{\text{uni}} = 1$, $D_{\text{RS,min}}/D_{\text{RS,uni}} = 0.1$ model. Same plotting conventions as Figure 4.12. 115
4.25 STFs from $\sigma_{\max}/\sigma_{\text{uni}} = 1.6$, $D_{\text{RS,min}}/D_{\text{RS,uni}} = 0.16$ model. Same plotting conventions as Figure 4.12. 116
4.26 Events with hesitant initial moment-rate release in models across normal-stress heterogeneity levels. The events are identified here using moment-rate threshold. This draws parallels to STFs of natural events from Ellsworth and Beroza (1995) shown in Figure 1.5. 117
4.27 Comparison of the median STFs (with the seismic moments normalized to unity) for events in different models. (Top) Models with modified fractal normal-stress distributions and $\sigma_{max}/\sigma_{uni} = 3, 4, 5, 6, 7, 8, 9, 10$. The median STFs are all similar, despite the differences between individual events and different models. (Bottom) Median STFs for the uniform model ($\sigma_{max}/\sigma_{uni} = 1$) and the model with the fractal stress ($\sigma_{max}/\sigma_{uni} = 1.6$) have different shapes. 118
4.28 Modifying the typical median STF shape from Figure 4.27 (red line) by assuming more gradual rupture arrest (black dashed line) and renormalizing the area to 1 (blue line) results in an STF shape (left plot) comparable to that of natural events (right plot, Meier et al., 2017). 120
4.29 STFs from $\sigma_{max}/\sigma_{uni} = 8$ model in the event size range $\log_{10}(M_o/\bar{M}_{o,\text{uniform}}) \in [-0.7, -0.5]$. Same plotting conventions as Figure 4.12. 122
4.30 STFs from $\sigma_{max}/\sigma_{uni} = 8$ model in the event size range $\log_{10}(M_o/\bar{M}_{o,\text{uniform}}) \in [-1.5, -1.4]$. Same plotting conventions as Figure 4.12. 123
4.31 STFs from $\sigma_{max}/\sigma_{uni} = 8$ model in the event size range $\log_{10}(M_o/\bar{M}_{o,\text{uniform}}) \in [-2.3, -2.1]$. Same plotting conventions as Figure 4.12. 124

4.32 Median STFs across different event size ranges from the $\sigma_{max}/\sigma_{uni} = 8$ model. (Top) Event duration is normalized by the time for the shear wave to propagate through the fault length while the moment rate is normalized by the peak moment rate from the uniform model. The STFs indicate that large events are small events that ran away. (Bottom) Event duration and moment are both normalized to 1. The smallest-scale event (shown in red) is least affected by the model dimensions and has the shape comparable to the typical behavior of natural earthquakes (Figure 1.6). 125

4.33 Slip velocity snapshots from the model with $\sigma_{max}/\sigma_{uni} = 8$ illustrating the beginning and end of a typical event from the different event-size ranges considered. The snapshots help visualize the rupture area of the events in each size range and how their dynamic propagation is affected by the finite geometry of the seismogenic region. 126

4.34 (Top) Median STFs across different event size ranges from the $\frac{\sigma_{\max}}{\sigma_{\text{uni}}} = 1, \frac{D_{RS,\min}}{D_{RS,\text{uni}}} = 0.1$ model. Event duration is normalized by the time for the shear wave to propagate through the fault length while the moment rate is normalized by the peak moment rate from the uniform model. Note that the small-scale events are so small that their median STFs are barely visible relative to the large-scale event. (Bottom) The initial rates of the median STFs across the size ranges are observed in a zoomed-in version. The median STF of the large event grows much faster initially than the much smaller events from the same model. . . 127

4.35 Source time function of a larger-scale event from $\sigma_{max}/\sigma_{uni} = 7$ model which shows a cascade-like sequence of small-scale ruptures preceding the larger-scale rupture. Plotted using a velocity-based threshold, the entire sequence is considered the same large-scale dynamic event. 129

4.36 Slip velocity snapshots visualizing the large-scale event from Figure 4.35 indicate the small-scale ruptures in S1, S6, and S10 which precede the large-scale event (Continued in next figure). 130

4.37 Slip velocity snapshots visualizing the large-scale event from Figure 4.35 indicate the complex rupturing and re-rupturing of asperities which build up to the large-scale event which eventually ruptures the entire interface. 131

4.38 Slip velocity snapshots from Figure 4.36 plotted in a color scale that emphasizes the triggering processes of the cascade sequence preceding the large-scale event. (Continued in next figure) 132
4.39 Slip velocity snapshots from Figure 4.37 plotted in a color scale that emphasizes the high frequency ruptures that accompany the large-scale event. 133
4.40 Maximum slip velocity history for the 5 mainshock cycles from $\sigma_{max}/\sigma_{uni} = 7$ model indicates the mainshocks and the location of intershocks relative to them. The rest of the small-scale events identified in this interval by the velocity threshold (8 small-scale events in total) occur as foreshock-like or aftershock-like events to the 5 mainshocks. 134
4.41 STFs of two larger-scale events from $\sigma_{max}/\sigma_{uni} = 7$ model plotted using a velocity-based threshold which shows one event (red) with a cascade-like sequence of small-scale ruptures preceding it. The second event (blue) has only a single, immediately preceding foreshock-like bump. 135
4.42 Maximum slip velocity history for the 5^{th} mainshock, indicated by the blue STF in Figure 4.41 from $\sigma_{max}/\sigma_{uni} = 7$ model during ~ 80 dynamic time scale units before the beginning of the event. There are no other foreshock-like small-scale events preceding it. 135
4.43 Slip velocity snapshots visualizing the larger-scale event indicated by the blue STF from Figure 4.41. The small foreshock-like bump is indicated by snapshots S4-S7, right before the moment rate builds up rapidly from S8. 136

LIST OF TABLES

Number *Page*

2.1 Model parameters used in our simulations 20

2.2 Fault models studied 25

2.3 Mean source properties for all models with two patches, from left to right: Mean seismic moment on the left patch, mean seismic moment on the right patch, mean recurrence time on the left patch, mean recurrence time on the right patch, mean stress drop on the left patch, and mean stress drop on the right patch. 53

2.4 Simulated source properties for all models with two patches, median values and inter-quartile ranges (IQR). 54

3.1 Fault parameters used in simulations 62

3.2 Comparison between σ_{uni}, σ_{mean}, h^*_{uni}, $h^*_{\sigma_{mean}}$ and h^*_{mean}. The differences between the mean parameter values and the parameter values corresponding to the uniform model result from removing part of the domain. 62

Chapter 1

INTRODUCTION

1.1 Motivation

Predicting the strength and stability of heterogeneous frictional interfaces is an outstanding problem, relevant to a broad range of fields—from biology and nano-mechanics to geophysics. Frictional interfaces, broadly, can have either stable slip or unstable slip (i.e., relative shear motion). On loading a frictional interface with a loading velocity V_{load}, the interface slips stably if it has the same or similar velocity. When the slip is unstable, it self-accelerates to slip velocities much larger than V_{load}. Even after stopping the loading, the slip keeps accelerating. The unstable slip is often inertially-controlled and dynamic. Frictional instability is observed in many mechanical systems and is considered desirable or undesirable, depending on the application.

In the field of earthquake mechanics, gaining a better understanding of frictional instabilities has implications on earthquake prediction and seismic hazard management. Tectonic earthquakes seldom occur by the sudden appearance and propagation of a new fault (shear crack). Instead, they mostly occur by sudden slippage along pre-existing faults or plate interfaces. They are therefore a frictional, rather than fracture, phenomenon. In other words, it is the frictional resistance on the fault that governs the occurrence of earthquakes and other slip behaviors on the fault.

Fault processes involve complex patterns of both dynamic events—seismic slip perceived as earthquakes—and quasi-static (aseismic) slip. Some fault segments remain locked (accumulating stress), some steadily creep (slow slippage). Scientists link this behavior to velocity strengthening and weakening properties of fault segments. For an interface to be unstable (have spontaneous stick-slip), a necessary condition for instability is that friction needs to weaken once slipping starts. Seismic slip and aseismic faulting, however, are just the end members of a continuous spectrum of behaviors.

Field and experimental observations have shown that slip behavior on natural faults exhibits spatio-temporal complexity over a wide range of scales, ranging from stable slip, aseismic transients, small repeating events, foreshock sequences to large earthquakes (McGuire et al., 2005; Bouchon et al., 2011; Kato et al., 2012; Bouchon

et al., 2013; McLaskey and Kilgore, 2013; McLaskey and Lockner, 2014; Brodsky and Lay, 2014; Avouac, 2015; Bürgmann, 2018; Michel et al., 2019). The same area of the fault can sometimes behave stably and sometimes unstably (Chen et al., 2010). Studies in the past have noted that heterogeneity in frictional properties on the fault zone has a sizable contribution in producing this rich diversity of slip behaviors (Hillers et al., 2006; Hillers et al., 2007; Kaneko and Lapusta, 2008; Chen and Lapusta, 2009; Dublanchet et al., 2013; Avouac, 2015; Lui and Lapusta, 2016; Jiang and Lapusta, 2016; Lui and Lapusta, 2018; Schaal and Lapusta, 2019). The variations in frictional properties can also correlate to heterogeneity in other fault zone properties like effective normal stress and critical slip weakening distance in a coupled fashion. Understanding this link between fault zone properties and resulting slip behavior, feeding into the eventual goal of developing a self-contained, physics-based model of the faults is crucial to the field of earthquake physics.

In this thesis, our focus is on understanding the mechanics of friction on fault interfaces with heterogeneous frictional properties and how that translates into the different slip patterns observed on natural faults. In particular, we investigate the effect of heterogeneity in fault properties on variability in repeating sequences, the earthquake initiation process and complexity of sequences and larger-scale ruptures.

1.2 Modeling variability and interaction of repeating earthquake sequences on heterogeneous faults

Repeating earthquake sequences are groups of events that have similar waveforms, locations, and magnitudes. They "repeat" with nearly identical locations but have aperiodic or quasi-periodic recurrence intervals (Vidale et al., 1994; Nadeau et al., 1994; Nadeau and Johnson, 1998; Ellsworth and Beroza, 1995; Chen et al., 2010). Due to their known locations and average recurrence times, repeating earthquakes present a great opportunity to learn more about earthquake source and its physics (Ellsworth and Dietz, 1990; Vidale et al., 1994; Marone et al., 1995; Nadeau and Johnson, 1998; Schaff et al., 1998; Nadeau and McEvilly, 1999; Nadeau and McEvilly, 2004; Bürgmann et al., 2000; Beeler et al., 2001; Sammis and Rice, 2001; Igarashi et al., 2003; Imanishi et al., 2004; Nadeau et al., 2004; Schaff and Beroza, 2004; Matsubara et al., 2005; Allmann and Shearer, 2007; Chen et al., 2007; Rubinstein et al., 2012). Since these events occur at depth, it is not possible to directly observe the physical conditions on the fault segment hosting them. A widely accepted interpretation is that they occur at separated instability-promoting patches or asperities, surrounded by a creeping segment that keeps loading them,

resulting in persistent localized instabilities at nearly identical locations (Chen and Lapusta, 2009; Lui and Lapusta, 2016; Lui and Lapusta, 2018).

Observations of the repeater sequences indicate that they display significant variability, both in their moment and recurrence time (Nadeau and Johnson, 1998; Rubinstein et al., 2012). The variability can be studied by comparing the behavior to time- and slip-predictable models (Bufe et al., 1977; Shimazaki and Nakata, 1980), which provide simplified physics-based interpretations of earthquake behavior. The slip-predictable model postulates that the final slip—and hence the size—of an earthquake grows proportionally with the time since the previous earthquake (and hence the slip can be predicted based on the recurrence time). The time-predictable model postulates that the time to the next earthquake scales proportionally with the size of the previous earthquake (and hence the time to next earthquake can be predicted based on the size of the previous event). An idealized repeater sequence with a constant event size and constant recurrence time would be both time- and slip-predictable. However, repeating earthquake sequences are found to substantially deviate from such simple models (Figure 1.1, Rubinstein et al., 2012).

In this study, we mainly focus on modeling the behavior of the San Francisco (SF) and Los Angeles (LA) repeating earthquake sequences (Figure 1.2) in the Parkfield creeping fault segment, which were the targets of the San Andreas Fault Observatory at Depth (SAFOD) (Hickman et al., 2004) project. Before the 2004 Parkfield earthquake, the SF and LA repeating sequences had occurred with a recurrence interval of $\sim$ 3 years and the mean moment magnitude of $\bar{M}_w = 2.04$ and $\bar{M}_w = 1.84$ for the SF and LA repeaters, respectively. The hypocenters of the repeaters are separated by $60 - 70$ m along strike, at similar depths of approximately 3 km (Nadeau and Johnson, 1998; Zoback et al., 2011). The recurrence times of SF repeaters was 2.89 ± 0.35 years (Lui and Lapusta, 2018). The time progression of moment magnitudes of the LA-SF repeater sequence indicates significant variability within the sequences (Figure 1.2a). The LA events occurred shortly after the SF events, pointing to strong interaction between the two sequences, with inter-event times spanning from few seconds to months. It is important to understand how much this interaction between the two repeater sources affects their variability of occurrence. The triggering times of the LA events by the SF events (Figure 1.2b) span a wide range, from a significant (0.25) to a tiny (10^{-6}) fraction of the recurrence interval. The time- and slip-predictability plots for the LA-SF repeating sequences (Figure 1.2c) further visualize their variability.

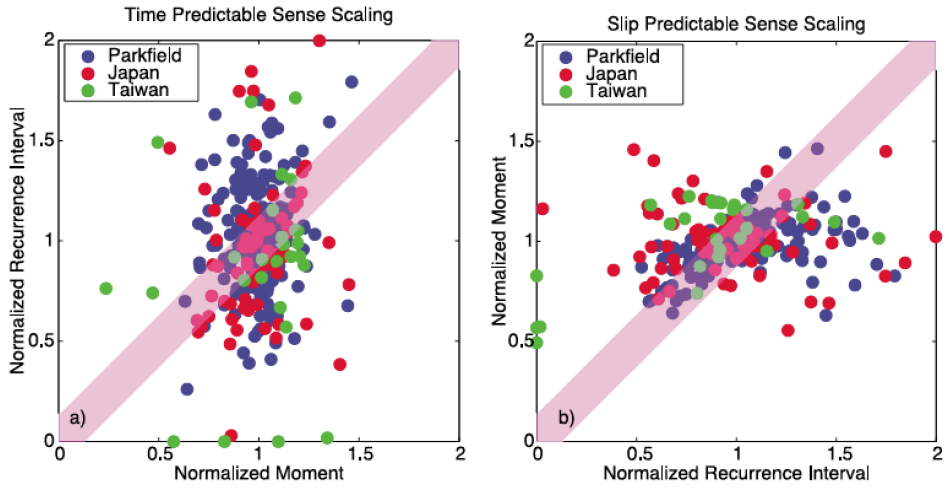

Figure 1.1: Repeating sequences from several tectonic regions are neither time- nor slip-predictable (adapted from Rubinstein et al., 2012). (Left) The recurrence time interval between events vs. the seismic moment of the preceding event, normalized by the mean recurrence interval and mean seismic moment, respectively. If the recurrence interval increases predictably with the moment of the preceding event, then it would fall onto the pink strip. (Right) The seismic moment of events vs. the recurrence interval preceding the event, normalized by the mean seismic moment and recurrence interval, respectively. If the seismic moment (and hence slip) increases predictably with the time since the previous event, then it would fall onto the pink strip.

On comparing the predictability plots for the seven LA-SF repeating event pairs (Figure 1.2c) to the corresponding plots for a number of repeating sequences taken together (Figure 1.1), we observe that the overall sense of variability is different. The predictability plots of the LA and SF events show more variation in seismic moment then in recurrence time, whereas the variability in recurrence time is seen to be more substantial than that in the seismic moment for several other sequences taken together. Since our models simulate the LA and SF repeaters, we aim to reproduce the variability exhibited by the (limited) data of the SF and LA events.

In order to quantify the variability of a sequence, we use the median and inter-quartile range (IQR), which are appropriate measures to characterize non-normal data. We use box plots (Figure 1.3) to provide illustrative insights regarding the distribution of source parameters. The box plots divide the sorted data into four sections or quartiles, which approximately contain 25% of the data each. The median is indicated by the red line that divides the box into two sections. The upper and lower quartiles, Q_1 and Q_3, enclose the middle 50% of the data and provides

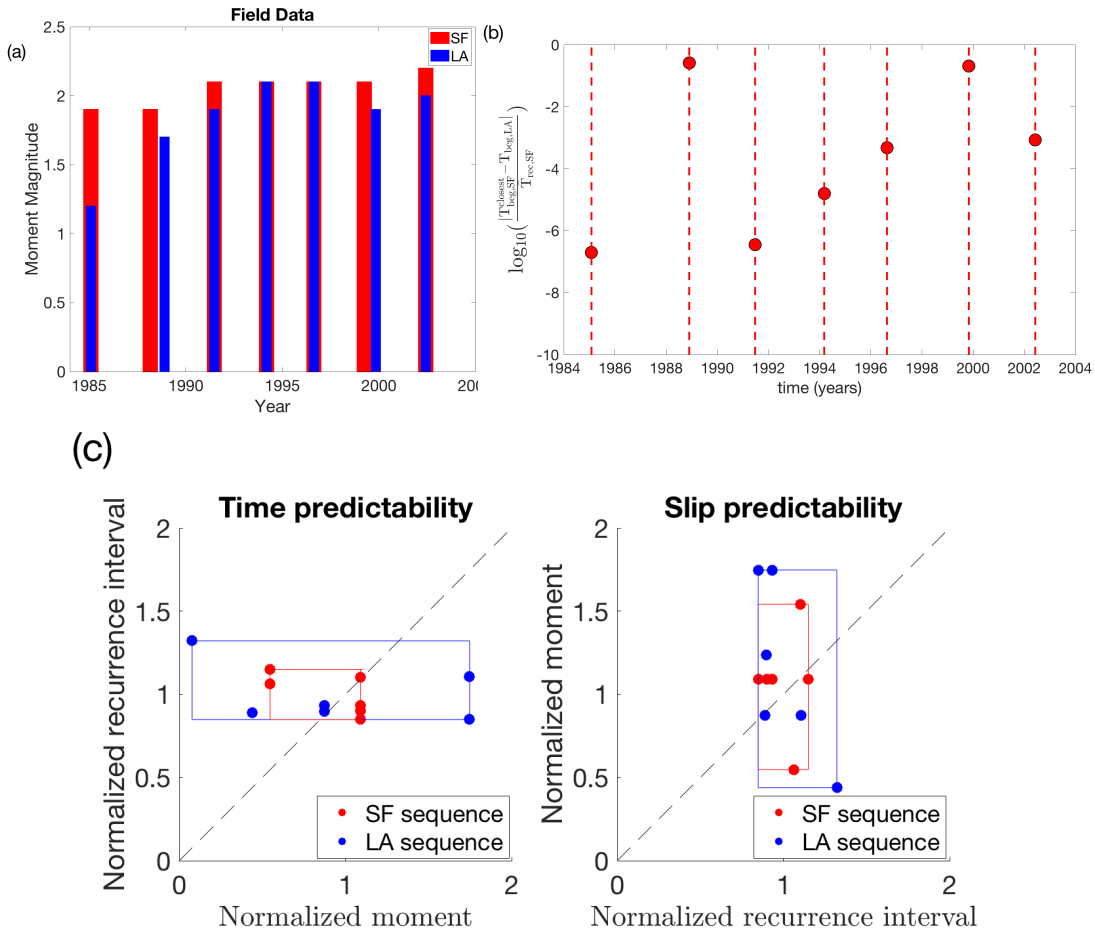

Figure 1.2: a. Time progression of moment magnitudes of SF-LA repeater sequences, before the 2004 M6 Parkfield earthquake. The LA events (blue bars) consistently happen soon after the SF events (red bars), indicating a strong interaction between the two sequences, with inter-event times spanning from seconds to months. (Data from Waldhauser and Schaff (2008)) b. Triggering times for the 7 SF-LA event pairs before 2004, plotted on a log-scale normalized with respect to the mean recurrence time of SF sequence. The triggering times range from seconds to months. c. Testing time predictability and slip predictability for 6 recurrence periods of SF and LA sequences before the 2004 M6 earthquake. The axes are normalized with respect to the mean quantities. The red and blue rectangles bound the variability of SF and LA events, respectively.

the IQR measure, IQR = $Q_3 - Q_1$. The upper and lower whiskers of the box plot indicate the range of the non-outlier data.

The box plots of the moment and recurrence times of SF-LA repeaters in Figure 1.3 are normalized with respect to their respective median quantities and illustrate

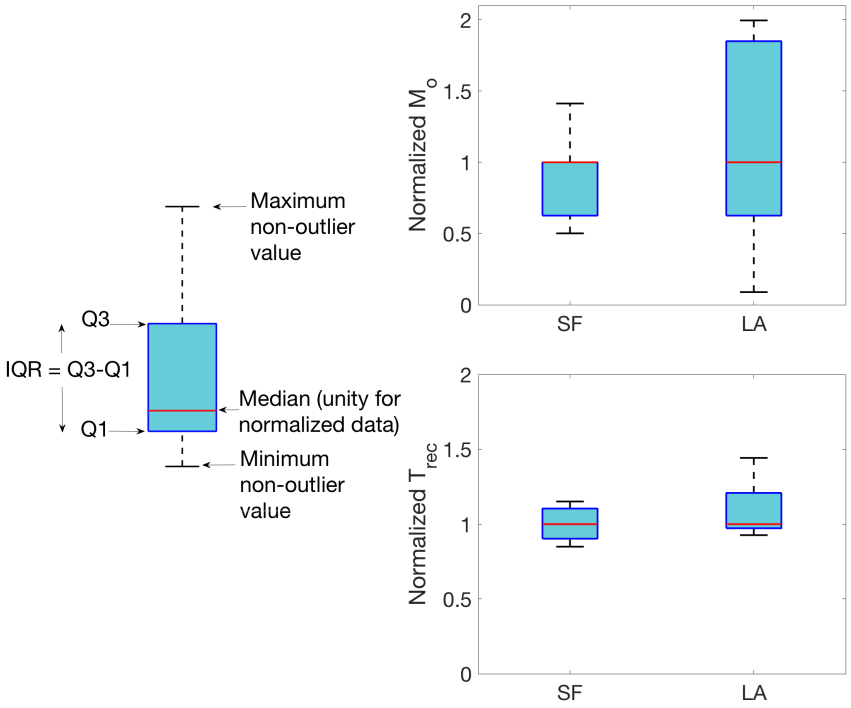

Figure 1.3: (Left) Schematic of a typical boxplot, indicating the median, inter-quartile range, the first (Q1) and second (Q3) quartiles bounding the middle 25% of data, with the maximum and minimum non-outlier values in the data set indicated by the whiskers. (Right) Box plots constructed for normalized seismic moment and recurrence times of SF and LA repeaters show the variability to be higher in the LA repeaters.

the larger variability in the LA events, especially in moment but also in recurrence time, when compared to the SF events. This is inferred from the larger box widths, and hence IQR measures, of the LA box plots, relative to SF events.

Some of the variability can be reproduced by the inherent complexity of slip, even in models of uniform circular seismogenic patches embedded within uniform creeping matrix, as the existing models show (Lui and Lapusta, 2016; Lui and Lapusta, 2018). However, the variability may be pointing to more heterogeneous fault properties. In natural faults, seismogenic sources are unlikely to be circular and homogeneous. Indeed, inversions of some of the repeating earthquakes based on the recordings from the SAFOD array show complex shapes of the resulting final slip (Dreger et al., 2007). For example, natural fault surfaces have roughness, shown to follow fractal trends (Candela et al., 2012; Sagy et al., 2007). Mature faults may be smoother, especially on short length scales relevant to recent fault slip (Sagy et al.,

2007; Brodsky et al., 2011). However, non-planarity may translate into significant variations of fault properties, giving rise to complex dynamics (Fang and Dunham, 2013; Tal et al., 2018). Faults can also contain regions with different friction properties (Igarashi et al., 2003; Kaneko et al., 2010; Fagereng and Sibson, 2010; Avouac, 2015). Such fault heterogeneity can have significant effects on spatio-temporal patterns of slip events (Hillers et al., 2006; Hillers et al., 2007; Kaneko et al., 2010; Skarbek et al., 2012; Dublanchet et al., 2013; Yabe and Ide, 2017; Luo and Ampuero, 2018).

In this study, we move one step beyond the current models of repeating earthquakes in the direction of realistic fault heterogeneity by considering more complex shapes of the source patches and the effect of nearby perturbing sub-critical patches. Our study is motivated by the ideas in Lui and Lapusta (2016), Lui and Lapusta (2018) that the observations, specifically the range of triggering times of the LA-SF sequences, can be used to constrain the properties of the velocity-strengthening region between the interacting patches, since most of the interaction in those studies was linked to the stress changes due to postseismic fronts that propagate through the velocity-strengthening region. However, one can also change the timing of the postseismic slip arriving at the other patch by changing the distributions of friction properties between the two patches to be more irregular, which can be accomplished through more complex shapes of the patches.

We find that realistic degree of variability in repeating sequences and the required range in the repeater triggering times are both reproduced by models with realistically complex patch geometries. Similar results are also reproduced by models with simple source patch geometries embedded in a more compliant creeping region. Hence the observed variability in moment magnitudes and recurrence times, and the observed range of triggering times, are not sufficient to constrain the fault properties even of the relatively geometrically simple models considered in this work.

1.3 Nucleation processes on interfaces with heterogeneous normal stress

Theoretical modeling and laboratory experiments have shown that a period of accelerating quasi-static slip precedes dynamic rupture growth (Dieterich, 1992; Ohnaka, 1992; Mikumo, 1992; Rice, 1993; Rubin and Ampuero, 2005; Kaneko et al., 2016). This process marking the transition from the locked interface to unstable, dynamic slip is termed earthquake nucleation, and the minimum size of the quasi-statically slipping zone before the inertially driven rupture is termed the nucleation size (h^*).

The nucleation process on a rate-and-state friction interface with uniform properties has a relatively well-understood progression of events (Dieterich, 1992; Rice, 1993; Lapusta et al., 2000). The slip begins at some location on the interface, spreads as it accelerates, reaches the nucleation length scale, and transitions to a dynamic slip event.

But fault interfaces are rarely homogeneous. Anderson (1951) recognized that natural fault surfaces are not planar, but irregular at all scales. Early measurements by Brown and Scholz (1985), Power et al. (1988), and Lee and Bruhn (1996) concluded that natural fault surfaces are self-similar fractals. Many recent studies have provided high resolution measurements of fault roughness, using a variety of techniques including analysis of surface traces at the largest scales, over orders of magnitude in length (Renard et al., 2006; Candela et al., 2009). Mature faults may be much smoother, especially on short length scales relevant to recent fault slip (Sagy et al., 2007; Brodsky et al., 2011). At larger scales however, non-planarity may translate into significant variations of compressive stress across the fault, giving rise to complex dynamics (Fang and Dunham, 2013; Tal et al., 2018).

Another source of evidence for heterogeneity in fault properties is the abundant field and laboratory observations showing significant spatio-temporal complexity in slip behavior on fault interfaces, ranging from stable slip, aseismic transients, small repeating events, foreshock sequences to large earthquakes (McGuire et al., 2005; Bouchon et al., 2011; Kato et al., 2012; Bouchon et al., 2013; McLaskey and Kilgore, 2013; McLaskey and Kilgore, 2013; McLaskey and Lockner, 2014; Brodsky and Lay, 2014; Avouac, 2015; Bürgmann, 2018; Michel et al., 2019). While part of that could be due to inherent complexity of slip even in simple geometries, due to a range of coupled and highly nonlinear fault processes, as the existing models show (Lui and Lapusta, 2016; Segall et al., 2010), such behavior may also be pointing to heterogeneity in fault properties (Hillers et al., 2006; Hillers et al., 2007; Kaneko and Lapusta, 2008; Chen and Lapusta, 2009; Avouac, 2015; Lui and Lapusta, 2016; Jiang and Lapusta, 2016; Lui and Lapusta, 2018; Schaal and Lapusta, 2019). Understanding the implications of heterogeneity in fault properties on initiation of earthquake slip is an important open problem which can be important in seismic hazard assessment.

On an interface with heterogeneous distribution of fault properties, the earthquake nucleation process is not as straightforward as the one on a uniform interface. For example, in the study of Schaal and Lapusta (2019), the interface contained several

strong round patches of high normal stress. As the quasi-static slip of the nucleation process surrounds such a patch, it can break into a dynamic event, resulting in the rupture starting from these local patches. These events either arrest quickly and remain small-scale events or, in the presence of favorable fault conditions, grow into larger-scale events that nucleate from scales much lower than that the mean nucleation size estimate corresponding to the background fault properties. There are multiple open questions in earthquake science regarding the nucleation processes and slip behavior on faults hosting such small-scale events. Do smaller earthquakes and larger earthquakes nucleate similarly? Are larger earthquakes just smaller events that ran away? Can the smaller events be recognized as foreshocks of the subsequent larger events?

On natural faults, many large earthquakes are preceded by foreshocks (e.g., Jones and Molnar, 1976; Jones and Molnar, 1979; Abercrombie and Mori, 1996; Dodge et al., 1995; Dodge et al., 1996; Zanzerkia et al., 2003; McGuire et al., 2005; Bouchon et al., 2011; Bouchon et al., 2013; Kato et al., 2012; Brodsky and Lay, 2014), which are defined as smaller seismic events that occur within a certain distance in time and space to the main event. The physical mechanisms for foreshocks as well as their potential role in the nucleation of larger events are currently open questions. One point of view is that foreshocks are due to clustering of microseismicity, which occasionally results in a much larger event, as manifested by Epidemic Type Aftershock Sequence (ETAS) models (e.g., Helmstetter et al., 2003). In this interpretation, the largest event is simply an aftershock of foreshocks, and there is no special relationship between foreshocks and the nucleation process of a larger event. An alternative explanation is that foreshocks occur on fault patches loaded by the surrounding quasi-static (slow) slip, potentially signifying the nucleation of an upcoming large event (e.g., Kanamori and Stewart (1976) and Jones and Molnar (1979)). Detailed studies in several areas have indeed shown that foreshocks require additional factors beyond typical aftershock interactions. For example, Dodge et al. (1995) investigated the foreshock sequence before the 1992 M 7.3 Landers earthquake and established that the foreshocks were too far to trigger each other by static stress changes, the typical explanation for aftershock interactions; they hypothesized that the foreshocks were driven by aseismic slip interacting with heterogeneities. McGuire et al. (2005) investigated foreshock and aftershock sequences on the East Pacific Rise transform faults, determined that the foreshocks are too numerous in comparison with aftershocks to be explained by the same ETAS model, and concluded that an additional factor is needed to trigger the foreshocks, such as slow

slip. Bouchon et al. (2013) analyzed foreshocks before large (M > 6.5) events from well-instrumented areas and found that there is significantly more seismicity before interplate events than before intraplate ones. They speculate that the reason for this difference is a slow nucleation process in the case of interplate events that triggers the foreshocks. Furthermore, observations from the 2011 M 9.0 Tohoku-Oki event (Kato et al., 2012) and 2014 M 8.1 earthquake in north Chile (Brodsky and Lay, 2014) reveal foreshock sequences that propagate along the fault, consistent with being triggered by slow slip; in the Tohoku-Oki case, the slow-slip explanation is further supported by the presence of repeating earthquakes among the foreshocks. The possibility of large-scale slow slip in areas where large earthquakes nucleate is further supported by the observations of slow slip transients (e.g., Segall et al. (2010) and references therein).

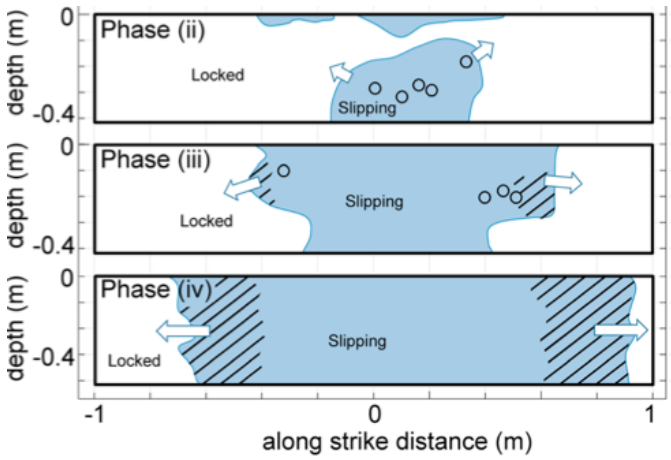

Figure 1.4: Schematics of slip evolution on the lab fault (from McLaskey and Kilgore, 2013). Slow earthquake nucleation (blue) that eventually grows into dynamic rupture (shaded blue) triggers microseismicity (circles). Presumably, similar processes occur during foreshock sequences on real faults, just on a different scale.

The nature of fault patches that could produce foreshocks can be glimpsed from unique laboratory experiments of earthquake nucleation in a meter-scale slab of granite (McLaskey and Kilgore, 2013; McLaskey et al., 2014). The experiments produce quasi-static accelerating slip (nucleation process) that grows into dynamic rupture. Significantly, smaller seismically detectable events—foreshocks—occur in the nucleation region, highlighting the potential role of heterogeneity in earthquake nucleation (Figure 1.4). The foreshocks observed in the experiment occur in locations that are consistent from one sample-spanning event to another, suggesting that they occur on persistent fault patches with properties that are different from the rest

of the sample. The study of Schaal and Lapusta (2019) suggested that patches of elevated normal stress can explain many aspects of the experimental observations.

Here, we explore the evolution of complex nucleation processes on fault interfaces with systematically increasing heterogeneity in normal stress. We choose to study the heterogeneity in normal stress for two reasons. First, significant variations in normal stress are a natural outcome of even slight local fault nonplanarity, so they are clearly present on natural faults. Second, this ubiquitous heterogeneity results in two competing effects on fault slip. On the one hand, the more compressed fault spots have higher shear resistance, for the same friction properties, so they are "stronger," while the less compressed spots are "weaker" and should promote slip. On the other hand, the nucleation sizes of unstable frictional slip that leads to dynamic rupture are inversely proportional to the normal stress (e.g., Equation 2.3), and hence the more compressed spots are more prone to instability and dynamic events. Together, these properties result in fascinating slip dynamics that we explore here. We study the transition in the style of nucleation of large-scale events and occurrence of small-scale events as we go from a uniform interface to an interface with strong normal-stress heterogeneities.

1.4 Effect of heterogeneous fault property distributions on complexity of sequences and evolution of dynamic ruptures

An important step in the path to constrain properties of natural faults is to quantify their heterogeneity by calibrating model outcomes with observations. To that end, we study how the heterogeneity in fault properties affects several characteristics of fault behavior that are observable, such as distribution of dynamic event sizes, stress drops, and moment-rate evolution (also called source-time functions) of the resulting dynamic events.

The distribution of dynamic event sizes on natural faults is typically described by the frequency-magnitude distribution of seismicity, with earthquake ruptures binned into magnitude ranges, with each bin characterized by the number of earthquakes of that size or larger. Field observations of the frequency-magnitude distribution are typically analyzed in the framework of the Gutenberg-Richter scaling law. The law is empirically expressed as

$$\log(N_c) = -bM_w + a, \tag{1.1}$$

where N_c is the cumulative number of earthquakes with moment magnitude above M_w and b and a being fit parameters (Gutenberg and Richter, 1944; Gutenberg, 2013). Using the relationship between moment magnitude M_w and seismic moment M_o,

$$M_w = \frac{2}{3}[\log_{10}(M_o) - 9.1], \tag{1.2}$$

we can rewrite the GR scaling law in terms of seismic moment:

$$\log(N_c) = \frac{-2b}{3}\log_{10}(M_o) + a'. \tag{1.3}$$

The b-value relates the number of large events to small events and generally takes the value of about one for large enough regions, such as Northern or Southern California (Field et al., 2014). Whether the scaling applies to individual fault segments and/or their immediate surroundings is still being investigated (Wesnousky, 1994; Ishibe and Shimazaki, 2012; Kagan et al., 2012; Page and Felzer, 2015; Page and Elst, 2018; Field et al., 2017). At the very least, the b-value can have substantial variability for smaller regions, ranging from 0.5 to 1.5 for faults in California (Schorlemmer and Wiemer, 2005; Tormann et al., 2014). Furthermore, some mature plate-boundary faults that host large destructive earthquakes, such as the Cholame and Carrizo segments of the San Andreas Fault, may have qualitatively different distributions of seismic events, with pronounced paucity of small and intermediate-sized events (Sieh, 1978; Wesnousky, 1994; Bouchon and Karabulut, 2008; Hauksson et al., 2012; Jiang and Lapusta, 2016; Michailos et al., 2019).

Complexity of dynamic earthquake rupture is often quantified in terms of the time history of their moment rate, often called source-time functions (STFs). The moment rate over a region is calculated according to the expression:

$$\dot{M} = \mu \int_A V dA \tag{1.4}$$

where μ is the shear modulus, A is the rupture area and V is the slip velocity over incremental area dA.

Two works analyzing source-time functions from natural earthquakes motivate our study of source-time functions in this work. The first one is the work by Ellsworth

and Beroza (1995) which identifies a non-linear, non-monotonic initial phase preceding the self-accelerating rupture in velocity seismograms (Figure 1.5). This controversial finding is explained by reluctant dynamic rupture propagation over the region that previously slipped quasi-statically and/or in foreshock events, as occurs for some events in our models. The second work is by Meier et al. (2017) where the authors analyze the STF catalogs of large subduction earthquakes, primarily from Ye et al. (2016), to find overarching patterns in STFs across event magnitude ranges (Figure 1.6). The individual STFs in that study are time-normalized by rupture duration and the moment rate prefactored such that the area under the curve is normalized to one. The STFs are binned into magnitude ranges and a median STF is calculated for each magnitude range. The median STFs when plotted in this normalized scale exhibits a near-triangular shape across magnitude ranges pointing to a typical temporal pattern (Figure 1.6). The peak moment rate in these median normalized STFs is reached at $35\% - 55\%$ of the rupture duration.

Motivated by these observations, we compute the frequency-magnitude distributions of our events and the source-time functions of the resulting dynamic events, focusing on how they are affected by increasing fault heterogeneity.

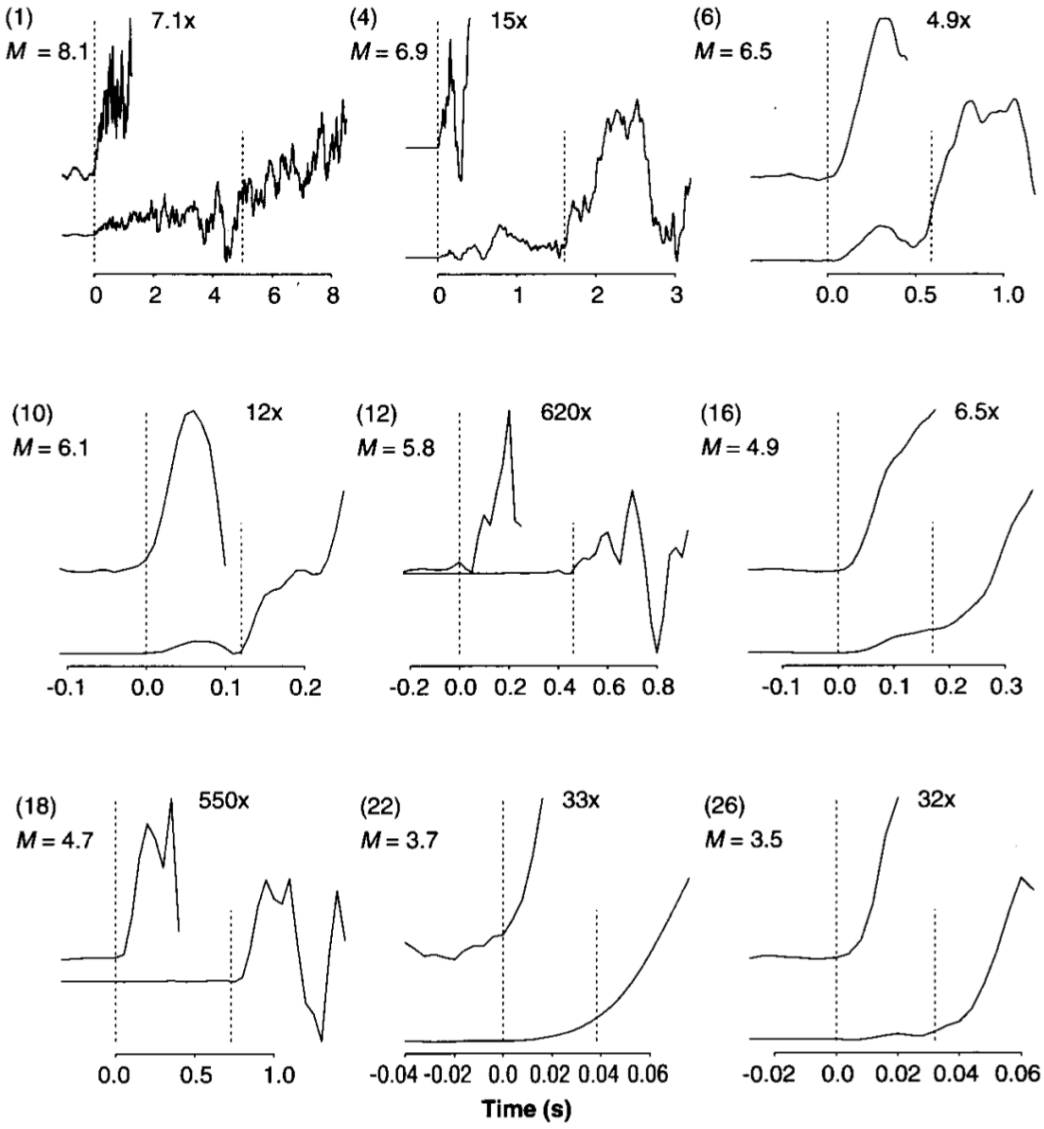

Figure 1.5: A representative set of velocity seismograms used in the analysis of Ellsworth and Beroza (1995) where the reluctant initial phase, dubbed "seismic nucleation" is observed (Reproduced with permission from Ellsworth and Beroza (1995)).

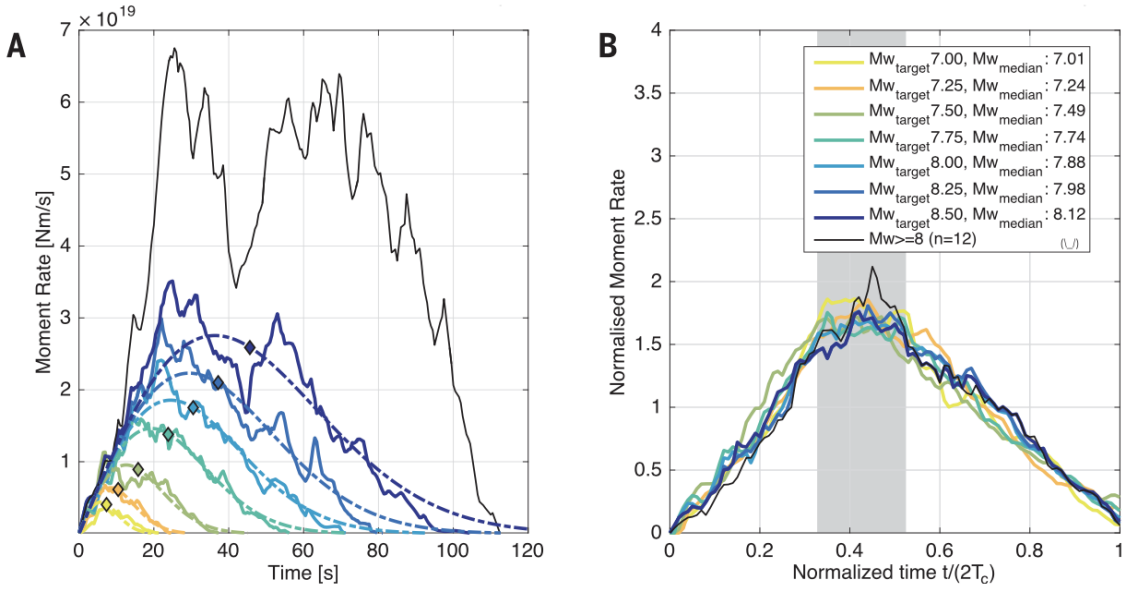

Figure 1.6: a. Median STFs of events in physical scale. b. Median STFs of events in normalized scales (Reproduced with permission from Meier et al. (2017)).

Chapter 2

MODELING VARIABILITY AND INTERACTION OF REPEATING EARTHQUAKE SEQUENCES ON RATE-AND-STATE FAULTS: REALISTIC SHAPES OF SOURCE PATCHES VS. PROPERTIES OF THE CREEPING REGION

Observations indicate that even repeating earthquake sequences display significant variability in their moment and recurrence time. In this chapter, we focus on how heterogeneity in fault properties affects this variability in repeating sequences by considering a specific example of the SF-LA repeaters in Parkfield segment. This chapter begins with a description the rate-and-state friction law governing the fault slip which governs the fault interfaces in all the simulations described in this thesis. The chapter continues on to present the general methodology we use for generating heterogeneous fractal-like fields in all the simulations in the thesis. The rest of the chapter describes various model configurations considered in the study of repeaters, our simulations of the slip behavior of single source patch models and double source patch models, their comparison with observations, and the effect of small-scale heterogeneity on the slip behavior.

2.1 Methodology

Fault friction

Developed to match laboratory observations from friction experiments, rate-and-state friction laws have been successful in capturing the main features of the fault slip, including slow slip during interseismic periods, earthquake rupture events, and post-seismic slip (Dieterich, 2007; Chen and Lapusta, 2009; Jiang and Lapusta, 2016; Kaneko and Lapusta, 2008; Lui and Lapusta, 2016; Lui and Lapusta, 2018). In these laws, the coefficient of friction is logarithmically dependent on the slip rate and its history, represented by the state variable θ. The form used in this study is Dieterich (1979) and Ruina (1983):

$$\tau_f = \bar{\sigma} f = \bar{\sigma} \left[f_* + a \ln(\frac{V}{V_*}) + b \ln(\frac{V_* \theta}{D_{RS}}) \right], \tag{2.1}$$

where τ_f is the frictional resistance, $\bar{\sigma}$ is the effective normal stress, f_* is a reference friction coefficient, V_* is the reference velocity corresponding to f_*, D_{RS} is the rate-

and-state characteristic slip distance, and a and b are rate-and-state parameters of the order 0.01. The state θ of the interface evolves according to the aging law:

$$\frac{\mathrm{d}\theta}{\mathrm{d}t} = 1 - \frac{V_*\theta}{D_{RS}}. \tag{2.2}$$

At steady state, $\theta = 0$, $\theta_{\mathrm{ss}} = \frac{D_{RS}}{V_*}$, and the friction coefficient f reduces to its steady-state value $\mathrm{f_{ss}} = (f_* + (a-b) * \ln\frac{V}{V_*})$. The sign of $(a-b)$ determines if the friction is instability-promoting or instability-suppressing. When $(a-b) > 0$, the steady-state friction coefficient increases with increasing sliding velocity, and the system is unconditionally stable. When $(a-b) < 0$, the steady-state friction coefficient decreases with increasing sliding velocity and the fault can host a spontaneously accelerating instability if it is large enough. These two cases are termed velocity-strengthening (VS) and velocity-weakening (VW) behavior, respectively.

A region being velocity-weakening (VW) is a necessary condition for instability to initiate; it is, however, not sufficient. The size of the VW region has to be larger than the nucleation size h^*. There are several theoretical estimates of the nucleation size that are derived from stability analyses. In our simulations, we make use of the 3-D estimate (Rubin and Ampuero, 2005; Chen and Lapusta, 2009):

$$h^* = \frac{\pi}{2}\frac{\mu D_{RS}}{\bar{\sigma}}\frac{b}{(a-b)^2}. \tag{2.3}$$

Fault model

We study a planar fault interface at $y = 0$ governed by the rate-and-state friction law and embedded between two isotropic, linear elastic half-spaces, which are pre-stressed and being sheared (Figure 2.1). The term "slip" (δ) indicates the magnitude of the discontinuity in the interface-parallel displacement vector between the two half spaces and slip velocity (also called “slip rate”) is the magnitude of the time derivative of the fault-parallel displacement vector. The interface is under compression at all times and there is no discontinuity in the interface-normal displacement.

Tectonic loading is simulated by steady sliding at long-term slip velocity V_{pl} in the direction x assumed around the fault region of interest where friction is applied (Figure 2.1). Hence most of the slip over the frictional portion of the fault occurs in the direction x although transient small component of slip can be in the direction of z, e.g., near the corners of the fault region.

A fully dynamic approach (Noda and Lapusta, 2010) is used to solve the resulting elastodynamic problem at every time step, with friction as a nonlinear boundary condition. The numerical simulations produce the evolution of slip and slip velocity over the fault, which can be then compared with experimental and/or natural fault observations.

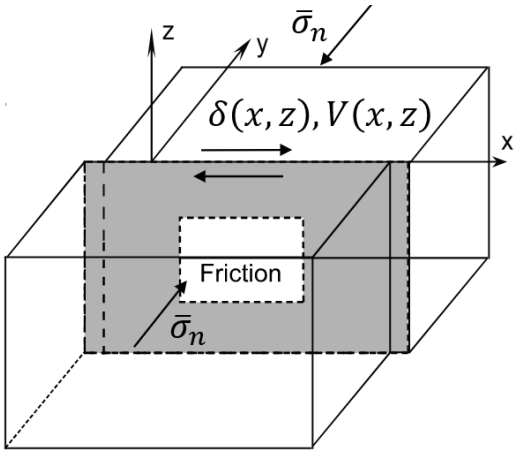

Figure 2.1: A model of a planar fault interface embedded between two isotropic, linear elastic half-spaces, which are pre-stressed and being sheared. The loading with the applied slip velocity V_{pl} outside of the frictional region simulates a case where long-term relative plate velocity of V_{pl} is driving the fault motion, resulting in slip with such slip rate everywhere on the fault except in the frictional region. The spectral approach used in the numerical simulations of the problem periodically repeat the fault domain of the frictional region and the surrounding loading region, with the repeat intervals of λ_x and λ_z, respectively.

The repeater sources are modeled as VW patches in the surrounding VS medium. In previous studies (Lui and Lapusta, 2016; Lui and Lapusta, 2018), the sources were modeled as circular VW patches. In this work, we aim to study the effect of more realistic patterns of VW and VS properties. In our models, we consider an infinite interface created by a periodically repeated domain. In each of these repeated domains, there is a non-frictional boundary region where the plate loading is applied. It surrounds a VS region that transmits this plate loading to the inner domain of interest, where we incorporate heterogeneities in the form of interlaced VW and VS patches (Figure 2.2a). In all figures, the spatial dimensions are normalized by the nucleation size, h^*, of the VW properties, which corresponds to 32 m for the parameter values used in this study. As can be observed in Figure 2.2a, the size of the domain of interest with interlaced VW and VS patches is designed to be $4h^* \times 4h^*$, the size of VS area surrounding it is $8h^* \times 8h^*$ and the total model domain

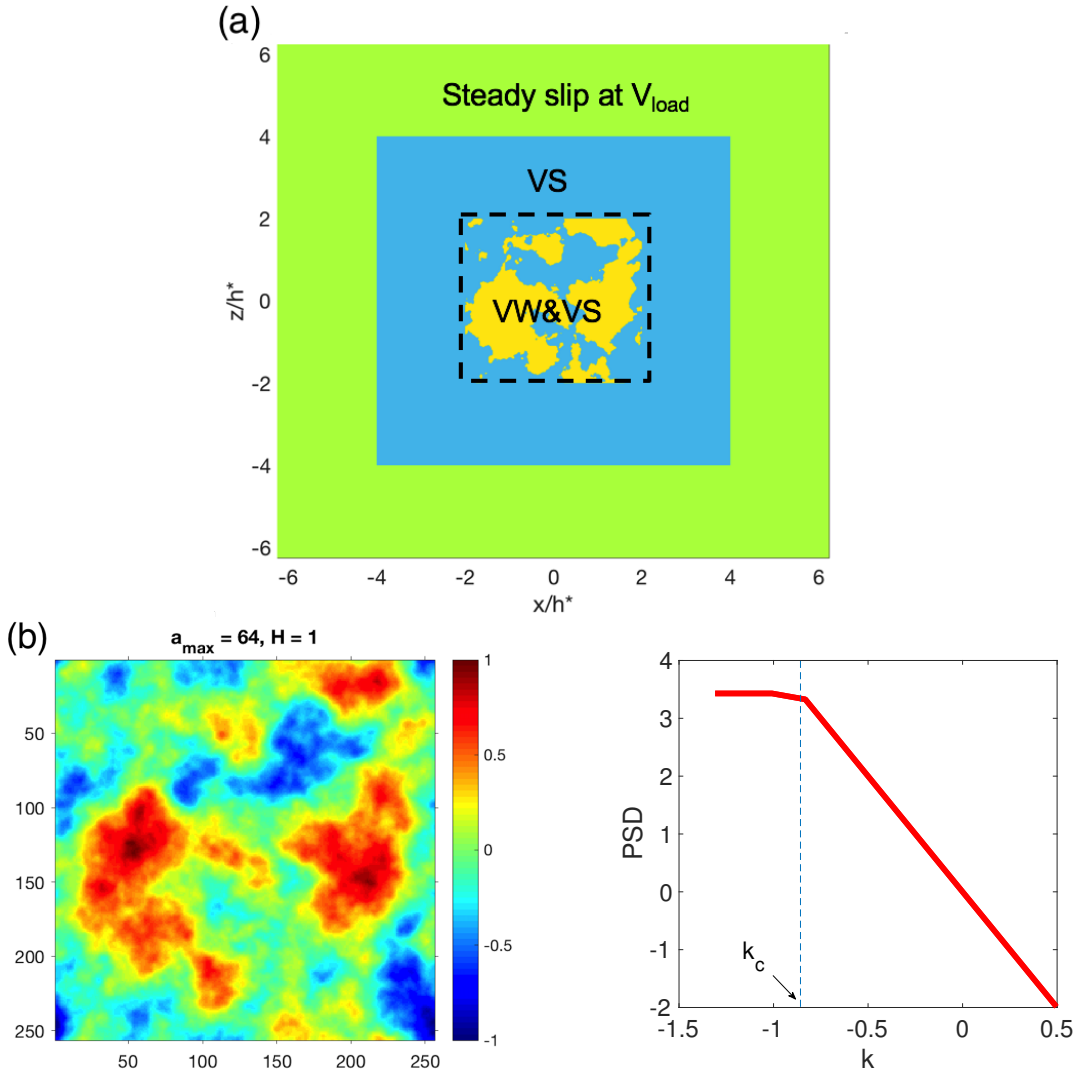

Figure 2.2: a. Representative model domain used in the simulations, normalized by the estimate of the nucleation size for the VW region (yellow), h^*. The domain of interest containing the heterogeneous property distribution is surrounded by load-transmitting VS region (blue), around which steady slip at V_{load} is applied (green) to simulate the steady creep of the larger surrounding region. b. (Left) A realization of the random field with two dominant areas that can serve as the source patches for the SF and LA sequences. The random field is characterized by the Hurst constant, H, that determines the spectral decay at high frequencies and a_{max}, which modulates the largest feature sizes; we choose H = 1 (self-similar). a_{max} = 64 is chosen to obtain the feature sizes comparable to h^*, given the computational restriction on the overall size of the heterogeneous domain (set to $4h^*$). (Right) Power spectral density of the fractal field. The dashed blue line indicates the corner wave number, k_c, beyond which the spectrum shows power law decay.

is approximately $12h^* \times 12h^*$.

Parameter	**Symbol**	**Value**
Rate-and-state parameters in VW regions	a_{VW}, b_{VW}	0.01, 0.014
Rate-and-state parameters in VS regions	a_{VS}, b_{VS}	0.016, 0.006
Effective normal stress in VS and VW regions	$\bar{\sigma}_{VS}$, $\bar{\sigma}_{VW}$	120 MPa, 300 MPa
Characteristic slip distance in VW and VS regions	D_{RS}	238 μm, 238 μm
Loading velocity	V_{pl}	12.75 mm yr^{-1}
Reference slip velocity	V^*	10^{-6} ms^{-1}
Reference friction coefficient in VW and VS region	f^*_{VS}, f^*_{VW}	0.15, 0.6
Shear wave speed	c_s	3 km s^{-1}
Shear modulus	μ	30 GPa
Poisson's ratio	ν	0.25

Table 2.1: Model parameters used in our simulations

Fault parameters used in all models are motivated by laboratory observations, field measurements, or previous studies, and they are listed in Table 2.1. The loading velocity is 12.75 mm yr^{-1}, which is less than 23 mm yr^{-1} used in Lui and Lapusta (2016; 2018), higher than the 4.5 mm yr^{-1} used in Chen and Lapusta (2009) and within the range 4-35 mm yr^{-1} suggested for the repeater-hosting portion of the San Andreas Fault by Harris and Segall (1987). The effective normal stress of 120 MPa has been inferred by SAFOD measurements (Hickman et al., 2004; Imanishi and Ellsworth, 2006; Zoback et al., 2010; Zoback et al., 2011), and we use it for the VS area. For the VW patches, which we envision as flattened asperities, we use the higher value of 300 MPa, following the work of Lui and Lapusta (2018); the study demonstrated that either such higher values of the effective normal stress or enhanced dynamic weakening is needed on the seismogenic patches to produce the observed high stress drops (Dreger et al., 2007; Abercrombie, 2014). The reference friction on the VS areas in our models are prescribed a low value of 0.15, following experimental observations (Lockner et al., 2011; Carpenter et al., 2011) and field studies (Hickman et al., 2004; Chang et al., 2013). For the VW areas, a higher reference friction coefficient value of 0.6 is used. The other resolution criterion of importance, is the cohesive (breakdown) length R_o, which is the distance behind the rupture tip where slip weakening occurs. The chosen cell size resolves R_o by at least 3 cells, a borderline but adequate resolution for dynamic rupture as suggested by the study of Day et al. (2005).

We use a velocity threshold to identify the beginning and end of earthquake rupture events. If the maximum velocity at any point on the fault exceeds the velocity

threshold, the beginning of an earthquake event is recorded. And if all points reach slip rates below the threshold, the event is considered to end. An analytical expression for slip rates at which a critical wavelength increases by a factor of $\sqrt{(2)}$ in a frictional stability problem with inertial effects (Rice et al., 2001) is given by:

$$V_{in} = c_s \frac{2\sqrt{a_{VW}(b_{VW} - a_{VW})}\sigma_{VW}}{\mu}, \tag{2.4}$$

where a_{VW}, b_{VW} are the rate-and-state parameters in the velocity-weakening region, σ_{VW} is the normal stress in the velocity-weakening region, μ is the shear modulus and c_s is the shear wave speed. For the model parameters used in this study, V_{in} is 0.378 m/s, indicating that inertial effects are clearly important at such slip rates. The inertial effects, however, can be important at velocities lower than this threshold. We choose the velocity threshold of $V_{dyn} = 0.06$ m/s, which is six times smaller than V_{in}. This threshold is similar to the typically used value of 0.1 m/s in other numerical studies (Lin and Lapusta, 2018).

Generation of heterogeneous property distributions

Finite-fault source inversions have revealed the complexity in earthquake slip distributions which can be characterized stochastically, using a technique called spatial random field modeling (Mai and Beroza, 2002). In this work, we use the same technique to generate fractal random fields for describing heterogeneity in fault friction. Using fractal fields is motivated by the fact that physical properties on faults, including roughness, are observed to follow fractal trends (Candela et al., 2012; Sagy et al., 2007).

A 2D fractal random field is described by the power spectral density (PSD) in the frequency domain (Voss, 1988):

$$P(k) = \frac{C}{k^{2(1+H)}}, \tag{2.5}$$

where k is a dimensionless wave number, C is a constant, and H is the Hurst exponent. H controls the decay of the PSD at high frequencies, and it is taken to be unity (self-similar distribution) in this study. The PSD decays with a power law beyond a corner wave number, k_c, which is related to the characteristic source dimension (Figure 2.2b). k_c and H are the two parameters that characterize the field. For a given set of parameters, we can generate infinitely many realizations of the random distributions, by convolving with differently seeded random matrices.

Amongst these, we choose the particular realization shown in Figure 2.2b as a starting point, due to the serendipitous existence of two dominant high-intensity patches, which could translate into the two repeater sources, when converted into frictional property distribution.

We translate the random field values into a pattern of friction properties. The spatial random field is normalized between -1 and 1. We select a threshold between -1 and 1, above/below which a cell acquires the VW/VS properties from Table 2.1, respectively. By varying this threshold, one generates heterogeneous frictional property distributions of varying area fractions of VW patches in a VS domain. For example, a distribution with the VW area fraction of 50% can be generated using the threshold value of 0.0212 for the particular distribution we use (Figure 2.3a).

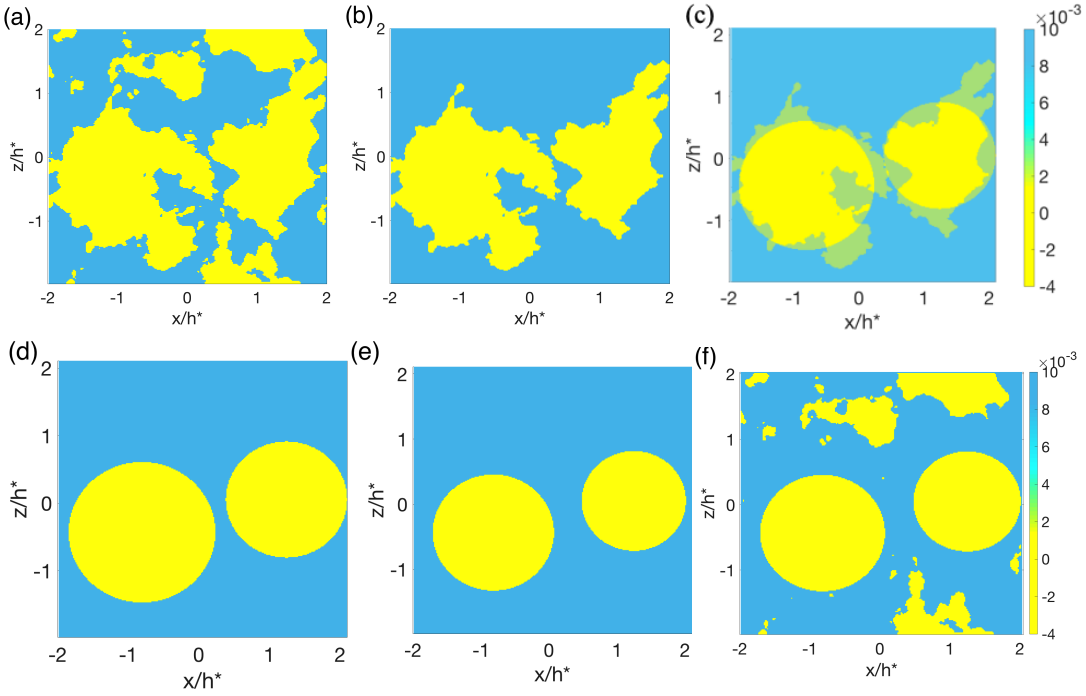

Figure 2.3: (a) Heterogeneous distribution of VW (yellow) and VS (blue) frictional properties obtained from the random field in Figure 4. (b) The distribution with only two main irregular patches and all other perturbing features removed. (c-d) Constructing analogous fault model with circular patches by fixing centroids of the two main patches and conserving their areas. (e) Fault model with circular patches of smaller radii that has similar moment magnitudes to the model with irregular patches from (a-b). (f) Fault model with circular patches and smaller perturbing patches from (a).

Note that the sizes of the two main patches in Figure 2.3a are of the order of h^*. This constraint ensures that there is significant aseismic slip at the repeater locations,

which is essential for obtaining reasonable source properties (Lui and Lapusta, 2018).

2.2 Models studied

We consider several factors that can potentially influence the variability of the slip patterns. First, the shape of the source patch can add complexity of slip. The size of the source patch with respect to the nucleation size determines the transition between stable slip and dynamic events. Moreover, keeping the size of source patches close to h^* produces substantial variability of slip (Lui and Lapusta, 2018). Interaction between two repeating sequences may play a major part in the variability. The properties of the surrounding velocity-strengthening region affect the extent to which the seismic slip spreads out and determines the speed of the post-seismic slip front, thereby affecting the interaction between nearby patches (Lui and Lapusta, 2016). In addition, the existence of sub-critical patches in the vicinity perturbs the slip by creating aseismic transients of their own. The effects of one factor can be coupled with another factor, e.g. changing the size of the patches can bring them closer to each other, thereby affecting the interaction between them.

We start with the pattern of VW and VS friction properties constructed from a fractal field as described in Section 2.3 (Figure 2.2b). Two dominating patches exist in this distribution and act as sources for the simulated SF and LA sequences (Figure 2.3a). This is our base model.

The construction and naming of the other models is as follows (Table 2.2). The source patches can be circular (C) or fractal (F). The VS properties are chosen from $(a-b)_{VS} = 0.01, 0.004, 0.002$ and labeled 1,2,3. The surrounding creeping region can contain the rest of the fractal field (and hence perturbing patches) or not (labeled p and n). Finally, the models can contain a single source patch (S) or two patches patches (D). Our base model is then labeled as F1p-D (Figure 2.3a). To obtain model F1n-D, we take the F1p-D model, use image processing tools to identify the two largest patches, which can act as sources with complex shapes, and remove the rest of the VW features (Figure 2.3b).

In order to develop a model with circular patches, we find the areas and centroids of the main two patches identified in F1n-D. By conserving areas, we construct equivalent circular patches at the centroid locations (Figure 2.3c, d), with radii calculated as follows:

$$r_{P1} = \sqrt{\frac{A_{P1}}{\pi}}, r_{P2} = \sqrt{\frac{A_{P2}}{\pi}}, \tag{2.6}$$

where A_{P1}, A_{P2} are the areas of left and right circular patches and r_{P1}, r_{P2} are the corresponding calculated radii.

However, the moment magnitude of events that occur on such circular patches are larger than for the base fractal model. This is likely because the effective rupture-able area of the fractal patches in F1n-D is smaller than the total numerical area of all the cells in the patches, due to their complex geometry. The area utilized in rupture nucleation and propagation may not include the narrow extremities of the complex patches. Therefore, in order to conserve moment magnitude, we use circular patches of smaller area, in model C1n-D (Figure 2.3e). Patch diameters of $d_L = 1.78h^*$ and $d_R = 1.42h^*$ allow the double circular source model (Figure 2.3e) to host events with mean moment magnitudes approximately matching the events in our complex patch source models.

The perturbing patches from the model of Figure 2.3a are used to add a perturbing effect on the circular source patches (Figure 2.3f).

2.3 Response of a representative two-patch model

In order to visualize the resulting slip behavior, let us consider slip velocity snapshots from slip simulations in a representative model (Figure 2.3a). A typical interaction between the two patches, obtained as a part of a long-term simulation of slip, proceeds as follows. A fast-slipping event nucleates in the bigger, left patch (Figure 2.4a-b); we assign time of zero to this snapshot for convenience. The post-seismic slip front triggers the right patch and an event is nucleated there about an hour later (Figure 2.4c-d). The perturbing patches and the smaller, right patch host aseismic transients (Figure 2.4e-h) in the ensuing interseismic period, and transfer stress onto the left patch, which subsequently nucleates again, almost 3 years after the previous event on this patch (Figure 2.4i-j). The post-seismic slip front triggers the right patch again, this time in 7 minutes (Figure 2.4k-l) and so on. The sequence of triggering of the right patch by the left patch in the top and bottom rows of Figure 2.4 is similar, yet the process is variable in terms of the location of nucleation and the triggering times. The slip behavior possesses the qualitative—and quantitative—features of repeating sequences that we aim to study in this work.

Now that we have established the features we seek to reproduce, the effect of different

Model name	Description
C1n – S	Single circular patch, perturbing patches absent, $(a-b)_{VS} = 0.01$
C1n – S, ↑ 20%	Single circular patch, perturbing patches absent, $(a-b)_{VS} = 0.01$
C3n – S	Single circular patch, perturbing patches absent, $(a-b)_{VS} = 0.002$
F1n – S	Single fractal patch, perturbing patches absent, $(a-b)_{VS} = 0.01$
F1n – S, ↑ 20%	Single fractal patch, perturbing patches absent , $(a-b)_{VS} = 0.01$
F3n – S	Single fractal patch, perturbing patches absent , $(a-b)_{VS} = 0.002$
C1n – D	Double circular patches, perturbing patches absent , $(a-b)_{VS} = 0.01$
C1p – D	Double circular patches, perturbing patches present , $(a-b)_{VS} = 0.01$
F1n – D	Double fractal patches, perturbing patches absent , $(a-b)_{VS} = 0.01$
F1p – D **(Base)**	Double fractal patches, perturbing patches present , $(a-b)_{VS} = 0.01$
C2n – D	Double circular patches, perturbing patches absent , $(a-b)_{VS} = 0.004$
C3n – D	Double circular patches, perturbing patches absent , $(a-b)_{VS} = 0.002$
F1p – D, ($a_{min} = 4$)	Double fractal patches, perturbing patches present , $(a-b)_{VS} = 0.01$
F1p – D, ($a_{min} = 8$)	Double fractal patches, perturbing patches present , $(a-b)_{VS} = 0.01$
F1p – D, ($a_{min} = 16$)	Double fractal patches, perturbing patches present , $(a-b)_{VS} = 0.01$
F1p – D, ($a_{min} = 32$)	Double fractal patches, perturbing patches present , $(a-b)_{VS} = 0.01$
F1p – D, ($a_{min} = 48$)	Double fractal patches, perturbing patches present , $(a-b)_{VS} = 0.01$
F1p – D, ($a_{min} = 55$)	Double fractal patches, perturbing patches present , $(a-b)_{VS} = 0.01$
F1p – D, ($a_{min} = 60$)	Double fractal patches, perturbing patches present , $(a-b)_{VS} = 0.01$
F1p – D, ($a_{min} = 63$)	Double fractal patches, perturbing patches present , $(a-b)_{VS} = 0.01$
F1n – D, ($a_{min} = 63$)	Double fractal patches, perturbing patches absent , $(a-b)_{VS} = 0.01$

Table 2.2: Fault models studied

factors on the variability of repeating event sequences can be systematically studied, from single-patch models to double-patch models.

All the source property values from the simulations are compiled in Tables 2.3, 2.4 and can be used for comparing model behaviors quantitatively.

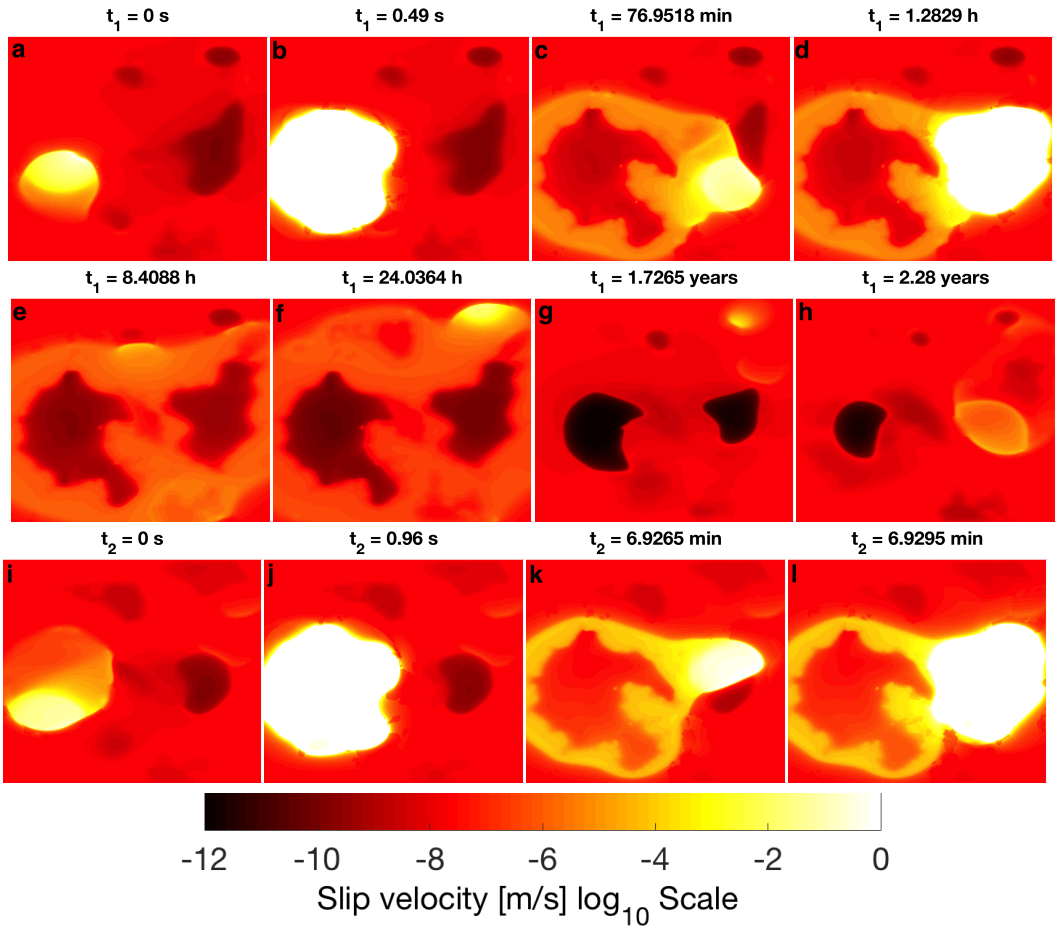

Figure 2.4: Slip velocity snapshots from the representative model F1p-D. The top row illustrates a typical triggering sequence where the post-seismic slip from the left-patch event triggers an event in the right patch. The middle row shows the subsequent interseismic period, marked by aseismic transients. The third row indicates the following triggering sequence in which the left patch event triggers the right patch yet again, albeit with a shorter triggering time and at a different location.

2.4 Single-Patch Studies

We start with simulations of a single VW patch to understand the variability of an isolated repeater sequence. By observing the behavior of the single patch, we can study the effect of shape and size of the patch on the slip behavior, without incorporating effects of interaction between the patches.

Effect of shape and size of the source

Adding complexity to shape of the source patch brings in complexity in slip patterns. Using single patch models with circular and fractal sources (Figure 2.5a), we can observe the changes in slip patterns produced. The fractal and circular patch sizes

are chosen to have similar source properties. It is interesting to note that the fractal patch models have higher mean moment, but a smaller recurrence interval when compared to the circular patch models (Figure 2.5b), which indicates that a true analogy in source properties is hard to achieve, once the shapes of the sources are different.

Models F1n-S and C1n-S exhibit similar variability in slip behavior (Table 2.4, Figure 2.6). As the patch sizes are increased, the effect of the complex patch shape on variability in slip behavior is, in general, amplified, especially for the recurrence time. When the patch shape is complex, we are introducing different possible nucleation sites and pathways for the rupture to extend into during propagation, owing to the asymmetry and irregular aspect ratio. Based on the stress distribution, the rupture can meander into the many different asymmetric pathways, resulting in more variable event sizes and recurrence times. For a smaller seismogenic patch, even if the event nucleates somewhere else in the patch due to the asymmetry of the complex shape, the entire patch still is ruptured. But for a bigger patch, the portions of the patch that get ruptured for different nucleation sites could potentially be different (Figure 2.7), leading to more variability in recurrence times and moment magnitude.

Let us use the results for patches of different sizes to consider the scaling between T_{rec} and M_o in the single-patch models (Figure 2.8). The observed recurrence times in Parkfield repeating sequences have been well approximated by $T_{rec} \approx 7 \times 10^4 M_o^{0.17}$, with T_{rec} measured in secs and M_o measured in dyne-cm (Nadeau and Johnson, 1998; Chen and Lapusta, 2009). The scaling is different from $T_{rec} \propto M_o^{\frac{1}{3}}$, obtained from a theoretical model of a circular source exclusively undergoing seismic slip. This difference in scaling exponent can be due to the presence of significant aseismic slip at the source locations (Chen and Lapusta, 2009; Lui and Lapusta, 2016), the fraction of which increases with reducing patch size, a factor not accounted for in the theoretical expression. In the work of Chen and Lapusta (2009), models of repeaters with $\Delta\tau \approx 3$ MPa and $V_{pl} \approx 4.5$ mm/yr are seen to reproduce the scaling relationship, as well as the absolute magnitudes of recurrence times. In Lui and Lapusta (2016; 2018), higher stress drops $\Delta\tau \approx 25 - 30$ MPa are seen to recover the scaling and the absolute recurrence time magnitudes even with the higher loading rate of $V_{pl} \approx 23$ mm/yr. In this work, we are considering models in between, with $\Delta\tau \approx 20$ MPa and $V_{pl} \approx 13$ mm/yr, and are able to reproduce the scaling behavior quantitatively and qualitatively (Figure 2.8).

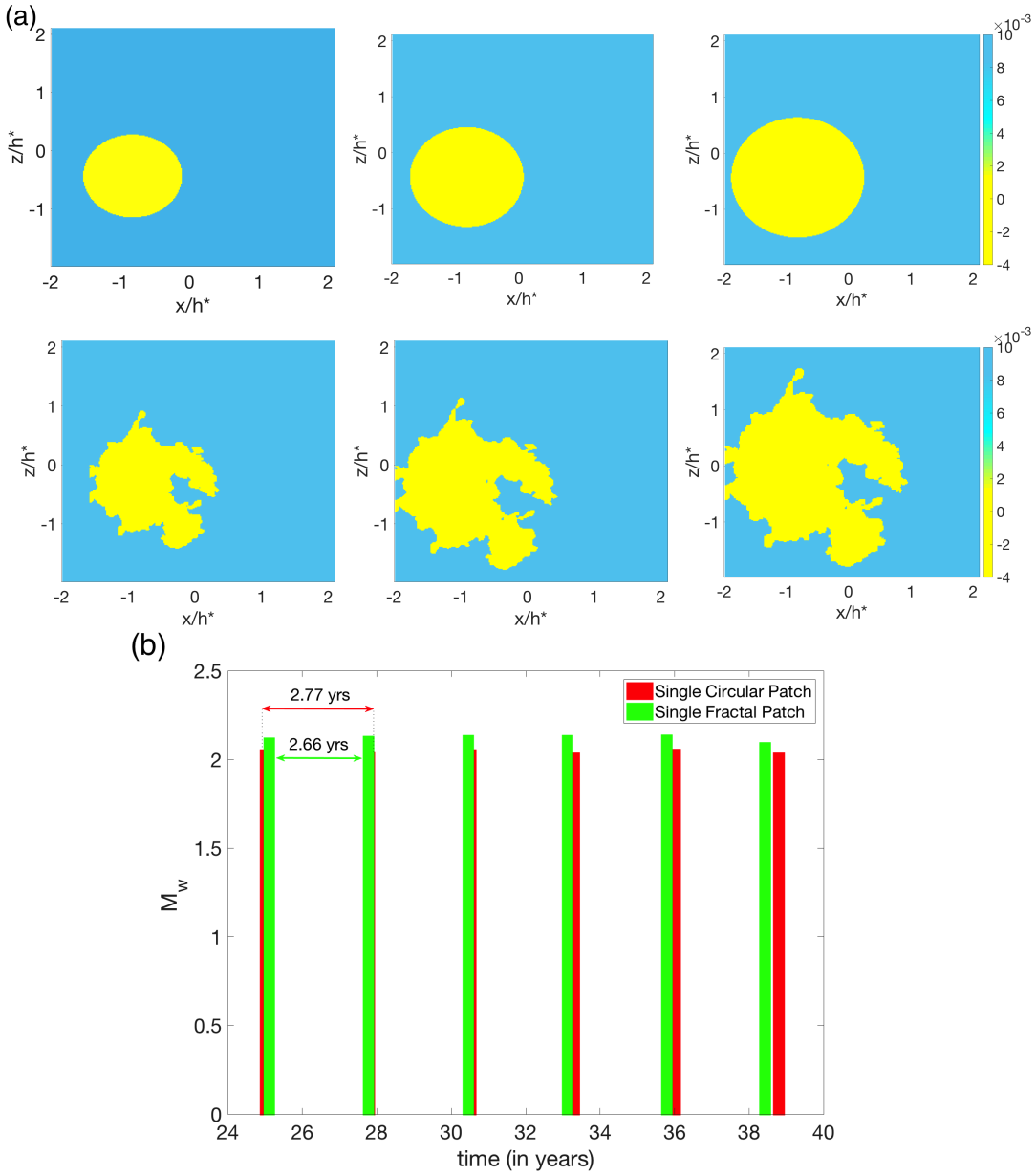

Figure 2.5: a. Single-patch models with different patch sizes: (top row, left to right) C1n-S Scaled down 20 %, C1n-S, C1n-S Scaled up 20%, (bottom row, left to right) F1n-S Scaled down 20%, F1n-S, F1n-S Scaled up 20% b. Comparison of moment and recurrence time of a single circular patch model (C1n-S) with a single fractal patch model (F1n-S). C1n-S has a lower mean recurrence time but higher mean seismic moment, implying that a complete analogy in properties between the two patch shapes might be difficult to produce.

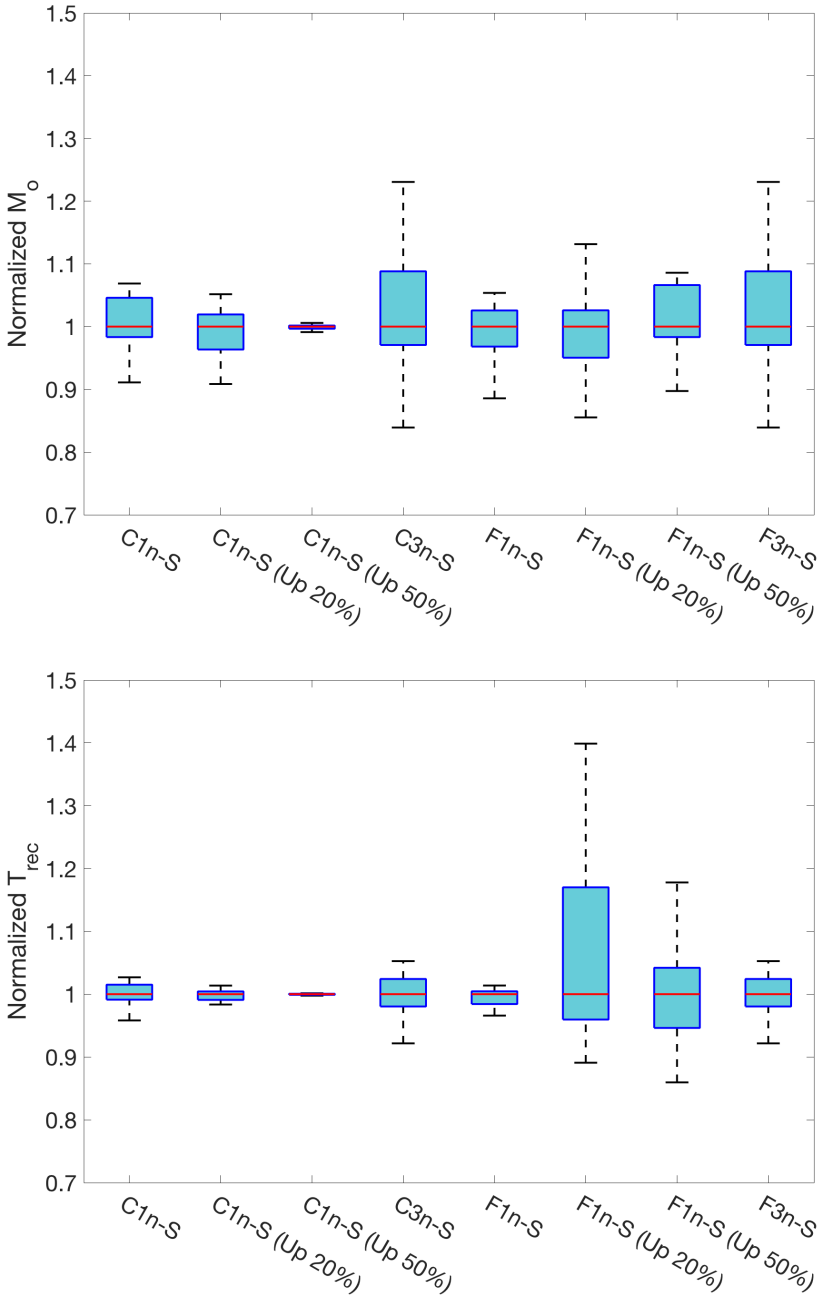

Figure 2.6: Box plots of the single-patch models comparing their seismic moment and recurrence time. The variability of moment and recurrence time generally increases with the coupled effect of a complex patch shape and increased patch size. Models with less strengthening region around the patches have larger variability (C3n-S and F3n-S vs. C1n-S and F1n-S).

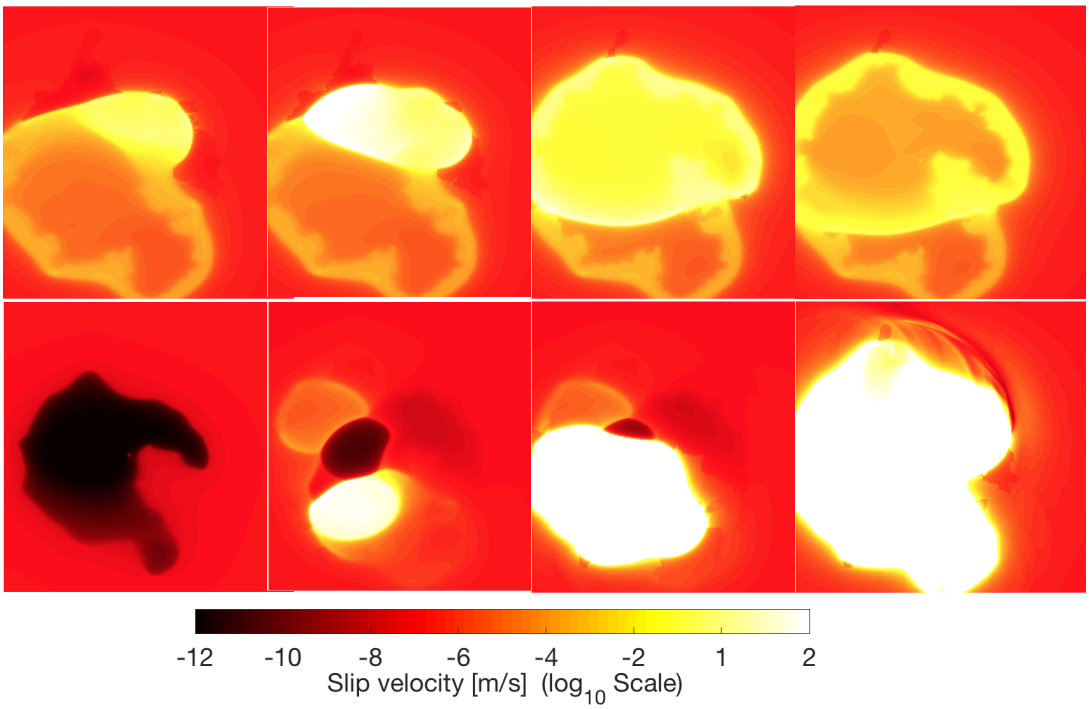

Figure 2.7: Slip velocity snapshots from the model F1n-S (with patch size larger by 25%) for two different dynamic events (top and bottom rows) illustrating the effect that the patch shape has on the nucleation and propagation of dynamic rupture. For a large patch with complex shape, patch can be ruptured differently—and with different area covered—in subsequent events.

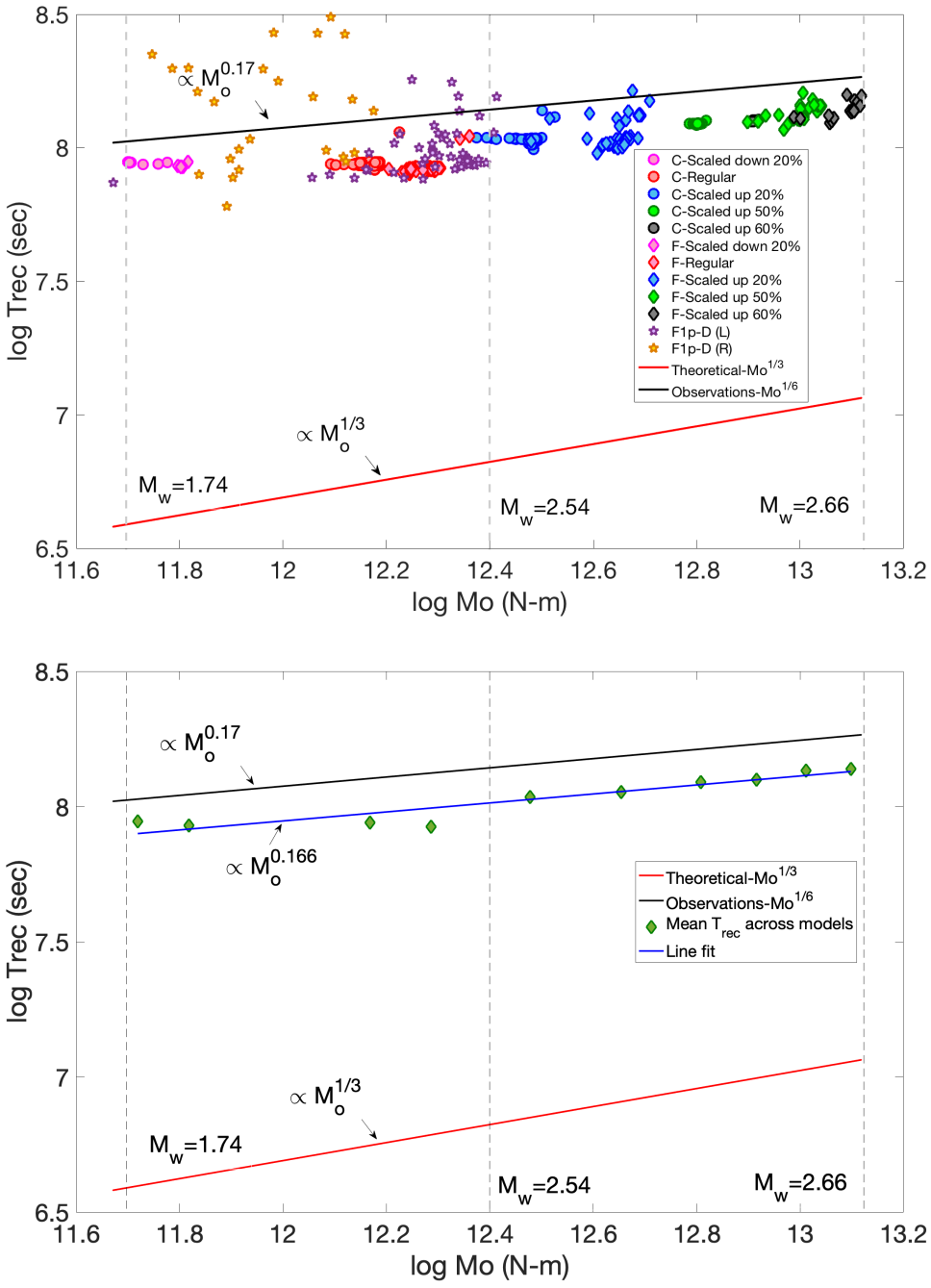

Figure 2.8: a. Scaling between the recurrence time of events in each repeating sequence T_{rec} vs. their seismic moment M_o for single-patch circular models (circular markers), single patch fractal models (diamond markers), and left and right patch events from the base model (F1p-D) (star markers). b. The scaling with the line fit for the mean recurrence times of each model. Results match the scaling observed for repeaters of the creeping section next to Parkfield (black line), approximated by the expression $T_{rec} \approx 7 \times 10^4 M_o{}^{0.17}$ (Chen and Lapusta, 2009). The theoretical scaling relation for the constant stress drops of 20 MPa is shown by the red line for comparison.

Effect of properties in the VS region

The properties of the VS region affect the speed of the post-seismic front and thereby affect patch interactions (Lui and Lapusta, 2016). Let us compare Model C1n-S with $(a-b)_{VS} = 0.01$ to Model C3n-S with $(a-b)_{VS} = 0.002$. The variation in recurrence time and moment is higher in C3n-S compared to C1n-S (Figure 2.6). Less velocity strengthening in the surrounding VS region results can be interpreted as an increase in the effective size of the patch, since the seismic slip can penetrate more into the VS region, which increases the net effective rupture area. As discussed in Section 2.4, an increase in the effective size of the patch loosens the size constraint on the events and results in a larger variability of event sizes. The same study is also conducted for a single fractal patch, more specifically, for the left patch in the base fractal distribution. A slight increase in the variation in moment and recurrence time are observed (Table 2.4).

2.5 Double-Patch Studies

Simulations with two patches allow us to study how they interact with each other and the effect of the interaction on variability. The presence of an interacting patch visibly increases the variability of slip behavior (Figure 2.9).

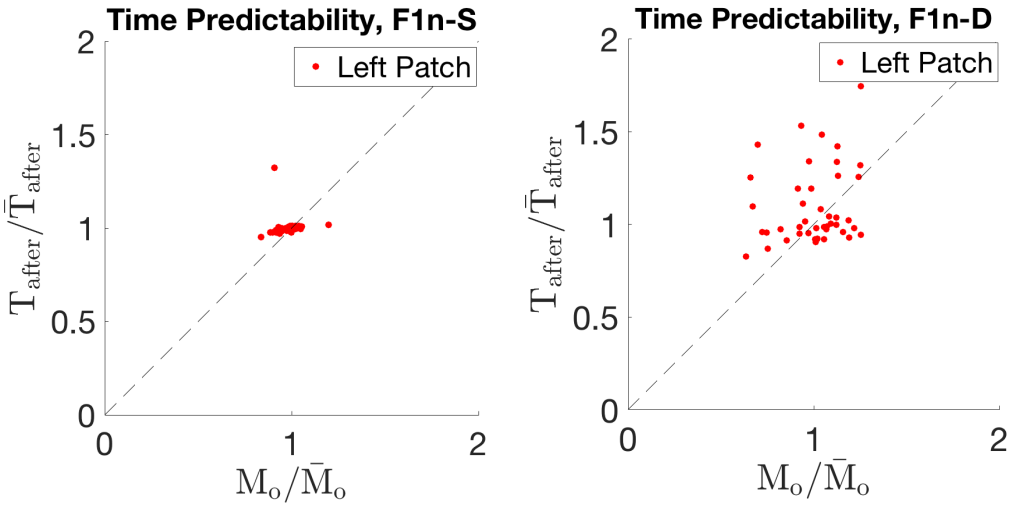

Figure 2.9: Comparing the time-predictability plots of models with single and double fractal patches (F1n-S and F1n-D) shows the increase in variability of slip behavior due to interaction between the patches.

Effect of shape of the source patches

In models with two source patches (Figure 2.10), interaction effects are coupled with the source shape effects. In particular, the smaller right fractal patch does not host as many events, as it did as a circular patch with events of similar moments. This could be because of the different aspect ratio, owing to the complex shape. The pinched section in the middle is of the order of the nucleation size (h^*) estimate, thereby constraining the events.

The time- and slip-predictability plots (Figure 2.11) show the increase in variability produced by incorporating more complexity in patch shape. The spread of data points in the predictability plots for the model with fractal patch shapes, F1n-D, is more substantial and more closely represents the data. The data points of model F1n-D exceed the confines of the bounding data rectangles, which could be attributed to the longer repeater sequence ($\sim$ 50 events) when compared to the SF-LA repeater sequence (14 events). This increase in variability is quantitatively described by the IQR measures given in Table 2.4. The variability in moment of the left patch increases by about 60% with the change from circular to fractal shape. The increase in recurrence time variability of the left patch by nearly 6 times is even more drastic (Figure 2.12).

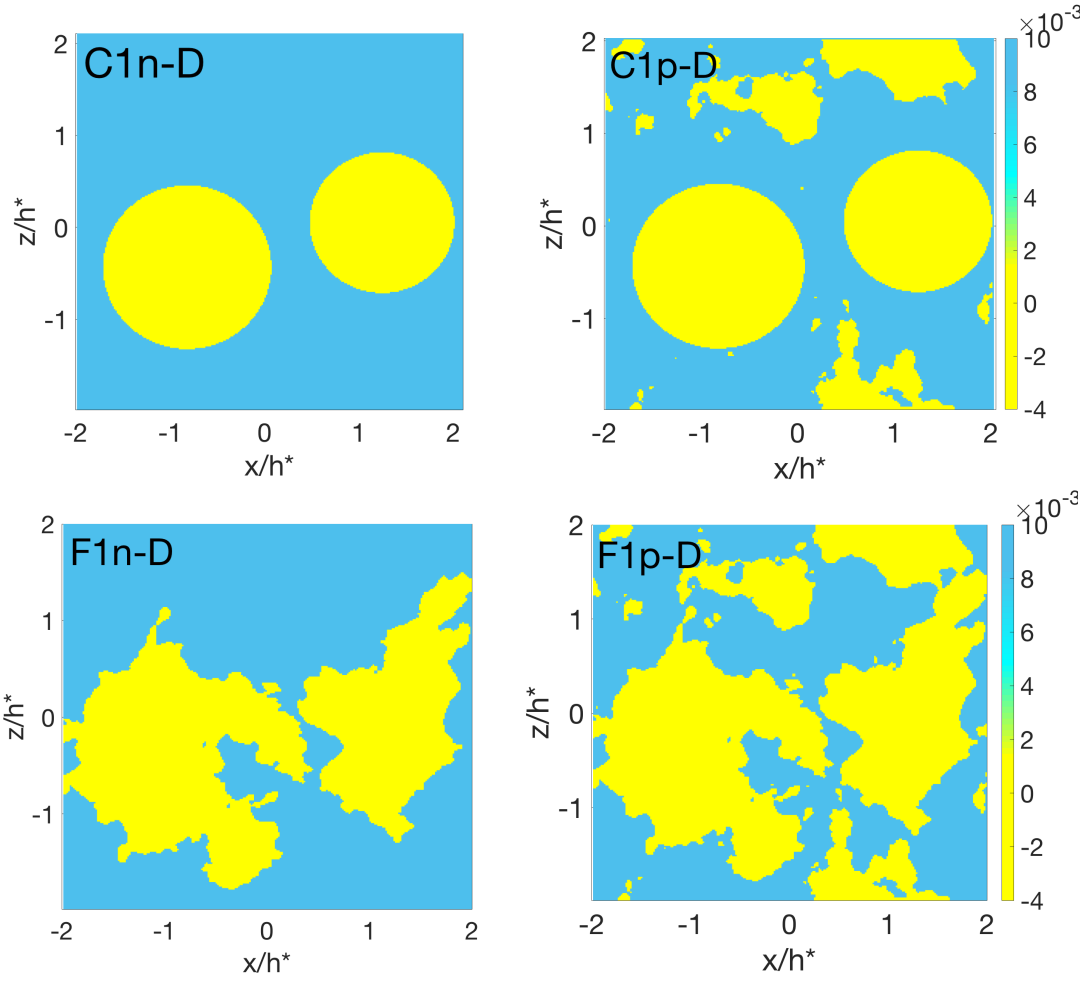

Figure 2.10: Fault models C1n-D, C1p-D, F1n-D, F1p-D for the double-patch simulations.

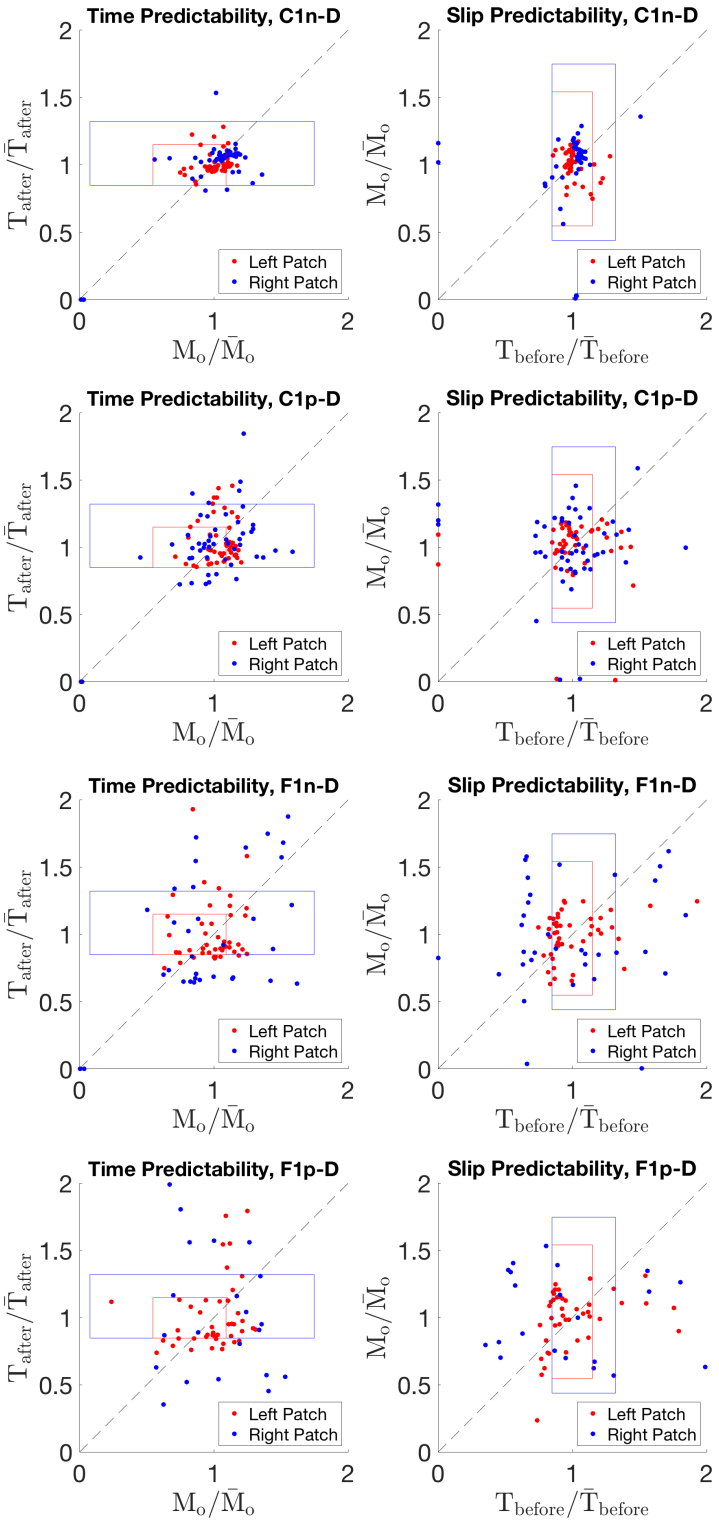

Figure 2.11: Slip-time predictability plots for the double-patch models. The data points in the case of the circular-patch model (C1n-D) are clustered, whereas the addition of sub-critical perturbing patches increases the spread of data points (C1p-D). The fractal source shape (F1n-D) significantly increases the scatter, which is further enhanced by addition of perturbing patches (F1p-D). The red and blue rectangles bounding the time- and slip-predictability data points of the SF-LA event pairs are superposed for comparison to models.

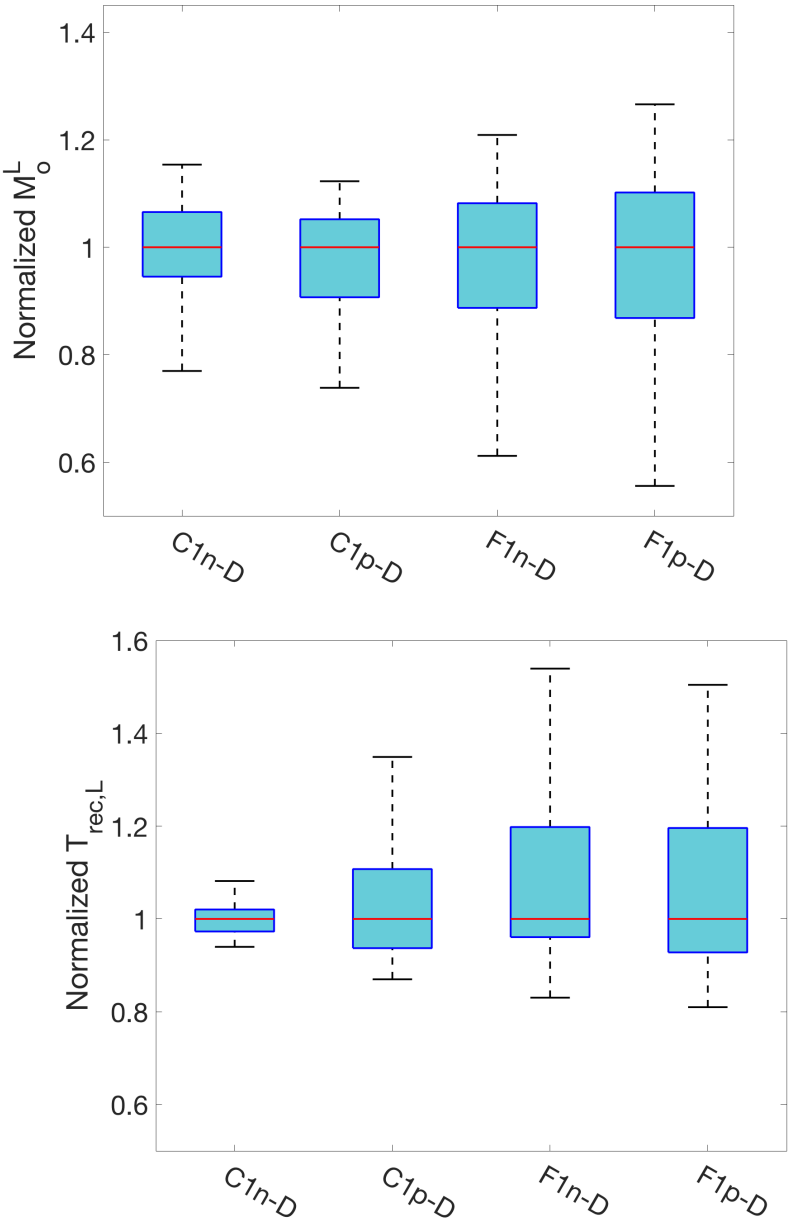

Figure 2.12: Comparison of moment and recurrence time box plots from the left-patch events in double-patch simulations. A substantial increase in variability is introduced by the fractal patch shape (F1n-D), with further, more subtle increase in variability with addition of perturbing patches (C1p-D, F1p-D).

In the double-patch simulations, a dynamic event in one patch often triggers events in the other patch, as discussed in Section 2.3 (Figure 2.4). Let us consider the time difference between an event in the right patch and the event in the left patch, normalized by the mean recurrence interval of the left-patch events (Figure 2.13). The red markers indicate the bigger, left patch ruptures first and triggers an event

in the smaller, right patch, which is similar to observations (Figure 1.2b). The blue markers indicate that the right patch ruptures first. To match the data, we need continuous sequences of at least 7 red data points. We observe that the triggering times of the fractal case (F1n-D) are more comparable to observations, both in terms of the order of triggering, as well as the range of triggering times. The short triggering times (1-100 s) seem to be absent in the circular model (C1n-D), owing to the simple nature of connection between the two patches.

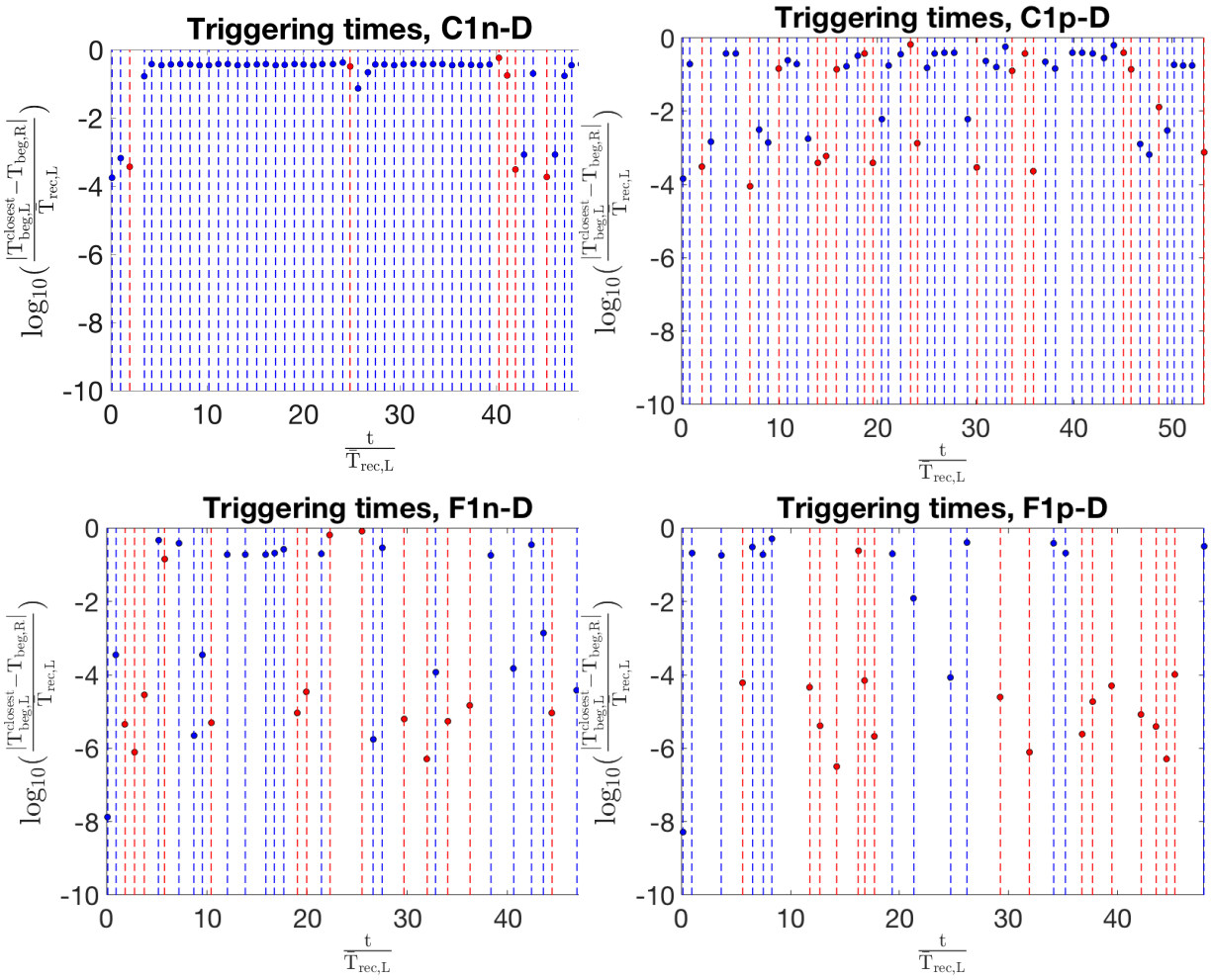

Figure 2.13: Triggering times in double-patch models. In the case of the circular-patch model (C1n-D), the lower triggering times are absent, with the addition of sub-critical perturbing patches increasing the range of triggering times, though still not to the extent of realistic behavior (C1p-D). The fractal source shapes (F1n-D) give rise to a wide range of triggering times comparable to the observations, which persist with addition of perturbing patches (F1p-D).

Effect of perturbing sub-critical patches

We further consider the effect of perturbing sub-critical patches which emerge naturally as we threshold the fractal distribution (Figure 2.2b, 2.3a). As expected, the additional patches perturb the system and add further variability (Figure 2.11). This can be quantitatively seen in Table 2.4, where the IQR measures of both seismic moment and recurrence time are seen to increase marginally from F1n-D to F1p-D, also pictorially represented by the box plots in Figure 2.12. A similar study can be performed by superposing these sub-critical perturbing patches on to the circular patch model, C1n-D, to get C1p-D (Figure 2.3f). On observing the slip and time predictability plots (Figure 2.11), we can observe the larger spread in recurrence time when compared to the spread in moment magnitude, as is the case with the observed data (Rubinstein et al., 2012). From Table 2.4, we can see that variability in moment increases marginally, whereas the variability in recurrence time increases almost 4-folds. This is pictorially represented by the box-plots, seen in Figure 2.12. The addition of perturbing patches is observed to not be sufficient to give rise to short triggering times in C1p-D (Figure 2.13). In the case of fractal patch models, the range of triggering times remain comparable between F1n-D and F1p-D.

Effect of VS properties

The study of Lui and Lapusta (2016) hypothesized that the properties of the repeating sequences, such as the triggering times, can be used to constrain the VS properties of the fault in between the patches. Let us compare the slip behavior of models C1n-D, C2n-D, and C3n-D, with $(a-b)_{VS} = 0.01, 0.004, 0.002$, respectively. As the VS region becomes less strengthening, the effective rupture areas of both patches increase, which results in higher average moments (Table 2.4). From the slip predictability—time predictability plots (Figure 2.14), we observe that as the VS region becomes less strengthening, the spread in recurrence time remains similar, while the spread in moment, particularly that of right patch events, increases.

A possible explanation for this is that as the VS region becomes weaker, the rupture areas and thereby, the moments of the events are impacted. On the other hand, since the source patch shapes remain simple, the nucleation process remains somewhat the same, which results in recurrence times staying within the same narrow range of variation. The IQR values (Table 2.4) indicate increased variation in moment and recurrence time in both C2n-D and C3n-D, relative to C1n-D, visualized by the box plots in Figure 2.15a.

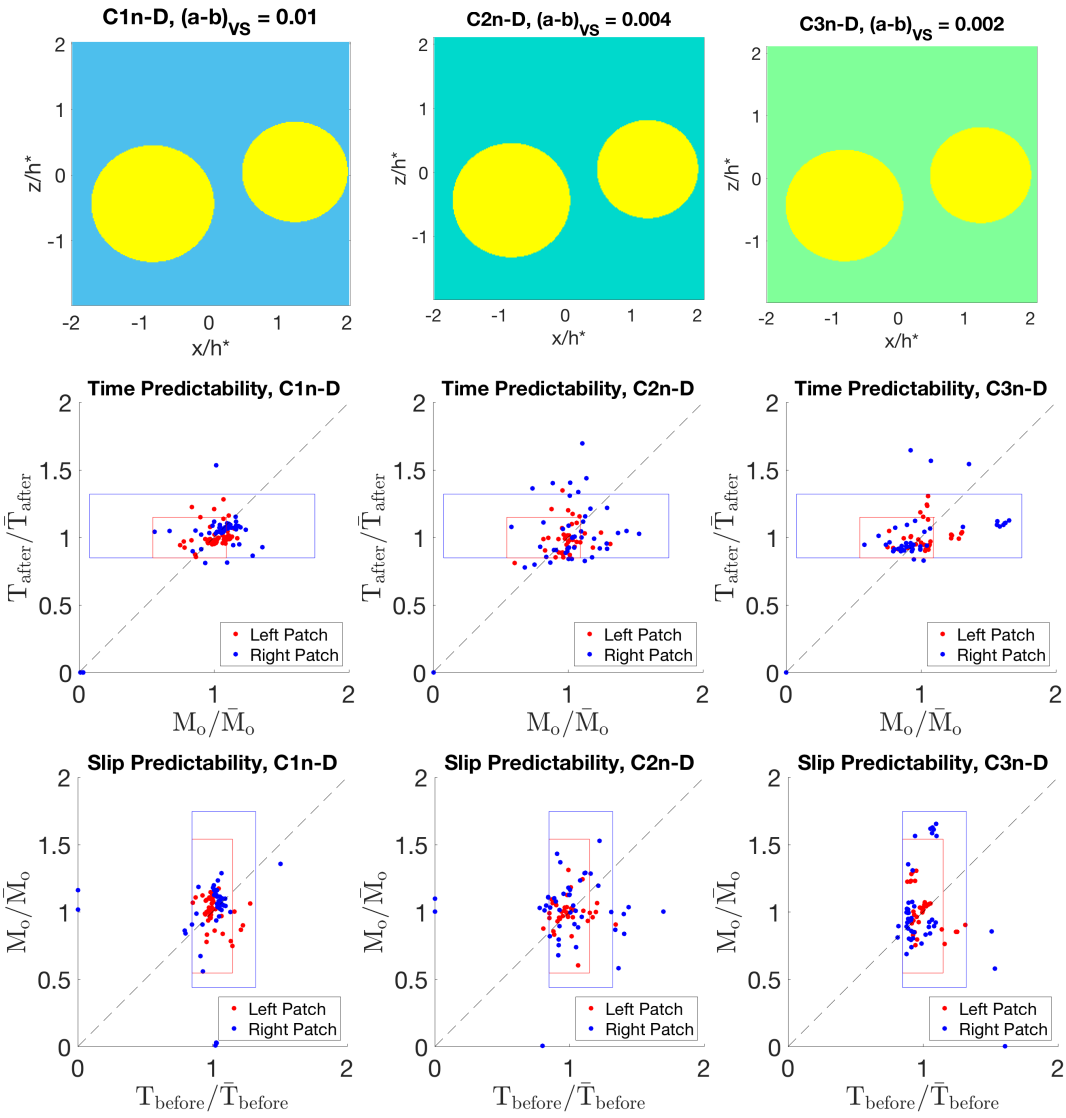

Figure 2.14: Time-predictability and slip-predictability plots for double-patch models with decreasing velocity strengthening in the region surrounding the patches (C1n-D, C2n-D, and C3n-D). The variability of seismic moments and recurrence times is similar, slightly increasing with the reduction in the strengthening.

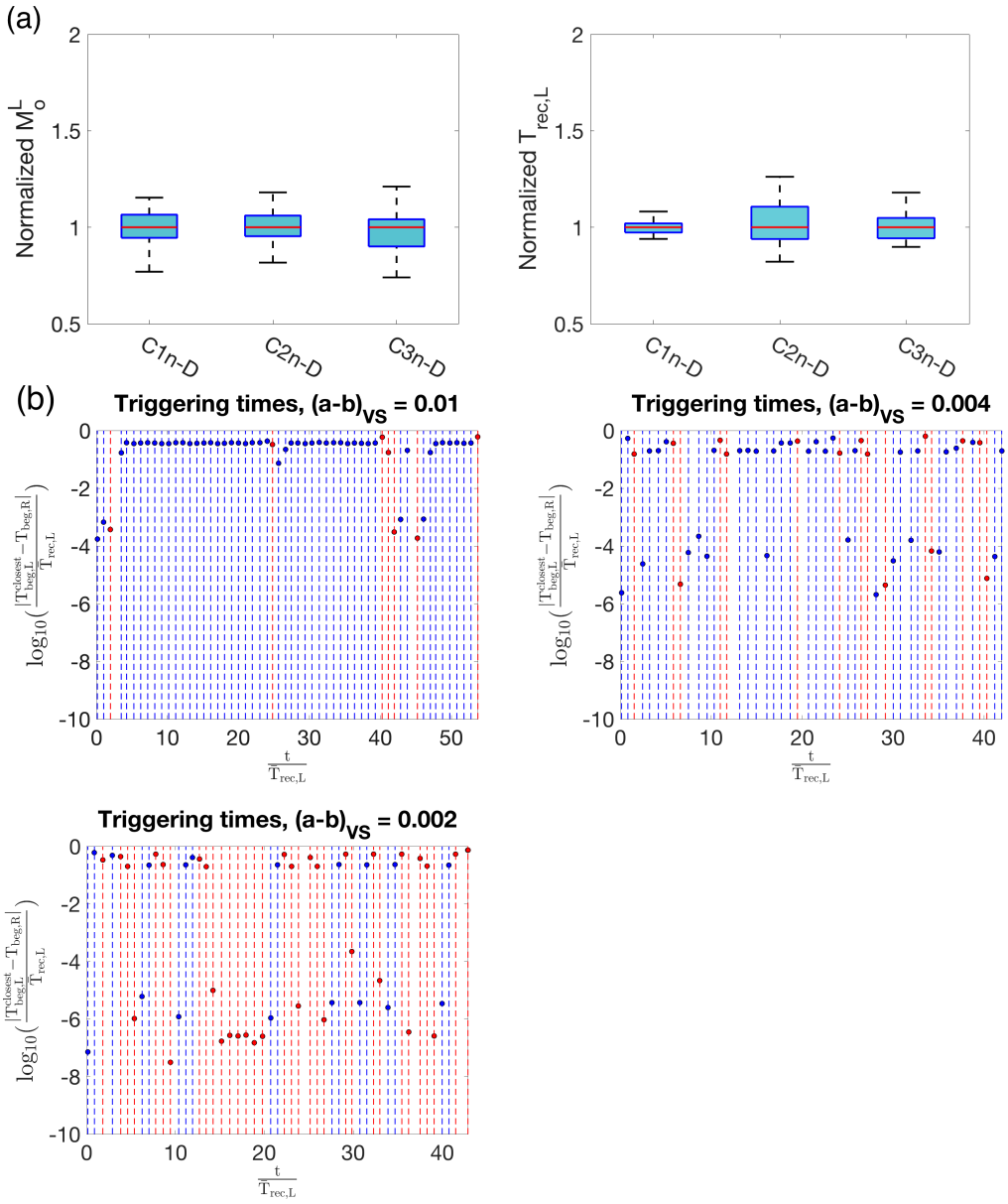

Figure 2.15: a. Box plots visualizing the variation in moment and recurrence time with varying VS properties. b. Triggering times of left and right patches for models with circular patches, C1n-D, C2n-D, C3n-D. The red points indicate inter-event times in which the bigger, left patch is triggering the smaller, right patch. The model with the reduced strengthening of the surrounding medium has response comparable to observations, with a range of triggering times.

As we reduce the strengthening of the VS region, there is more triggering of events on the right patch by the left patch (Figure 2.15b). Of particular interest is the case of circular patches with the smallest value of the strengthening, $(a - b)_{VS} = 0.002$ (Model C3n-D). For two differently sized VW patches comparable to the nucleation size, with all other properties remaining the same, one would expect the smaller patch to nucleate first and more often, and trigger the bigger patch. This is because, since the patch is smaller but comparable to the nucleation size, slow slip that can lead to nucleation has less distance to travel from the boundaries to the center of the patch, making the whole patch creep and potentially destabilize sooner. But from our simulations, this is not necessarily the case. If the bigger patch has a stress state more conducive to hosting an event, the occurrence of that event can establish a chain of event sequences where the bigger patch triggers the smaller one (Figure 2.15b).

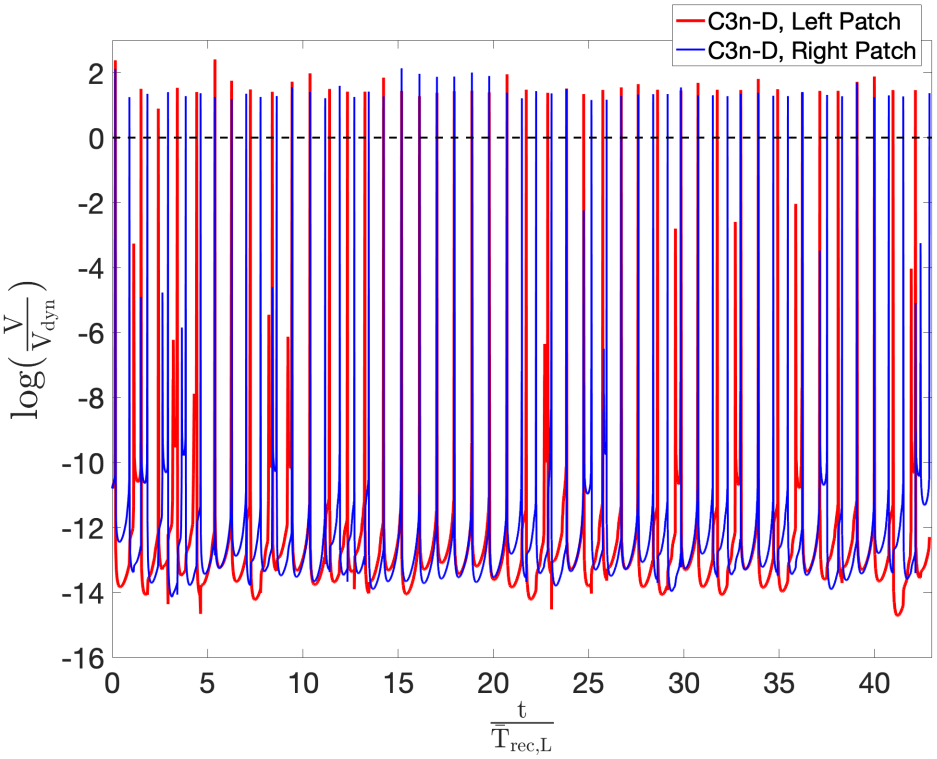

Figure 2.16: Slip velocity history at the centers of left (red) and right (blue) patches in model C3n-D. The history shows the behavior alternating between periods in which event in one patch triggers an event in the other patch nearly instantaneously compared to the average recurrence time of each sequence (e.g. during 15-20 time units) and periods in which the left and right patch events occur more spaced out in time, with their interevent time being a large fraction of the average recurrence time (e.g. during 10-15 time units).

As an example, in the simulation with circular patches and $(a-b)_{VS} = 0.002$, during the period between 15-20 time units normalized with respect to the mean recurrence interval of the left patch, there are ~ 7 event pairs in which the larger left patch keeps triggering the right patch(2.15b). This triggering behavior varies with time. When we look at the slip velocity history at the two patches (Figure 2.16), between 10-15 time units, the events in each patch are a significant fraction of the recurrence time apart. During such periods, each time an event occurs on one patch, the postseismic front from the event triggers an aseismic transient on the other patch (Figure 2.17a), relieving stress and delaying the nucleation of subsequent event in that patch. However, at some point, the left-patch event occurs when the right patch is more ready to host a seismic event, starting a sequence of event pairs between 15-20 time units where an event in the left patch triggers an event in the right patch

nearly instantaneously compared to the average recurrence time of each sequence. In these event sequences, the right patch is in a state favorable for rupture, and so the postseismic front from the left patch event triggers a seismic event (Figure 2.17b) on the right patch each time, until it does not, after 7 triggering cycles. This complex dynamics arises from the fact that both patches are of similar size, just above nucleation size, and are similarly able to nucleate. Depending on the state of the neighboring patch when the post-seismic slip front from an event reaches it, either an aseismic transient or a dynamic event can occur. This results in two types of behaviors in which the left and right patch events appear to occur almost independently with respect to each other vs. periods where event in one patch clearly triggers an event in the other patch.

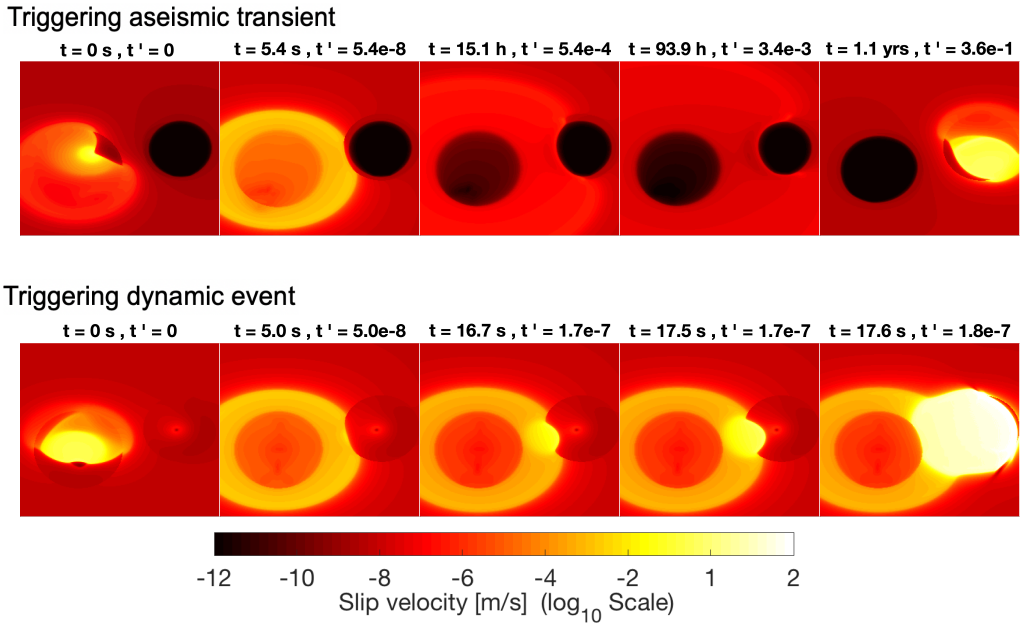

Figure 2.17: Two types of interaction between patches observed in C3n-D model. Time t is the simulated time since an event in the left patch as shown in the left-most panel. Time t' refers to the simulated time normalized with respect to mean recurrence time of left patch events ($T_{rec,L}$). (Top row) The postseismic front from a left-patch event triggers an aseismic transient in the right patch, with the nucleation of the next seismic event there occurring in 1.1 years or 0.4 of the recurrence interval. b. The postseismic front from a left-patch event triggers a dynamic event in the right patch within seconds or nearly instantaneously compared to the recurrence period, owing to the favorable state of stress in the right patch.

In this study, we do not ensure that the bigger, left patch always triggers the smaller, right patch. Instead, the presented simulated slip patterns contain subsets of the event sequences that behave that way. To ensure that the right patch is always

triggered by the left patch, we can make the nucleation size of the right patch larger than its diameter, for example, by increasing the characteristic slip distance (D_{RS}), as done in a previous study Lui and Lapusta (2018). The resulting subcritical nature of the right patch would ensure that the events hosted by the right patch are always triggered by the left patch.

It is interesting to note that when the same study of varying VS properties is conducted in models with double fractal patches, the values of $(a-b)_{VS} = 0.004, 0.002$ result in both patches rupturing together in models F2n-D and F3n-D. This is because the irregular shapes of the patches are such that they narrow the distance between the two patches in places, promoting rupture propagation.

Matching the observed variability

As discussed in Section 1.2 (Figure 1.2, 1.3), the variability of the LA-SF repeating sequences is characterized by a certain spread of data points in the predictability plots as well as by the presence of both relatively long and short triggering times. The models with similar behaviors are F1n-D, F1p-D, and C3n-D (Figures 2.10c, d 2.14c).

The model with two circular VW patches and the least-strengthening region around them (C3n-D) exhibits the right range of triggering times as well as produces variability in seismic moment comparable to that of to the SF-LA repeater data (Figure 1.2). The other models with circular patches either do not have enough variability, or do not have the right range of triggering times, or both.

The models with complex patch shapes, F1n-D and F1p-D, exhibit the co-existence of short and long triggering times, as well as significant variability in both moment and recurrence time (Figure 2.11, 2.13). The data points in the predictability plots exceed the bounds of the rectangles indicating the variability of the 7 SF-LA event pairs, which can potentially be explained by the longer model event sequences. The predictability plots from the complex patch models also replicate the variability in recurrence time being larger than the variability in seismic moment seen in Figure 1.1. So, from the perspective of matching the variability of larger sets of repeater observations, the models with complex patches fare better.

2.6 Effect of small-scale heterogeneity on slip behavior

For complex property distributions, a naturally stemming area of interest is the effect of small-scale heterogeneity on the system response. The working hypothesis is that

heterogeneity on the scales comparable to or larger than the important length scales in the problem, such as the nucleation size h^* or cohesive zone size R_o, influences slip behavior, while features much smaller than them would be averaged out.

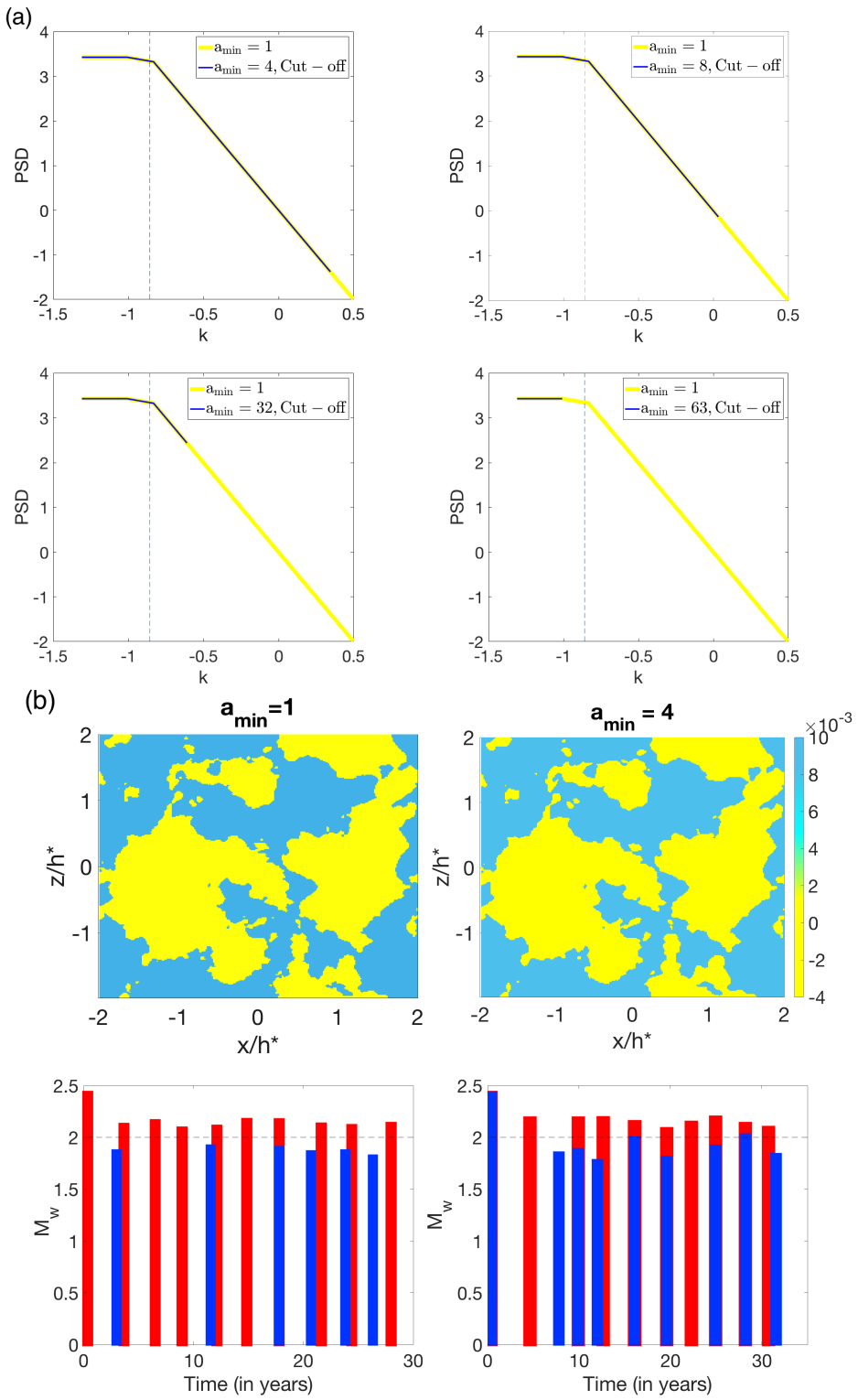

Figure 2.18: a. Removing small-scale heterogeneity by thresholding the power spectral density of the underlying fractal distribution. b. The property distributions for a_{min} = 1 and a_{min} = 4 appear visually identical to the observer, whereas the resulting slip behavior exhibits visible differences.

To examine the effect of small-scale heterogeneity, we cut the power spectral density of the underlying fractal distribution above a wave number threshold (Figure 2.18). This results in the removal of frequencies higher than the threshold from the distribution, which results in the distribution being smoother at smaller scales (Figure 2.19). As we smooth the distribution (Figure 2.19), the fractal features disappear and the two dominating patches come into contact with each other at around $a_{min} = 16$, thereupon coalesce into a single connected area, and eventually getting separated at $a_{min} = 60$. The maximum smoothing that can be applied to the distribution, $a_{min} = 63$, renders the patches relatively simple in shape.

As the small-scale features are removed, the variability exhibited by the models and the interaction between the two patches stays similar for a while, within the range of $a_{min} = 1$ to 32 (Figures 2.20 and 2.21). The exact slip behavior changes, but the bounds of variability and triggering times are comparable between the models in this range. As can be observed from the box plots in Figure 2.22, the IQRs across models are comparable within that range of smoothing. For $a_{min} = 48$ and larger, however, with most of the features smoothed on scales comparable to h^*, the variability changes and the short triggering times (1-100 secs) vanish, diverging from observations. The absolute values of moment magnitudes are observed to reduce with noticeable smoothing, since the removal of small-scale features eventually chips away at the size of the patches.

Let us compare the smoothest case ($a_{min} = 63$), stripped of its surrounding perturbing patches, to the double circular-patch model (C1n-D) (Figure 2.23). The smooth but irregular shapes of the patches still result in the higher degree of variability than the circular patches. This increase in variability, particularly in recurrence time, is also reflected in the box plots comparing the two models (Figure 2.23c), and is quantitatively observed in Table 2.4. On comparing the triggering times between the two models (Figure 2.23d), we see that the slightly complex shape results in more realistic, variable triggering behavior, with the bigger, left patch triggering events in the smaller, right patch more frequently than in the circular patch model. The short triggering times, however, are absent in both the models. This could be partly resolved by reducing the strengthening properties of the VS region.

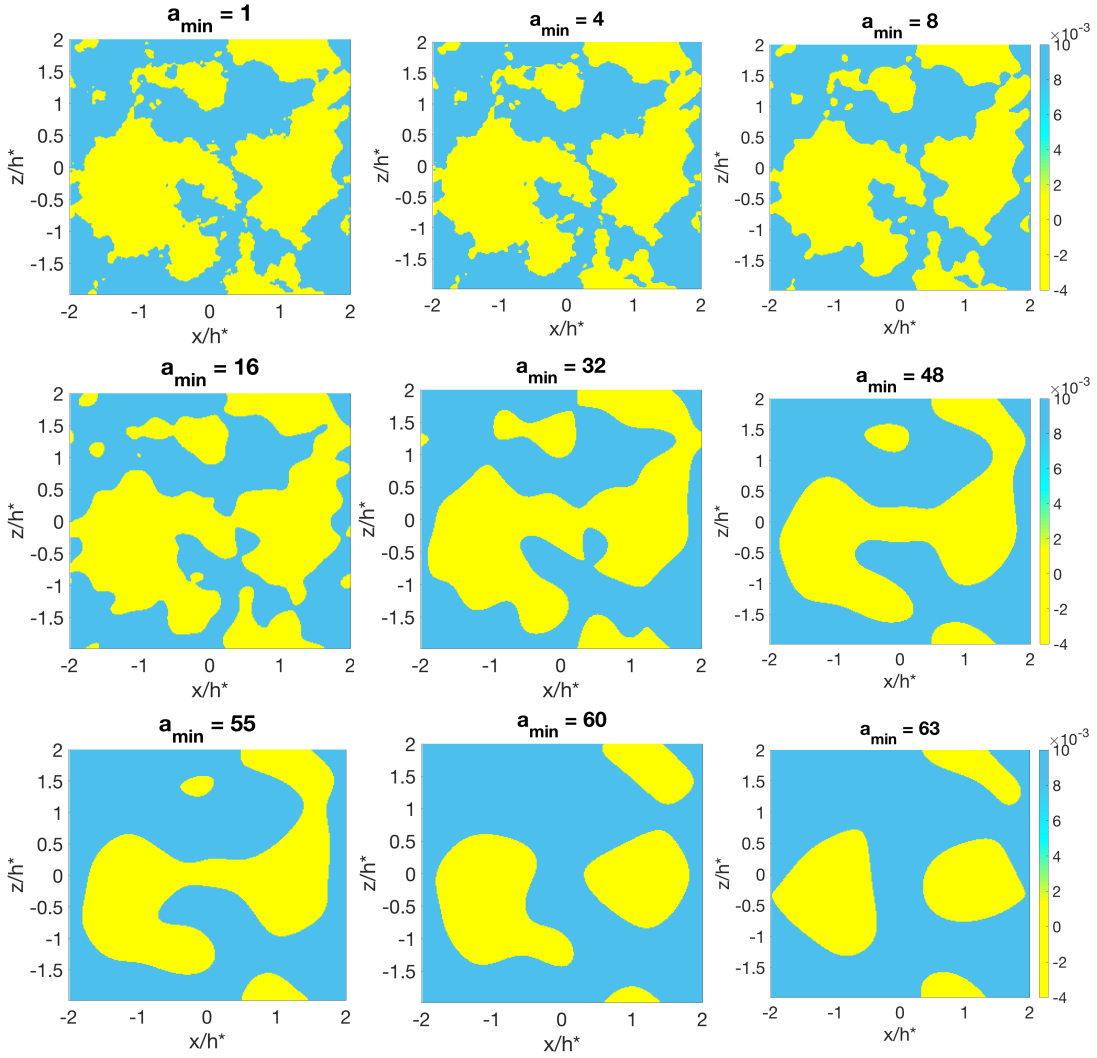

Figure 2.19: Models obtained by smoothing of the patch shapes by eliminating high-frequency contributions. The fractal features gradually disappear, and the separate patches coalesce to form a single area for some models. At a_{min} = 63, the patches present as relatively simple shapes, with the power-law decay completely removed from the spectra (Figure 2.18). Note that a_{min} = 32 still preserves heterogeneous features at the scale of the nucleation size, with larger values of a_{min} resulting in significant modifications of the shape at that scale.

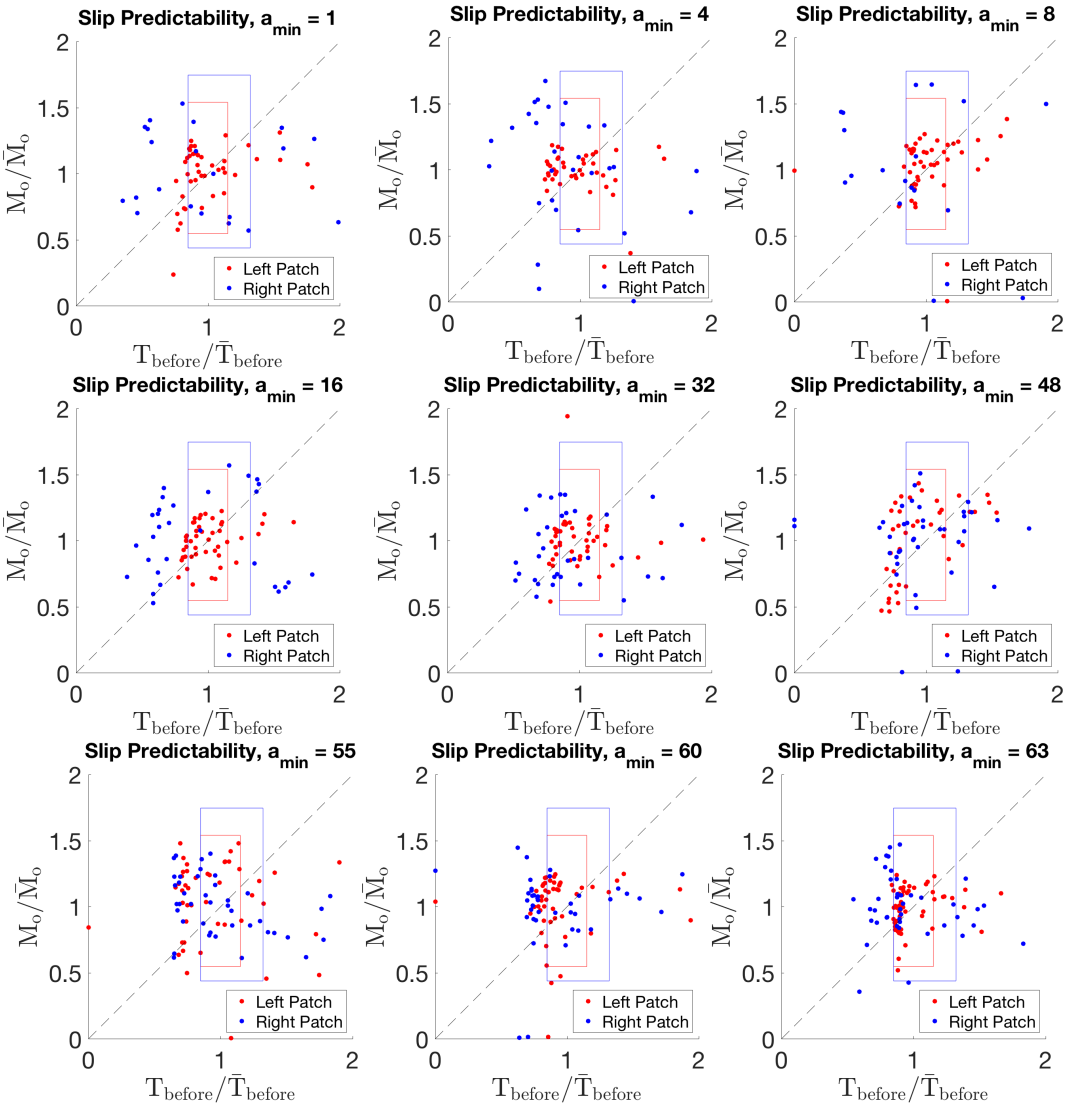

Figure 2.20: Slip predictability in models with increasingly smoother distributions. The variability exhibited is similar in models with small enough features removed, for a_{min}=1 to 32. Beyond that, as the fractal features get wiped off, the data points in the predictability plots become increasingly clustered. See also Figure 2.22 for more quantitative measure.

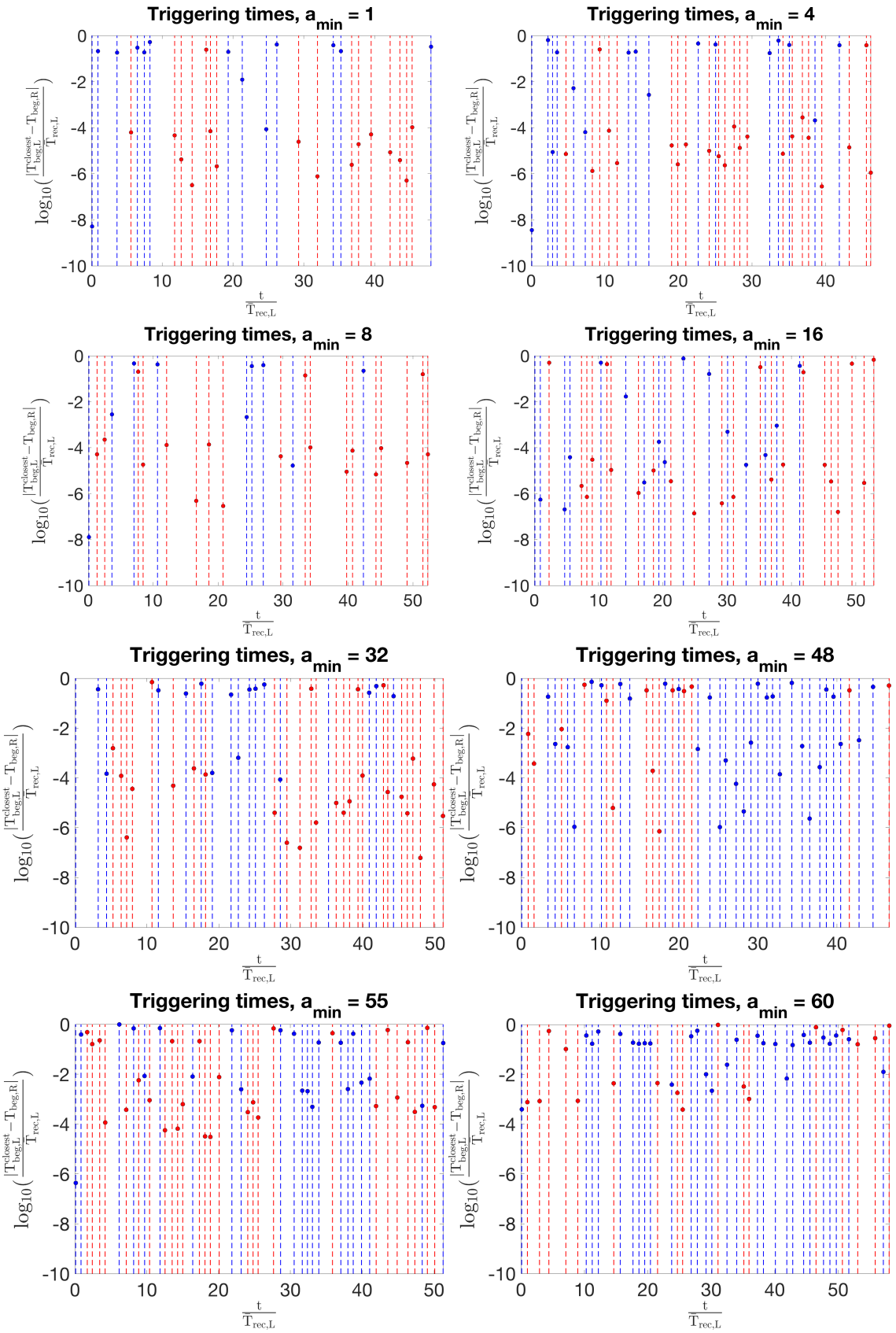

Figure 2.21: Triggering times are compared across models subjected to smoothing of fractal features. The range of triggering times is similar in models with small enough features removed, for a_{min} = 1 to 32. The shorter triggering times vanish, diverging from the field observations, as the distribution is smoothed further.

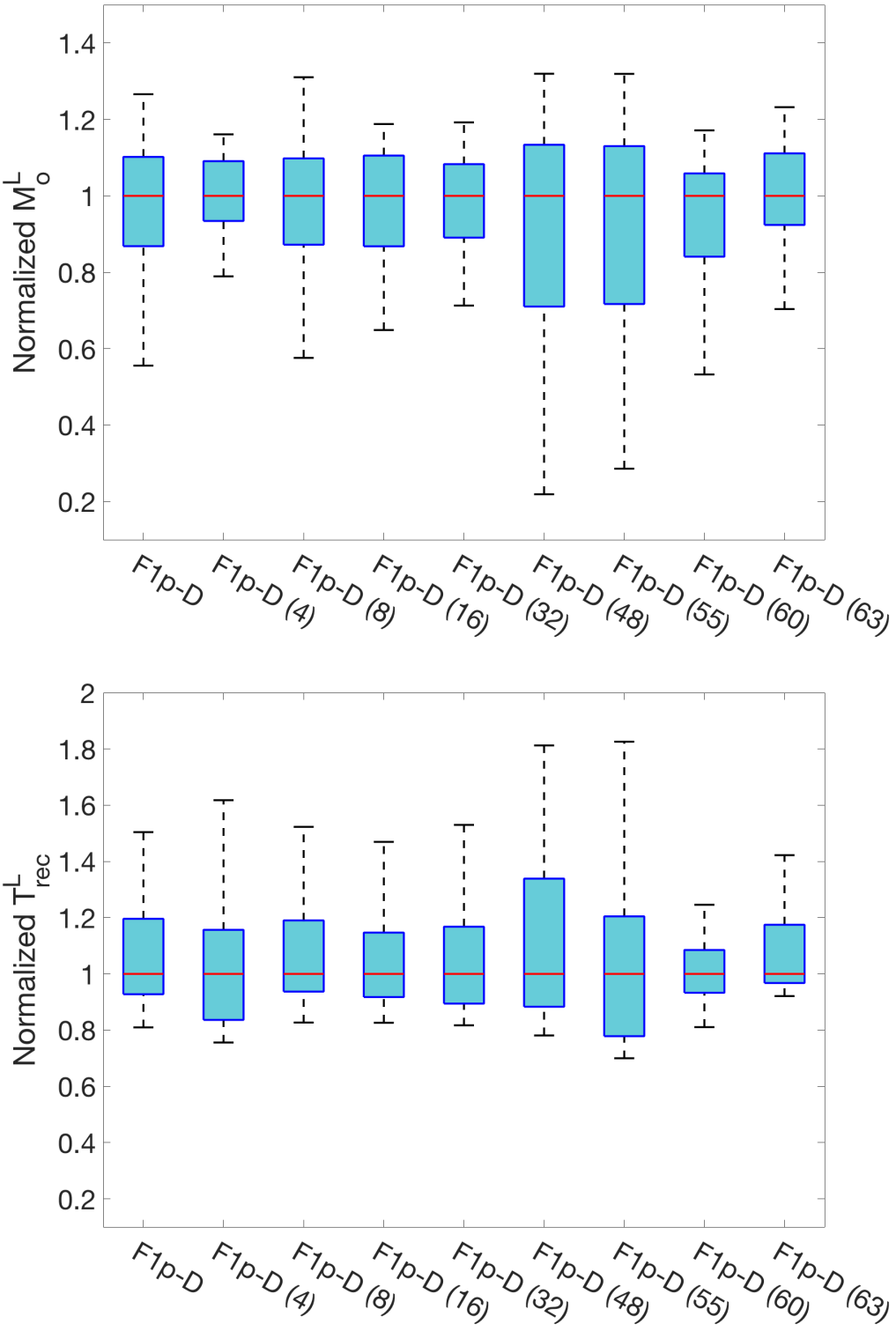

Figure 2.22: Box plots comparing variability in gradually smoothed distributions. The variability is most similar in the models with small enough features removed, for a_{min} = 1 to 32, have most similar. Beyond that, the variability first increases and then decreases.

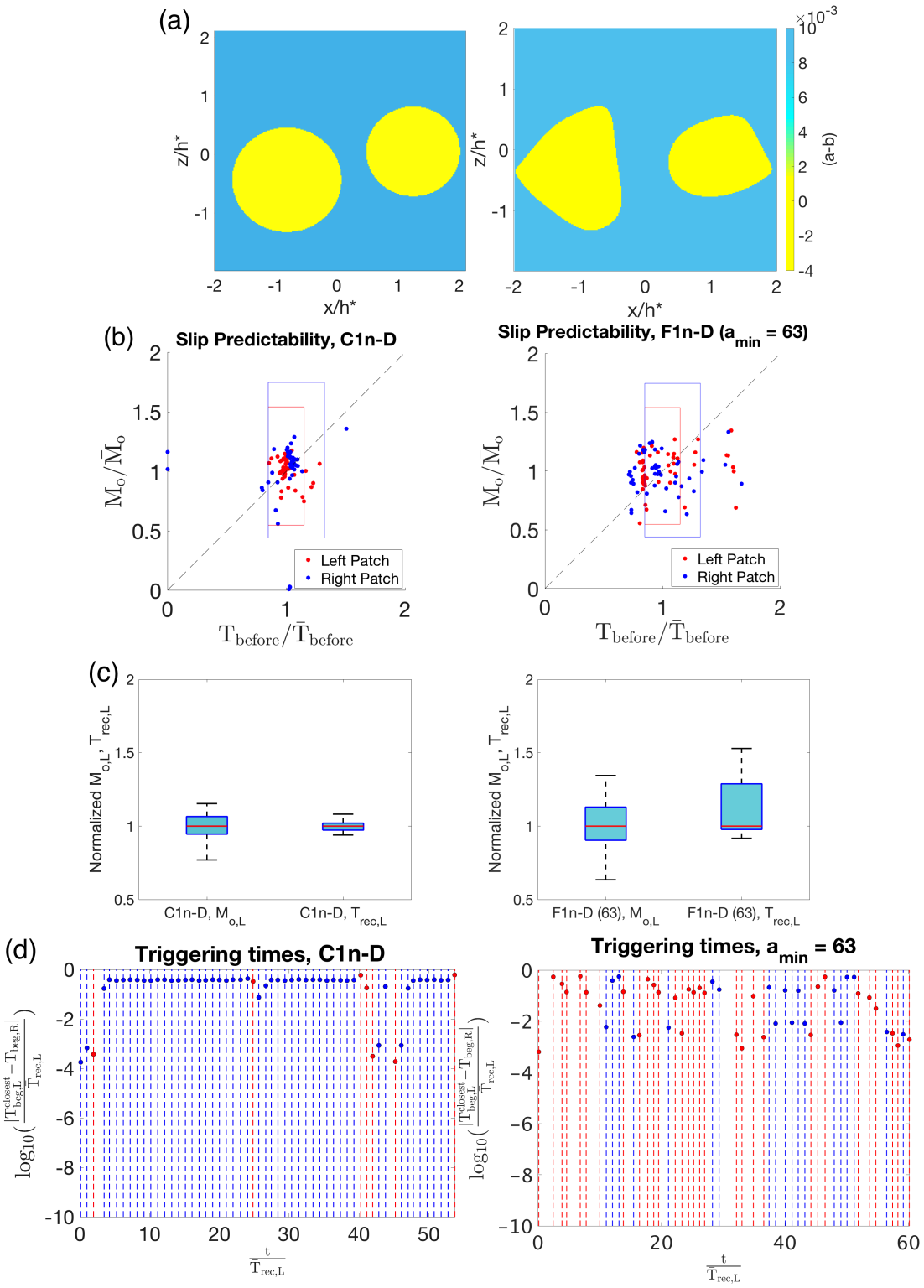

Figure 2.23: a. Comparison between the circular patch model (C1n-D) and the most smoothed fractal patch model (F1n-D, a_{min}=63). b. The slip predictability plots show more variability for F1n-D (a_{min}=63) compared to C1n-D. c. The left-patch box plots of models C1n-D and F1n-D (a_{min}=63). The variability is again larger for the fractal patch model. d. The slight complexity in shape produces more variable triggering times, though not broad enough compared to the natural sequences.

Model	$\bar{M}_{o,L}(\times 10^{11})$	$\bar{M}_{o,R}(\times 10^{11})$	$\bar{T}_{rec,L}$ (yrs)	$\bar{T}_{rec,R}$ (yrs)	$\Delta\bar{\tau}_L$ (MPa)	$\Delta\bar{\tau}_R$ (MPa)
Repeaters (Data)	16.29	10.18	2.89	2.89	25 – 65	1 – 20
F1n-S	19.03		2.73		19.55	
C1n-S	14.51		2.76		22.07	
F1n-S ↑ 20%	44.16		3.54		21.57	
C1n-S ↑ 20%	29.99		3.44		24.81	
F3n-S	37.75		3.26		16.4	
C3n-S	22.89		3.01		18.17	
F1n-D	20.91	8.73	3.04	4.05	20.67	21.12
F1p-D	19.7	9.66	3.19	5.48	20.31	20.66
C1n-D	16.75	8.85	2.96	2.69	25.28	23.11
C2n-D	21.74	10.87	3.14	2.66	22.39	20.04
C3n-D	26.61	14.92	3.15	2.64	19.65	18.35
C1p-D	15.57	8.41	2.93	2.74	24.22	22.09
F1p-D (a_{min} = 4)	20.81	9.57	3.33	4.24	20.81	21.42
F1p-D (a_{min} = 8)	18.31	8.46	2.94	6.09	20.87	22.33
F1p-D (a_{min} = 16)	21.06	10.72	3.01	4.29	20.75	20.89
F1p-D (a_{min} = 32)	19.79	10.82	3.05	3.61	20.89	21.02
F1p-D (a_{min} = 48)	14.57	8.55	3.05	3.03	20.78	20.49
F1p-D (a_{min} = 55)	12.21	7.67	2.89	3.15	20.7	20.11
F1p-D (a_{min} = 60)	12.75	5.51	2.73	3.29	21.71	20.43
F1p-D (a_{min} = 63)	11.19	5.88	2.61	3.11	21.79	19.02
F1n-D (a_{min} = 63)	10.74	5.91	2.78	2.96	21.07	19.28

Table 2.3: Mean source properties for all models with two patches, from left to right: Mean seismic moment on the left patch, mean seismic moment on the right patch, mean recurrence time on the left patch, mean recurrence time on the right patch, mean stress drop on the left patch, and mean stress drop on the right patch.

Model	$\tilde{M}_{o,L}(\times 10^{11})$	IQR/$\tilde{M}_{o,L}$	$\tilde{M}_{o,R}(\times 10^{11})$	IQR/$\tilde{M}_{o,R}$	$\tilde{T}_{rec,L}$ (yrs)	IQR/$\tilde{T}_{rec,L}$	$\tilde{T}_{rec,R}$ (yrs)	IQR/$\tilde{T}_{rec,R}$
Repeaters (Data)	17.78	0.374	8.91	1.2236	2.88	0.2	2.65	0.23
F1n-S	19.1	0.05			2.65	0.02		
C1n-S	14.29	0.06			2.74	0.02		
F1n-S ↑ 20%	44.9	0.07			3.37	0.07		
C1n-S ↑ 20%	29.9	0.05			3.41	0.01		
F3n-S	37.25	0.11			3.2	0.04		
C3n-S	23.14	0.06			3.03	0.03		
F1n-D	20.91	0.2	7.84	0.57	2.72	0.27	3.62	0.75
F1p-D	20.46	0.23	8.62	0.66	2.89	0.3	4.86	0.96
C1n-D	16.95	0.12	9.43	0.13	2.9	0.04	2.86	0.05
C2n-D	21.77	0.09	11.24	0.22	3.09	0.15	2.66	0.22
C3n-D	26.53	0.14	13.85	0.19	3.05	0.1	2.5	0.18
C1p-D	16.35	0.15	8.45	0.3	2.87	0.18	2.83	0.19
F1p-D (a_{min} = 4)	20.91	0.14	9.58	0.61	3.25	0.3	3.6	0.6
F1p-D (a_{min} = 8)	19.2	0.25	8.24	0.72	2.8	0.25	5.6	0.86
F1p-D (a_{min} = 16)	21.5	0.23	10.5	0.6	2.8	0.23	3.1	1.01
F1p-D (a_{min} = 32)	19.9	0.2	9.43	0.54	2.8	0.25	3.08	0.59
F1p-D (a_{min} = 48)	15.9	0.38	9.26	0.24	2.6	0.44	2.76	0.48
F1p-D (a_{min} = 55)	13.5	0.4	7.84	0.35	2.59	0.46	2.86	0.52
F1p-D (a_{min} = 60)	13.9	0.21	5.83	0.21	2.4	0.15	2.74	0.46
F1p-D (a_{min} = 63)	11.2	0.2	5.68	0.33	2.38	0.2	2.78	0.31
F1n-D (a_{min} = 63)	10.7	0.22	5.94	0.24	2.38	0.3	2.68	0.32

Table 2.4: Simulated source properties for all models with two patches, median values and inter-quartile ranges (IQR).

2.7 Conclusions

We have explored several potential sources of the observed variability in the SF-LA repeating sequences and their interaction using rate-and-state models with various shapes of the VW patches and properties of the VS regions. Our models reproduce many observations about the repeating sequences, including their mean seismic moment, recurrence times, stress drops, and the observed non-trivial scaling between the seismic moment and the recurrence times for repeating sequences more broadly. We find that multiple models produce slip behaviors similar to the observations. Models with fractal shapes of VW patches introduce substantial variability into the system, comparable to the variability in the SF-LA sequences, and result in the right range of triggering times. Another model that reproduces variability comparable to the SF-LA sequences and includes shorter triggering times is the one with simple, circular patches as in prior studies but within a VS region with smaller values of velocity strengthening. One can further increase the variability of the slip patterns in all models by adding perturbing sub-critical patches which arise naturally from the underlying fractal distribution. In the models with fractal patches, this introduces variability stronger than what is observed in the SF-LA event pairs and more comparable to the observations from a larger data set of repeating events (Figure 1.1).

Hence there is a trade-off between the shape of the repeating patches and the level of velocity strengthening of the surrounding region, and there could be infinitely many parameter combinations that reproduce similar variability in slip behavior and interaction matching observations. Triggering processes between the two patches are observed to be strongly affected by the nature of the region between the two source patches. The region can be modified both by changing its strengthening properties (Lui and Lapusta, 2016) and by incorporating complexity in the patch shapes, thereby affecting the separation between the patches. Less strengthening friction between the two patches promotes larger dynamic rupture sizes and faster postseismic slip, allowing for shorter triggering times. Fractal shapes of the patches result in the narrowing of the region between the two patches in places, again allowing for shorter triggering times.

We have studied how the small-scale features of heterogeneity affect the model response. Removing even the high frequencies in the underlying distribution of VW/VS properties changes the behavior of the fractal-patch model in terms of specific sequences of events, highlighting the highly non-linear nature of the problem. However, the overall variability and the range of triggering times remain similar, until smoothing of the distribution eliminates fractal features of the order of relevant length scales such as the nucleation size. For the largest possible smoothing, the patches, while of irregular shape, resemble circular ones, and the behavior becomes similar to the model with circular patches, although still more variable. We note here that even very small features cannot be ignored or averaged over if they change the relevant local length scales, such as the nucleation size; for example, small-scale patches of high normal stress that reduce the nucleation size locally can lead to qualitatively different behavior (Schaal and Lapusta, 2019).

Our results shows that the combination of variability in moment magnitudes and recurrence times with the range of triggering times cannot be used to individually constrain VS properties or the shape of the VW patches. Other aspects of the fault properties can be heterogeneous, such as the distributions of normal stress and friction properties within both VW patches and VS region around the patches; such additional heterogeneity can bring additional trade-offs. Furthermore, other mechanisms can be important, such as various fluid effects (Rice, 1992; Liu and Rice, 2007). One could consider constraining the problem further by matching the specific behavior of the repeaters, i.e., the exact sequence of magnitudes, recurrence times, and triggering times rather than their variability/range. However, such study may be

intractable, given that specific sequence behaviors change in response to variations in properties even on small scales compared to the patch size and nucleation size.

Chapter 3

NUCLEATION PROCESSES ON INTERFACES WITH HETEROGENEOUS NORMAL STRESS

In this chapter, we explore the evolution of complex nucleation processes on fault interfaces with systematically increasing heterogeneity in normal stress. The earthquake nucleation process, particularly in heterogeneous conditions, is still not fully understood. Better understanding of how natural earthquakes initiate on complex fault geometries can hold the key to answering fundamental questions regarding the entire earthquake process.

3.1 Model description and methodology

The focus of this work is to study the nucleation of slip events on heterogeneous frictional interfaces.

Heterogeneity in normal stress

We consider models with increasing heterogeneity in normal stress distributions (Figure 3.1) and compare them to the homogenous fault. First we consider the pure fractal-like distribution which has a 60% variation in normal stress ($\sigma_{max}/\sigma_{uni}$ = 1.6). To obtain a rectangular fault domain that enables study of nucleation and propagation of events, the same fractal field (Figure 3.2) is repeated twice along length. For numerical convenience and a larger aspect ratio of the domain, the width of the rectangular domain is reduced by 25% to create the final fault interface (Figure 3.1b).

To study the nucleation process in interfaces with systematically stronger heterogeneity, up to $\sigma_{max}/\sigma_{uni} = 10$, while avoiding tensile stresses, we need to further modify the fractal distribution. In a purely fractal-like distribution with compressive stresses, the mean normal stress of the distribution cannot be mathematically less than half the maximum normal stress. To obtain higher strength contrast relative to the background, we modify the underlying fractal distribution as follows. A threshold level σ_{th} is chosen as discussed below. The minimum compressive normal stress of the modified distribution is chosen, $\sigma_{min} = 0.1 \times \sigma_{th}$. The distribution is divided into two sections, one where the stress values are below σ_{th}, and the other section has stress values above σ_{th}. We separately interpolate the two sections, section 1

between σ_{max} and σ_{th} and section 2 between σ_{th} and σ_{min}. This results in a modified fractal distribution, where the peaks are stretched up, and the remaining distribution is compressed, resulting in separated peaks. The threshold level, σ_{th}, is chosen such that the mean of the modified distribution is equal to the mean of the original fractal distribution. As for the fractal case, to create the final fault interface, the modified fractal normal stress distribution is repeated twice and then the domain width is reduced by 25% (Figure 3.1 c, d).

The most heterogeneous model interface we consider in the study has a maximum normal stress to uniform normal stress ratio ($\sigma_{max}/\sigma_{uni}$) of 10. While this factor may appear too large to be realistic, it can actually be quite reasonable. We are motivated by stress distributions here where σ_{uni} is low, about 5 MPa, motivated by lab experiments and reports of low normal stress on many natural fault zones (Lockner et al., 2011; Carpenter et al., 2011). This implies that σ_{max} in the most heterogeneous distribution we study is about 50 MPa. Considering characteristic elastic Young's moduli of 40-100 GPa, a difference between maximum and uniform normal stress of about 45 MPa due to fault roughness would correspond to additional normal strains of the order of 10^{-3}, which are within the elastic regime. Note that studies of non-planar surfaces (Fang and Dunham, 2013) indicate that rough faults can have additional resistance in the form of roughness drag. Additional peak normal strains of 10^{-3} would be obtained from similar amplitude-to-wavelength (α) ratios of roughness. For such α values and large-scale nature of the locations of peaked stresses compared to fault slips, the roughness drag would be small relative to frictional resistance, as calculated by equation 6 from Fang and Dunham (2013). Alternatively, if the fault is permeated with fluids, the difference in the effective normal stress distribution can come from the heterogeneous distribution of pore pressure due to different permeabilities on the fault, as assumed in some prior studies (Luo and Ampuero, 2018). The two effects can also combine, with some effective normal stress increase coming from large compressive stresses due to local non-planarity and some increase coming from lower pore fluid pressure due to lower permeability of such spots.

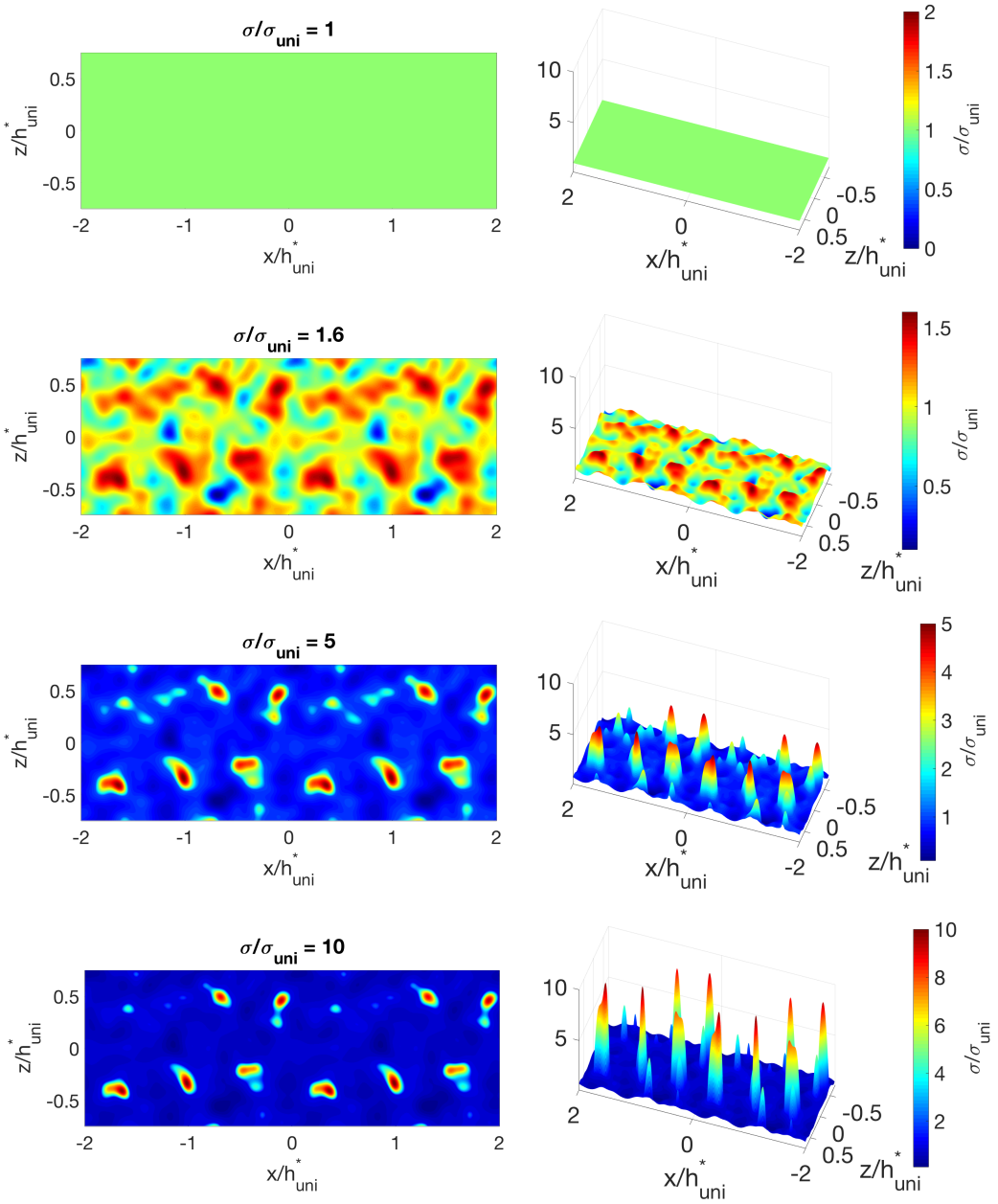

Figure 3.1: 2D and 3D views of several normal stress distributions studied in this work. a. Uniform normal stress ($\sigma_{max}/\sigma_{uni}$=1). b. Fractal normal stress ($\sigma_{max}/\sigma_{uni}$ = 1.6). c. Modified fractal normal stress ($\sigma_{max}/\sigma_{uni}$ = 5). d. Modified fractal normal stress ($\sigma_{max}/\sigma_{uni}$ = 10).

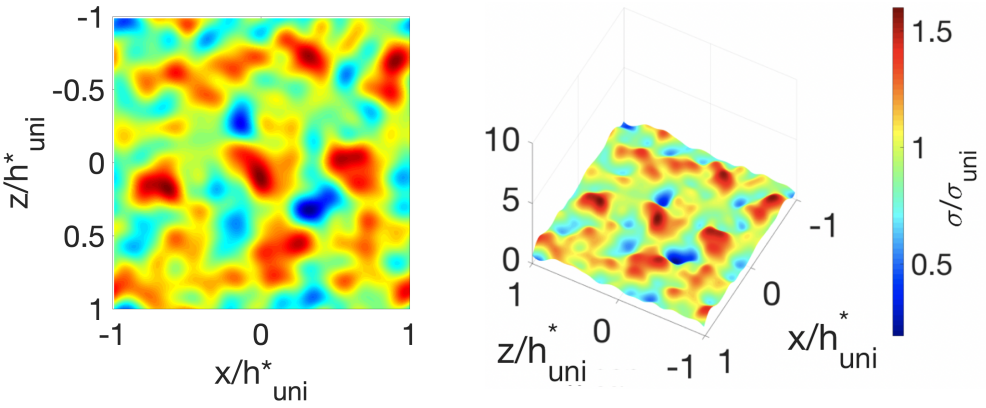

Figure 3.2: A realization of the random field with multiple source patches. The fractal field is characterized by the Hurst constant H that determines the spectral decay at high frequencies and parameter k_c that modulates the sizes of the largest features. We choose $H = 1$ (self-similar distribution) and $k_c = 0.14$ such that there are multiple similarly-sized high-normal-stress patches within the field.

Fault Model

The planar fault domain of interest with the heterogeneous normal stress distribution has velocity-weakening (VW) rate-and-state friction properties (Figure 3.3). It is surrounded by a velocity-strengthening (VS) region that creeps in response to plate loading and hence loads the VW region. The VS region also serves as a barrier to arrest the resulting dynamic ruptures.

This planar fault is embedded into an elastic bulk and slow, tectonic loading is applied by steady sliding outside of the VS region. We use a 3D, fully dynamic simulation code (Noda and Lapusta, 2010) to solve the resulting elastodynamic problem with friction as a nonlinear boundary condition. The simulations produce quantities of interest such as time evolution of slip, slip rate, and stresses on the fault, which we can then compare with experimental and real-world data. The main differences in the model used in this chapter when compared to the modeling of repeaters in Chapter 2 are the specific realization of fractal field used for generating the heterogeneity and the fact that the heterogeneity is introduced in normal stress and, in some models, in the characteristic slip D_{RS}; all other frictional properties remain uniform.

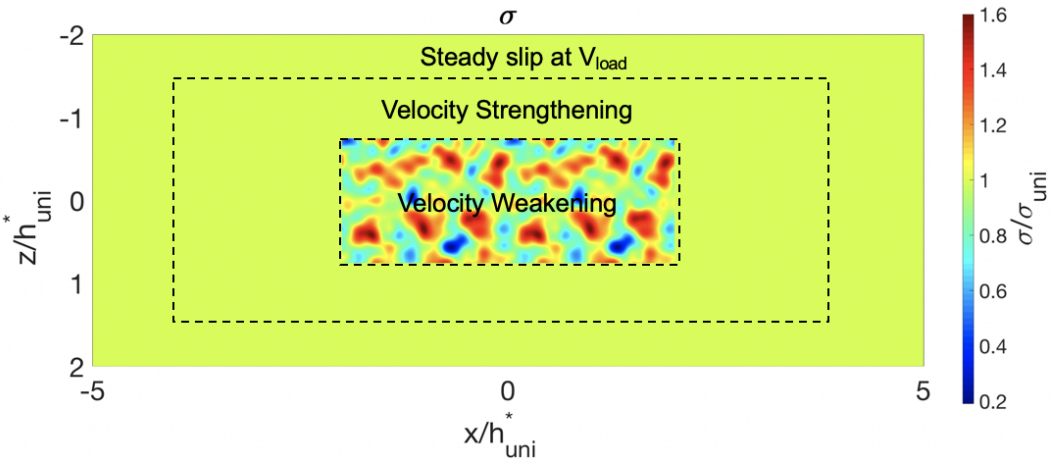

Figure 3.3: Representative model domain used in the simulations, normalized with respect to h^*_{uni}, the nucleation size estimate corresponding to σ_{uni}.

Fault parameters used in all models are the same as those used in Schaal and Lapusta (2019), which reproduce the experimental conditions used by McLaskey and Kilgore (2013), and they are listed in Table 3.1. Fluid effects are not considered in this study, and the effective normal stress $\bar{\sigma} = \sigma - p = \sigma$, where p is the pore pressure. The normal stress corresponding to the uniform normal stress model, σ_{uni}, is 5 MPa,

and the nucleation size estimate, h^*_{uni}, corresponding to σ_{uni} and other properties in Table 3.1 is 1 m. The mean normal stresses in all the models are similar to σ_{uni}, the nominal differences among the two arising due to trimming of the width of the original rectangular distribution to facilitate rupture propagation. (Table 3.2).

Parameter	**Symbol**	**Value**
Rate and state parameters in VW region	a_{vw}, b_{vw}	0.01, 0.0255
Rate and state parameters in VS region	a_{vs}, b_{vs}	0.0255, 0.01
Normal stress in the uniform model	σ_{uni}	5 MPa
Peak normal stress	σ_{max}	5 - 50 MPa
Characteristic slip distance	D_{RS}	1 μm
Loading velocity	V_{pl}	4 $\times 10^{-8}$ m/s
Reference slip velocity	V^*	10^{-6} m/s
Reference friction coefficient	f^*	0.6
Shear wave speed	c_s	3 km/s
Shear modulus	μ	30 GPa
Poisson's ratio	ν	0.25

Table 3.1: Fault parameters used in simulations

Model	$\sigma_{mean}/\sigma_{uni}$	$h^*_{\sigma_{mean}}/h^*_{uni}$	h^*_{mean}/h^*_{uni}
$\sigma_{max}/\sigma_{uni} = 1$	1	1	1
$\sigma_{max}/\sigma_{uni} = 1.6$	0.992	1.009	1.06
$\sigma_{max}/\sigma_{uni} = 3$	0.996	1.004	1.17
$\sigma_{max}/\sigma_{uni} = 4$	1.000	0.999	1.22
$\sigma_{max}/\sigma_{uni} = 5$	1.006	0.995	1.26
$\sigma_{max}/\sigma_{uni} = 6$	1.011	0.990	1.29
$\sigma_{max}/\sigma_{uni} = 7$	1.016	0.983	1.31
$\sigma_{max}/\sigma_{uni} = 8$	1.021	0.980	1.33
$\sigma_{max}/\sigma_{uni} = 9$	1.022	0.977	1.35
$\sigma_{max}/\sigma_{uni} = 10$	0.950	1.053	1.42

Table 3.2: Comparison between σ_{uni}, σ_{mean}, h^*_{uni}, $h^*_{\sigma_{mean}}$ and h^*_{mean}. The differences between the mean parameter values and the parameter values corresponding to the uniform model result from removing part of the domain.

In all the figures, the spatial dimensions are normalized by h^*_{uni}, which is the nucleation size estimate calculated by equation 2.3 for the uniform normal stress model. The domain of interest with heterogeneous normal stress distribution and VW properties is $1.5h^*_{uni} \times 4h^*_{uni}$ (Figure 3.3). The surrounding VS area is $3h^*_{uni} \times 8h^*_{uni}$ and the total model domain is $4h^*_{uni} \times 10h^*_{uni}$. Slip velocity is normalized with respect to the dynamic slip velocity threshold (V_{dyn}), calculated using equation

2.4. For the model parameters used in this study, the corresponding V_o for which inertia becomes important comes out to be 0.0124 m/s, which we chose to be the representative velocity threshold, V_{dyn}, for all the simulations in this work. We use V_{dyn} to identify the beginning and end of earthquake rupture events. If the maximum velocity at any point on the fault exceeds V_{dyn}, the beginning of an event is recorded. And if all points reach slip rates below V_{dyn}, the event is considered to end.

Quantities like normal stress, stress drops, seismic moments and moment rates are normalized with respect to their corresponding mean values in the model.

Time is normalized by the ratio of the fault length to the shear wave speed, $t_{norm} = L/c_s$, which is the approximate time required by a shear wave to fully traverse the fault length (L). Each instance when a dynamic event begins, t_{norm} is re-initialized to 0 in Figures, and timestamps of the subsequent snapshots of the dynamic event and its aftermath are calculated from that point (Figures 3.7, 3.8, 3.10, 3.12, 3.13, 3.14). When the analysis focuses on the timing of the event sequences, as in Figure 3.5, time is normalized with respect to the event recurrence time in the uniform normal stress model ($T_{\mathrm{rec},\,\sigma_{\mathrm{uni}}}$).

3.2 Qualitative similarity between models with uniform and fractal normal stress

We start by considering the behavior of the model with the uniform normal stress distribution; all the other properties are also uniform over the velocity-weakening region. The simulation produces a sequence of repeating similar events (Figure 3.5). In each event, there is an accelerating nucleation process (Figure 3.4, left, snapshots U1-U2) followed by dynamic rupture propagation (snapshots U3-U5). The nucleation size, i.e. the size of the actively slipping region when the dynamic slip rate threshold is reached, is comparable to the theoretical estimate (Figure 3.6).

In the model with a fractal distribution of normal stress on the interface, with the mean normal stress equal to the uniform case, the normal stress variation from σ_{mean} is ±60% (Figure 3.1b), making for a reasonably strong heterogeneity. The fault slip in this model is indeed different, although somewhat marginally. After a relatively short initial period, the simulation again produces repeating similar dynamic ruptures, although their recurrence time is slightly shorter and their peak slip rates are slightly larger (Figure 3.5). The nucleation and propagation of dynamic events are affected by the presence of heterogeneity in terms of spatial irregularity of slip (Figure 3.4, right) although the dynamic events overall are similar to the uniform

normal stress case. All the dynamic events are through-going, and nucleate at length scales close to h^*_{uni}, although from a scale slightly smaller than the homogeneous case (Figure 3.6), resulting in rupture nucleation closer to the edge of the VW region. The irregular shapes of the locked region, nucleation zone, and the dynamic slip front indicate that the fractal normal stress distribution makes the slip pattern of each event more complex.

The reduction in the recurrence time of the fractal case relative to the recurrence time of the uniform normal stress model is related to its reduction in the nucleation size. The events in the fractal case are able to nucleate sooner on locations of elevated normal stress—often called "asperities"—due to a lower nucleation size there. Note that $\sigma_{max}/\sigma_{uni} = 1.6$ corresponds to $h^*_{min}/h^*_{uni} = 1.6$, although the 1.6-time reduction in nucleation size is achieved only over a point, and the reduction over an asperity region would be lower. The higher frictional resistance on such asperities is reached due to quasi-static slip in the surrounding weaker—and more stable—regions. Hence the recurrence time in these two cases is determined by the nucleation time. The events in the fractal normal stress model are also seen to achieve marginally higher slip velocities, likely due to longer rupture propagation region remaining outside the nucleation zone.

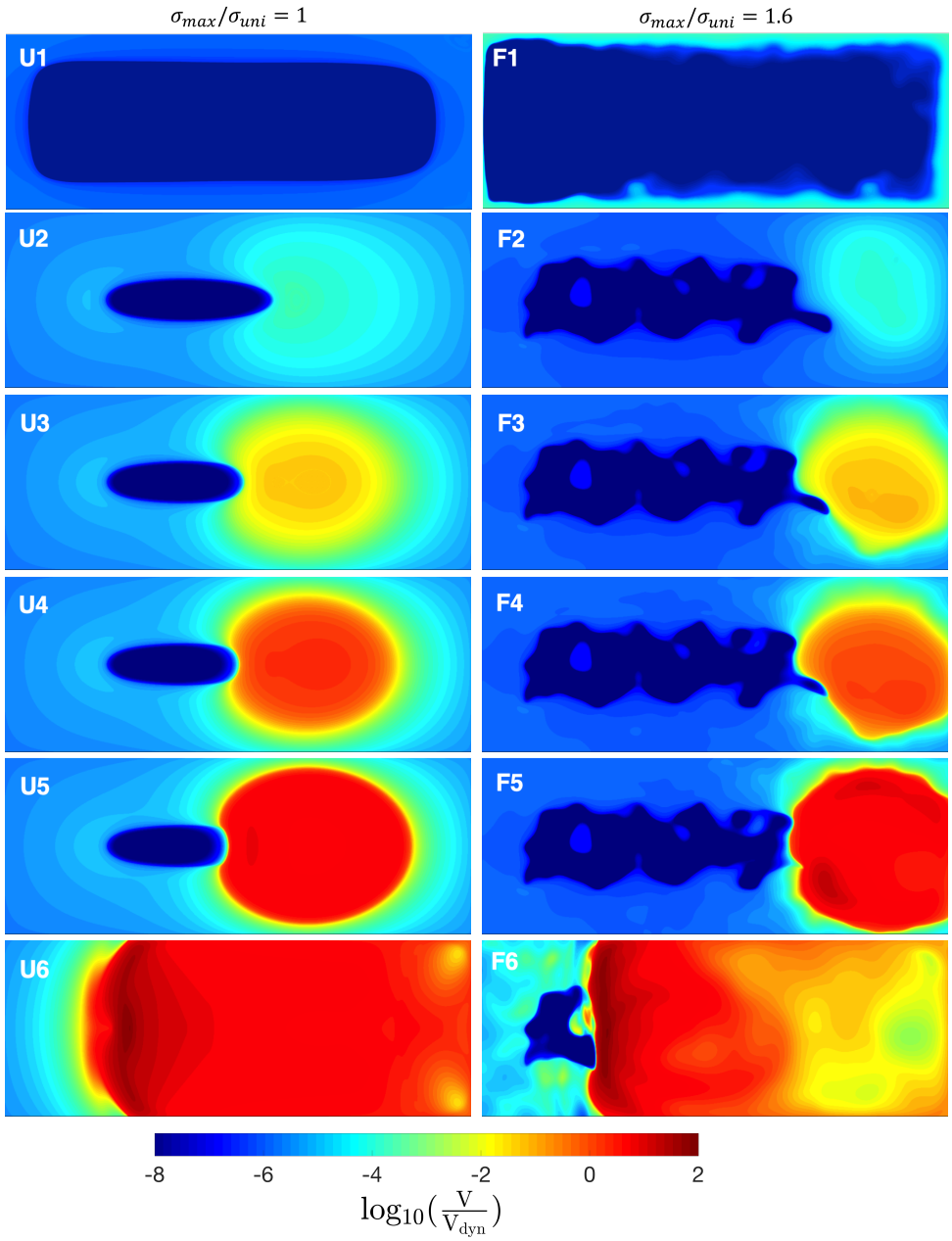

Figure 3.4: Slip velocity snapshots for a typical dynamic rupture event from models with $\sigma_{max}/\sigma_{uni} = 1$ (left) and $\sigma_{max}/\sigma_{uni} = 1.6$ (right). The events are similar in that they span the entire VW region and nucleate from a similar scale comparable to the nucleation size estimate for the model with uniform normal stress. The fractal distribution results in slightly smaller nucleation size and more complex slip pattern for each event.

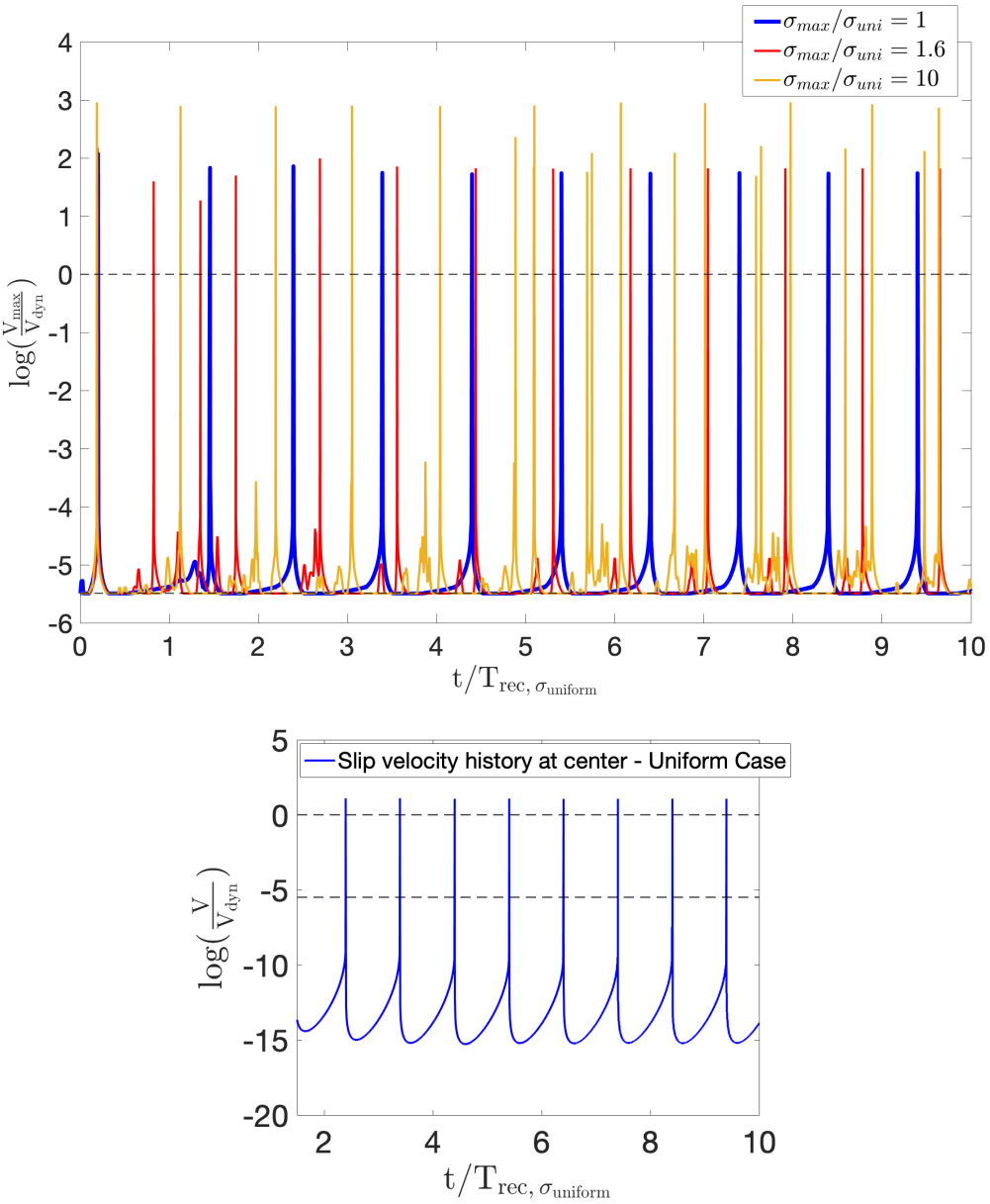

Figure 3.5: (Top) Evolution of the maximum slip velocity over the fault for the models with the uniform (blue line), fractal (red line), and modified fractal normal stress with $\sigma_{max}/\sigma_{uni} = 10$ (yellow line). The maximum slip velocity is normalized with respect to the dynamic velocity threshold (V_{dyn}). The time is normalized with respect to the mean recurrence time of events in the model with uniform normal stress. Each vertical line signifies dynamic rupture, as slip rates become much larger than the dynamic threshold (upper dashed line). Flat sections correspond to the loading plate rate. The uniform and fractal cases result in comparable sequences of events, with quasi-periodic model-spanning events in both cases, although the recurrence interval is slightly shorter in the fractal case. The modified fractal case with stronger normal stress heterogeneity exhibits more complex events, with smaller events appearing in between larger events. (Bottom plot) Slip velocity history at the middle of the VW fault region in the uniform normal stress model. Dynamic events are separated by inter-event periods of essentially locked interface, with slip rates several orders of magnitude lower than the loading plate rate (lower dashed line).

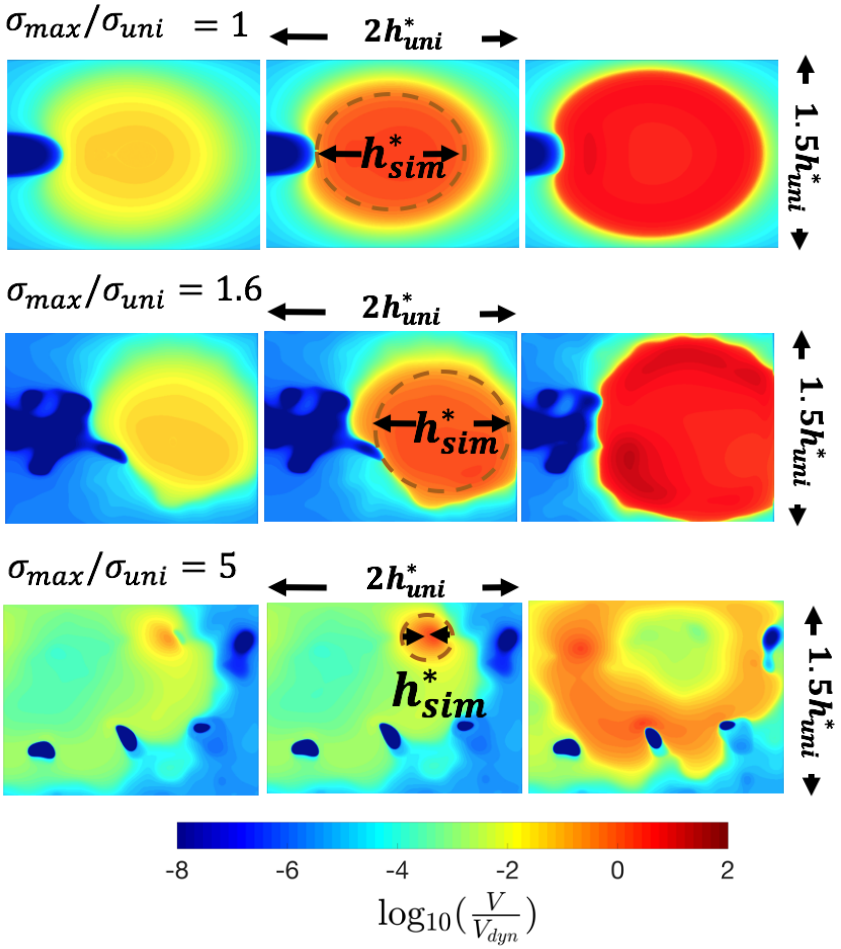

Figure 3.6: Slip velocity snapshots of a typical event nucleation on (a) an interface with uniform normal stress, (b) interface with fractal normal stress, and (c) interface with stronger normal stress heterogeneity of $\sigma_{max}/\sigma_{uni} = 5$. To facilitate the comparison, the size of each panel is the same, $2h^*_{uni}$ by $1.5h^*_{uni}$. The actual simulated nucleation size, h^*_{sim}, is similar to h^*_{uni} in the homogenous case, as expected. h^*_{sim} is measured by the approximate size of the (bright-orange-to-red) area that slips with velocities higher than $0.1V_{dyn}$ when the maximum slip velocity at any point on the fault matches the dynamic velocity threshold V_{dyn}. In the fractal stress case, the event nucleates similarly, from a slightly more irregular patch. The h^*_{sim} is slightly smaller but comparable to h^*_{uni}. In the model with stronger normal stress heterogeneity, model-spanning earthquakes initiate from scales much smaller than the nucleation size estimates calculated based on average properties. The nucleation behavior is governed by the smaller-scale nucleation size based on the local normal stress peaks, i.e. by the length scale of the heterogeneity, rather than h^*_{uni}.

3.3 Qualitatively different outcomes in models with stronger heterogeneity: smaller-scale events and asperity-driven nucleation

It is clear from the results that smaller-scale events cannot be achieved from such a fractal property distribution. Hence these results do not capture the observations recorded in lab experiments by McLaskey and Kilgore (2013), where small-scale events are observed in the nucleation region of the larger-scale event. Such smaller-scale events are often called "foreshocks," and the subsequent larger event is often called "mainshock." The persistent locations of these small-scale events in the experiments imply fixed asperities on the fault interface hosting them. Schaal and Lapusta (2019) reproduced these laboratory observations of small-scale events occurring in between the mainshock cycles in rate-and-state fault models using circular patches of higher compression and referred to these small-scale events as 'intershocks.'

In order to obtain such intershocks in our models, we create modified fractal distributions with more separated patches that have a higher strength contrast relative to the background, as described in Section 3.1. To systematically study the evolution of complexity in the nucleation process, we incrementally sharpen the heterogeneity by increasing the maximum normal stress of the modified fractal distribution, from $\sigma_{max}/\sigma_{uni} = 3$ to $\sigma_{max}/\sigma_{uni} = 10$. The simulated time is conserved for all models, for ease of comparison.

As the maximum normal stress is increased in the modified fractal distributions, resulting in well-defined isolated asperities (Figure 3.1), smaller-scale events appear, i.e., events that rupture a small portion of the potentially seismogenic velocity-weakening interface. Events also become more irregular, as will be discussed in the following. In this study, we define events that ruptures at least 90% of the VW region to be larger-scale events that we will also call "mainshocks." The rest of the events are considered intershocks or smaller-scale events.

At $\sigma_{max}/\sigma_{uni} = 5$, the fault response includes a few smaller-scale events within some of the mainshock cycles. But many of the mainshocks occur without smaller-scale seismicity in between them. Figure 3.7 shows a sequence of two consecutive model-spanning events with no small-scale events in between.

However, the stronger heterogeneity results in another key difference: the larger-scale events now often nucleate from the (small) scale of the asperities, which is much smaller than the mean nucleation size estimate. Note that $h^*_{min}/h^*_{uni} = \sigma_{max}/\sigma_{uni}$, i.e., the nucleation size is reduced by the same factor as the normal stress

is increased. Once the normal stress on the asperities becomes high enough so that the corresponding small-scale nucleation size fits within the asperities, they can initiate unstable slip. There is still quasi-static slip corresponding to the nucleation process on the scale of the mean nucleation size (e.g., blue region in snapshot S2 of Figure 3.7); this quasi-static (slow) slip loads the stronger but more prone to instability small-scale asperities, which accelerate to dynamic slip rates and grow into model-spanning events. Hence the actual nucleation size h^*_{sim} is governed by the scale of the local normal stress peaks, or the length scale of the heterogeneity, rather than averaging out to the mean nucleation size estimate (Figure 3.6).

As normal-stress heterogeneity increases, the small-scale events appear in more mainshock cycles, as quantified in Section 4.1. At $\sigma_{max}/\sigma_{uni} = 10$ (Figure 3.1d), we have even more pronounced scale separation in terms of the difference in the mean and minimum nucleation sizes and can observe a regular pattern of 3 or 4 small-scale events in each mainshock cycle (Figure 3.8). In Figure 3.8, three small-scale events (in snapshots S1-S2, S5-S6, S8-S9) occur before the larger-scale event (snapshot S12). Both the small-scale events and the larger-scale event nucleates from small, asperity scale in this sequence (Figure 3.9). The peak normal stress (σ_{max}) is 10 times the mean normal stress (σ_{mean}), which means the minimum nucleation size (h^*_{min}) corresponding to the asperity peak is one-tenth that of h^*_{uni}, or about one-twentieth the size of the panel length in Figure 3.9. The measured nucleation length scale h^*_{sim} is much smaller than h^*_{uni}, yet larger than h^*_{min}, since the nucleation size would be averaged over the asperity where the event is nucleated. Note that these events are separated by long enough times in comparison to the typical dynamic event duration to be considered separate events seismologically.

At the same time, the last two small-scale events occur soon enough before the larger-scale event to be considered foreshock-like. The typical recurrence time of the larger-scale events ("mainshocks") in this model is $\sim 10^6$ normalized time units, where 1 unit corresponds to the time for the shear wave to propagate through the length of the fault and hence 1 unit is comparable to the duration of a large-scale event. The third small-scale event in Figure 3.8 is separated from the following larger-scale event by only 106 units, and the second small-scale event is separated from the third small-scale event by 6644 units, a much shorter time than the "mainshock" recurrence time. For example, if the typical mainshock duration were 100 s, these separation times would be about 2 hours and 8 days, respectively, which is short enough for such events to be clearly labeled "foreshocks," given their spatial proximity to the

initiation location of the subsequent larger-scale event. The first small-scale event is separated from the others by about 23,000 units, or, in the example above, 26 days, and it occurs away from the nucleation location of the "mainshock," so it classification would depend on the exact definitions employed.

Note that some larger-scale events still nucleate from scales comparable to h^*_{mean} even for the case of $\sigma_{max}/\sigma_{uni} = 10$ (Figure 3.10, S12), illustrating the complexity of nucleation in these models. This larger-scale event is again preceded by several foreshock-like small-scale events (snapshots S2-S3, S6-S7, S10) that nucleate from small scales. The last such small-scale event is separated from the larger-scale event by only about 4 normalized time units, Hence the last small-scale event immediately precedes and triggers the larger-scale event.

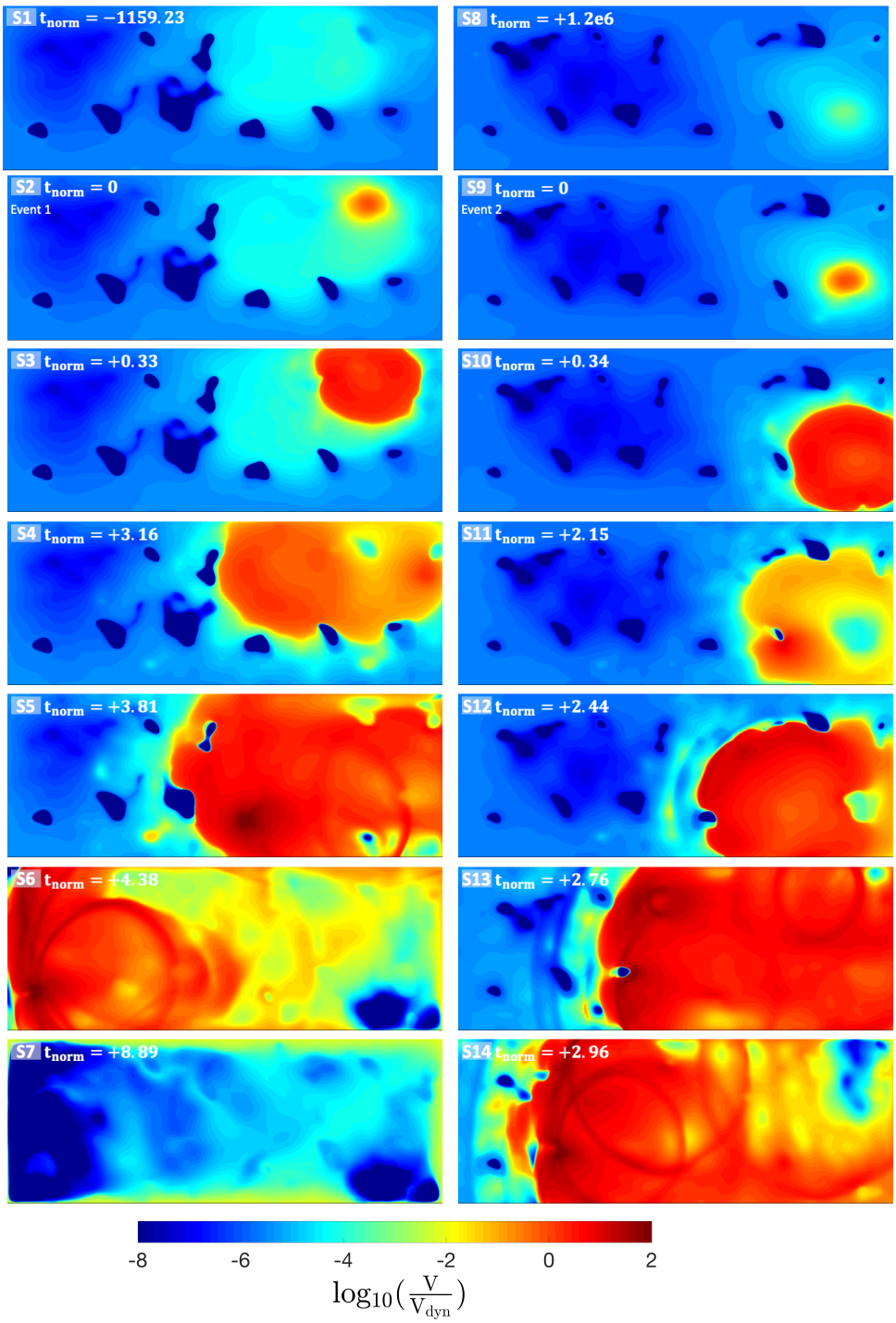

Figure 3.7: Slip velocity snapshots from two consecutive model-spanning events from the model with $\sigma_{max}/\sigma_{uni} = 5$. There are no smaller-scale events in between. The larger-scale events are nucleating from the asperity scale much smaller than the mean nucleation size estimate.

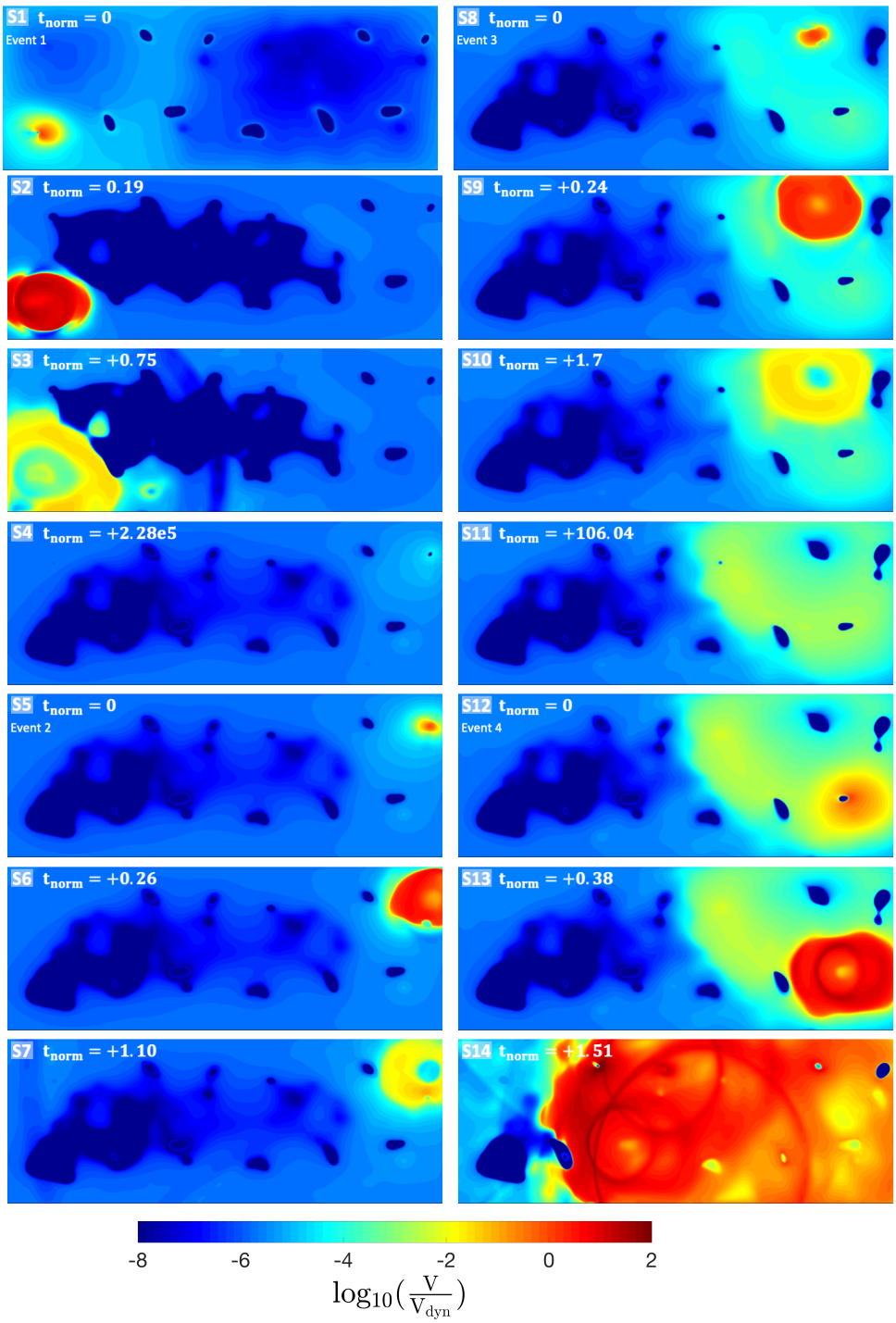

Figure 3.8: Slip velocity snapshots from the model with $\sigma_{max}/\sigma_{uni} = 10$. Small-scale events (panels S1-S2, S5-S6, S8-S9) precede the larger-scale event (S12-S14) and the larger-scale event also nucleates from scales much smaller than h^*_{mean}. The time difference between snapshots S7 and S8 is 6644 normalized time units and the time difference between snapshots S11 and S12 is 47 normalized time units, where 1 unit corresponds to the time for the shear wave to propagate through the length of the fault and hence 1 unit is comparable to the duration of a large-scale event. Hence these events are separated by long enough times to be considered separate events, but short enough times in comparison to the average recurrence time of the large-scale events for the smaller events to be considered a foreshock.

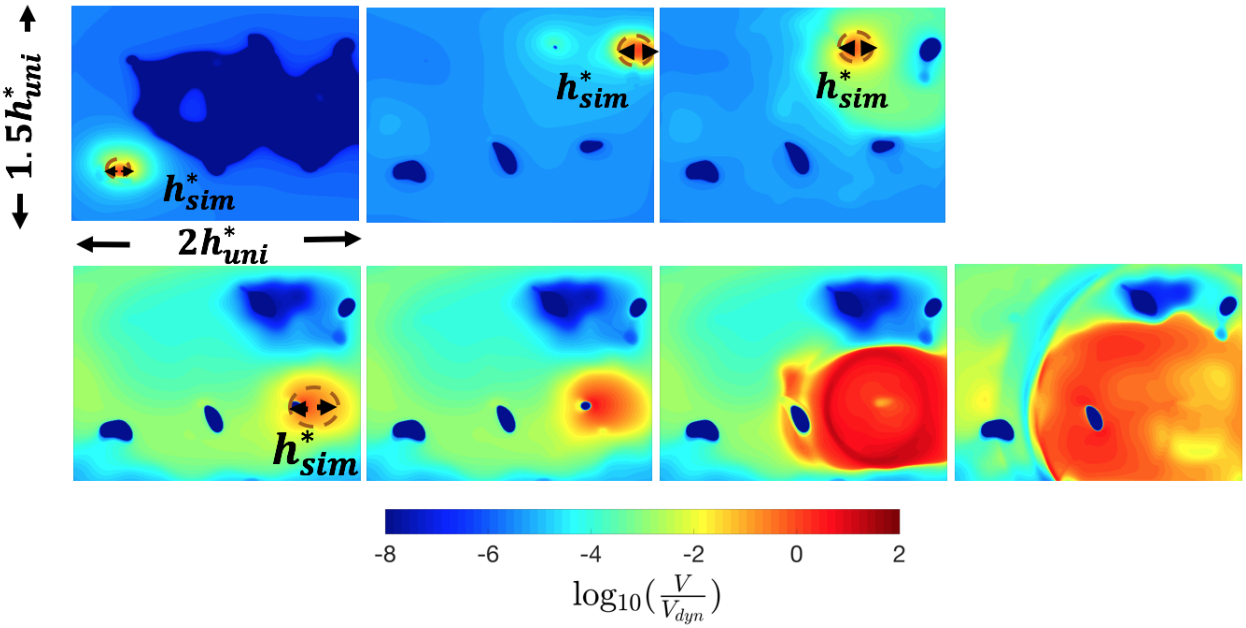

Figure 3.9: Slip velocity snapshots of typical dynamic event nucleation zones on an interface with modified fractal normal stress and $\sigma_{max}/\sigma_{uni} = 10$ (Figure 3.1d), for small-scale events (top row) and a larger-scale event (bottom row). Both small and large events tend nucleate from scales much smaller than the mean nucleation size and close to the asperity—or heterogeneity—scale, although some large events nucleate differently (Figure 3.10).

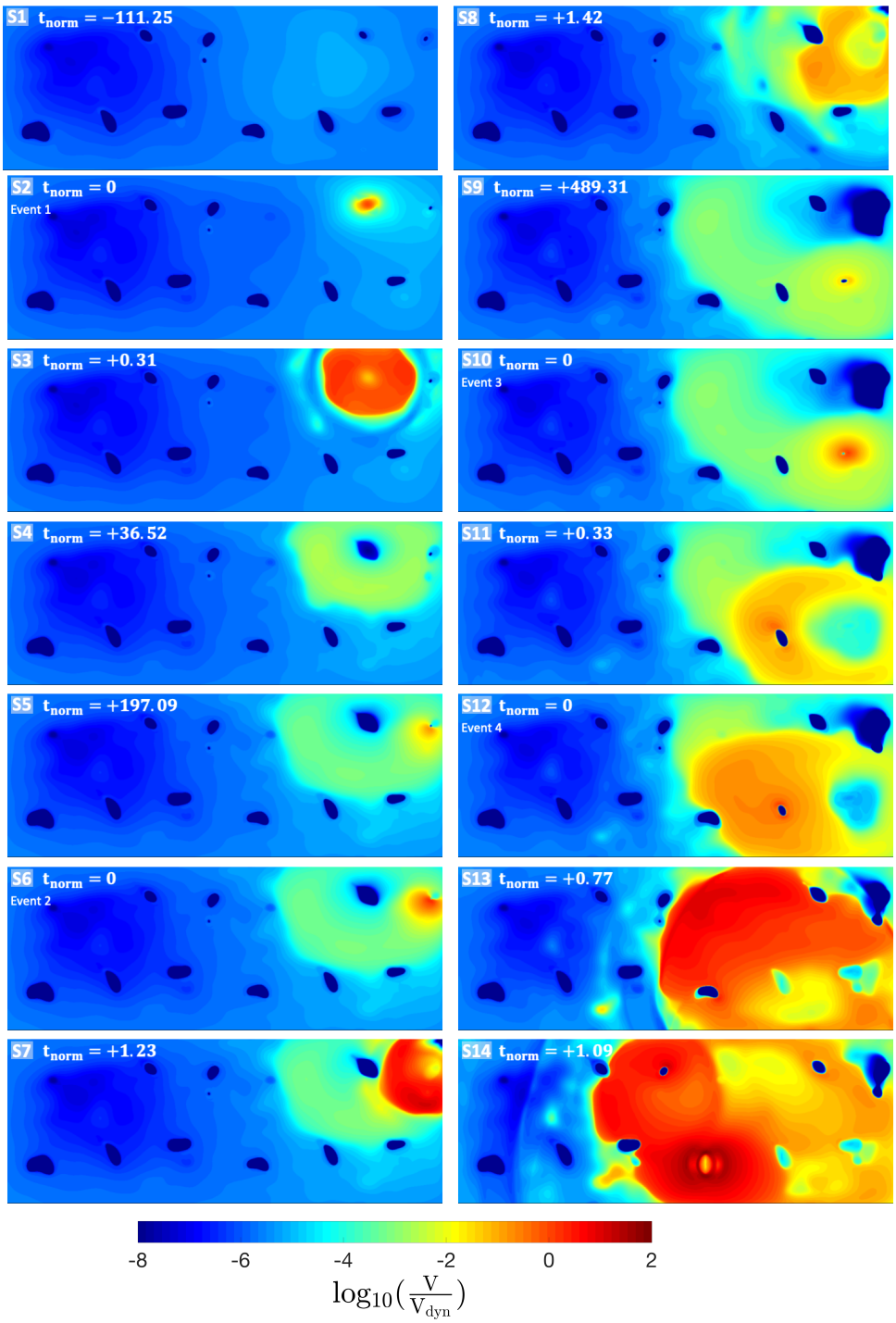

Figure 3.10: Slip velocity snapshots from the model with $\sigma_{max}/\sigma_{uni} = 10$ showing a case of a larger-scale event nucleating from a slipping zone comparable in size to h^*_{uni} (S12). The larger-scale event is still preceded by three small-scale foreshock-like events, separated from the larger-scale event by 4, 4+490 = 494, and 494+197 = 691 time units (snapshots S9-S10, S6-S7, and S2-S3, respectively).

3.4 Cases with ten-fold variations in nucleation sizes achieved through combined variations in normal stress and rate-and-state characteristic slip

Here, we explore whether the same distribution of the nucleation size estimate over the fault, but achieved by varying other fault properties, would result in significantly different slip behavior. So far, the heterogeneous nucleation size distribution has resulted from heterogeneity in the normal stress, which also caused a heterogeneous distribution of shear strength, effectively creating stronger (but more instability-prone) asperities. However, theoretical nucleation size estimates (Equation 2.3) indicate that different nucleation sizes can be achieved by varying other fault properties.

Here, we explore heterogeneity in the characteristic slip D_{RS} of the rate-and-state friction that governs the evolution of the state variable. Smaller D_{RS} results in velocity-weakening occurring more readily, over smaller slips, promoting frictional instability.

We choose the case of the most extreme variation in the nucleation size estimates considered, with $\sigma_{max}/\sigma_{uni} = 10$ (Figure 3.11a) which corresponds to $h^*_{uni}/h^*_{min} = 10$ (Figure 3.11b), and consider two additional cases with the same distribution of the nucleation size estimate: (M1) a case with $\sigma_{max}/\sigma_{uni} = 1.6$ (fractal normal stress) and variations in D_{RS} to achieve the same nucleation size distribution (Figure 3.11c) and (M2) a case with $\sigma_{max}/\sigma_{uni} = 1$ (uniform normal stress) and variations in D_{RS} to achieve the same nucleation size distribution (Figure 3.11d).

The nucleation of large-scale events in the fault models M1 and M2 with the much more modest or no variation in normal stress and modified D_{RS} proceeds much differently than in the modified fractal case with $\sigma_{max}/\sigma_{uni} = 10$, despite the same distribution of the local estimate of the nucleation size (Figures 3.12-3.13, Figure 3.14). In the modified fractal case with $\sigma_{max}/\sigma_{uni} = 10$, the nucleation of larger-scale events mostly occurs from the scale of local asperities, which is much smaller than the mean nucleation size (Figures 3.9). In contrast, the nucleation process of larger-scale events in models M1 and M2 is similar to that on the homogeneous fault, in that it occurs as an acceleration of slip in a slowly expanding zone that approaches the nucleation size estimate for the homogeneous fault (the brightening green to orange colors in snapshots S12-S22 of Figures 3.12-3.13; and snapshots S10-S12 of Figure 3.14). In fact, the simulated nucleation size is even larger in model M2 with the uniform normal stress and modified D_{RS} than on the completely uniform fault, as in model M2 the entire fault starts slipping slowly before the large-scale

event nucleates (snapshots S6-S13 of Figure 3.14), whereas in the uniform-fault case, a portion of the interface is still locked when the event nucleates, indicating smaller needed extent of quasi-static slip for instability nucleation (Figure 3.4). This is consistent with the mean nucleation size estimate over the entire VS region being 1.4 times larger than the nucleation size estimate for the uniform fault.

This mean-nucleation-scale style of larger-scale event nucleation occurs despite models M1 and M2 exhibiting an increase in small-scale events between larger-scale, model-spanning events, compared with the modified fractal case with $\sigma_{max}/\sigma_{uni} = 10$. At least 8 small-scale events precede a representative larger-scale event in model M1, as shown in Figures 3.12-3.13. Many of the small-scale events occur on the same patches of reduced nucleation size and hence represent repeating earthquakes (Set 1: events in snapshots S2, S4, S8; Set 2: events in snapshots S6, S14; Set 3: events in snapshots S10, S16 etc). The small-scale earthquakes do not repeat for the modified fractal normal stress distribution with $\sigma_{max}/\sigma_{uni} = 10$.

The differences between the slip patterns in the models can be explained by the fact that, in models M1 and M2, the patches of the reduced nucleation size have only up to 1.6 times higher frictional strength as the rest of the fault, whereas in the modified fractal case, they are significantly stronger than the surrounding fault, about 10 times. Hence it is much easier to load these patches by the nearby quasi-static slip in models M1 and M2, resulting in repeating small-scale earthquakes. Furthermore, dynamic stress drops during smaller-scale events are lower on patches in M1 and M2, resulting in smaller dynamic stress transfer onto the surrounding fault and much smaller to negligible effect of the failure of the patches on the larger-scale nucleation processes. Indeed, ruptures initiated on stronger asperities considered in the previous section extend further away from the asperities, create substantial postseismic slip, and trigger each other, with some of them growing into the fault-spanning events. In contrast, ruptures on the small-nucleation patches of M1 and M2 are largely driven by the large-scale nucleation process, with relatively minor effect on it (Figures 3.12-3.13, Figure 3.14).

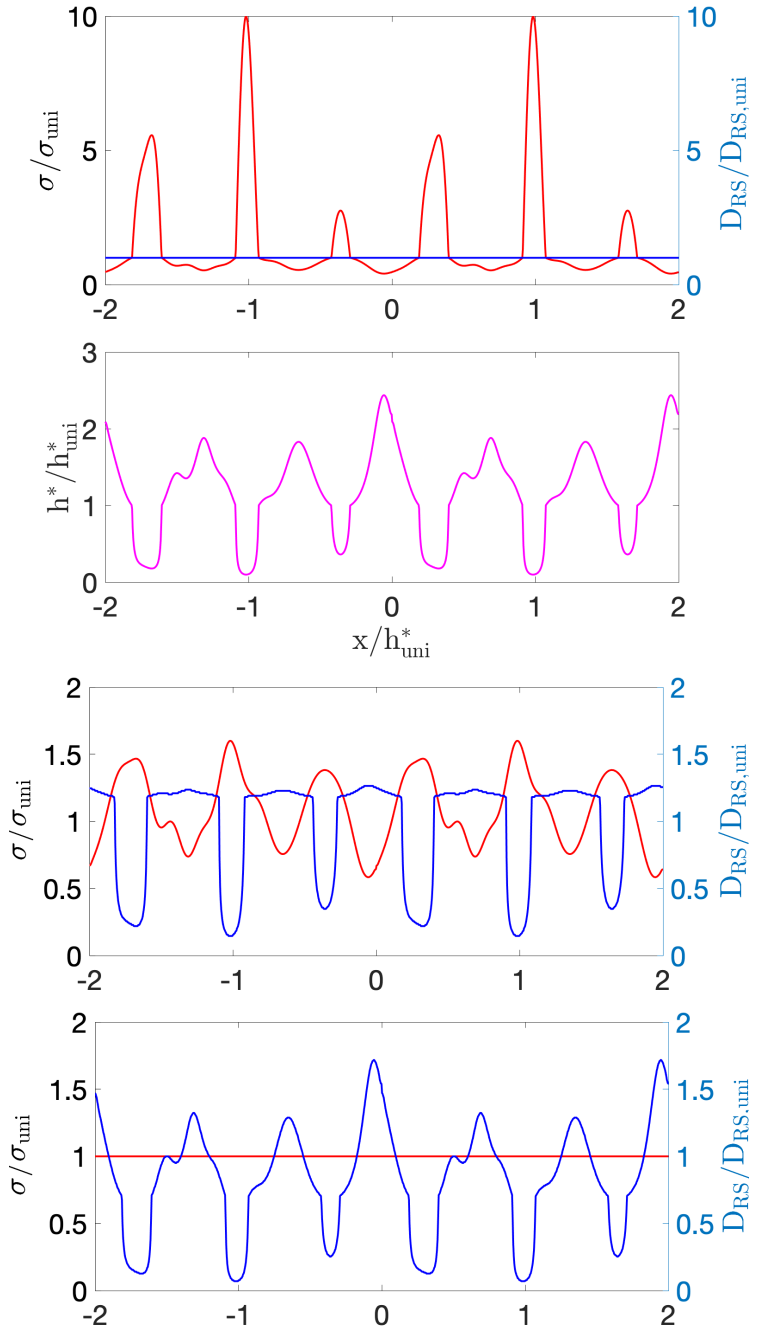

Figure 3.11: Models with ten-fold variations in nucleation sizes achieved through combined variations in normal stress and rate-and-state characteristic slip D_{RS}, illustrated by property distributions along the mid-depth of the fault. (a) Distributions of the normal stress and D_{RS} for the case of modified fractal normal stress distribution with $\sigma_{max}/\sigma_{uni} = 10$ considered in the previous section; D_{RS} is uniform in this case. (b) The corresponding distribution of the nucleation size estimate. (c) The case of a fractal normal stress with $\sigma_{max}/\sigma_{uni} = 1.6$ and modified D_{RS} that result in the same distribution of the nucleation size estimate as in (b). (d) The case of uniform normal stress with $\sigma_{max}/\sigma_{uni} = 1$ and modified D_{RS} that result in the same distribution of the nucleation size estimate as in (b).

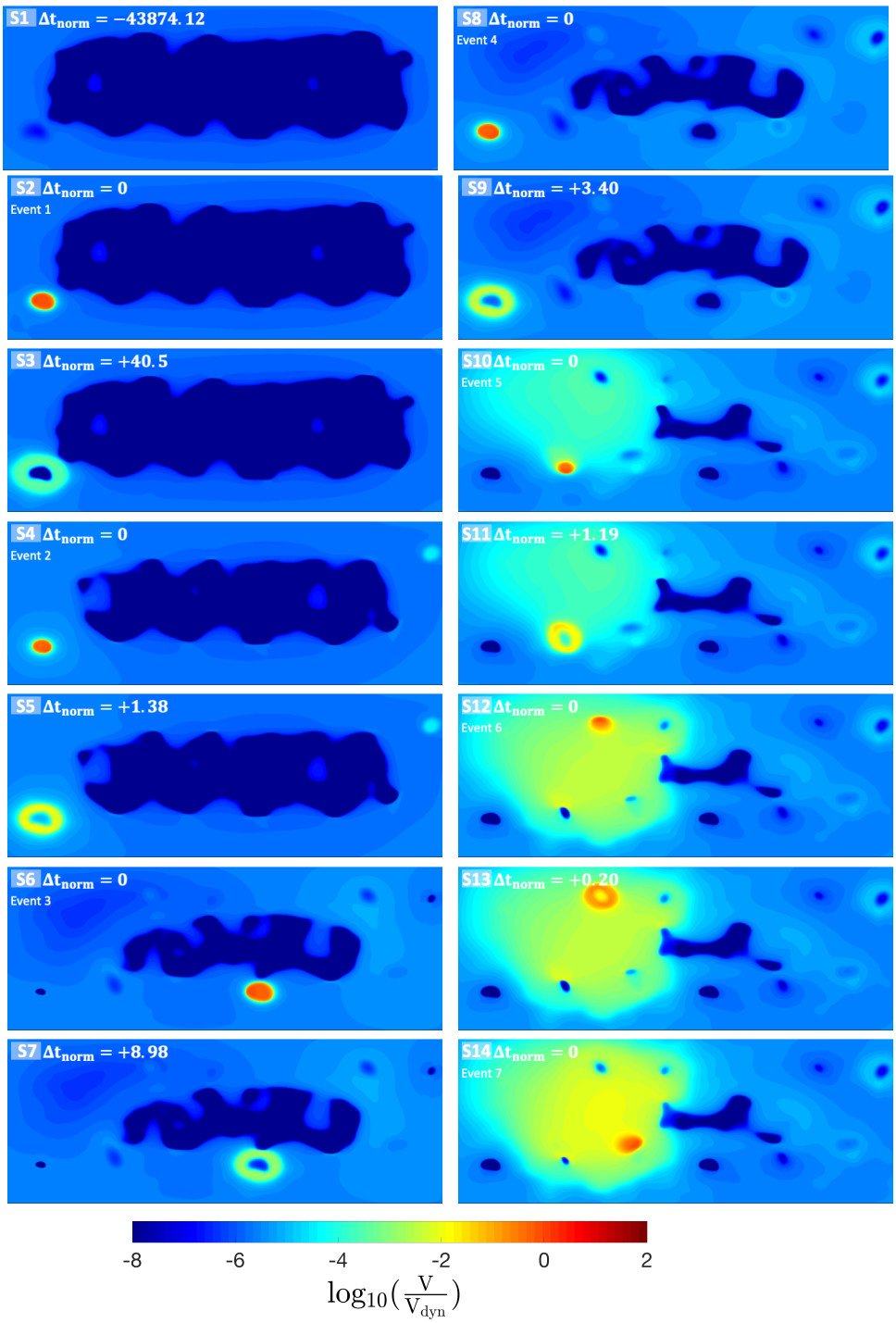

Figure 3.12: Slip velocity snapshots from the model M1 with the same distribution of the nucleation size estimate as for the modified fractal normal stress $\sigma_{max}/\sigma_{uni} = 10$ (and hence with $h^*_{uni}/h^*_{min} = 10$ but achieved through a fractal distribution of normal stress with $\sigma_{max}/\sigma_{uni} = 1.6$ and variations in D_{RS}); the snapshots continue in Figure 3.13. The patches of the low nucleation size produce multiple small-scale foreshock-like events, some of which repeat in the same locations. These foreshocks appear to be triggered by the quasi-static nucleation of the subsequent larger-scale event that nucleates from the larger scale comparable to the mean nucleation size.

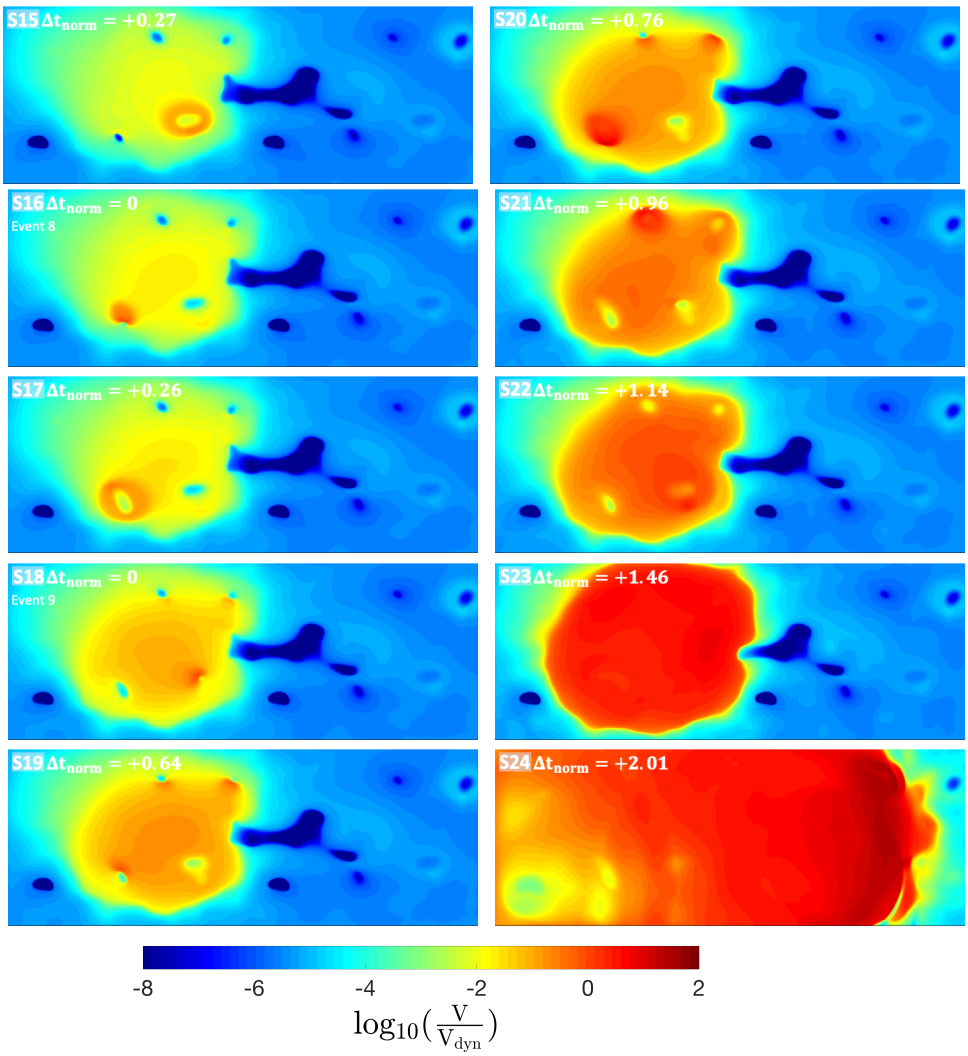

Figure 3.13: Slip velocity snapshots from the model M1 with the same distribution of the nucleation size estimate as for the modified fractal normal stress $\sigma_{max}/\sigma_{uni} = 10$ (and hence with $h^*_{uni}/h^*_{min} = 10$ but achieved through a fractal distribution of normal stress with $\sigma_{max}/\sigma_{uni} = 1.6$ and variations in D_{RS}); continued from Figure 3.12. The patches of the low nucleation size produce multiple small-scale foreshock-like events, some of which repeat in the same locations. These foreshocks appear to be triggered by the quasi-static nucleation of the subsequent larger-scale event that nucleates from the larger scale comparable to the mean nucleation size.

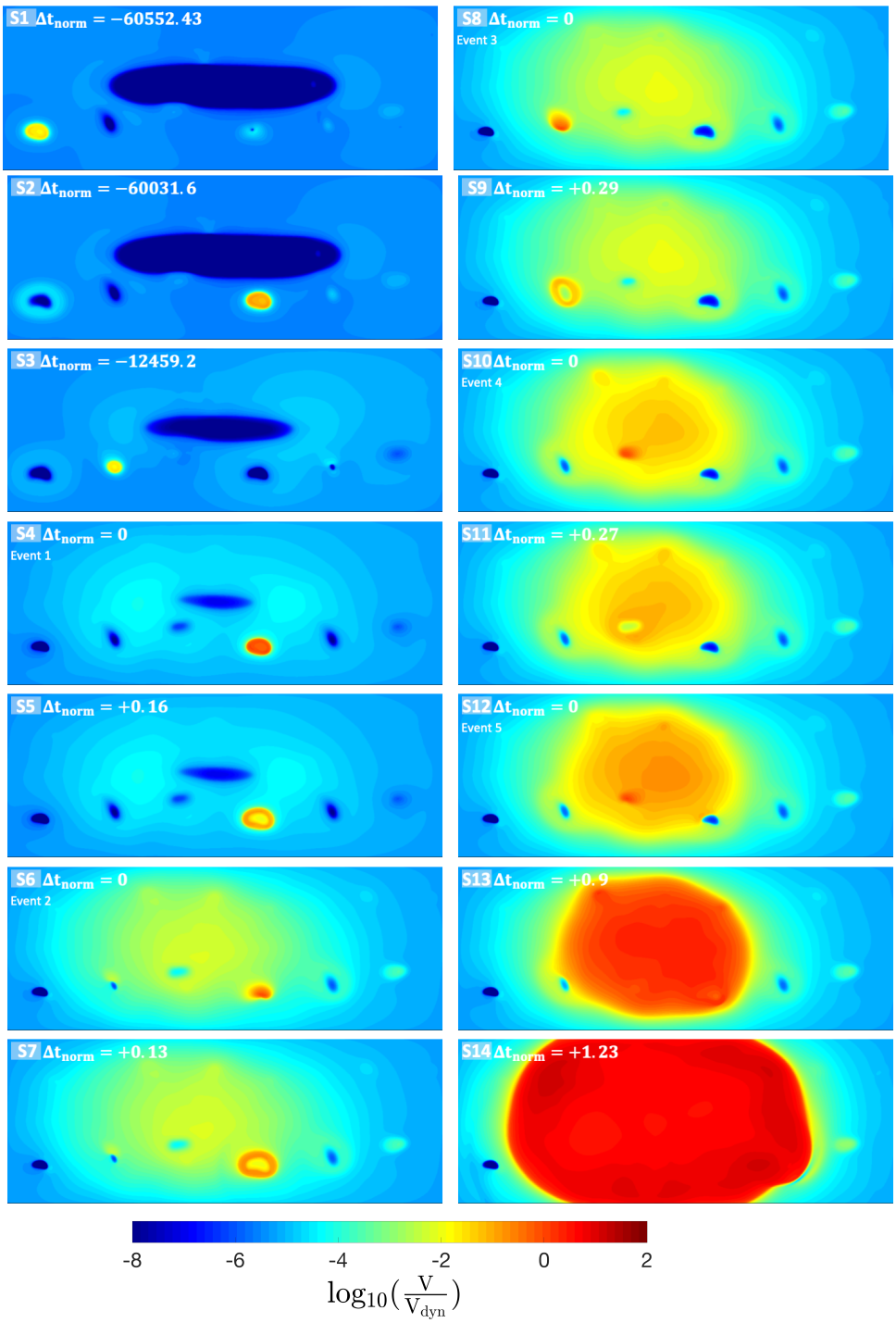

Figure 3.14: Slip velocity snapshots from the model M2 with the same distribution of the nucleation size estimate as for the modified fractal normal stress $\sigma_{max}/\sigma_{uni} = 10$ (and hence with $h^*_{uni}/h^*_{min} = 10$ but achieved through uniform normal stress with $\sigma_{max}/\sigma_{uni} = 1$ and variations in D_{RS}). As for model M1, the patches of the low nucleation size produce multiple small-scale foreshock-like events, some of which repeat in the same locations. These foreshocks appear to be triggered by the quasi-static nucleation of the subsequent larger-scale event that nucleates from the larger scale comparable to the mean nucleation size.

3.5 Conclusions

With systematic increase in normal-stress heterogeneity, we observe a continuum of behaviors ranging from purely fault-spanning events to persistent foreshock-like events interspersed between larger-scale "mainshock" events. Differences in normal stress induce two types of heterogeneity in the model relevant to slip patterns: a heterogeneity in the instability length scale, aka nucleation size, which is inversely proportional to the normal stress, and a heterogeneity in friction strength which is directly proportional to the normal stress. Hence more compressed spots are frictionally stronger (that is, asperity-like) but more prone to instability.

A relatively strong heterogeneity in normal stress is required to create smaller-scale dynamic events, with $\sigma_{max}/\sigma_{uni} = 5$ or more. For a significant but much more modest normal stress variation of $\sigma_{max}/\sigma_{uni} = 1.6$ in a fractal normal stress distribution, the behavior is qualitatively similar to that of a uniform fault, with quasi-periodic, if somewhat perturbed, fault-spanning ruptures nucleating from the nucleation scale similar to that of the uniform fault. The nucleation process in both the uniform and fractal cases takes the form of the gradually accelerating and expanding quasi-static slip within the VW—seismogenic—fault region, which abruptly accelerates into a dynamic event upon reaching the spatial dimensions similar to the mean nucleation size.

We use modified versions of fractal fields to create increasingly heterogeneous interfaces with more compressed spots while keeping the normal stress compressive everywhere, as expected on natural faults. As we enhance the most compressed peaks of the fractal normal stress distribution, some larger-scale dynamic events start to nucleate from this smaller heterogeneity scale. The large-scale quasi-static nucleation process still exists, and it serves to load the asperity spots and allow them to accelerate to fast slip rates. The resulting unstable slip typically spreads to the entire fault for the intermediate levels of normal stress heterogeneity, such as $\sigma_{max}/\sigma_{uni} = 5$, although occasionally these ruptures arrest shortly upon exiting the nucleating asperity, creating small-scale events. The behavior depends on the complex evolving fault shear stress which is the result of all prior slip, quasi-static and dynamic.

Hence even for $\sigma_{max}/\sigma_{uni} = 5$, small-scale events do not occur reliably between two larger-scale events. This behavior implies that, in natural faults, foreshocks need not reliably occur in between larger-scale events, and the fact that there were foreshocks at a fault region at an instance in the past need not guarantee that the region would

have them at a future time.

On interfaces with even stronger normal-stress heterogeneities, with $\sigma_{max}/\sigma_{uni}$ of 6 to 10, a majority of the larger-scale events initiate from the heterogeneity scale of the compressed peaks, which is increasingly smaller than the mean nucleation size that would govern their nucleation on a uniform fault. Furthermore, most larger-scale events are preceded by multiple smaller-scale events, most of which occur close enough in time and space to the larger-scale events to be classified as foreshocks. These foreshock-like events often appear as a cascade, triggering each other before one of them runs away to rupture the entire simulated fault.

While the variations in normal stress induce inversely proportional variations in the instability length scale or nucleation size, we find that the nucleation-size variations by themselves are insufficient to cause nucleation of larger-scale events from the smallest heterogeneity scales, and that the associated strong heterogeneity in frictional strength is also required. To distinguish between the effects of heterogeneity in the nucleation size alone vs. the heterogeneity in both the nucleation size and the friction strength, we examine slip behavior in fault models that achieve all or most of their nucleation-size heterogeneity by variations in the characteristic slip D_{RS} of the rate-and-state friction, with uniform or mild variations in normal stress. (Smaller values of the characteristic slip D_{RS} lead to friction weakening over smaller slips, thus promoting instability and reducing the nucleation size.) In such models, patches with small nucleation sizes, driven by the larger-scale quasi-static nucleation processes, do generate small-scale events. But these events arrest soon after exiting these patches and entering the nearby fault regions with increasing values of D_{RS}—and hence decreasing rates of weakening—and they do not appear to have much effect on the larger-scale quasi-static nucleation process, which eventually grows into a fault-spanning, large-scale dynamic event just like on a uniform fault. So the whole nucleation process appears quite similar to that on a uniform fault, but slightly more irregular and accompanied by multiple small-scale events which also tend to be repeating.

Note that an obvious difference between the small-scale events nucleating on highly compressed spots vs. on spots with average compression is that the former events would experience a much higher dynamic stress drop, for the same change in friction, then the latter events. This dynamic stress drop gets redistributed around the expanding event through dynamic waves, both promoting the event propagation and increasing its impact on the surrounding fault regions. Consistently with this

consideration, the small-scale events are much larger—by orders of magnitude in terms of seismic moment released—for models with highly heterogeneous normal stresses than for models with most heterogeneity achieved through D_{RS}, as shown in Chapter 4. At the same time, all dynamic events in our models have similar static stress drops—within a factor of 2 or less from the static stress drops on a uniform fault—as also discussed in Chapter 4.

Collectively, our modeling with different amounts and types of heterogeneity reveals a broad range of potential nucleation processes of larger-scale events, without and with foreshock-like events of different type. While all of our nucleation processes are driven by the underlying quasi-static accelerating slip, the observational appearance of the outcomes could be quite different. In our simulations, on the one hand, faults with strong heterogeneity in normal stress produce energetic foreshocks that occur next to each other and significantly contribute to triggering each other and the eventual mainshock. Such foreshocks may dominate observations, since small amounts of quasi-static slip at depth may be difficult to capture geodetically, making the nucleation process appear as merely a cascade of dynamic events, as hypothesized by some studies (e.g., Helmstetter et al., 2003). In the same model, one can have several foreshocks before one larger-scale event and none before another, as the very first potential foreshock just grows into the larger-scale event due to a particular state of stress on the fault. On the other hand, faults with strong heterogeneity in the characteristic slip distance have much smaller foreshock-like events in relation to the size of the quasi-statically slipping region; such events, in addition, tend to occur repeatedly and do not interact much with each other, appearing more disconnected at different parts of the larger quasi-static nucleation, consistent with some observations (e.g., Brodsky and Lay, 2014). On such faults, foreshock-like events would tend to more reliably occur. Of course, one should get intermediate or mixed behaviors in models between these two end-members or with two types of heterogeneity mixed together.

Chapter 4

EFFECT OF HETEROGENEOUS FAULT PROPERTY DISTRIBUTIONS ON COMPLEXITY OF SEQUENCES AND EVOLUTION OF DYNAMIC RUPTURES

Chapter 3 focuses on how heterogeneity in physical properties affects the nucleation process of both smaller-scale and larger-scale events. While those findings are informative in terms of the range of possibilities, it may not be easy to use them alone to constrain fault properties. The quasi-static nucleation processes at depth are generally difficult to capture geodetically, unless the nucleation size is in tens to hundreds of kilometers; indeed, many models treat the large-scale slow slip transients relatively recently discovered on faults as ongoing nucleation attempts (Segall et al., 2010; Liu and Rice, 2005; Liu and Rice, 2007; Dal Zilio et al., 2020). Furthermore, foreshocks are not universally observed before large events. If there are no foreshocks, does this mean that the fault is relatively homogeneous or, alternatively, so strongly heterogeneous that the very first foreshock-to-be grows into a large event? Clearly, it is important to investigate the effect of fault heterogeneity on other observables.

In this chapter, we focus on how heterogeneity in fault properties influences several potentially observable earthquake source properties, such as the complexity of earthquake sequences, event size distributions, and evolution of moment release in dynamic ruptures. The fault models are the same as discussed in Section 3.1.

4.1 Complexity in earthquake sequences with increasing heterogeneity

Size distributions of dynamic events

To study complexity of earthquake sequences in our models, we quantify the size distribution of dynamic events in each simulation, as done for natural faults. We determine the fraction of the dynamic events in a given moment range and plot them both on linear and logarithmic scales (Figures 4.1-4.2). In the case of the uniform normal stress model, all the events appear identical to each other in size. This is maintained, with slight irregularities, in the fractal normal stress case. As the heterogeneity in the normal stress increases, smaller events appear, and the larger events themselves have more variation in their sizes. Increasing the normal-stress heterogeneity generally increases the relative fraction of smaller-scale events

when compared to the larger-scale events. The event size distribution also becomes richer, with more sizes represented, as we make the interface more heterogeneous, as evident from the log-scale plots (Figure 4.2).

As discussed in Section 3.4, the most heterogeneous normal-stress distribution we consider, with $\sigma_{max}/\sigma_{uni} = 10$, corresponds to more than an order of magnitude variation in the nucleation length scale. Section 3.4 discusses two additional models with the same nucleation scale distribution, but with the normal stress distribution being uniform and fractal, and with the characteristic slip distance (D_{RS}) modified to preserve the (highly heterogeneous) local nucleation size distribution (Figure 3.11). The event size distributions in these two 'modified D_{RS}' models ($\frac{\sigma_{\max}}{\sigma_{\text{uni}}} = 1$, $\frac{\mathrm{D_{RS,min}}}{\mathrm{D_{RS,uni}}} = 0.1$ and $\frac{\sigma_{\max}}{\sigma_{\text{uni}}} = 1.6$, $\frac{\mathrm{D_{RS,min}}}{\mathrm{D_{RS,uni}}} = 0.16$) are significantly different. They indicate the presence of numerous small-scale events and only a marginal variation in the sizes of larger-scale events in comparison to the case with strong variations in normal stress (Figure 4.3-4.4). This confirms our conclusions in Chapter 3 that the heterogeneity in D_{RS} has much more mild effect on larger-scale events, for example, during nucleation, mostly just producing small events triggered by larger-scale processes. The size range of the small-scale events in the modified D_{RS} models are orders of magnitude smaller than the small-scale events in models with uniform D_{RS} and significant normal stress heterogeneity, as discussed in Chapter 3, as the events nucleating on asperities of high normal stress get a strong initial push due to much larger dynamic shear stress drop, for the same frictional properties, then the events nucleating on patches of much smaller D_{RS} but similar normal stress to the surrounding fault.

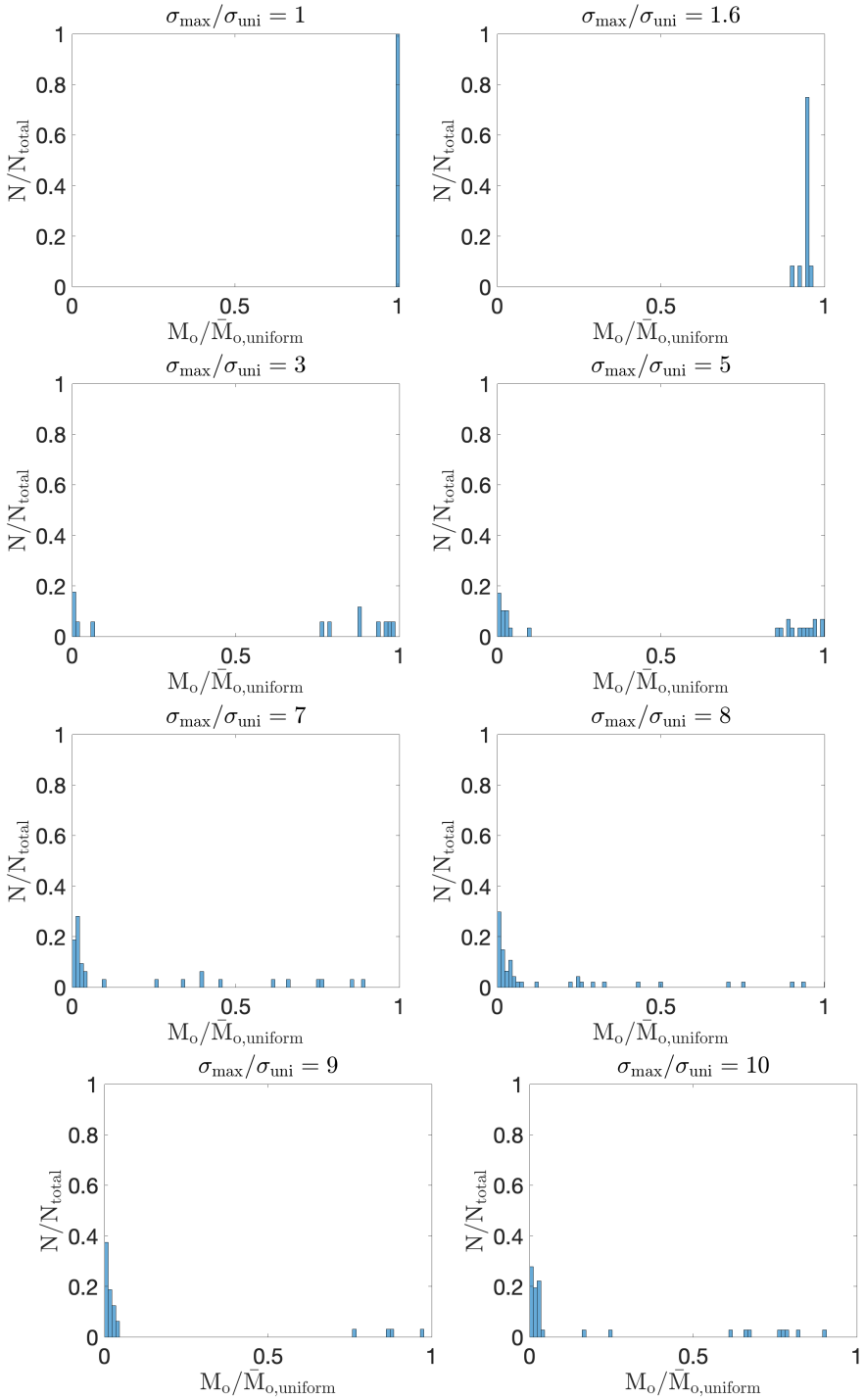

Figure 4.1: Distribution of event sizes across the models with heterogeneous normal stress. The seismic moments on the horizontal axis are normalized with respect to the mean moment of events from the uniform normal stress model. The fraction of the events in a given moment range is plotted on the vertical axis. Increasing heterogeneity generally leads to increasing complexity in the sizes of larger events and appearance of significantly smaller events.

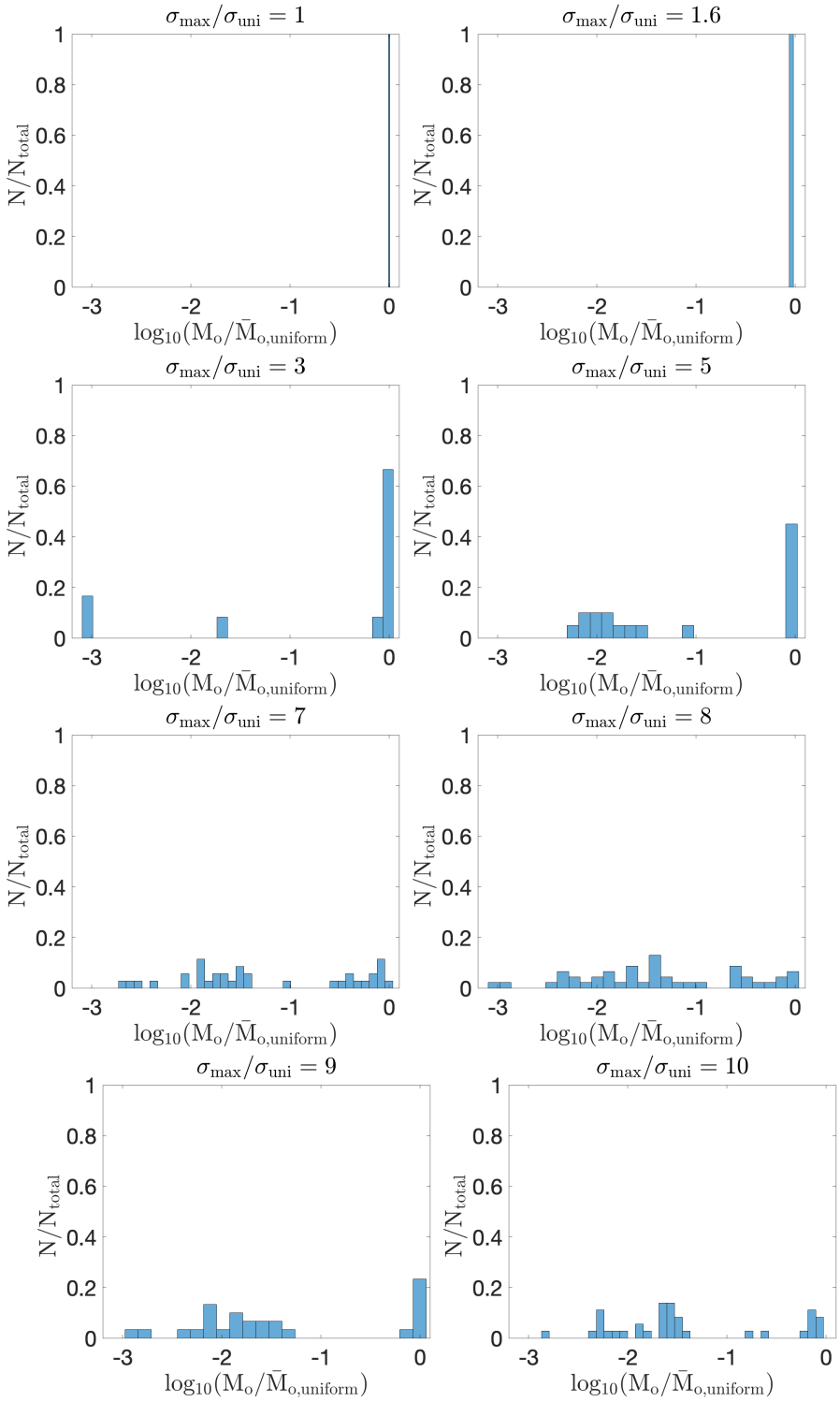

Figure 4.2: Distribution of event sizes across the models with heterogeneous normal stress. The seismic moments on the horizontal axis is normalized with respect to the mean moment of events from the uniform normal stress model and plotted in the logarithmic scale. The fraction of events in a given log-normalized moment range is plotted on the vertical axis. The moments plotted in log scale elucidate the richer size distribution, with more sizes represented, with increasing heterogeneity.

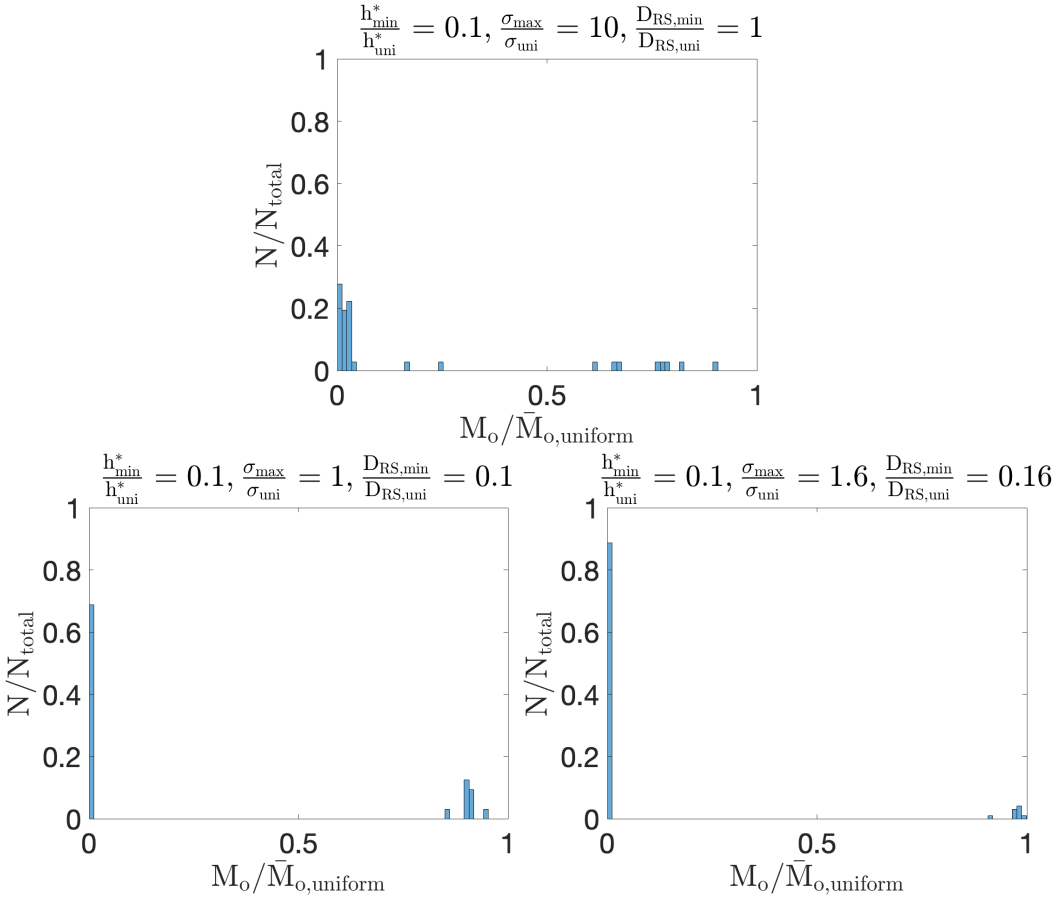

Figure 4.3: Distribution of event sizes across models with the same distribution of the nucleation size estimate as for the modified fractal normal stress $\sigma_{max}/\sigma_{uni} = 10$ (and hence with $h^*_{uni}/h^*_{min} = 10$). The seismic moments on the horizontal axis are normalized with respect to the mean moment of events from the model with uniform normal stress and D_{RS}. The fraction of the events in a given moment range is plotted on the vertical axis. (Top) Results for the modified fractal distribution with $\sigma_{max}/\sigma_{uni} = 10$ and uniform D_{RS}. (Bottom left) Results for uniform normal stress and modified D_{RS}. (Bottom right) Results for a fractal distribution of normal stress with $\sigma_{max}/\sigma_{uni} = 1.6$ and modified D_{RS}. Strong heterogeneity in normal stress results in more significant variation in sizes of the larger events while the heterogeneity in D_{RS} generates a large fraction of small-scale events.

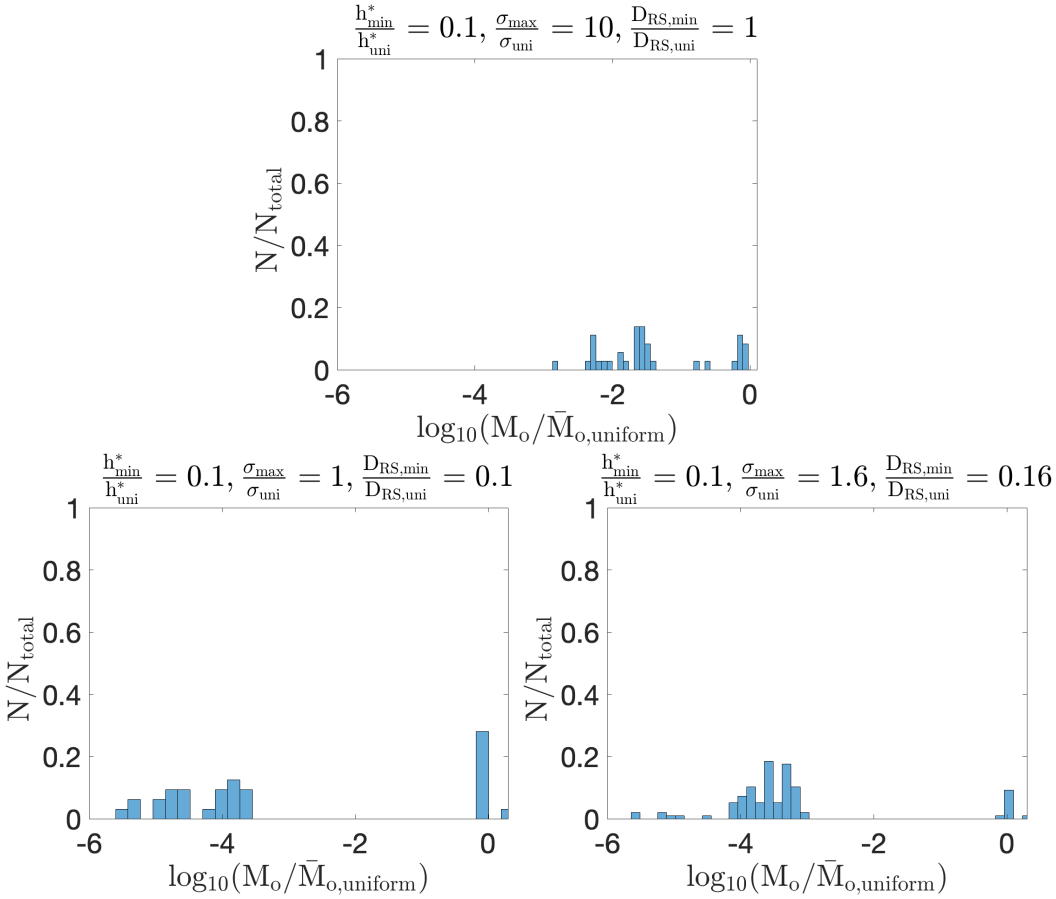

Figure 4.4: Distribution of event sizes across models with the same distribution of the nucleation size estimate as for the modified fractal normal stress $\sigma_{max}/\sigma_{uni} = 10$ (and hence with $h^*_{uni}/h^*_{min} = 10$). The seismic moments on the horizontal axis are normalized with respect to the mean moment of events from the uniform normal stress model and plotted in the logarithmic scale. The fraction of the events in a given log-normalized moment range is plotted on the vertical axis. (Top) Results for the modified fractal distribution with $\sigma_{max}/\sigma_{uni} = 10$ and uniform D_{RS}. (Bottom left) Results for uniform normal stress and modified D_{RS}. (Bottom right) Results for a fractal distribution of normal stress with $\sigma_{max}/\sigma_{uni} = 1.6$ and modified D_{RS}. Strong normal stress heterogeneity results in a more significant variation of larger-scale events and some intermediate events. Cases with the modifying D_{RS} distribution generate a larger number of much smaller events and no intermediate events.

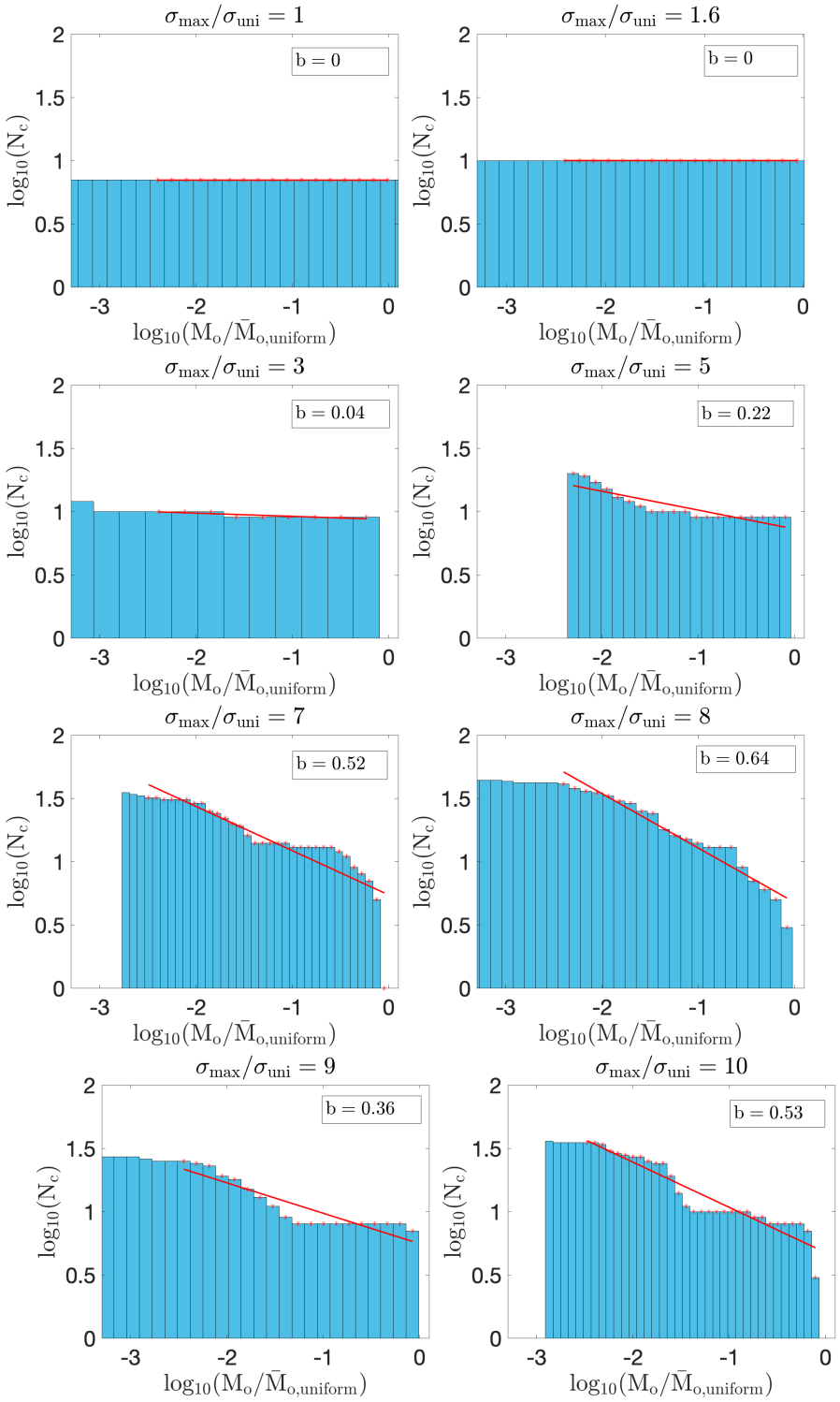

Figure 4.5: Cumulative distributions of event sizes representing all events occurring above each log normalized moment range plotted in log scale for models with normal-stress heterogeneity. b-values of the Gutenberg-Richter scaling law are calculated for each model for the moment range $\log_{10}(M_o/\bar{M}_{o,uniform}) \in [-2.5, 0]$). The b-values first systematically increase with increasing heterogeneity until $\sigma_{max}/\sigma_{uni} = 8$ and then stay in the range of $0.35 - 0.55$ after.

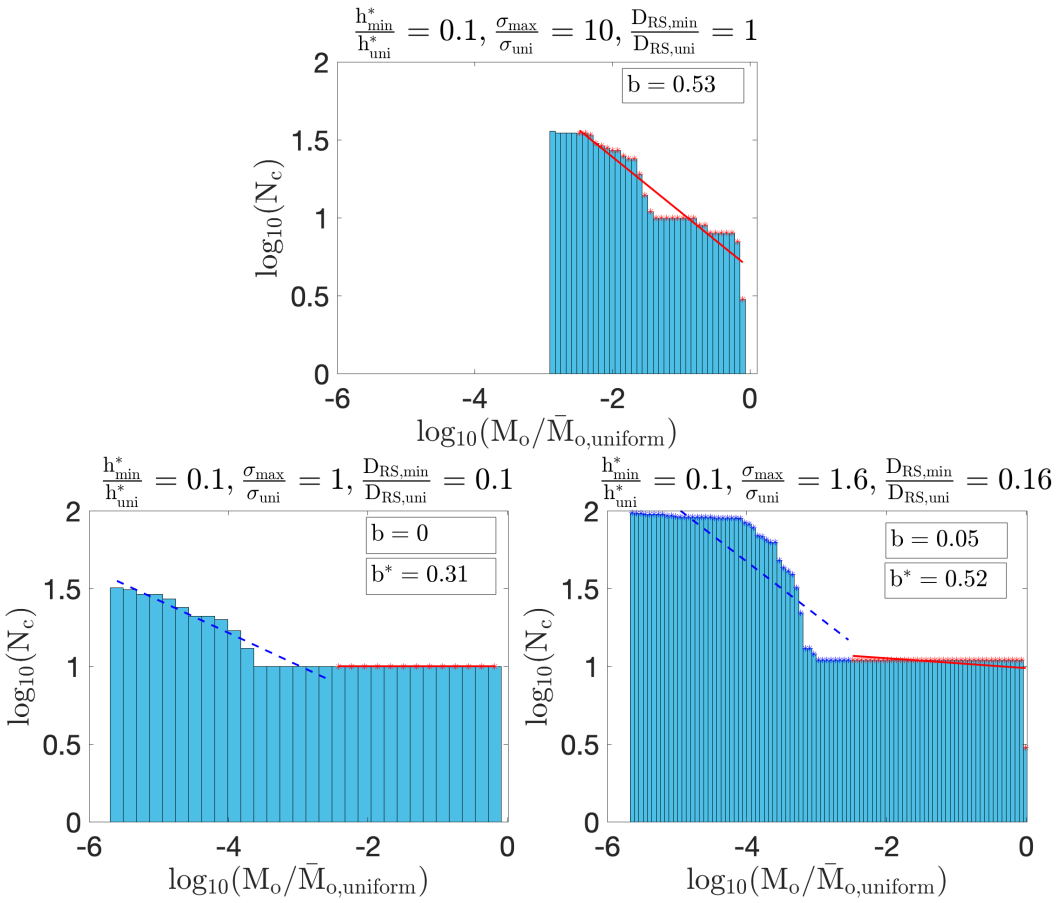

Figure 4.6: Cumulative distribution of event sizes representing all events occurring above each log normalized moment range, plotted in log scale, for models with the same distribution of the nucleation size estimate as for the modified fractal normal stress with the largest heterogeneity $\sigma_{max}/\sigma_{uni} = 10$ (and hence with $h^*_{min}/h^*_{uni} = 0.1$). b-values are close to 0 for the models with modified D_{RS} distribution in the event size range $\log_{10}(M_o/\bar{M}_{o,uniform}) \in [-2.5, 0]$, reflecting the absence of intermediate-scale events and lack of variation in the larger-scale event sizes. For the models with modified D_{RS} distribution, b-values are also calculated in the range $\log_{10}(M_o/\bar{M}_{o,uniform}) \in [-6, -3]$, denoted by b^*.

The distribution of event sizes on natural faults is also commonly characterized by plotting the cumulative number of earthquakes that occur above a certain moment (Figure 4.5, 4.6). This distribution of events can be analyzed in the framework of Gutenberg-Richter (GR) scaling law discussed in Section 1.4. To recall, the scaling is empirically expressed as $\log(N_c) = -bM_w + a$, where N_c is the cumulative number of earthquakes above moment magnitude M_w. Using the relationship between moment magnitude and seismic moment, $M_w = \frac{2}{3}[\log_{10}(M_o) - 9.1]$, we can rewrite the GR scaling law in terms of seismic moment, $\log(N_c) = \frac{-2b}{3}\log_{10}(M_o) + a'$.

The b-value relates the number of large events to small events and takes on values ranging from 0.5 – 2.5 when natural earthquake catalogs are considered, with the average value for b over large regions—and globally—typically being taken as 1. The b-values are calculated by fitting a linear trend to the cumulative frequency-magnitude distributions of each simulation (Figure 4.5) within the same size range $\log_{10}(\mathrm{M_o}/\bar{\mathrm{M}}_{\mathrm{o,uniform}}) \in [-2.5, 0]$. Note that b-values can be estimated alternatively using the maximum-likelihood estimate as discussed in Aki (1965). The b-value systematically increases with increasing normal stress heterogeneity till $\sigma_{max}/\sigma_{uni} = 8$, where it has value of 0.64. For larger heterogeneity, the b-value fluctuates, while staying in the range $0.35-0.6$. The fluctuation could be due to insufficient number of events to establish the stable statistics and/or the result of the particular relation between the compressed asperities and the geometry of the VW region; the results need to be verified with longer simulations and larger simulation domains. In the modified D_{RS} models, the b-values are ~ 0 within the range $\log_{10}(\mathrm{M_o}/\bar{\mathrm{M}}_{\mathrm{o,uniform}}) \in [-2.5, 0]$, reflecting the absence of intermediate-scale events and lack of variation in larger-scale event sizes (Figure 4.6). A separate GR fit for the events in the size range $\log_{10}(\mathrm{M_o}/\bar{\mathrm{M}}_{\mathrm{o,uniform}}) \in [-6, -3]$ gives higher b-values, indicating some complexity of event sizes in this range.

Nearly heterogeneity- and magnitude-invariant static stress drops in our models

One of the fascinating properties of dynamic earthquake source events on natural faults are their magnitude-invariant static stress drops, averaging 1-10 MPa for an extremely broad range of event sizes from microseismicity to the greatest plate-boundary earthquakes in all tectonic environments (Abercrombie and Leary, 1993; Allmann and Shearer, 2009; Baltay et al., 2011). At the same time, the stress drop estimates exhibit significant scatter, from 0.01 to 100+ MPa. The static stress drops are interpreted as the difference between average shear stress on the fault before and after the dynamic event, although the exact nature of the averaging and biases implicit in different stress-drop estimation methods are the topic of active current research (Kaneko and Shearer, 2014; Kaneko and Shearer, 2015; Noda et al., 2013; Lin and Lapusta, 2018).

Given the observed magnitude-invariance of static stress drops on natural faults, it is important to examine the stress drops of the events in our models, which collectively cover about 6 orders of magnitude in seismic moment, especially given all the different heterogeneous conditions under which the events nucleate. The average stress drop calculated in this study is the energy-related σ_E measure from

Noda et al. (2013), where the distribution of the static stress change over the fault is averaged with the pointwise final slip as the weighting function.

Remarkably, most static stress drops for the events in our models vary by about a factor of 0.5 to 2 from the static stress drops of model-spanning events in the uniform fault model (Figures 4.7-4.9). In all cases, the stress drops for the larger-scale events stress remain nearly equal to the stress drops on the uniform fault, as would be expected given similar average fault properties and recurrence times. For the models with increasing normal stress heterogeneity (Figure 4.7), the stress drops of the smaller-scale events marginally increase, with the median stress drop normalized by that of the uniform case increasing from 1 to 1.2 as the peak normal stress heterogeneity over the mean normal stress varies from 1 to 10. For the models with the modified D_{RS}, the median stress drops are lower than $\Delta\tau_{uni}$, by a factor of 2 in one model (Figure 4.8).

Such potentially counter-intuitive behavior can be explained by the dynamics of the earthquake rupture events (e.g., Schaal and Lapusta, 2019). The events nucleating on highly compressed spots indeed experience much higher dynamic stress drop, for the same change in friction, then events nucleating on a uniform fault or on a patch of modified D_{RS}. This dynamic stress drop gets redistributed around the expanding event through dynamic waves, promoting the event propagation and resulting in events of larger sizes. Yet, for the event to arrest, it needs to start experiencing negative stress drops, with rupture increasing the shear stress ahead of itself through dynamic shear stress concentration. The average static stress drops average between the (positive) stress drop where events initiate and zero to negative stress drops where the rupture slows down and arrests. Our simulations show that this highly dynamic and nonlinear process results in similar average static stress drops for a wide range of fault heterogeneity.

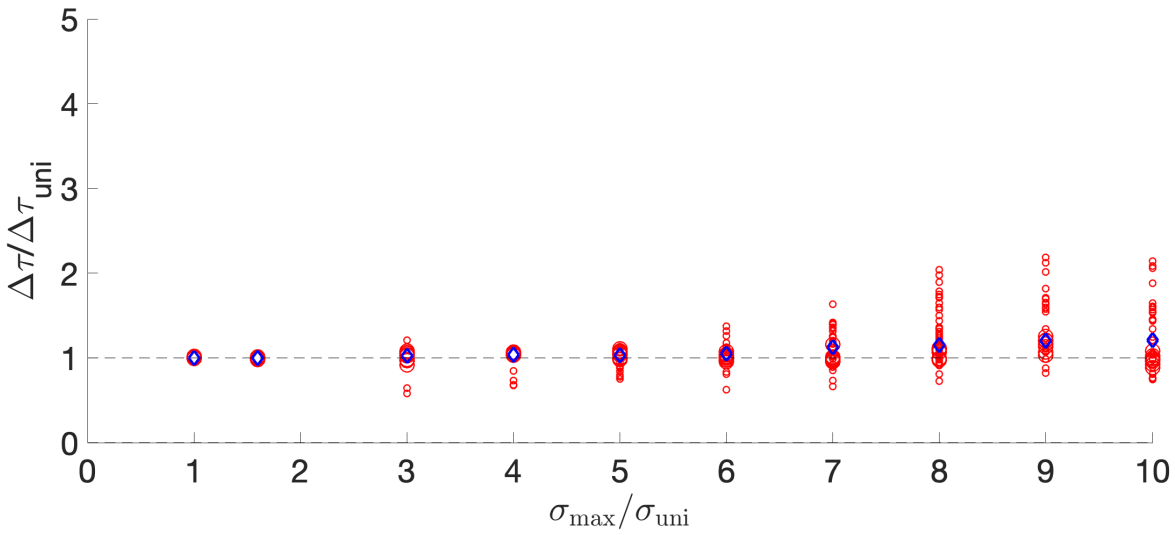

Figure 4.7: Static (shear) stress drops across different models with increasing heterogeneity in normal stress. The stress drops of larger-scale events are indicated by bigger red circles and those of other events by smaller circles. The larger-scale event stress drops are nearly the same with increasing normal stress heterogeneity. The median stress drops at each heterogeneity level are indicated by blue diamonds, and have a nominally increasing trend.

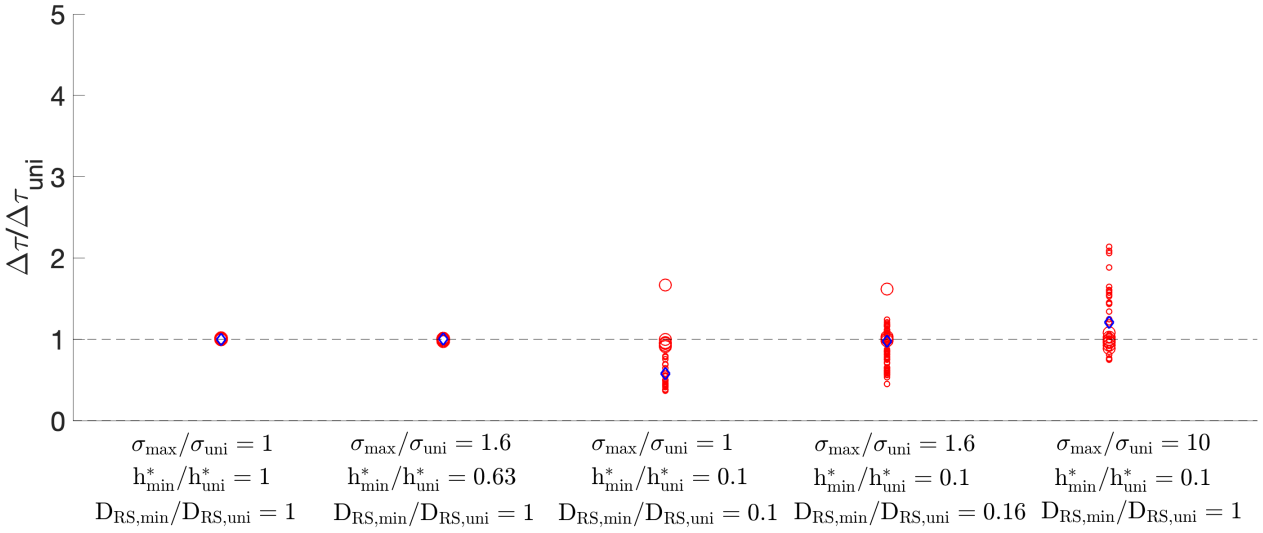

Figure 4.8: Variation of stress drops for models with uniform normal stress, fractal normal stress, and three models with the same distribution of the nucleation size estimate as for the modified fractal normal stress with the largest heterogeneity $\sigma_{max}/\sigma_{uni} = 10$. The stress drops of larger-scale events are indicated by bigger red circles and those of other events by smaller circles. The median stress drops at each heterogeneity level are indicated by blue diamonds. The models with modified D_{RS} distributions have median stress drops below $\Delta\tau_{uni}$.

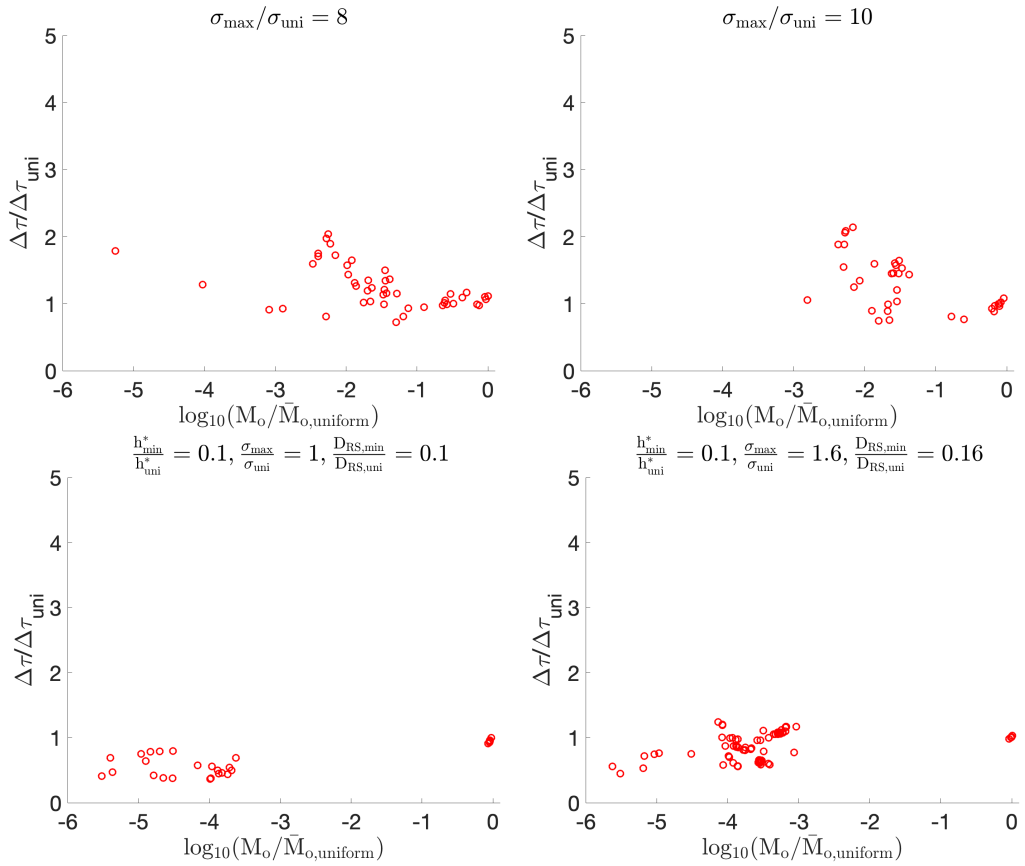

Figure 4.9: Variation of stress drops with event sizes for several models.

4.2 Effect of heterogeneity on progression of dynamic ruptures

Recurrence time of larger-scale events

The recurrence times of larger-scale events (defined as events that rupture more than 90% of the seismogenic, VW fault area) across different models is similar, generally within ±20% of the recurrence time on the homogeneous fault (Figure 4.10—4.11), which is perhaps not surprising, given that all models have the same mean fault properties.

However, there is no systematic variation of the deviations from the uniform fault model with the increasing normal stress heterogeneity. Perhaps this is also not surprising, given the following considerations. The recurrence time is affected by both nucleation processes as well as the conditions on the fault (shear stress, state variable) at the time of each nucleation attempt; the fault has to be loaded enough on average for the dynamic rupture to propagate. The presence of the strong asperities result in two potential effects on recurrence time which trade off with each other. On the one hand, when the fault is not yet loaded enough, nucleation

of dynamic rupture on nucleation-prone asperities would generate a smaller-scale event that would reduce the shear stress, potentially delaying the next larger-scale event and hence the recurrence time. On the other hand, at some point a smaller-scale nucleation attempt may occur when the fault is ready and initiate a larger-scale event, perhaps sooner than would be possible with a longer, larger-scale nucleation process. The nucleation attempts in our models are discrete events that depend on the distribution of the nucleation-prone features and their location within the fault domain. Hence the effects would combine differently in different models, as our simulation results indicate.

The larger-scale-event recurrence times in models with modified D_{RS} distributions have less variation and remain comparable to the uniform normal stress model (Figure 4.11). This is likely due to the fact that the smaller-scale events in those models are much smaller than in the models with strong normal stress variations and have a minor effect on the nucleation processes as discussed in Chapter 3.

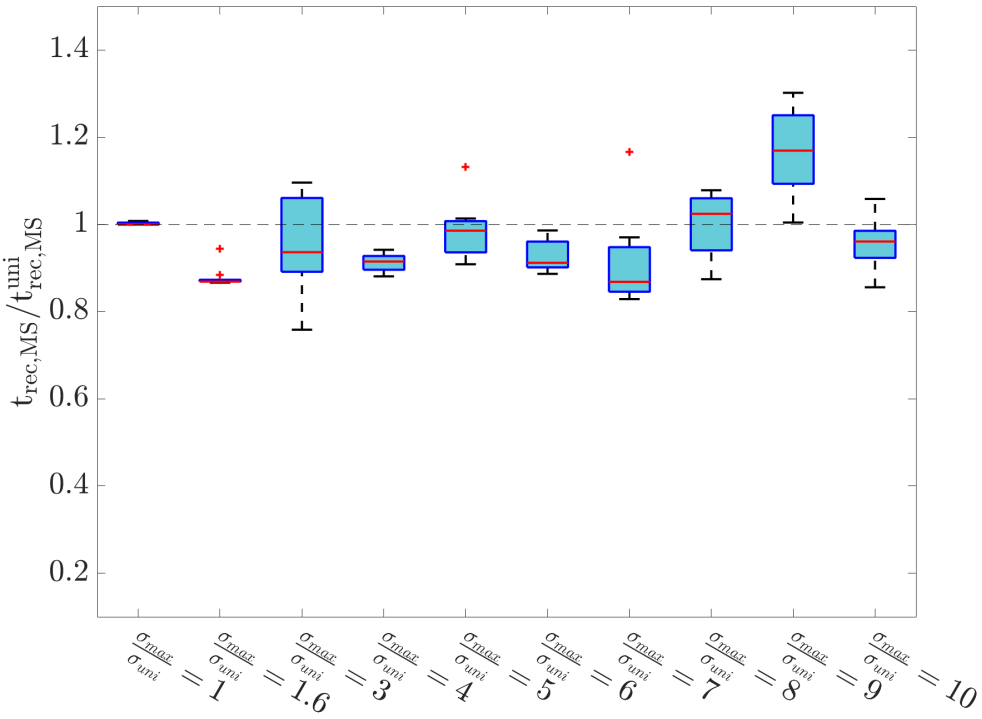

Figure 4.10: Variation of larger-scale-event recurrence time with increasing normal stress heterogeneity levels, visualized by box plots. The median recurrence time at each heterogeneity level is indicated by the red line. The recurrence times are normalized with respect to the recurrence time of events in the uniform normal stress model. The larger-scale-event recurrence times remain more or less comparable with increasing normal-stress heterogeneity.

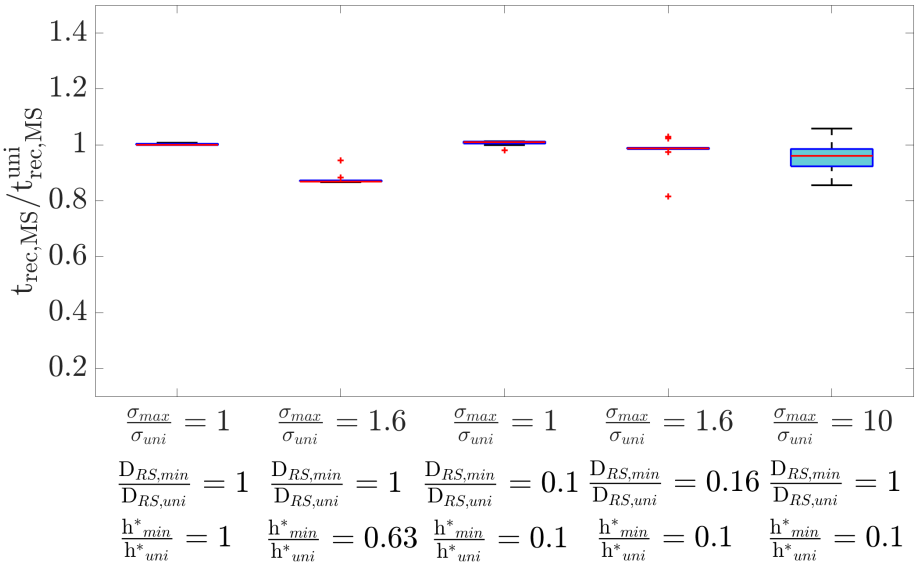

Figure 4.11: Variation of larger-scale-event recurrence time, visualized by box plots, for the models with uniform normal stress, fractal normal stress, and models preserving the local nucleation size distribution with $h^*_{min}/h^*_{uni} = 0.1$, in different ways. The median larger-scale-event recurrence time for each model is indicated by the red line. The recurrence times are normalized with respect to the recurrence time of events in the uniform normal stress model. The larger-scale-event recurrence times in the models with modified D_{RS} distributions have less variation.

Source-time functions

Source-time functions (STFs) describe the rate of seismic moment release by the earthquake rupture as a function of time and are proportional to integrated dynamic slip rates over the rupture area. Let us consider STFs for 5 selected larger-scale dynamic events from each model discussed in the previous chapter (10 models focusing on normal stress heterogeneity and the two 'modified' D_{RS} models) (Figures 4.12, 4.13, 4.16 - 4.25). In the panel (a) of every figure, a velocity threshold ($V_{dyn} \sim$ 0.01 m/s) is used to identify the event beginning and end. This procedure sometimes results in counting as one dynamic event two or more events that would be considered separate seismologically, and other artifacts, as discussed later. To circumvent these issues, we also use a moment-rate threshold to identify the beginning and end of the events, with the value chosen to be $\sim 10^8$ Nm/s or $\sim 1\%$ the max moment rate achieved across models, which is $\sim 10^{10}$ Nm/s, and these STFs are plotted as panels (b) in each Figure. The STFs in panels (a-b) are normalized by the peak moment rate of in the uniform normal-stress mode. Time is normalized by the time taken by the shear wave to traverse the seismogenic, VS region, since natural earthquakes propagate with rupture tip speeds that are a significant fraction of the shear wave speed, and this form of time normalization enables us to make conclusions about approximate rupture speed of events. Panels (c) in each Figure normalize the STFs in the way done for natural earthquake ruptures in the work of Meier et al. (2017): the time for each rupture is normalized by its own rupture duration and the moment rate of individual STFs is multiplied by a constant such that the area under the STF is reduced to 1. The median STF (indicated by a dashed black line) is plotted for these normalized STFs; this median STF can be compared to the conclusions for natural earthquakes (Figure 1.6).

The STFs corresponding to events in the uniform normal stress model (Figure 4.12) are all nearly the same, indicating that all events nucleate and rupture in similar fashion. This is also the case in the fractal normal stress model ($\sigma_{max}/\sigma_{uni} = 1.6$) (Figure 4.13). An interesting comparison can be made by comparing the source time functions corresponding to the uniform and fractal normal stress model (Figure 4.14). The area under the source time functions in both cases is similar, with the area for the uniform case being slightly higher, consistent with the event size distribution plots, indicating higher seismic moment. The moment rate accumulates in significantly different ways, however. In the uniform case, the rupture nucleates closer to the middle of the fault and reaches a higher moment-rate peak more rapidly due to initial bi-lateral propagation along the fault. In the model with the fractal

normal stress, the rupture nucleates closer to the edge of the fault and has longer uni-driectional propagation distance to the other end and hence longer duration; the rupture speed is actually nearly identical between the two cases. The lower and sustained moment rate in the fractal normal-stress model is due to more pulse-like rupture propagation, either because of the higher aspect ratio of the rupture propagation length to the fault width, or perhaps because of local healing behind the rupture front, resulting in lower dynamically slipping area at any time instant (Figure 4.14, bottom slip-rate snapshots). The moment-rate irregularity is due to fault heterogeneity.

To distinguish between the effect of the aspect ratio vs. local healing, we simulate earthquake sequences in another homogenous model but with 20% smaller characteristic slip distance (D_{RS}), enabling the events in the uniform normal-stress model to nucleate closer to the edge, as in the fractal normal stress model (Figure 4.15). Events in both models now have to propagate uni-directionally for a longer distance along the fault, although the events in the uniform fault case still nucleate a bit close to the center and have a slightly smaller nucleation size, resulting in the initial bilateral propagation and hence higher initial moment rates. Otherwise, the STFs of both models now look more similar, with a region of similar sustained moment rate release, reflecting the importance of the event nucleation location, the shape of rupture area, and rupture directivity on the shape of the STF.

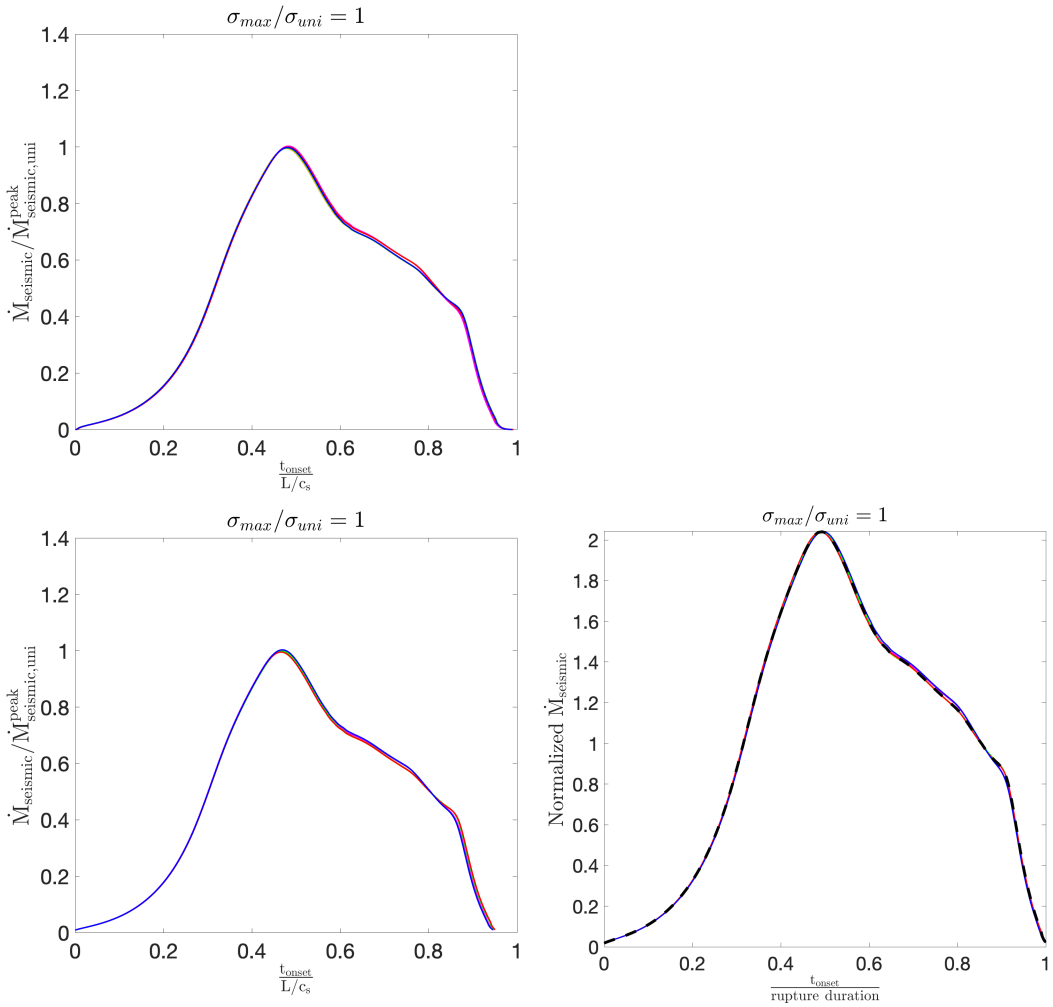

Figure 4.12: STFs from the uniform fault model, $\sigma_{\text{max}}/\sigma_{\text{uni}} = 1$. a. STF using slip-velocity threshold for event identification. Time is normalized by the time for the shear wave to traverse the length of the VW fault region. Moment rate is normalized by the peak moment rate of the uniform fault model. b. STF using moment-rate threshold for event identification c. STF using moment rate threshold for event identification with a different normalization: time is normalized by each rupture duration and moment rate is normalized such that the area integrates to unity.

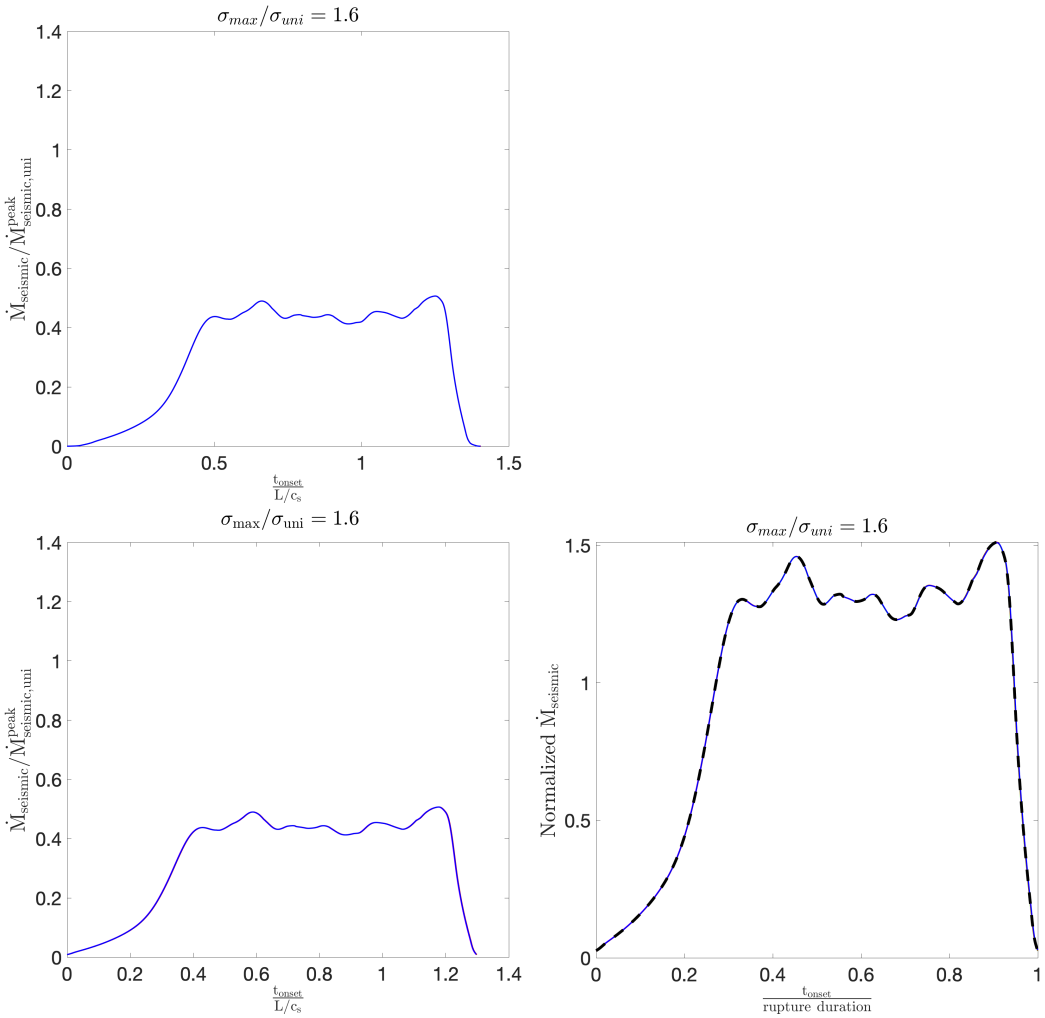

Figure 4.13: STFs from the fractal normal-stress model with $\sigma_{\text{max}}/\sigma_{\text{uni}} = 1.6$. Same plotting conventions as Figure 4.12.

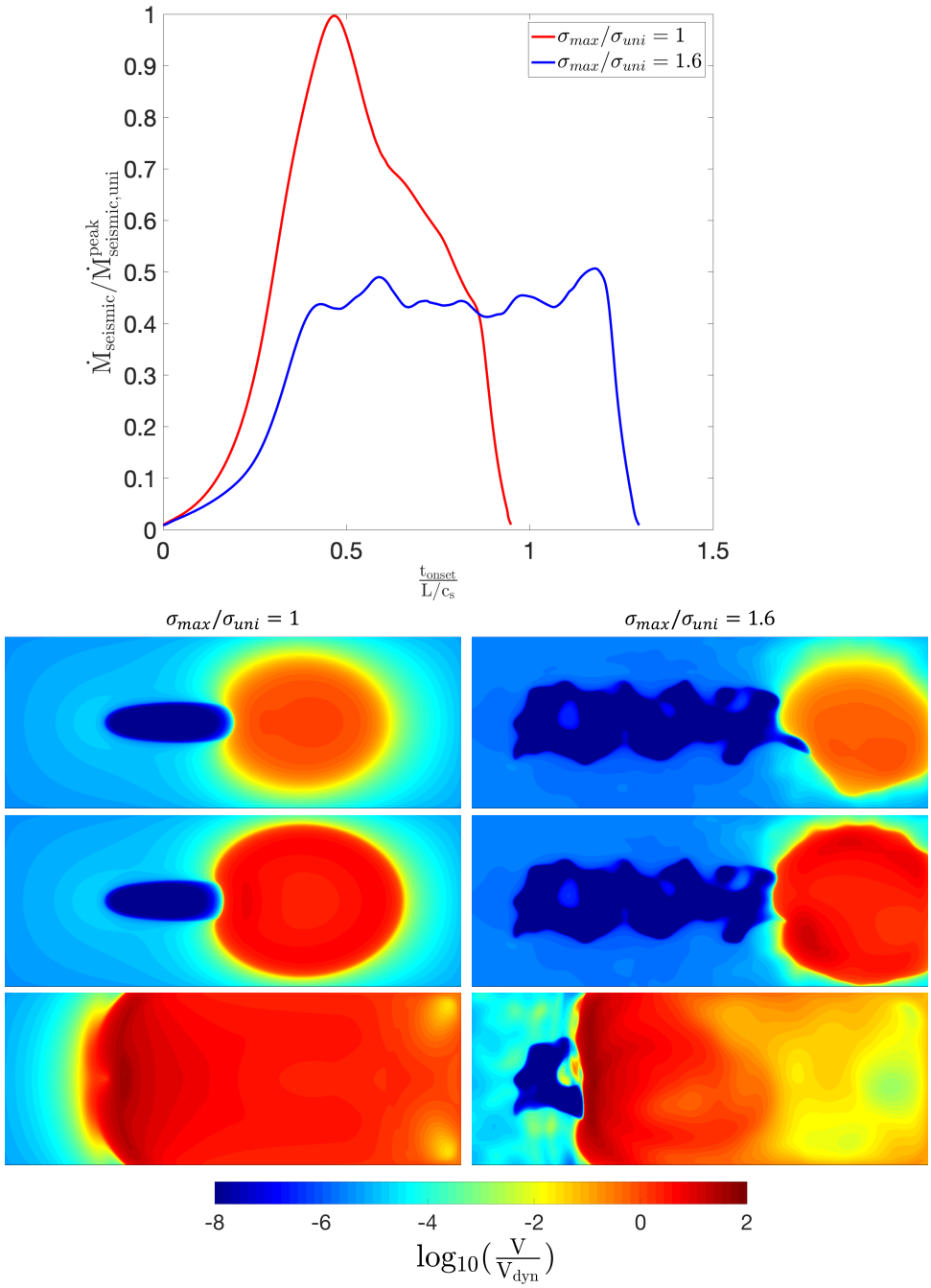

Figure 4.14: Comparison of typical events in the models with uniform ($\sigma_{\max}/\sigma_{\text{uni}} = 1$) and fractal ($\sigma_{\max}/\sigma_{\text{uni}} = 1.6$) normal-stress distributions. (Top) STFs. (Bottom) Slip-rate snapshots. The differences in the shape of STF and peak moment rates reached is affected by where the event nucleates and rupture directivity.

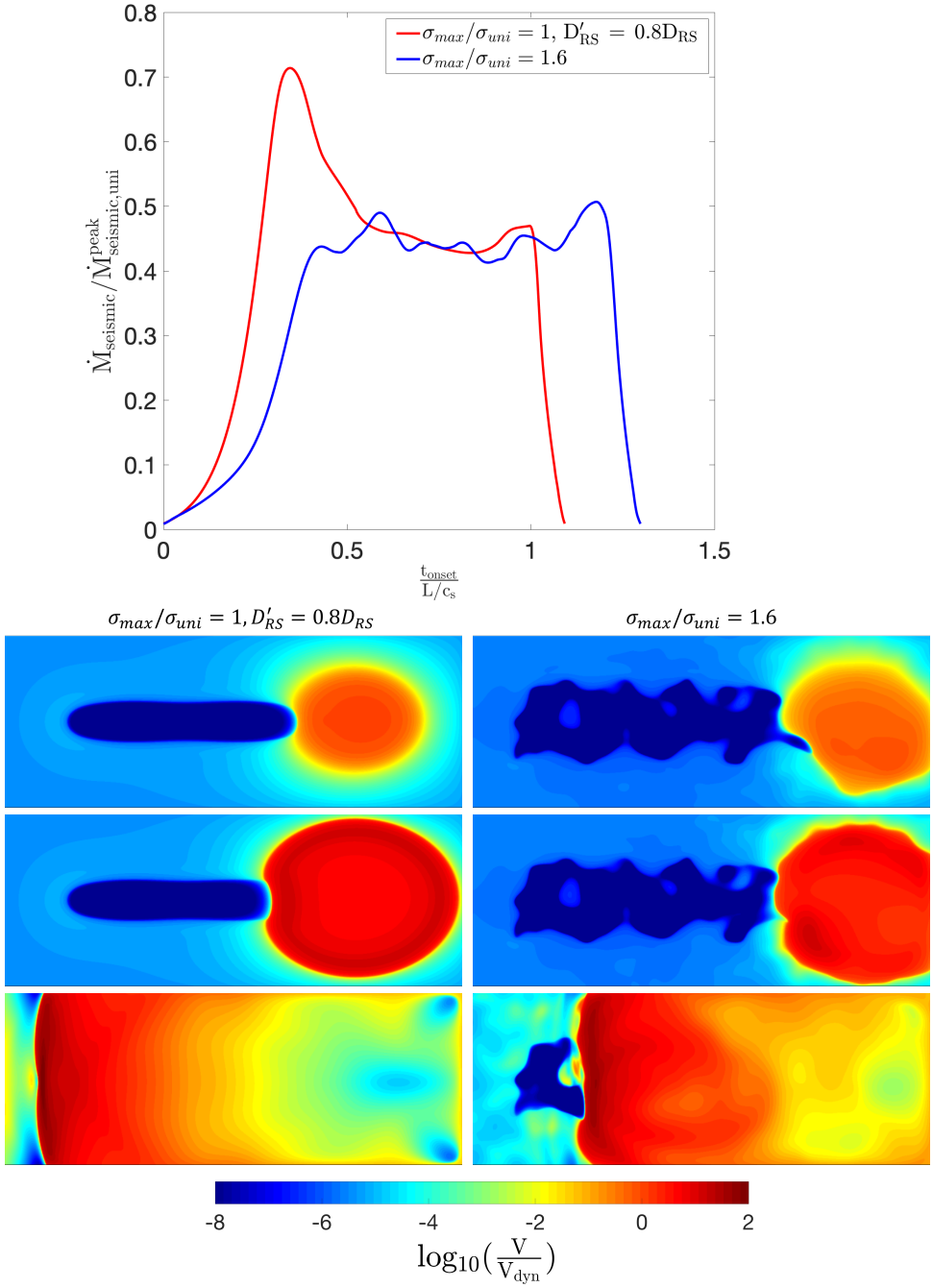

Figure 4.15: Comparison of typical events in the model with uniform normal stress and reduced D_{RS} and in the model with the fractal normal stress ($\sigma_{max}/\sigma_{uni} = 1.6$). The event in the uniform model with lower D_{RS}—and hence lower nucleation size—nucleates closer to the edge, becoming more similar to the fractal case.

For models with modified fractal normal stress with $\sigma_{max}/\sigma_{uni} = 3$ and larger, the source time functions of the individual events generally have different shapes and durations, with higher-frequency features (Figures 4.16-4.23). Upon plotting the STFs so that the seismic moment is normalized to unity (bottom right plot in each Figure), the variations between the events in each model, in terms of varying rupture durations and the reluctant initiation phases, are mostly obscured. The median STF plotted by dashed black line does not seem to capture the characteristic features of the events in each model.

The STFs of events identified by the velocity threshold and moment-rate threshold can be significantly different when precursory slips are involved. For the models with $\sigma_{max}/\sigma_{uni} = 5, 6, 7$ (Figures 4.18, 4.19, 4.20), many events have an initial acceleration followed by near-zero moment rates (given the plotting scale) and then another acceleration, after a time period different for different events, reflecting the complexity of rupture initiation processes. Given the relatively long duration of the low moment rate between the two accelerations, they may be identified as separate events seismologically. Indeed, identifying events by the moment rate threshold removes most of these features. This is most apparent in the $\sigma_{max}/\sigma_{uni} = 7$ model (Figure 4.20). The event represented by red STF in the top plot clearly represents a rapid sequence of foreshock-like events preceding the large peak. The diversity in the events in this model warrants further discussion and is examined in 4.2. Interestingly, at $\sigma_{max}/\sigma_{uni} = 8$ normal-stress heterogeneity level, the source time functions of the chosen events are more similar to each other. Whether this is a inherent feature of this model or a result of relatively short simulation times would require further research.

Across models, multiple events have initially more muted moment-rate release, presumably due to rupture propagation over areas with reduced shear stress due to foreshock-like events and quasi-static preslip. Parallels can be drawn to the seismic nucleation phases identified by Ellsworth and Beroza (1995) (Figure 1.5). A few select STFs that exhibit these nucleation phases are plotted in Figure 4.26. The work of Ellsworth and Beroza (1995) linked the duration of these seismic nucleation phases to the ultimate size of the event. Our events arrest not because of the fault heterogeneity but because of the VS region surrounding the VW, seismogenic portion of the fault. So while we cannot meaningfully examine the relation between this reluctant phase and the ultimate size of the earthquake in our current models, this can be done in suitably designed future modeling efforts.

The STFs in models with the modified D_{RS} (Figures 4.24, 4.25) are generally similar for different events in the same model and also similar to their uniform D_{RS} analogues with the same normal stress distributions (Figures 4.12, 4.13), with some notable differences. The modified D_{RS} model with the uniform normal stress has larger nucleation size than the purely uniform model, as discussed in Chapter 3, and the events accelerate more gradually from the middle of the fault, modifying the STFs. The modified D_{RS} model with the fractal normal stress has more variability in the STFs that the corresponding model with the uniform D_{RS}.

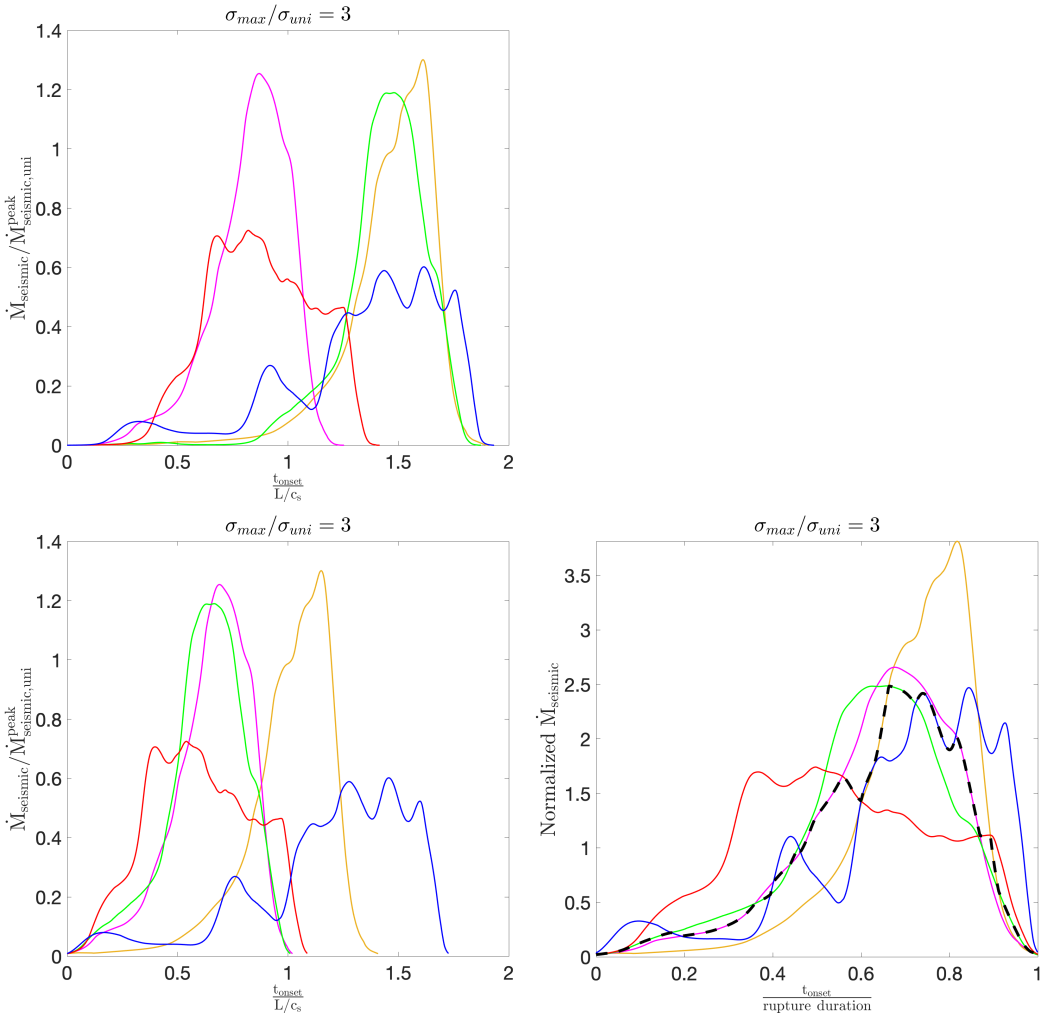

Figure 4.16: STFs from $\sigma_{\text{max}}/\sigma_{\text{uni}} = 3$ model. Same plotting conventions as Figure 4.12.

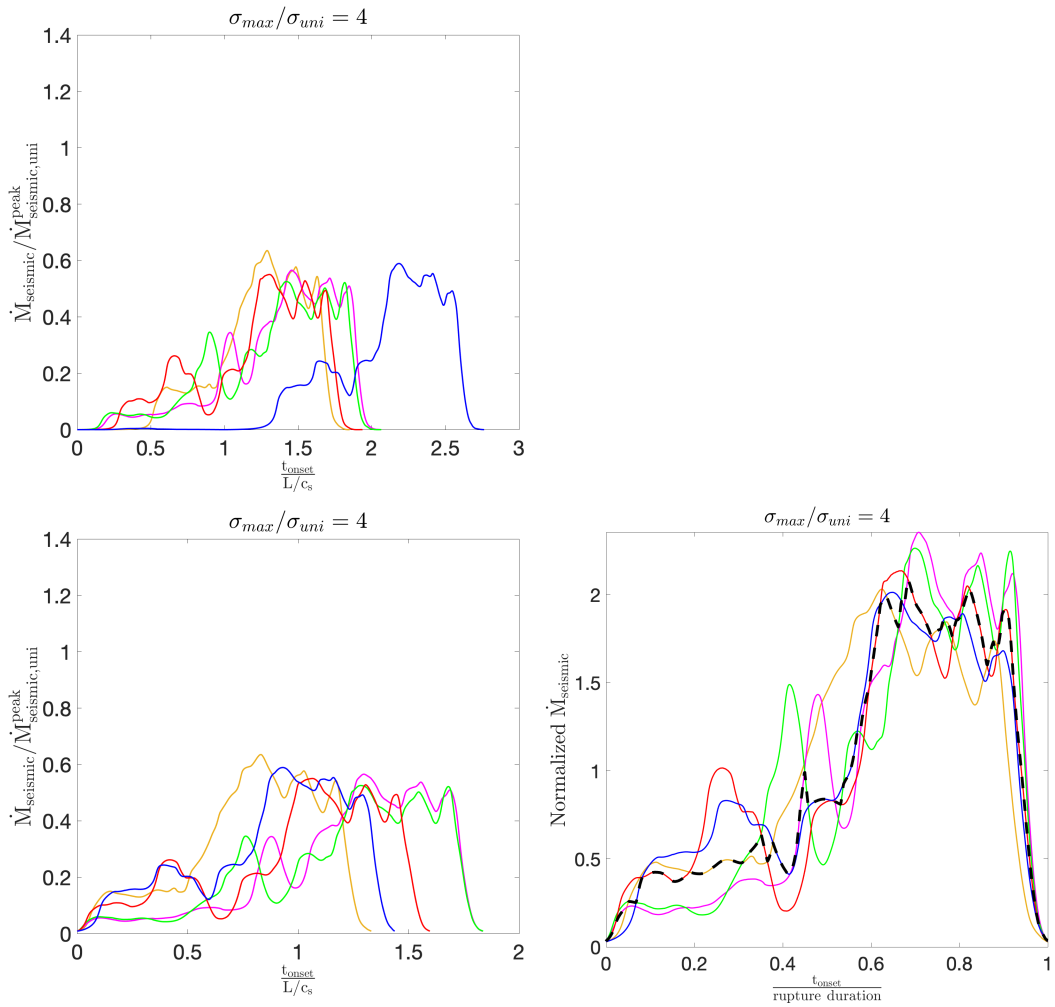

Figure 4.17: STFs from $\sigma_{\text{max}}/\sigma_{\text{uni}} = 4$ model. Same plotting conventions as Figure 4.12.

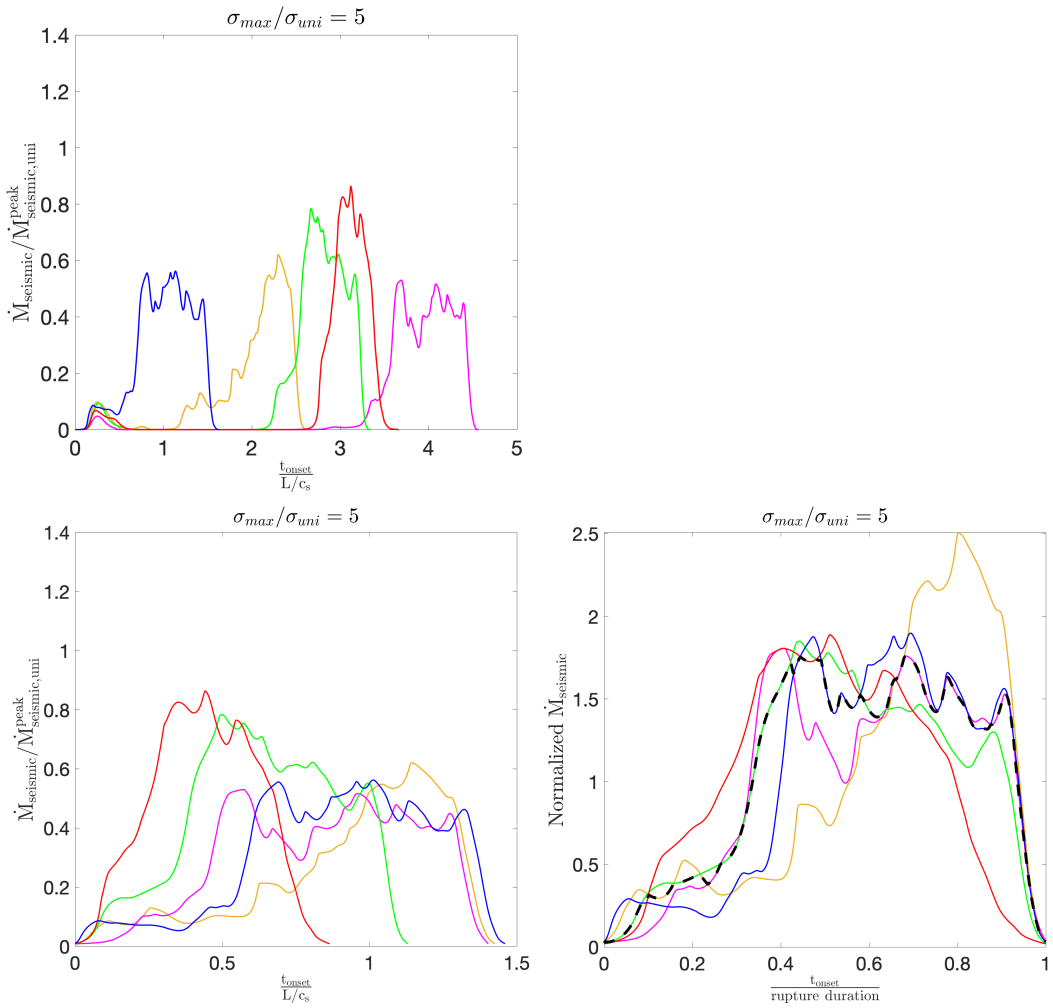

Figure 4.18: STFs from $\sigma_{\text{max}}/\sigma_{\text{uni}} = 5$ model. Same plotting conventions as Figure 4.12.

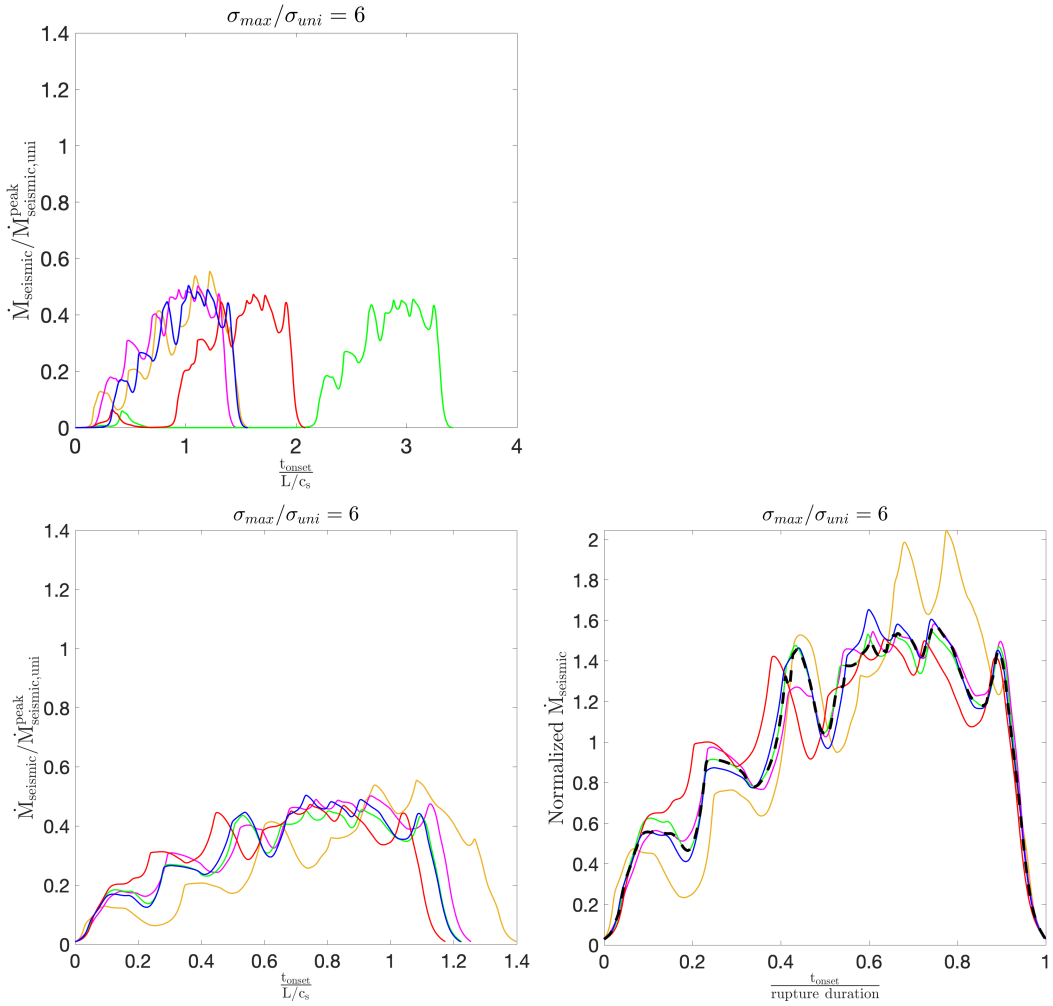

Figure 4.19: STFs from $\sigma_{\text{max}}/\sigma_{\text{uni}} = 6$ model. Same plotting conventions as Figure 4.12.

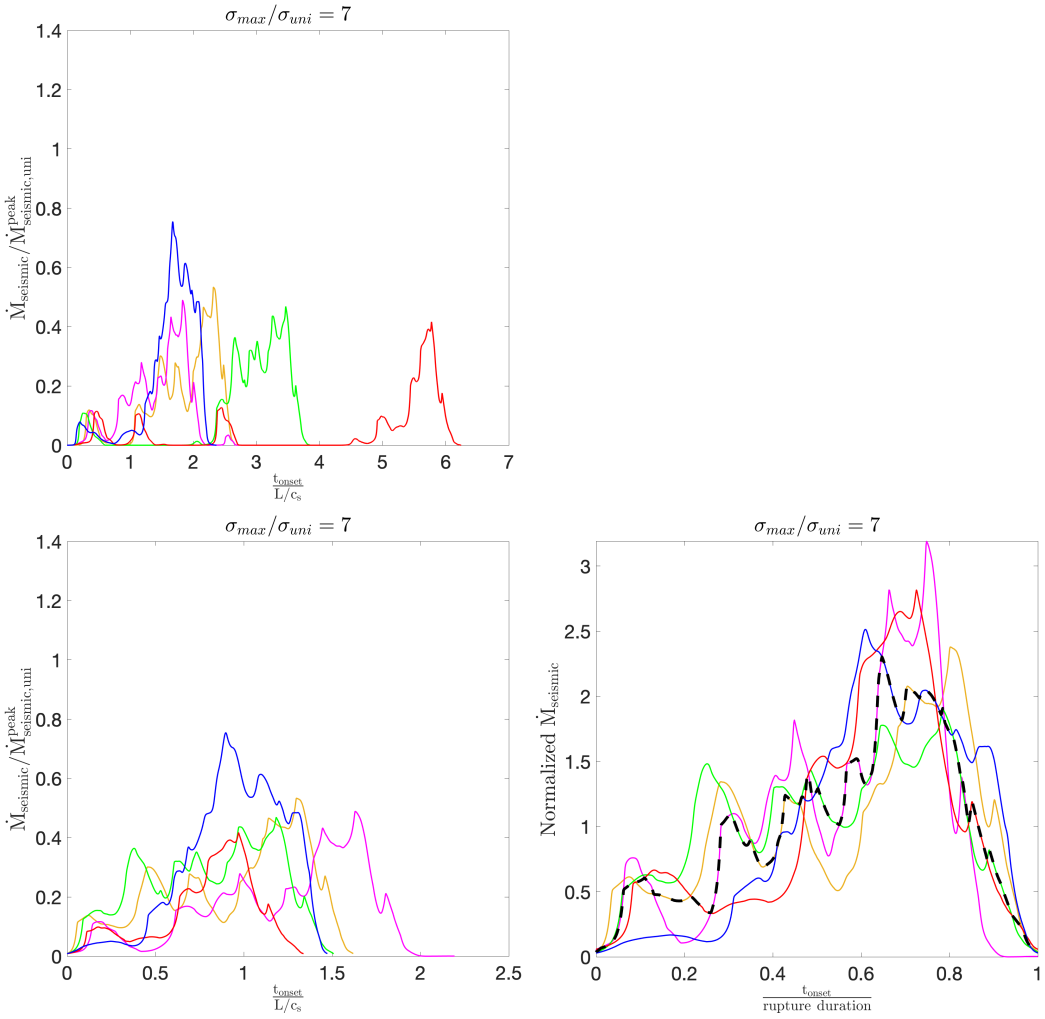

Figure 4.20: STFs from $\sigma_{\text{max}}/\sigma_{\text{uni}} = 7$ model. Same plotting conventions as Figure 4.12.

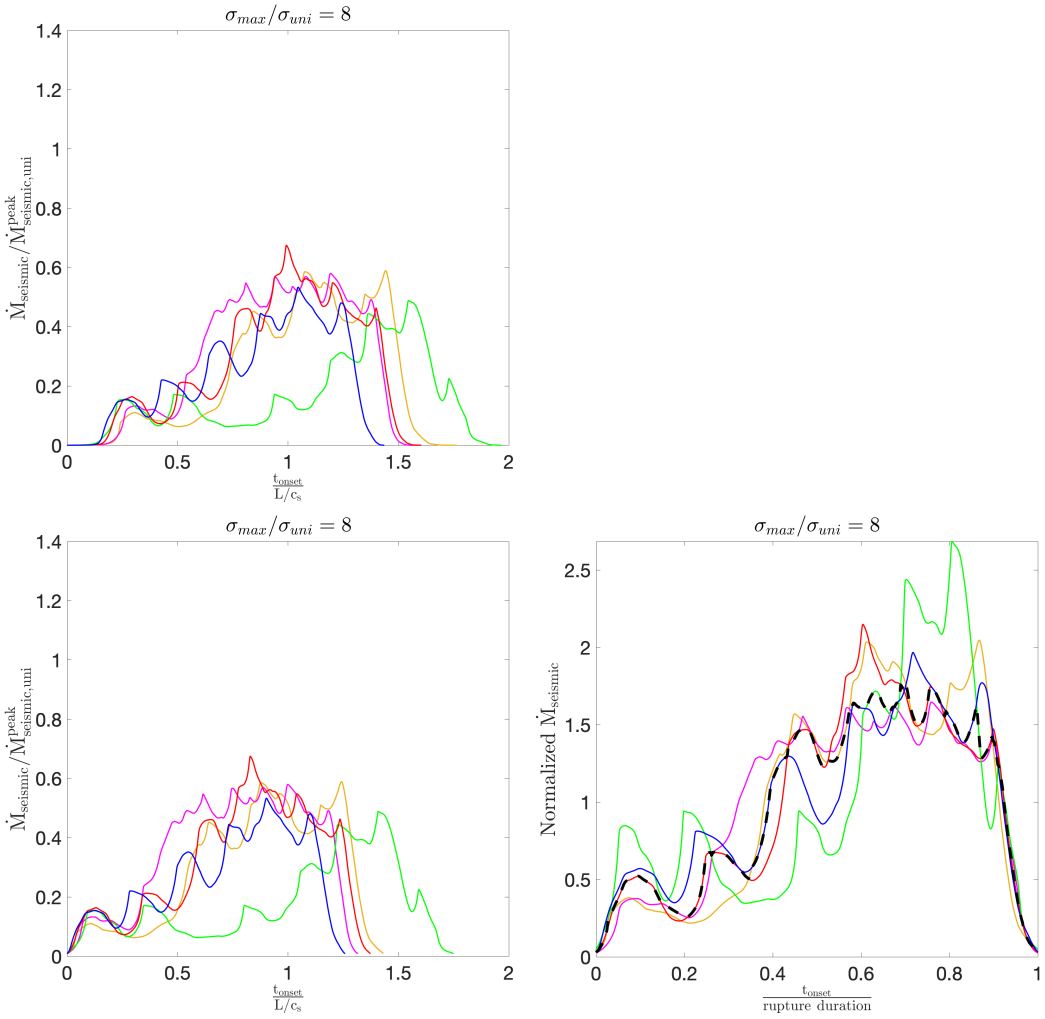

Figure 4.21: STFs from $\sigma_{\text{max}}/\sigma_{\text{uni}} = 8$ model. Same plotting conventions as Figure 4.12.

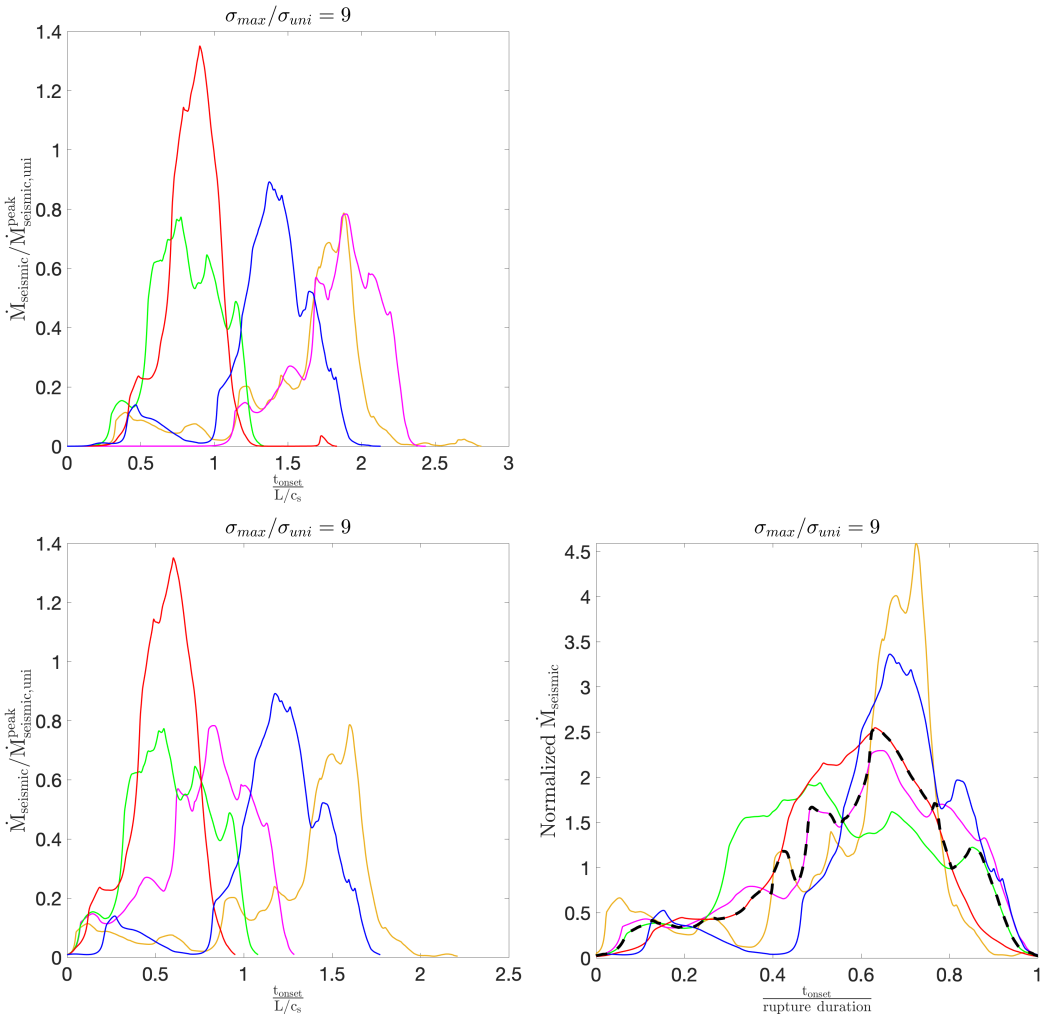

Figure 4.22: STFs from $\sigma_{\text{max}}/\sigma_{\text{uni}} = 9$ model. Same plotting conventions as Figure 4.12.

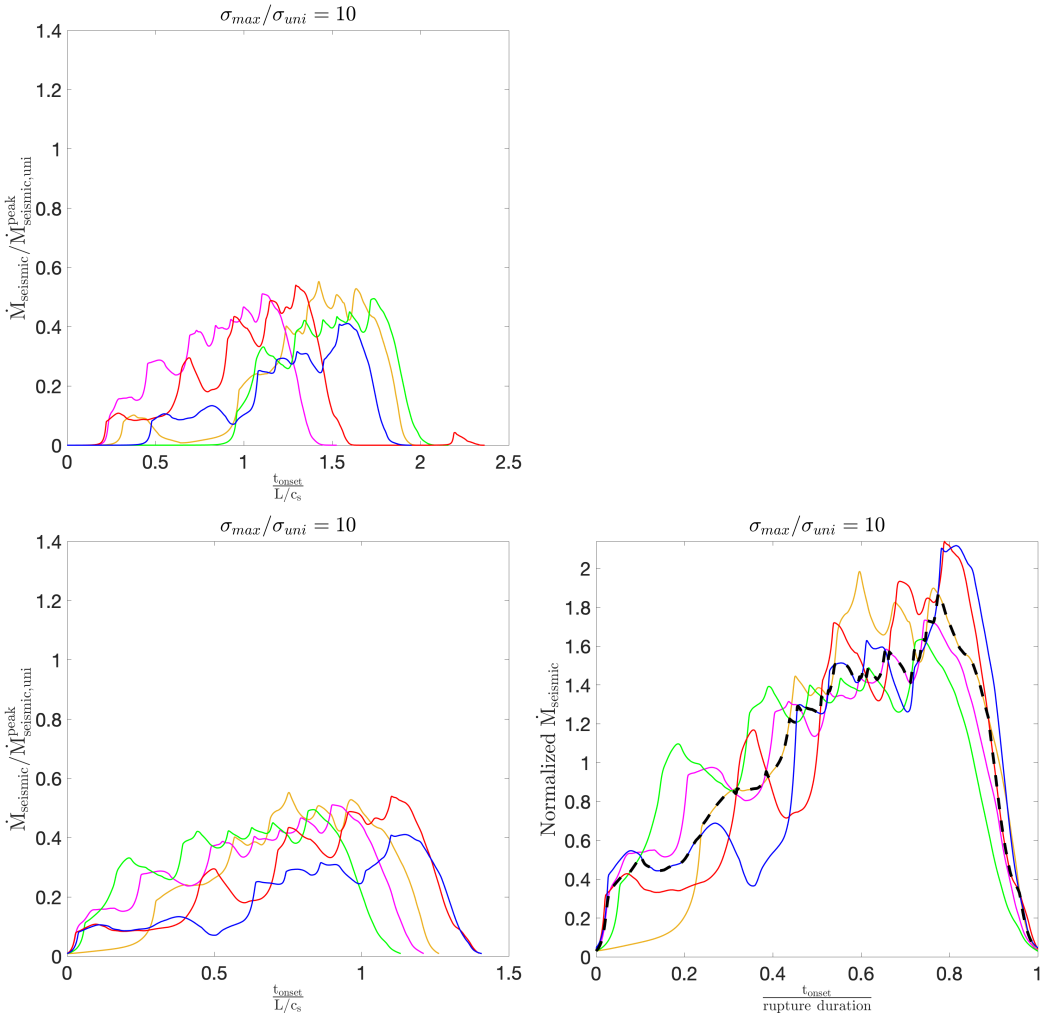

Figure 4.23: STFs from $\sigma_{\text{max}}/\sigma_{\text{uni}} = 10$ model. Same plotting conventions as Figure 4.12.

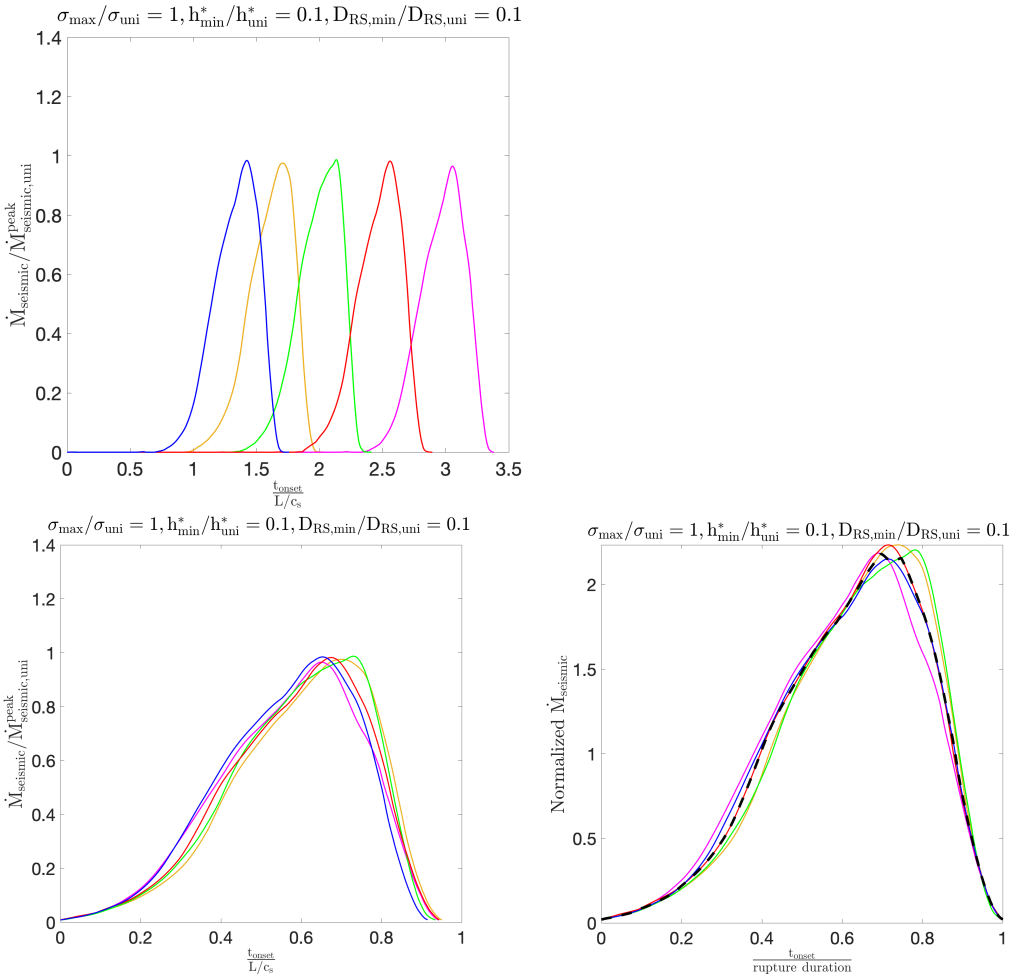

Figure 4.24: STFs from $\sigma_{max}/\sigma_{uni} = 1$, $D_{RS,min}/D_{RS,uni} = 0.1$ model. Same plotting conventions as Figure 4.12.

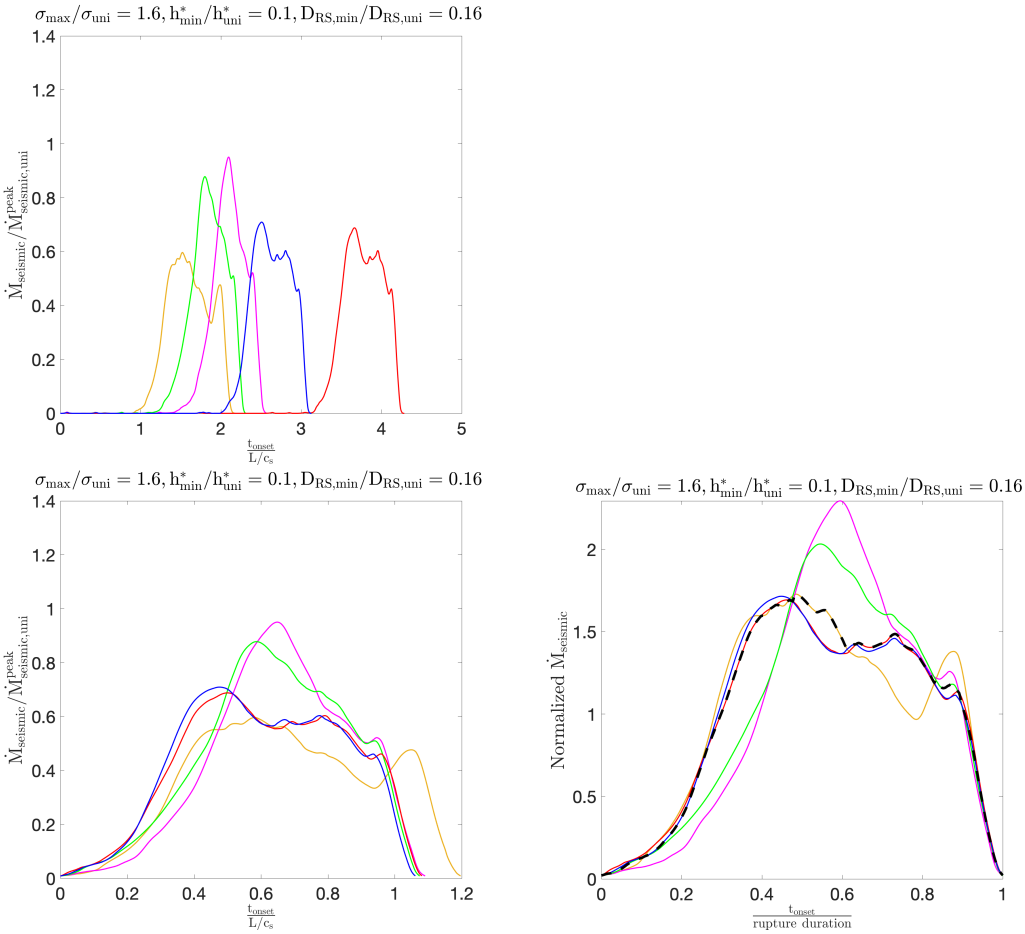

Figure 4.25: STFs from $\sigma_{max}/\sigma_{uni} = 1.6$, $D_{RS,min}/D_{RS,uni} = 0.16$ model. Same plotting conventions as Figure 4.12.

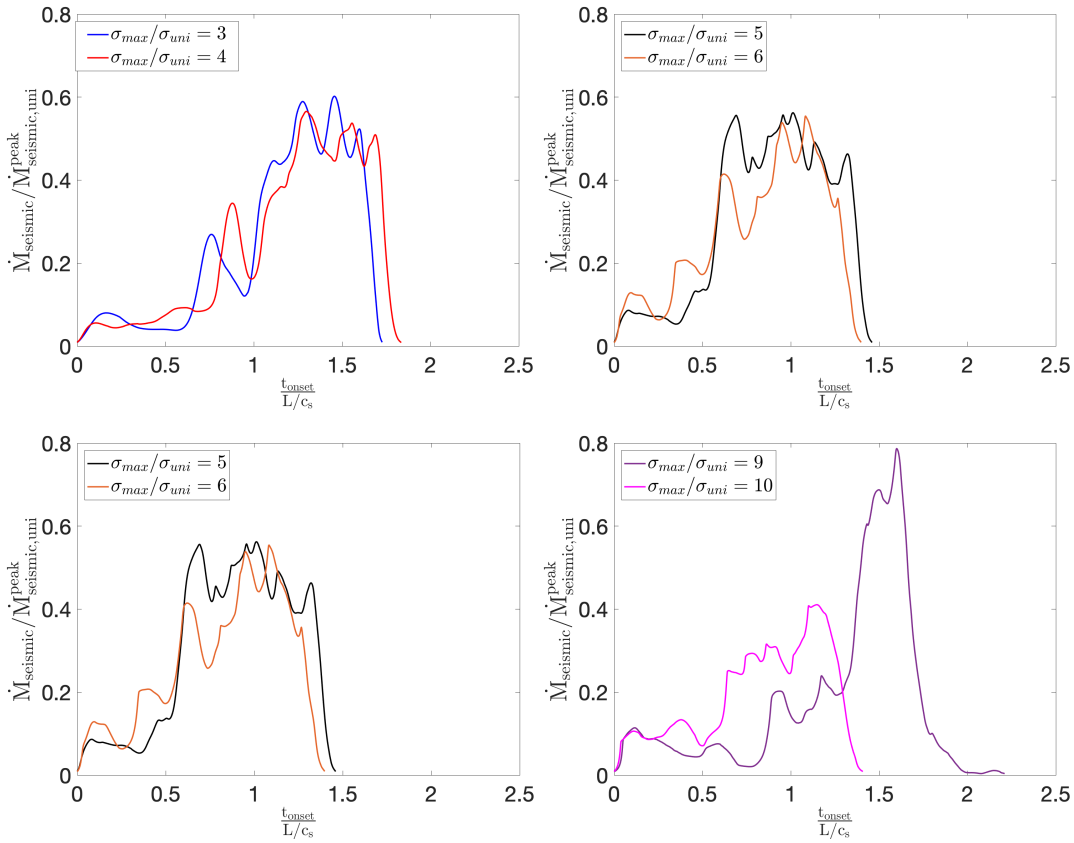

Figure 4.26: Events with hesitant initial moment-rate release in models across normal-stress heterogeneity levels. The events are identified here using moment-rate threshold. This draws parallels to STFs of natural events from Ellsworth and Beroza (1995) shown in Figure 1.5.

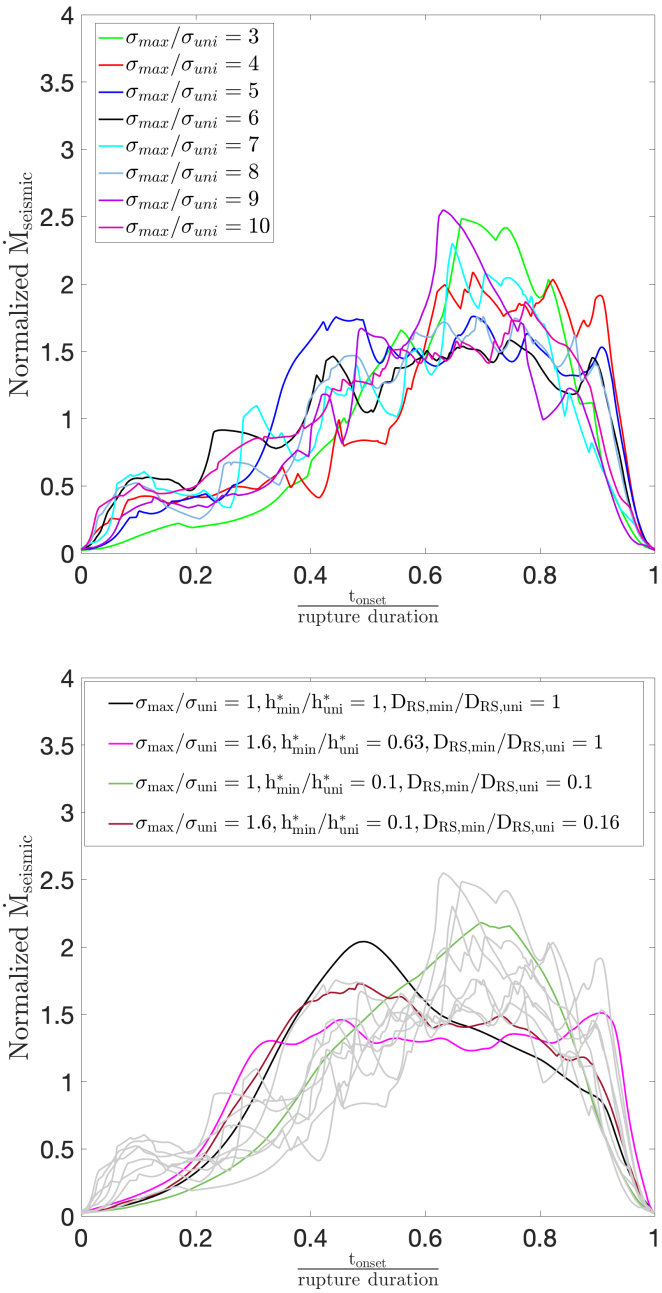

Figure 4.27: Comparison of the median STFs (with the seismic moments normalized to unity) for events in different models. (Top) Models with modified fractal normal-stress distributions and $\sigma_{max}/\sigma_{uni} = 3, 4, 5, 6, 7, 8, 9, 10$. The median STFs are all similar, despite the differences between individual events and different models. (Bottom) Median STFs for the uniform model ($\sigma_{max}/\sigma_{uni} = 1$) and the model with the fractal stress ($\sigma_{max}/\sigma_{uni} = 1.6$) have different shapes.

In Figure 4.27, we superimpose the median STFs from different models. For the models with significant normal stress heterogeneity, $\sigma_{max}/\sigma_{uni} = 3, 4, 5, 6, 7, 8, 9, 10$, we observe that, even with all the variation in the shape and duration of the individual STFs, the median source time functions collapse within the same band in this normalized scale. This supports the conclusions from the study of Meier et al. (2017) that STFs are remarkably similar when considered in this median and normalized fashion. The median normalized STF of the models with the uniform normal stress and with fractal normal stress have different shapes. Curiously, the median normalized STF of the model with the uniform normal stress and modified D_{RS} almost exactly follows the trend of the STFs from models with significant normal-stress heterogeneity, highlighting the fact that similar median normalized STF shapes can result from completely different fault models and rupture dynamics.

The universal STF shape in Meier et al. (2017) reaches its peak at about 45% of the rupture duration, whereas the median STFs for our models with normal-stress heterogeneity levels reach their peak between $0.6 - 0.8$ of the rupture duration (Figure 4.27). One reason for the discrepancy could be unrealistic rupture arrest in our models. Most of the large-scale events in the models arrest rather abruptly in the VS barrier region, and not because they encounter unfavorable stressing conditions and lose steam gradually. As a trivial thought exercise (Figure 4.28), the simplified median STF from our simulations, with peak moment rate reached at 70% of rupture duration (red lines) is modified to have its peak at the 45% of the new rupture duration, assuming more gradual arrest (black dashed line). This modified STF, when re-normalized to the duration and area of 1 (blue line), assumes the shape of median STF for natural events from Meier et al. (2017). This exercise suggests that the arrest of the events in our models is unrealistically abrupt compared to natural events, or at least to their median normalized representation. The more gradual arrest in our models can be achieved by using either less strengthening VS barriers or a larger fault which can accommodate natural arrest of events by running out of prestress.

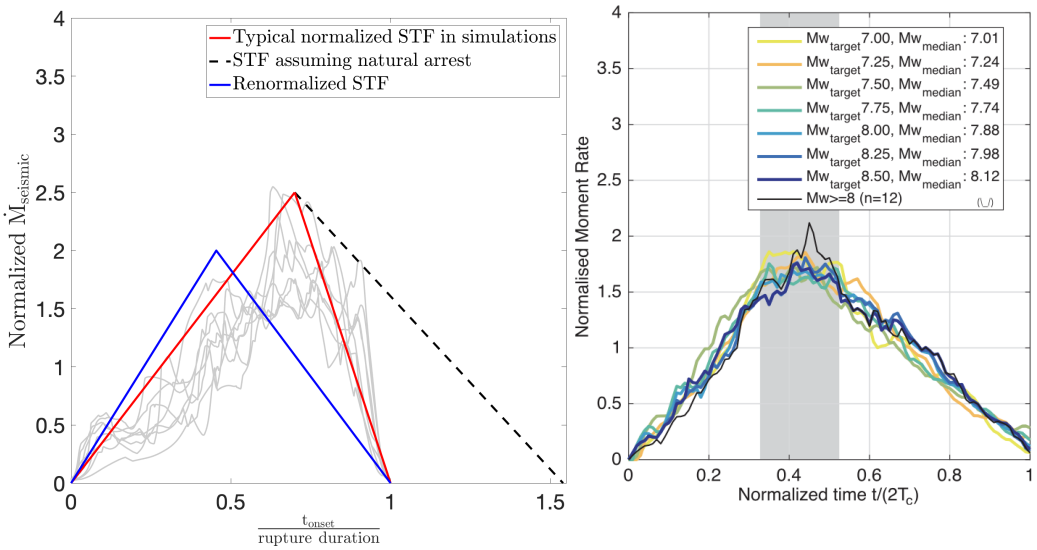

Figure 4.28: Modifying the typical median STF shape from Figure 4.27 (red line) by assuming more gradual rupture arrest (black dashed line) and renormalizing the area to 1 (blue line) results in an STF shape (left plot) comparable to that of natural events (right plot, Meier et al., 2017).

To confirm our hypothesis that the discrepancy in the median normalized STFs between some of our models and natural earthquakes is caused by unrealistically abrupt arrest, we examine the STFs of smaller-scale events. Such events arrest differently, depending on their size. The smaller the events, the less their arrest has to do with the VS barriers. We examine the smaller-scale events for the $\sigma_{max}/\sigma_{uni} = 8$ model which has almost a uniform distribution of event sizes (Figure 4.5). In addition to the larger-scale event size range of $\log_{10}(M_o/\bar{M}_{o,uniform}) \in [-0.2, 0]$ already plotted in Figure 4.21, we select five events from three more size ranges of $\log_{10}(M_o/\bar{M}_{o,uniform}) \in [-0.7, -0.5], [-1.5, -1.4], [-2.3, -2.1]$ (Figures 4.29-4.31). The median STFs from each event-size range are plotted in Figure 4.32. Plotting slip velocity snapshots of a typical event in each size range illustrates the rupture area of these events and the constraints of the model geometry on them (Figure 4.33).

We observe different shapes of the STFs for the different event sizes, with more gradual arrest of events of the smaller size, as expected (top plot, Figure 4.32. The events in the bottom two size ranges are least affected by the geometry of the fault model and arrest gradually. The events in the top two size ranges ($\log_{10}(M_o/\bar{M}_{o,uniform}) \in [-0.7, -0.5], [-0.2, 0]$) hit the width of the fault and complexities emerge. The events in the intermediate size range $\log_{10}(M_o/\bar{M}_{o,uniform}) \in [-0.7, -0.5]$, indicated by the purple STF, arrest soon after the complex phase, whereas the com-

plexity resembles a hesitant initiation phase for the larger-scale events characterized by the blue STF. The median STFs for the smallest-scale events (bottom plot, Figure 4.32, which arrest mostly because of insufficient prestress, have remarkably similar overall shape to Figure 4.28. As the events grow larger in size, their propagation and arrest are more and more affected by the finite width and length of the VW fault and the properties of the surrounding VS barrier. This supports our hypothesis that, to reproduce the median STF shape based on observations, we need to facilitate more gradual arrest of our larger-scale events.

Remarkably, the median STFs of events across different size ranges initially grow at similar rates and are quite similar (top plot, Figure 4.32). The takeaway from this plot is that one cannot tell the eventual size of the earthquake just by observing the initial phase. The STFs indicate that large events are small events that ran away, which was also the conclusion by observing the nucleation processes of larger-scale and small-scale events in the previous chapter. Interestingly, the results are different in the case of models where small and large events nucleate from substantially different scales, such as our models with minimal variation in normal stress and D_{RS} modified to preserve a large variation in nucleation size distribution. The initial rates of events from size ranges $\log_{10}(\mathrm{M_o}/\bar{\mathrm{M}}_{\mathrm{o,uniform}}) \in [-5.6, -4.8], [-4.2, -3.6], [-0.2, 0]$ from the model with $\frac{\sigma_{\mathrm{max}}}{\sigma_{\mathrm{uni}}} = 1$, $\frac{\mathrm{D_{RS,min}}}{\mathrm{D_{RS,uni}}} = 0.1$ are seen to be starkly different (Figure 4.34).

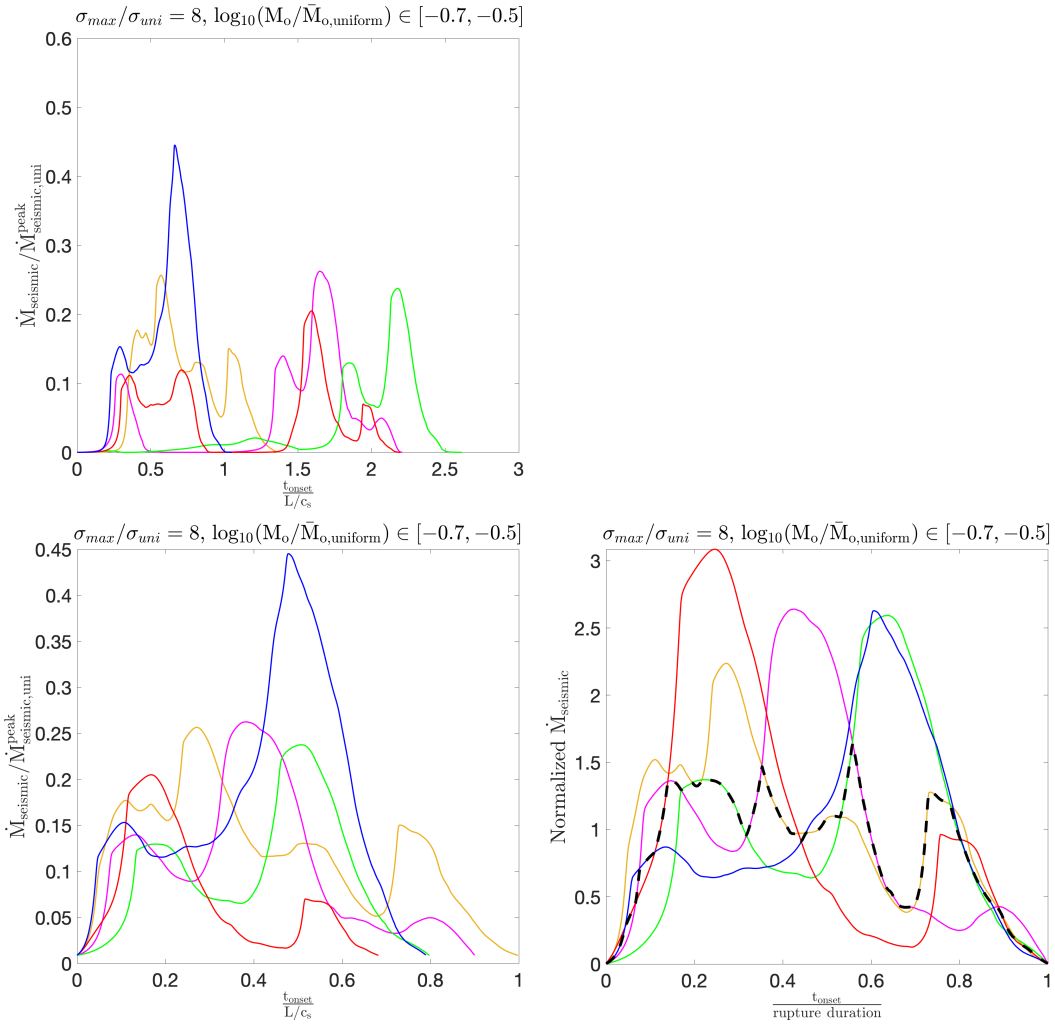

Figure 4.29: STFs from $\sigma_{max}/\sigma_{uni} = 8$ model in the event size range $\log_{10}(\mathrm{M_o}/\bar{\mathrm{M}}_{\mathrm{o,uniform}}) \in [-0.7, -0.5]$. Same plotting conventions as Figure 4.12.

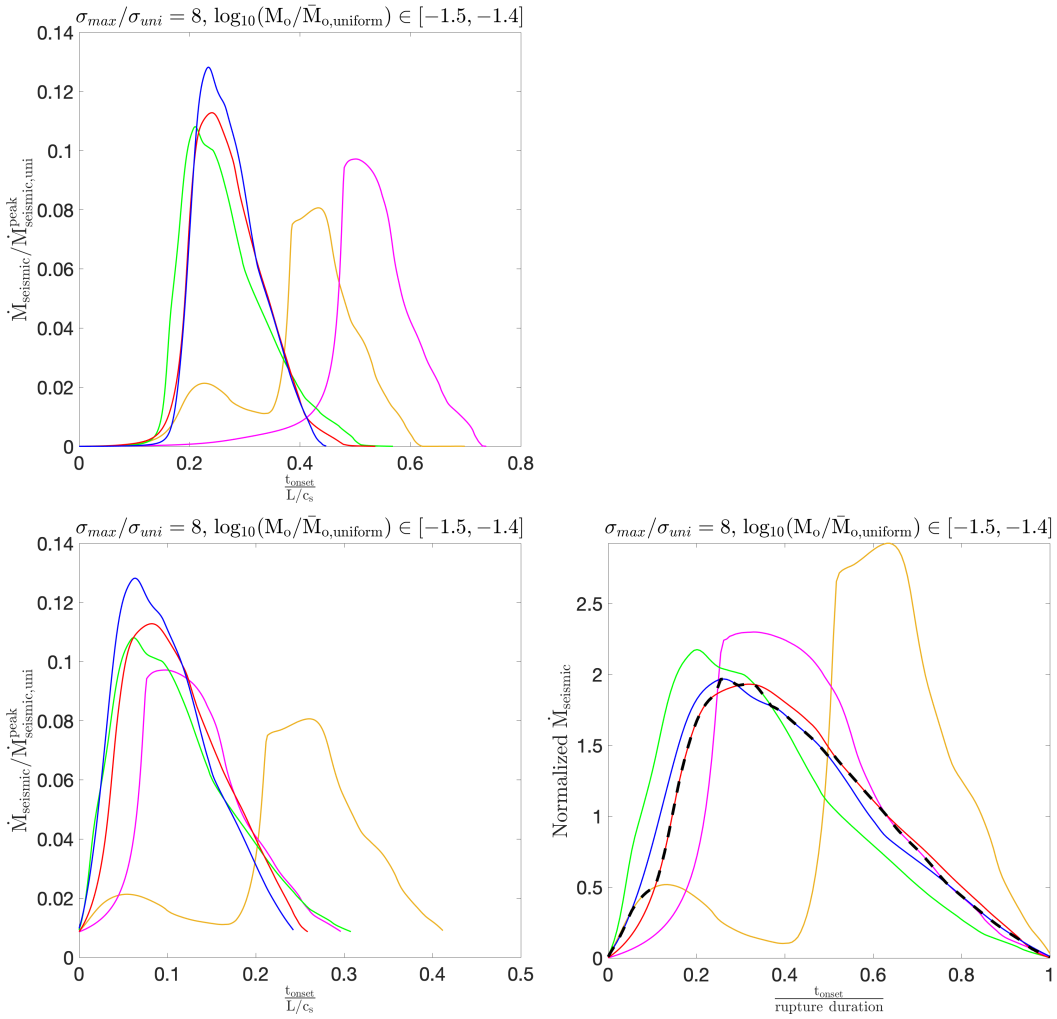

Figure 4.30: STFs from $\sigma_{max}/\sigma_{uni} = 8$ model in the event size range $\log_{10}(\mathrm{M_o}/\bar{\mathrm{M}}_{\mathrm{o,uniform}}) \in [-1.5, -1.4]$. Same plotting conventions as Figure 4.12.

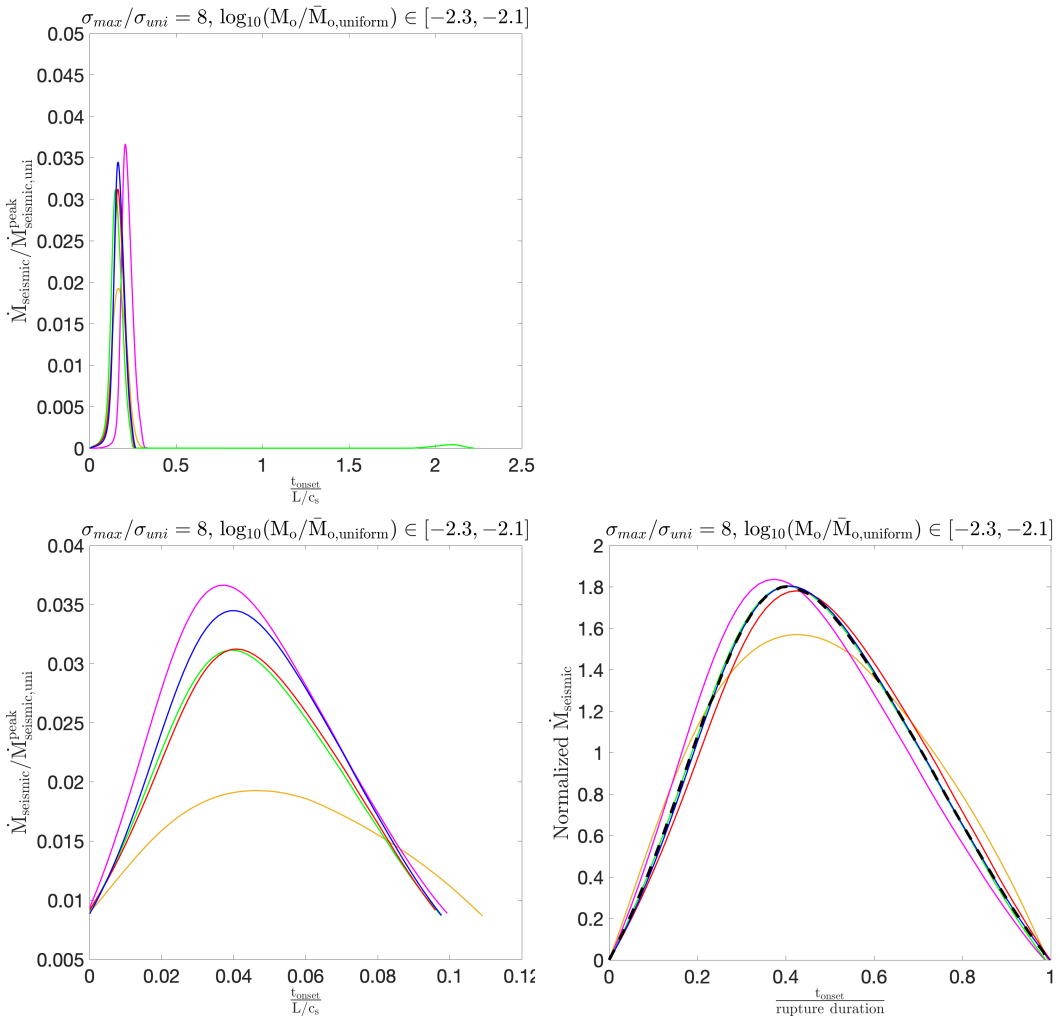

Figure 4.31: STFs from $\sigma_{max}/\sigma_{uni} = 8$ model in the event size range $\log_{10}(\mathrm{M_o}/\bar{\mathrm{M}}_{\mathrm{o,uniform}}) \in [-2.3, -2.1]$. Same plotting conventions as Figure 4.12.

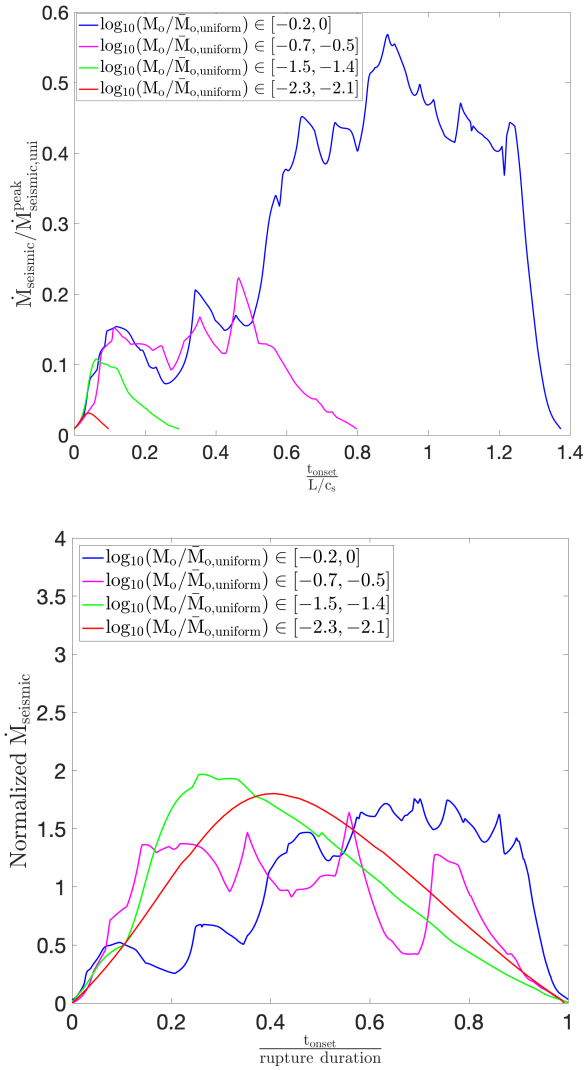

Figure 4.32: Median STFs across different event size ranges from the $\sigma_{max}/\sigma_{uni} = 8$ model. (Top) Event duration is normalized by the time for the shear wave to propagate through the fault length while the moment rate is normalized by the peak moment rate from the uniform model. The STFs indicate that large events are small events that ran away. (Bottom) Event duration and moment are both normalized to 1. The smallest-scale event (shown in red) is least affected by the model dimensions and has the shape comparable to the typical behavior of natural earthquakes (Figure 1.6).

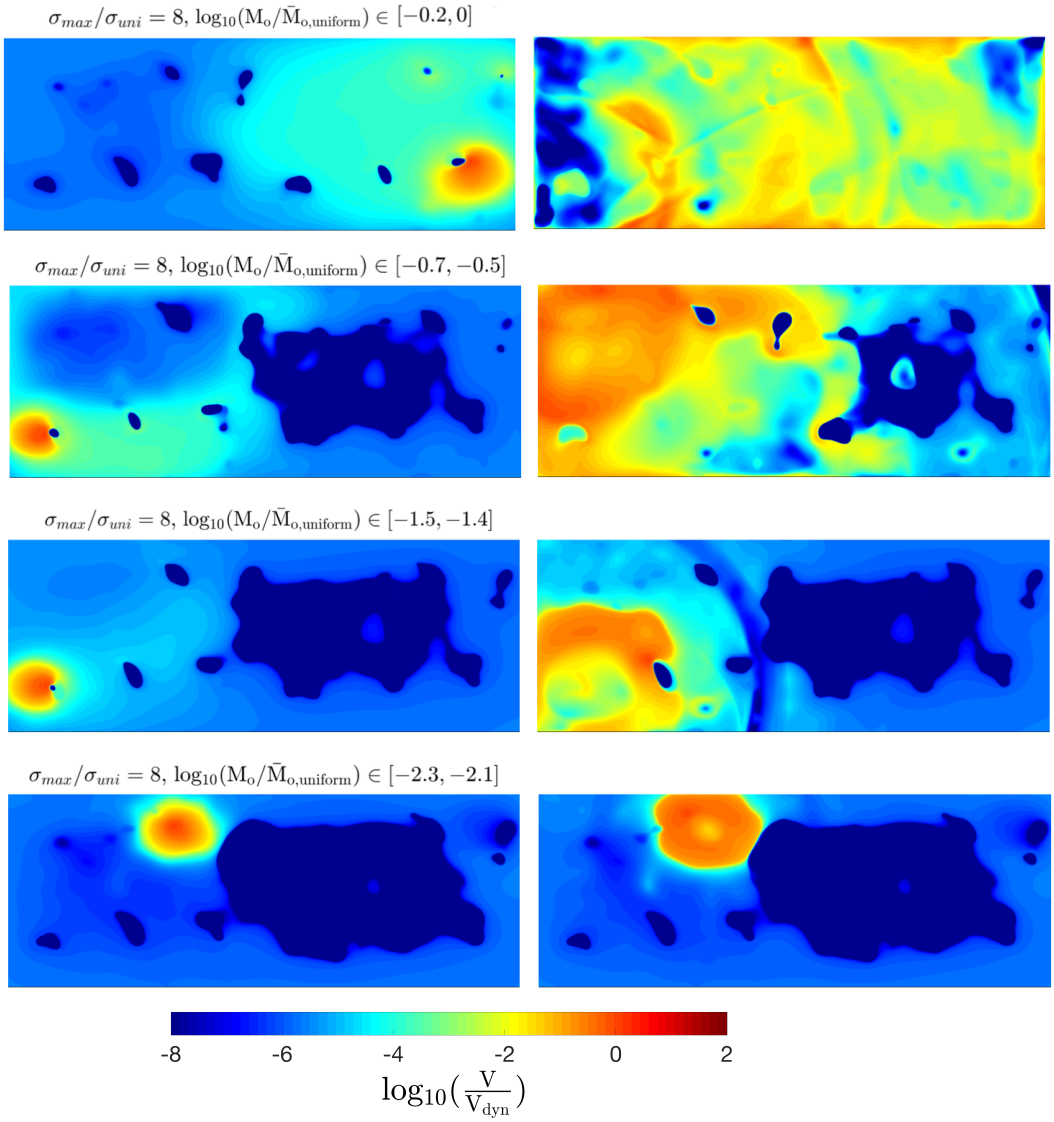

Figure 4.33: Slip velocity snapshots from the model with $\sigma_{max}/\sigma_{uni} = 8$ illustrating the beginning and end of a typical event from the different event-size ranges considered. The snapshots help visualize the rupture area of the events in each size range and how their dynamic propagation is affected by the finite geometry of the seismogenic region.

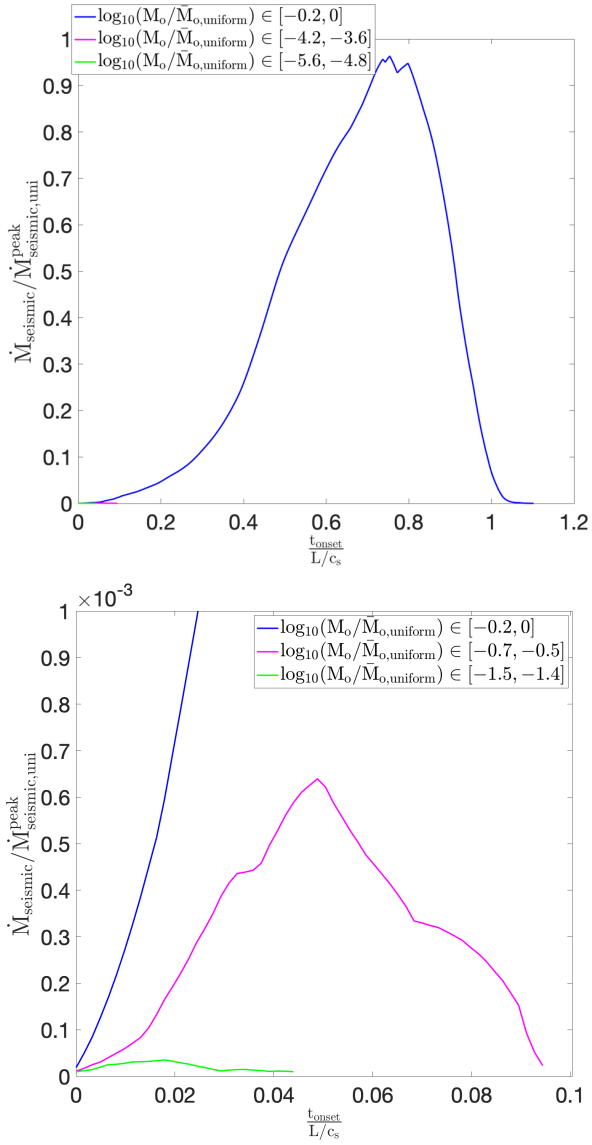

Figure 4.34: (Top) Median STFs across different event size ranges from the $\frac{\sigma_{max}}{\sigma_{uni}} = 1, \frac{D_{RS,min}}{D_{RS,uni}} = 0.1$ model. Event duration is normalized by the time for the shear wave to propagate through the fault length while the moment rate is normalized by the peak moment rate from the uniform model. Note that the small-scale events are so small that their median STFs are barely visible relative to the large-scale event. (Bottom) The initial rates of the median STFs across the size ranges are observed in a zoomed-in version. The median STF of the large event grows much faster initially than the much smaller events from the same model.

Identifying dynamic events: slip-velocity threshold and variability of events within the same model

To quantify simulated patterns of fault slip, one needs to use thresholding criteria which delineate aseismic versus seismic slip. In the numerical simulations in this thesis, a slip-velocity threshold is chosen, as typically done in numerical modeling. The value of the threshold depends on the frictional properties of the fault interface.

However, the analysis of the STFs of multiple events from the same model (Figure 4.16—4.25) highlights the problematic nature of using a slip-velocity threshold in simulations on heterogeneous interfaces. On relatively homogeneous interfaces, reaching a certain, relatively high, slip rate, signifies that slip acceleration to instability is ongoing and the dynamic rupture propagation is imminent, and the exact value of the slip-rate threshold may not matter much. On heterogeneous interfaces like the ones considered in this work, a small foreshock-like event may elevate slip rates over a part of the larger-scale nucleation zone when the main nucleation process is not yet in its final accelerating phase. That would result in a significant time delay between the slip-velocity threshold being reached and dynamic rupture propagation occurring, resulting in various artificial outcomes, such as excessively long event durations. For this reason, the STFs generated using slip-velocity threshold can temporally translate otherwise similar-looking events within the same models.

An interesting example of this phenomenon is an event STF from $\sigma_{max}/\sigma_{uni} = 7$ model (Figure 4.20, plotted in red). Observing this event in isolation, we see clearly separated small-scale events preceding the eventual larger-scale event (Figure 4.35). Using slip-velocity threshold, the entire sequence is classified as a single larger-scale dynamic event. These small-scale precursors are separated by dynamic time scales, yet their rupture durations are smaller than the separation time scale, hence it is apparent that this is not one dynamic event. The precursors are close in space and time and building up towards the nucleation of the dynamic event, making them a classic cascading sequence of foreshock-like events preceding the mainshock. Sequences like this can be used to draw comparisons to and study properties of the hesitant initiation phase, termed as seismic nucleation phase from Ellsworth and Beroza (1995), seen in Figure 1.5. The slip velocity snapshots corresponding to the event are plotted in Figure 4.36, 4.37. The same snapshots are plotted in a different color scale, which emphasizes the triggering process by only considering the velocities two orders below and above dynamic velocity threshold ($\sim 10^{-4} - 1$ m/s) in Figure 4.38, 4.39.

There is a wide variation in the type of larger-scale events occurring at this level of heterogeneity. The time history of the maximum slip velocity between these five mainshocks considered for construction of STFs from the $\sigma_{max}/\sigma_{uni} = 7$ model shows the location of intershocks with respect to the 5 mainshocks (Figure 4.40). Out of the 8 small-scale events in this time interval, 3 occur as intershocks. The rest of the small-scale events occur as foreshock-like or aftershock-like events to the 5 mainshocks. An interesting example is the last mainshock (MS5), the STF of which is indicated in blue in Figure 4.41. There is one foreshock-like event right before the moment rate ramps up rapidly, a pattern quite different from the event shown in red (note that the foreshock-like bump becomes a separate event based on the moment-rate threshold. The history of maximum slip velocity for ~ 80 dynamic time scale units preceding the blue event demonstrates the absence of other foreshock-like events (Figure 4.42). The slip velocity snapshots for this event indicate the absence of any evident precursory behavior for this event (Figure 4.43).

This contrast between the two events demonstrates that, even on a fault with the same persisting heterogeneity, entirely different initiation of larger-scale events can occur, depending on how the interface is stressed, where the event starts, and how powerful the initial slip acceleration is.

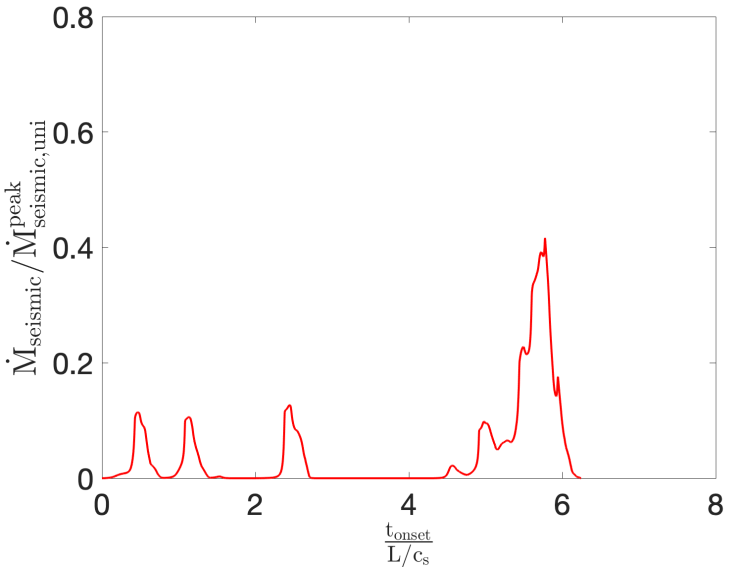

Figure 4.35: Source time function of a larger-scale event from $\sigma_{max}/\sigma_{uni} = 7$ model which shows a cascade-like sequence of small-scale ruptures preceding the larger-scale rupture. Plotted using a velocity-based threshold, the entire sequence is considered the same large-scale dynamic event.

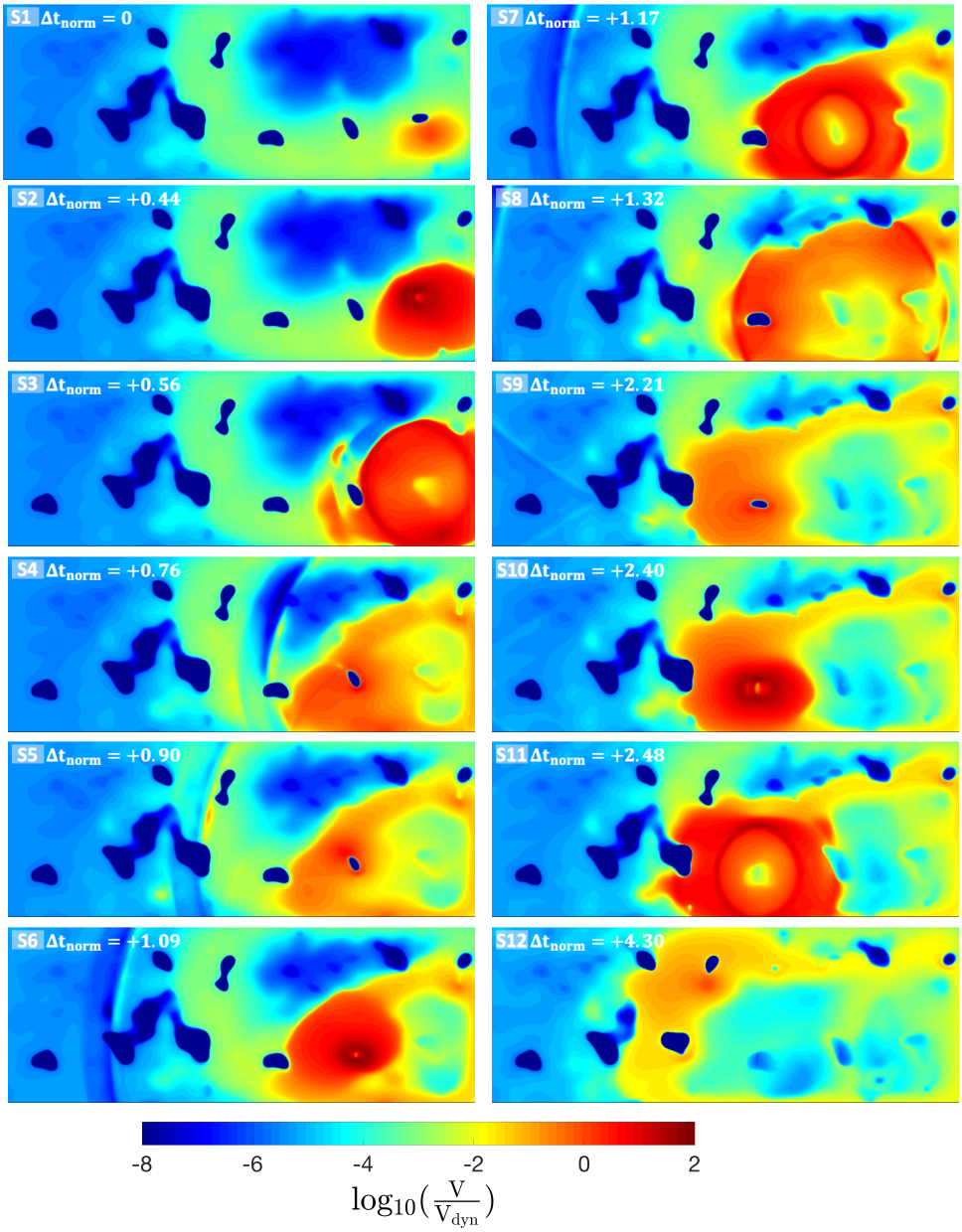

Figure 4.36: Slip velocity snapshots visualizing the large-scale event from Figure 4.35 indicate the small-scale ruptures in S1, S6, and S10 which precede the large-scale event (Continued in next figure).

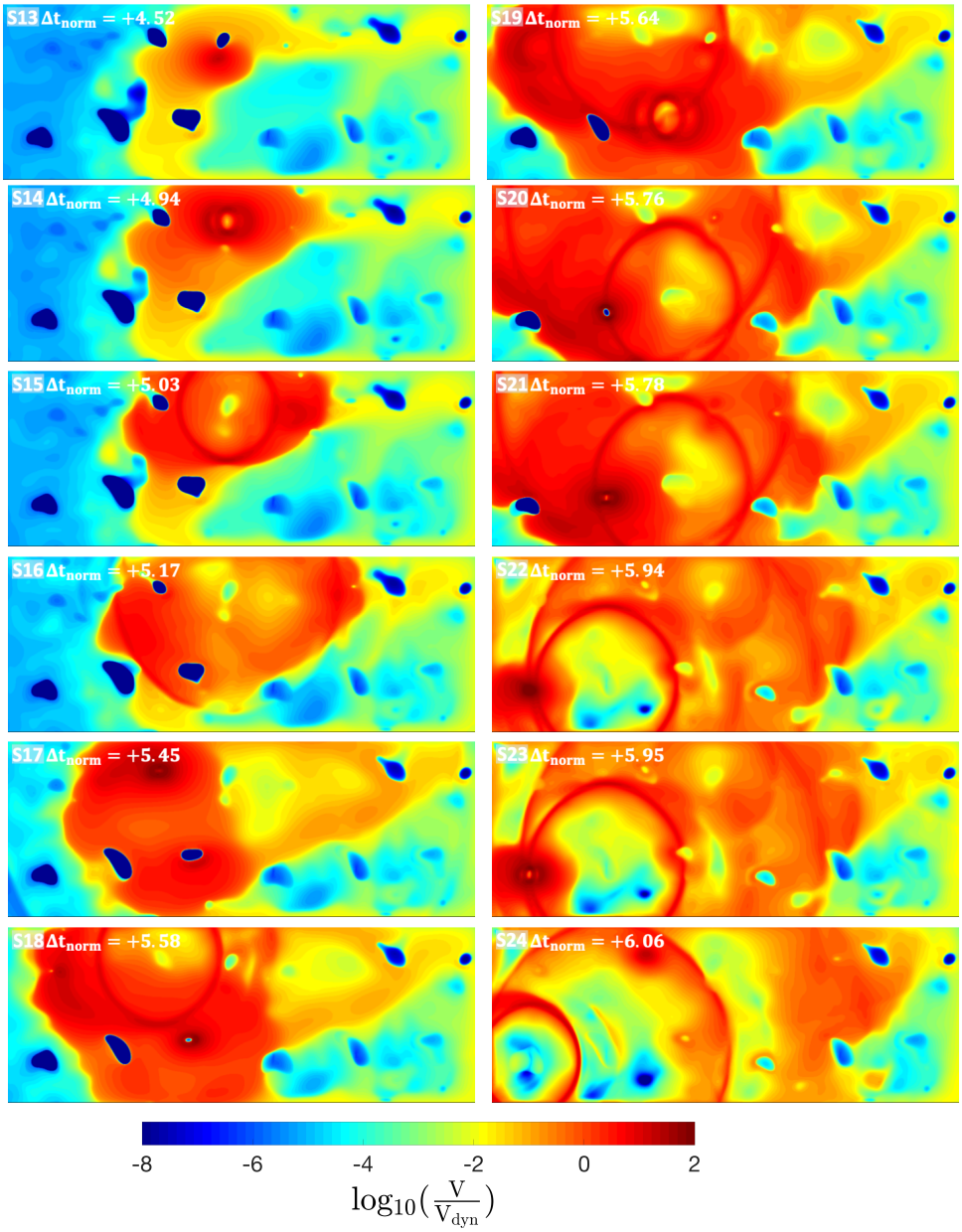

Figure 4.37: Slip velocity snapshots visualizing the large-scale event from Figure 4.35 indicate the complex rupturing and re-rupturing of asperities which build up to the large-scale event which eventually ruptures the entire interface.

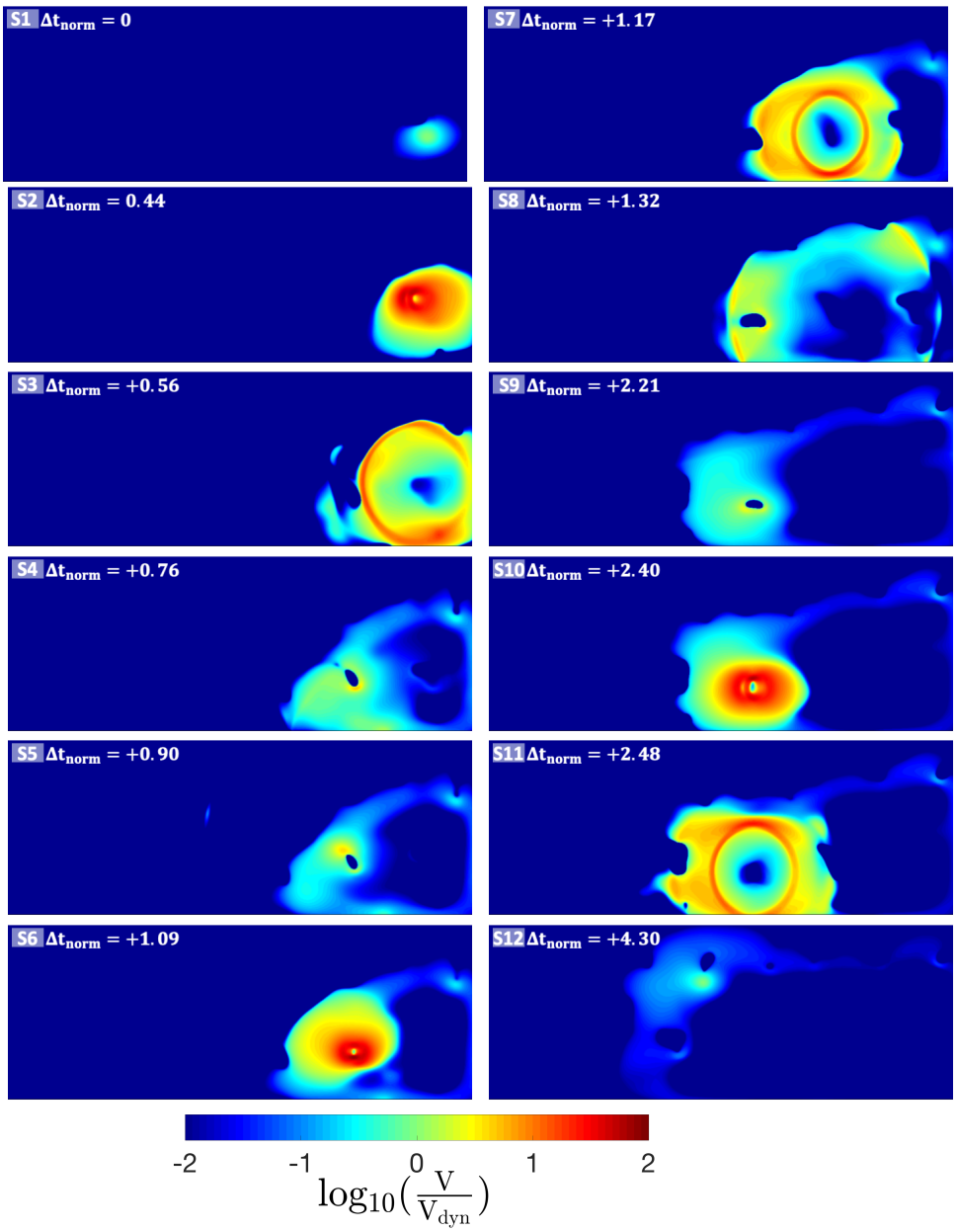

Figure 4.38: Slip velocity snapshots from Figure 4.36 plotted in a color scale that emphasizes the triggering processes of the cascade sequence preceding the large-scale event. (Continued in next figure)

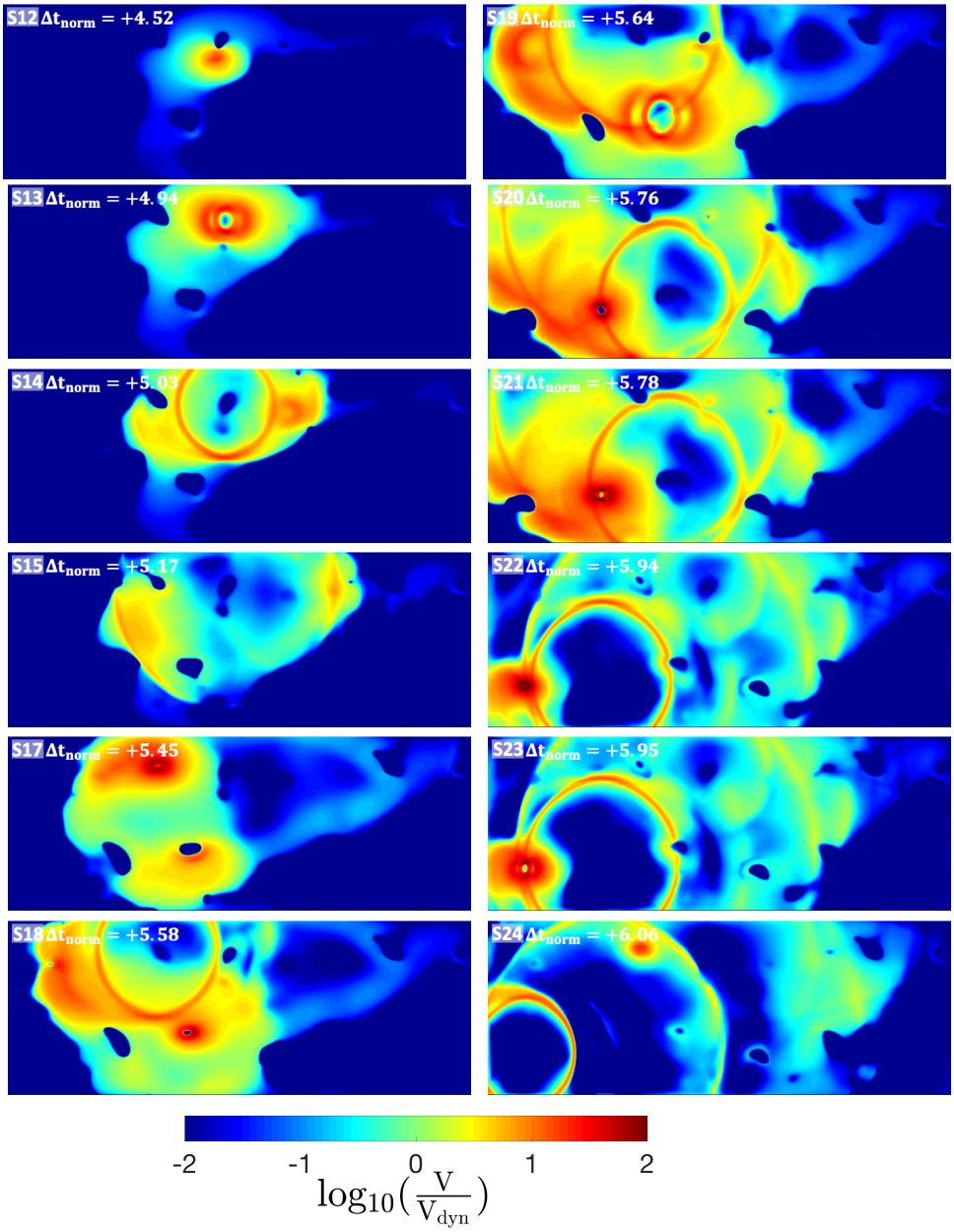

Figure 4.39: Slip velocity snapshots from Figure 4.37 plotted in a color scale that emphasizes the high frequency ruptures that accompany the large-scale event.

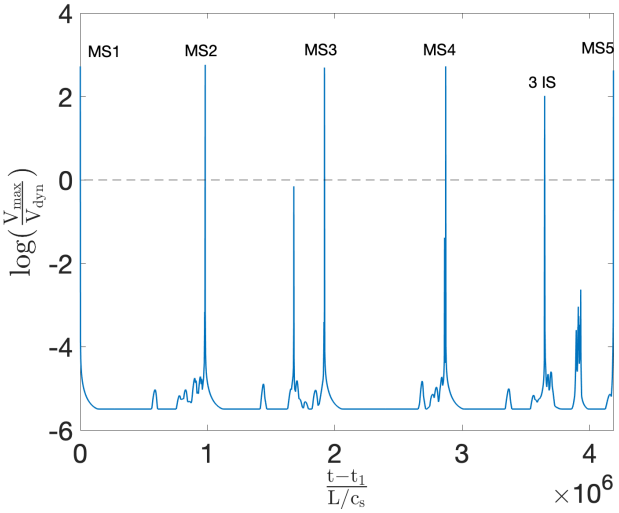

Figure 4.40: Maximum slip velocity history for the 5 mainshock cycles from $\sigma_{max}/\sigma_{uni} = 7$ model indicates the mainshocks and the location of intershocks relative to them. The rest of the small-scale events identified in this interval by the velocity threshold (8 small-scale events in total) occur as foreshock-like or aftershock-like events to the 5 mainshocks.

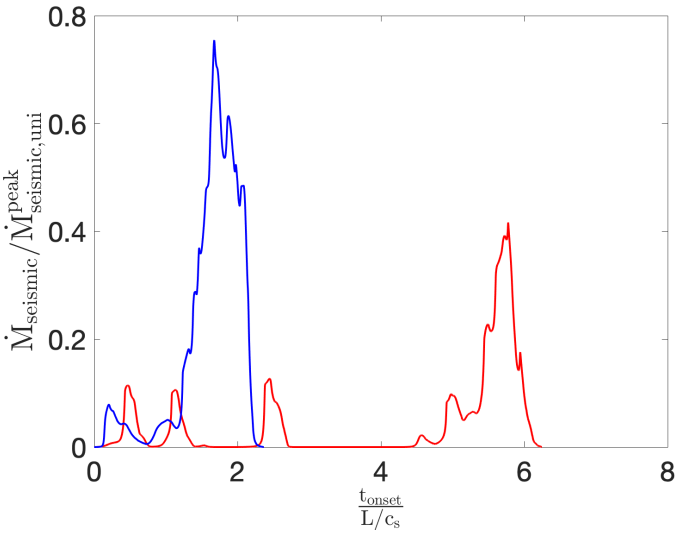

Figure 4.41: STFs of two larger-scale events from $\sigma_{max}/\sigma_{uni} = 7$ model plotted using a velocity-based threshold which shows one event (red) with a cascade-like sequence of small-scale ruptures preceding it. The second event (blue) has only a single, immediately preceding foreshock-like bump.

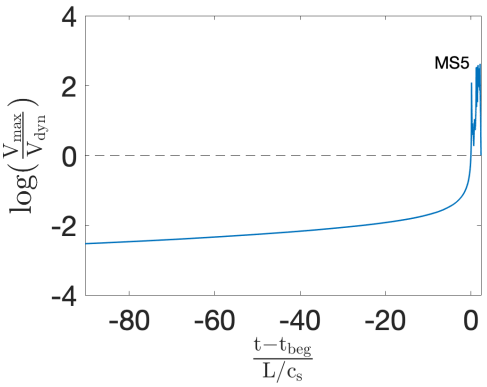

Figure 4.42: Maximum slip velocity history for the 5^{th} mainshock, indicated by the blue STF in Figure 4.41 from $\sigma_{max}/\sigma_{uni} = 7$ model during $\sim$ 80 dynamic time scale units before the beginning of the event. There are no other foreshock-like small-scale events preceding it.

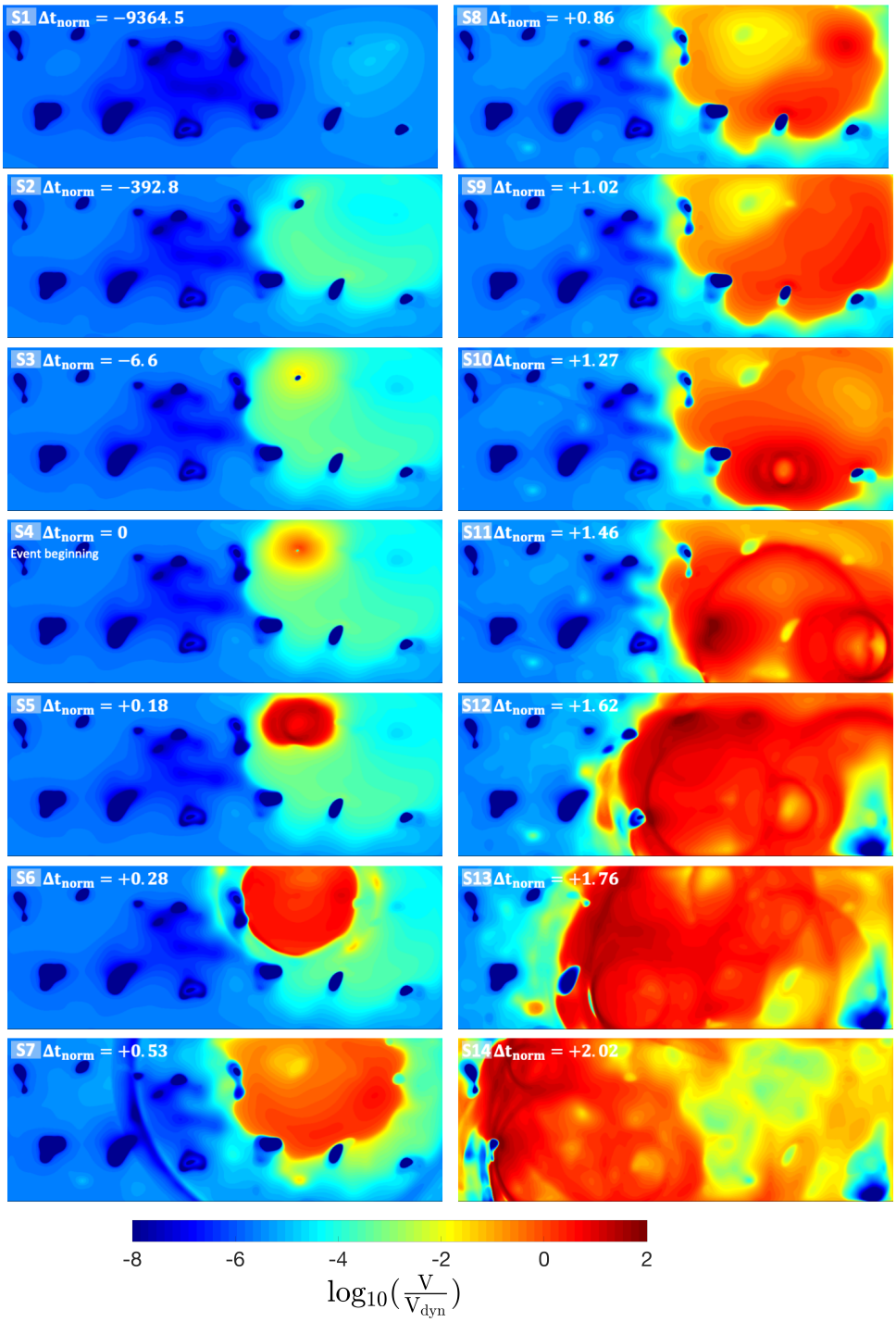

Figure 4.43: Slip velocity snapshots visualizing the larger-scale event indicated by the blue STF from Figure 4.41. The small foreshock-like bump is indicated by snapshots S4-S7, right before the moment rate builds up rapidly from S8.

4.3 Conclusions

With systematic increase in heterogeneity, we observe growing complexity in slip behavior, revealed by variation in large-scale event sizes, appearance of small-scale events, changing b-values, and complexity in shapes of source-time functions. Increasing normal stress heterogeneity by enhancing the asperity peaks leads to increasing complexity of large events and appearance of small events. Modifying D_{RS} whilst preserving heterogeneity in nucleation sizes results in a larger fraction of smallest-scale events, yet this does not have significant effect on large-event sizes. The static stress drops are remarkably similar across all our models, with median stress drops in models with significantly different normal stress heterogeneity levels increasing only marginally, by $\sim$ 20%. The larger-scale event recurrence time is another quantity that remains more or less comparable across normal stress heterogeneity levels as well as with modified D_{RS}. The b-values systematically increase with increasing normal stress heterogeneity until about $\sigma_{max}/\sigma_{uni} = 8$ and then fluctuate within a range.

Quantifying larger-scale ruptures using STFs shows increasing complexity in the STF shape and rupture duration with increasing normal stress heterogeneity. We can observe more reluctant initial moment release in many events across models as observed for natural events in Ellsworth and Beroza (1995), although our study does not produce events of sufficiently different sizes to study whether there is any relation between the duration of this reluctant release and the eventual event size. The construction of STFs using both slip-velocity and moment-rate threshold reveals that using a moment-rate threshold makes more sense seismologically. The shape of the STFs produced in our models are found to depend on multiple factors: where the event is nucleated with respect to the fault dimensions, how powerful the initial slip acceleration is, and the event size. Comparing the STFs of events from our models to natural observations, it is clear that natural events arrest more gradually, without clear geometric boundaries. The events from our models which exhibit the best match with the typical STF shape from natural observations are the smallest-scale events which are least affected by the finite width and length of the VW, seismogenic fault region. Therefore, to match natural observations, the arresting mechanisms employed in our models should facilitate the gradual arrest of the larger-scale events. This could be achieved by simulating large enough faults, or by having smooth transitions between VW and VS with velocity-neutral (VN) areas etc.

The comparison of two larger-scale events from a model with the same heterogeneity shows that, at different times on the same fault, larger-scale events can occur either with clear sequence of cascade-like foreshocks or with hardly any obvious foreshock-like events preceding them. So foreshocks may or may not reliably occur even on the faults where they have been previously observed. Furthermore, the absence of clear foreshocks for a given event may indicate that the fault is not heterogeneous enough or may be specific to the dynamics of the system at that instant of time even on a highly heterogeneous fault. The situation would be even more complex in the presence of evolving fault heterogeneity, i.e., due to fluid flow.

In our models with significant normal-stress heterogeneity, plotting source-time functions across different event-size ranges in the same fault model shows remarkably similar initial growth rate of differently-sized events, which suggests that one cannot tell the eventual size of the earthquake just by observing the initial phase. In both the study of nucleation processes in Chapter 3 and the source time functions in this chapter, our models with significant normal-stress heterogeneity indicate that large events are small events that ran away. The results are different for the models where small events and large events nucleate from substantially different scales, such as in our model with uniform normal stress but significant variability in the nucleation size achieved through the modified characteristic slip distance. In such models, the initial growth rates of the events of different sizes are significantly different. These qualitatively different behaviors of models with the same heterogeneity in nucleation size achieved differently, via heterogeneity in normal stress vs. heterogeneity in characteristic slip distance, opens the possibility of distinguishing the nature of heterogeneity on natural faults.

Chapter 5

CONCLUSIONS AND FUTURE WORK

This work investigates the link between heterogeneity in fault properties and different aspects of slip behavior on fault interfaces by conducting numerical simulations of long-term slip histories on heterogeneous frictional interfaces.

We begin by exploring how irregular fault geometry affects the variability in repeating sequences, by investigating a specific example of SF- LA repeating earthquakes in the Parkfield segment of San Andreas Fault. Our models reproduce many observations about the SF-LA repeating sequences, including their mean moment, mean recurrence times, stress drops, the observed non-trivial scaling between the seismic moment and recurrence times of the repeaters, the ranges of variability in moment and recurrence time, and the ranges of triggering times between the two sequences. We find that multiple models fit the data within reasonable ranges. The first is a model with complex source patch shapes and the other with simple circular source patch shapes within a velocity strengthening area that is more compliant. This implies the existence of infinitely many models generated by changing the shapes of repeating patches and varying the velocity strengthening nature of the surrounding area which can potentially match the observed variability and interactions of the repeaters. We also explore the impact of small-scale heterogeneity on the system response, and found that smoothing the distribution over scales smaller than length scales relevant to the system preserves key characteristics of the system. The slip behavior however changes qualitatively when features on the scale of relevant length scales are eliminated.

A conceptual understanding gained from this work is the infeasibility of incorporating individual variations in different type of heterogeneities in numerical models to match observations. There are many ways to add heterogeneity in fault properties and when calibrating with observations, distinguishing between the different kinds of heterogeneities can be challenging since different features in the model trade off, even to create long-term response. This highlights the importance of laboratory experiments and theoretical studies to better the understanding of connections between different fault properties. For example, regions with high normal stress may have more localized shear zones and be more susceptible to velocity-weakening behavior.

These compressed areas may also have a tendency to become smoother with time, represented by lower D_{RS}. Such coupled heterogeneity distributions informed by lab experiments can make constraining fault properties using observations more tractable.

In the second study, we investigate the effect of increasing heterogeneity in normal stress on the earthquake nucleation process. We modify fractal-like distributions to systematically increase the normal stress heterogeneity on the interface and observe a continuum of behaviors ranging from purely fault-spanning events to persistent foreshock-like events between larger-scale events. In cases with stronger normal stress heterogeneity, a majority of the large-scale events nucleate from the heterogeneity scale of the compressed peaks, which is increasingly smaller than the mean nucleation size that would govern their nucleation on a uniform fault. In these cases, large-scale events are small-scale events that run away. Modifying D_{RS} to achieve low nucleation sizes in models with uniform or mild normal stress variation results in a large fraction of small-scale events driven by the larger-scale quasi-static nucleation processes. These small-scale events do not appear to have much impact on the nucleation sizes of the large-scale events.

The final work presented in this thesis investigates the effect of increasing heterogeneity in normal stress on complexity in sequences and features of dynamic ruptures using the same models from Chapter 3. The complexity in slip behavior with systematic increase in heterogeneity is manifested as variation in large-scale event sizes, appearance of small-scale events, changing b-values and complexity in source-time functions. Quantifying the complexity of larger-scale ruptures using source-time functions shows increasing complexity in the shape and rupture duration with increasing normal stress heterogeneity. We observe prolonged initiation phases in models, similar to some observations, once realistic heterogeneity in normal stress is incorporated. The shape of the source time functions produced in our models are found to depend on multiple factors; the location of event initiation, how powerful the initial rupturing of an asperity is, how the interface is stressed at that time instant and the model geometry. The construction of source time functions using both velocity and moment rate thresholds for event identification reveals that using a moment rate threshold might make more sense seismologically. Source-time functions plotted across different event size ranges from a model with strong normal stress heterogeneity show similar initial growth rates. This re-emphasizes the conclusion from the study of nucleation processes from Chapter 3 that in models

with strong normal stress heterogeneity, larger-scale events are small-scale events that ran away.

A lot can be learnt from source time functions regarding how well the numerical fault model represents real faults. Any kind of geometric constraint on event arrest makes the source time functions from our models deviate from the average STFs of natural earthquakes. This suggests that generally earthquakes on real faults arrest gradually, and not by running into abrupt barriers. To match natural observations, the arresting mechanisms employed in our models should facilitate the gradual arrest of the largest-scale events.

An important point to highlight is that all the complex slip behaviors generated in our fault models are consistent with the idea that the system is driven by larger-scale quasi-static (slow) slip. The observed complexity in slip behavior in our heterogeneous fault models, such as small-scale events, larger-scale events nucleating from asperity scales, cascade-like sequences of foreshocks triggering each other prior to a mainshock etc., are ultimately manifestations of the background quasi-static slip loading the asperity spots and allowing them to accelerate to fast slip rates. In some cases, the aseismic slip is negligible compared to the resulting seismic signatures, which may lead to the observational conclusion that the seismic events are triggering each other without any aseismic slip.

There are many interesting possibilities to continue the analysis conducted in the last two chapters. In this study, we have considered models with mild or uniform normal stress distribution and modified D_{RS} to achieve nucleation sizes corresponding to the strongest normal stress heterogeneity. Comparing the responses from these modified D_{RS} models to the strongest normal heterogeneity model has revealed quite a difference in behaviors, opening the possibility of quantifying the nature of fault heterogeneity by matching its behavior. It would be worthwhile to systematically study the effect of modifying different aspects of friction properties to map out the resulting behaviors and compare them to observations. In this work, we have considered the effect of increasing normal stress heterogeneity on properties of source time functions and frequency moment distributions. The effect of the systematic change in heterogeneity on other observables like radiated energy and its frequency content would be of particular interest to seismologists. Additionally, the models considered in the analyses in Chapter 3 and 4 do not consider fluid or thermal effects. On natural faults, highly-localized shear deformation in the presence of fluids can lead to additional dynamic weakening of friction due to mechanisms like thermal

pressurization of pore fluids and flash heating being activated (Rice, 2006). An interesting future study would be to incorporate this additional effect of enhanced dynamic weakening on heterogeneous faults, to study its effects.

BIBLIOGRAPHY

Abercrombie, R. E. (2014). Stress drops of repeating earthquakes on the San Andreas fault at Parkfield. *Geophysical Research Letters* 41.24, pp. 8784–8791.

Abercrombie, R. E., and Mori, J. (1996). Occurrence patterns of foreshocks to large earthquakes in the western United States. *Nature* 381.6580, pp. 303–307.

Abercrombie, R., and Leary, P. (1993). Source parameters of small earthquakes recorded at 2.5 km depth, Cajon Pass, southern California: Implications for earthquake scaling. *Geophysical Research Letters* 20.14, pp. 1511–1514.

Aki, Keiiti (1965). Maximum likelihood estimate of b in the formula log N= a-bM and its confidence limits. *Bull. Earthq. Res. Inst., Tokyo Univ.* 43, pp. 237–239.

Allmann, B. P., and Shearer, P. M. (2007). Spatial and temporal stress drop variations in small earthquakes near Parkfield, California. *Journal of Geophysical Research: Solid Earth* 112.B4.

Allmann, B. P., and Shearer, P. M. (2009). Global variations of stress drop for moderate to large earthquakes. *Journal of Geophysical Research: Solid Earth* 114.B1.

Anderson, E. M. (1951). The Dynamics of Faulting, Etc.(Revised.). Edinburgh, London.

Avouac, J. P. (2015). From geodetic imaging of seismic and aseismic fault slip to dynamic modeling of the seismic cycle. *Annual Review of Earth and Planetary Sciences* 43, pp. 233–271.

Baltay, A. et al. (2011). Variability in earthquake stress drop and apparent stress. *Geophysical Research Letters* 38.6.

Beeler, N. M., Lockner, D. L., and Hickman, S. H. (2001). A simple stick-slip and creep-slip model for repeating earthquakes and its implication for microearthquakes at Parkfield. *Bulletin of the Seismological Society of America* 91.6, pp. 1797–1804.

Bouchon, M., and Karabulut, H. (2008). The aftershock signature of supershear earthquakes. *Science* 320.5881, pp. 1323–1325.

Bouchon, M. et al. (2011). Extended nucleation of the 1999 Mw 7.6 Izmit earthquake. *Science* 331.6019, pp. 877–880.

Bouchon, M. et al. (2013). The long precursory phase of most large interplate earthquakes. *Nature Geoscience* 6.4, pp. 299–302.

Brodsky, E. E., and Lay, T. (2014). Recognizing foreshocks from the 1 April 2014 Chile earthquake. *Science* 344.6185, pp. 700–702.

Brodsky, E. E. et al. (2011). Faults smooth gradually as a function of slip. *Earth and Planetary Science Letters* 302.1-2, pp. 185–193.

Brown, S. R., and Scholz, C. H. (1985). Broad bandwidth study of the topography of natural rock surfaces. *Journal of Geophysical Research: Solid Earth* 90.B14, pp. 12575–12582.

Bufe, C. G., Harsh, P. W., and Burford, R. O. (1977). Steady-state seismic slip–A precise recurrence model. *Geophysical Research Letters* 4.2, pp. 91–94.

Bürgmann, R. (2018). The geophysics, geology and mechanics of slow fault slip. *Earth and Planetary Science Letters* 495, pp. 112–134.

Bürgmann, R. et al. (2000). Earthquake potential along the northern Hayward fault, California. *Science* 289.5482, pp. 1178–1182.

Candela, T. et al. (2009). Characterization of fault roughness at various scales: Implications of three-dimensional high resolution topography measurements. *Mechanics, Structure and Evolution of Fault Zones*. Springer, pp. 1817–1851.

Candela, T. et al. (2012). Roughness of fault surfaces over nine decades of length scales. *Journal of Geophysical Research: Solid Earth* 117.B8.

Carpenter, B. M., Marone, C., and Saffer, D. M. (2011). Weakness of the San Andreas Fault revealed by samples from the active fault zone. *Nature Geoscience* 4.4, p. 251.

Chang, S. H. et al. (2013). Spatially variable fault friction derived from dynamic modeling of aseismic afterslip due to the 2004 Parkfield earthquake. *Journal of Geophysical Research: Solid Earth* 118.7, pp. 3431–3447.

Chen, K. H., Nadeau, R. M., and Rau, R. J. (2007). Towards a universal rule on the recurrence interval scaling of repeating earthquakes? *Geophysical Research Letters* 34.16.

Chen, K. H. et al. (2010). Postseismic variations in seismic moment and recurrence interval of repeating earthquakes. *Earth and Planetary Science Letters* 299.1-2, pp. 118–125.

Chen, T., and Lapusta, N. (2009). Scaling of small repeating earthquakes explained by interaction of seismic and aseismic slip in a rate and state fault model. *Journal of Geophysical Research: Solid Earth* 114.B1.

Dal Zilio, L., Lapusta, N., and Avouac, J. P. (2020). Unraveling scaling properties of slow-slip events. *Geophysical Research Letters* 47.10, e2020GL087477.

Day, S. M. et al. (2005). Comparison of finite difference and boundary integral solutions to three-dimensional spontaneous rupture. *Journal of Geophysical Research: Solid Earth* 110.B12.

Dieterich (1979). Modeling of rock friction: 1. Experimental results and constitutive equations. *Journal of Geophysical Research: Solid Earth* 84.B5, pp. 2161–2168.

Dieterich (2007). Applications of rate-and state-dependent friction to models of fault-slip and earthquake occurrence. *Treatise on Geophysics* 4, pp. 107–129.

Dieterich, J. H. (1992). Earthquake nucleation on faults with rate-and state-dependent strength. *Tectonophysics* 211.1-4, pp. 115–134.

Dodge, D. A., Beroza, G. C., and Ellsworth, W. L. (1995). Foreshock sequence of the 1992 Landers, California, earthquake and its implications for earthquake nucleation. *Journal of Geophysical Research: Solid Earth* 100.B6, pp. 9865–9880.

Dodge, D. A., Beroza, G. C., and Ellsworth, W. L. (1996). Detailed observations of California foreshock sequences: Implications for the earthquake initiation process. *Journal of Geophysical Research: Solid Earth* 101.B10, pp. 22371–22392.

Dreger, D., Nadeau, R. M., and Chung, A. (2007). Repeating earthquake finite source models: Strong asperities revealed on the San Andreas Fault. *Geophysical Research Letters* 34.23.

Dublanchet, P., Bernard, P., and Favreau, P. (2013). Interactions and triggering in a 3-D rate-and-state asperity model. *Journal of Geophysical Research: Solid Earth* 118.5, pp. 2225–2245.

Ellsworth, W. L., and Beroza, G. C. (1995). Seismic evidence for an earthquake nucleation phase. *Science* 268.5212, pp. 851–855.

Ellsworth, W. L., and Dietz, L. D. (1990). Repeating earthquakes: Characteristics and implications. *Proceedings of Workshop XLVI, the 7th US-Japan Seminar on Earthquake Prediction, US Geol. Surv. Open File Rep. 90*. Vol. 98, pp. 226–245.

Fagereng, Å., and Sibson, R. H. (2010). Melange rheology and seismic style. *Geology* 38.8, pp. 751–754.

Fang, Z., and Dunham, E. M. (2013). Additional shear resistance from fault roughness and stress levels on geometrically complex faults. *Journal of Geophysical Research: Solid Earth* 118.7, pp. 3642–3654.

Field, E. H. et al. (2014). Uniform California earthquake rupture forecast, version 3 (UCERF3)—The time-independent model. *Bulletin of the Seismological Society of America* 104.3, pp. 1122–1180.

Field, E. H. et al. (2017). A synoptic view of the third Uniform California Earthquake Rupture Forecast (UCERF3). *Seismological Research Letters* 88.5, pp. 1259–1267.

Gutenberg, B. (2013). Seismicity of the earth and associated phenomena. Read Books Ltd.

Gutenberg, B., and Richter, C. F. (1944). Frequency of earthquakes in California. *Bulletin of the Seismological Society of America* 34.4, pp. 185–188.

Harris, R. A., and Segall, P. (1987). Detection of a locked zone at depth on the Parkfield, California, segment of the San Andreas fault. *Journal of Geophysical Research: Solid Earth* 92.B8, pp. 7945–7962.

Hauksson, E., Yang, W., and Shearer, P. M. (2012). Waveform relocated earthquake catalog for southern California (1981 to June 2011). *Bulletin of the Seismological Society of America* 102.5, pp. 2239–2244.

Helmstetter, A., Sornette, D., and Grasso, J. R. (2003). Mainshocks are aftershocks of conditional foreshocks: How do foreshock statistical properties emerge from aftershock laws. *Journal of Geophysical Research: Solid Earth* 108.B1.

Hickman, S., Zoback, M., and Ellsworth, W. (2004). Introduction to special section: Preparing for the San Andreas Fault Observatory at depth. *Geophysical Research Letters* 31.12.

Hillers, G., Ben-Zion, Y., and Mai, P. M. (2006). Seismicity on a fault controlled by rate-and state-dependent friction with spatial variations of the critical slip distance. *Journal of Geophysical Research: Solid Earth* 111.B1.

Hillers, G. et al. (2007). Statistical properties of seismicity of fault zones at different evolutionary stages. *Geophysical Journal International* 169.2, pp. 515–533.

Igarashi, T., Matsuzawa, T., and Hasegawa, A. (2003). Repeating earthquakes and interplate aseismic slip in the northeastern Japan subduction zone. *Journal of Geophysical Research: Solid Earth* 108.B5.

Imanishi, K., and Ellsworth, W. L. (2006). Source scaling relationships of microearthquakes at Parkfield, CA, determined using the SAFOD pilot hole seismic array. *Earthquakes: Radiated Energy and the Physics of Faulting* 170, pp. 81–90.

Imanishi, K., Ellsworth, W. L., and Prejean, S. G. (2004). Earthquake source parameters determined by the SAFOD Pilot Hole seismic array. *Geophysical Research Letters* 31.12.

Ishibe, T., and Shimazaki, K. (2012). Characteristic earthquake model and seismicity around late Quaternary active faults in Japan. *Bulletin of the Seismological Society of America* 102.3, pp. 1041–1058.

Jiang, J., and Lapusta, N. (2016). Deeper penetration of large earthquakes on seismically quiescent faults. *Science* 352.6291, pp. 1293–1297.

Jones, L. M., and Molnar, P. (1979). Some characteristics of foreshocks and their possible relationship to earthquake prediction and premonitory slip on faults. *Journal of Geophysical Research: Solid Earth* 84.B7, pp. 3596–3608.

Jones, L., and Molnar, P. (1976). Frequency of foreshocks. *Nature* 262.5570, pp. 677–679.

Kagan, Y., Jackson, D. D., Geller, R. J., et al. (2012). Characteristic earthquake model, 1884–2011, RIP. *arXiv preprint arXiv:1207.4836*.

Kanamori, H., and Stewart, G. S. (1976). Mode of the strain release along the Gibbs fracture zone, Mid-Atlantic Ridge. *Physics of the Earth and Planetary Interiors* 11.4, pp. 312–332.

Kaneko, Y., Avouac, J. P., and Lapusta, N. (2010). Towards inferring earthquake patterns from geodetic observations of interseismic coupling. *Nature Geoscience* 3.5, pp. 363–369.

Kaneko, Y., and Lapusta, N. (2008). Variability of earthquake nucleation in continuum models of rate-and-state faults and implications for aftershock rates. *Journal of Geophysical Research: Solid Earth* 113.B12.

Kaneko, Y., Nielsen, S. B., and Carpenter, B. M. (2016). The onset of laboratory earthquakes explained by nucleating rupture on a rate-and-state fault. *Journal of Geophysical Research: Solid Earth* 121.8, pp. 6071–6091.

Kaneko, Y., and Shearer, P. M. (2014). Seismic source spectra and estimated stress drop derived from cohesive-zone models of circular subshear rupture. *Geophysical Journal International* 197.2, pp. 1002–1015.

Kaneko, Y., and Shearer, P. M. (2015). Variability of seismic source spectra, estimated stress drop, and radiated energy, derived from cohesive-zone models of symmetrical and asymmetrical circular and elliptical ruptures. *Journal of Geophysical Research: Solid Earth* 120.2, pp. 1053–1079.

Kato, A. et al. (2012). Propagation of slow slip leading up to the 2011 Mw 9.0 Tohoku-Oki earthquake. *Science* 335.6069, pp. 705–708.

Lapusta, N. et al. (2000). Elastodynamic analysis for slow tectonic loading with spontaneous rupture episodes on faults with rate-and state-dependent friction. *Journal of Geophysical Research: Solid Earth* 105.B10, pp. 23765–23789.

Lee, J. J., and Bruhn, R. L. (1996). Structural anisotropy of normal fault surfaces. *Journal of Structural Geology* 18.8, pp. 1043–1059.

Lin, Y. Y., and Lapusta, N. (2018). Microseismicity simulated on asperity-like fault patches: On scaling of seismic moment with duration and seismological estimates of stress drops. *Geophysical Research Letters* 45.16, pp. 8145–8155.

Liu, Y., and Rice, J. R. (2005). Aseismic slip transients emerge spontaneously in three-dimensional rate and state modeling of subduction earthquake sequences. *Journal of Geophysical Research: Solid Earth* 110.B8.

Liu, Y., and Rice, J. R. (2007). Spontaneous and triggered aseismic deformation transients in a subduction fault model. *Journal of Geophysical Research: Solid Earth* 112.B9.

Lockner, D. A. et al. (2011). Low strength of deep San Andreas fault gouge from SAFOD core. *Nature* 472.7341, pp. 82–85.

Lui, S. K., and Lapusta, N. (2016). Repeating microearthquake sequences interact predominantly through postseismic slip. *Nature Communications* 7, p. 13020.

Lui, S. K., and Lapusta, N. (2018). Modeling high stress drops, scaling, interaction, and irregularity of repeating earthquake sequences near Parkfield. *Journal of Geophysical Research: Solid Earth*.

Luo, Y., and Ampuero, J. P. (2018). Stability of faults with heterogeneous friction properties and effective normal stress. *Tectonophysics* 733, pp. 257–272.

Mai, P. M., and Beroza, G. C. (2002). A spatial random field model to characterize complexity in earthquake slip. *Journal of Geophysical Research: Solid Earth* 107.B11, ESE–10.

Marone, C., Vidale, J. E., and Ellsworth, W. L. (1995). Fault healing inferred from time dependent variations in source properties of repeating earthquakes. *Geophysical Research Letters* 22.22, pp. 3095–3098.

Matsubara, M., Yagi, Y., and Obara, K. (2005). Plate boundary slip associated with the 2003 Off-Tokachi earthquake based on small repeating earthquake data. *Geophysical Research Letters* 32.8.

McGuire, J. J., Boettcher, M. S., and Jordan, T. H. (2005). Foreshock sequences and short-term earthquake predictability on East Pacific Rise transform faults. *Nature* 434.7032, pp. 457–461.

McLaskey, G. C., and Kilgore, B. D. (2013). Foreshocks during the nucleation of stick-slip instability. *Journal of Geophysical Research: Solid Earth* 118.6, pp. 2982–2997.

McLaskey, G. C., and Lockner, D. A. (2014). Preslip and cascade processes initiating laboratory stick slip. *Journal of Geophysical Research: Solid Earth* 119.8, pp. 6323–6336.

Meier, M. A., Ampuero, J. P., and Heaton, T. H. (2017). The hidden simplicity of subduction megathrust earthquakes. *Science* 357.6357, pp. 1277–1281.

Michailos, K. et al. (2019). Variations in seismogenic thickness along the Central Alpine Fault, New Zealand, revealed by a decade's relocated microseismicity. *Geochemistry, Geophysics, Geosystems* 20.1, pp. 470–486.

Michel, S., Gualandi, A., and Avouac, J. P. (2019). Similar scaling laws for earthquakes and Cascadia slow-slip events. *Nature* 574.7779, pp. 522–526.

Mikumo, T. (1992). Earthquake source physics and earthquake precursors. Elsevier.

Nadeau, R. M., and Johnson, L. R. (1998). Seismological studies at Parkfield VI: Moment release rates and estimates of source parameters for small repeating earthquakes. *Bulletin of the Seismological Society of America* 88.3, pp. 790–814.

Nadeau, R. M., and McEvilly, T. V. (1999). Fault slip rates at depth from recurrence intervals of repeating microearthquakes. *Science* 285.5428, pp. 718–721.

Nadeau, R. M., and McEvilly, T. V. (2004). Periodic pulsing of characteristic microearthquakes on the San Andreas fault. *Science* 303.5655, pp. 220–222.

Nadeau, R. M. et al. (2004). Detailed kinematics, structure and recurrence of microseismicity in the SAFOD target region. *Geophysical Research Letters* 31.12.

Nadeau, R. et al. (1994). Seismological studies at Parkfield III: Microearthquake clusters in the study of fault-zone dynamics. *Bulletin of the Seismological Society of America* 84.2, pp. 247–263.

Noda, H., and Lapusta, N. (2010). Three-dimensional earthquake sequence simulations with evolving temperature and pore pressure due to shear heating: Effect of heterogeneous hydraulic diffusivity. *Journal of Geophysical Research: Solid Earth* 115.B12.

Noda, H., Lapusta, N., and Kanamori, H. (2013). Comparison of average stress drop measures for ruptures with heterogeneous stress change and implications for earthquake physics. *Geophysical Journal International* 193.3, pp. 1691–1712.

Ohnaka, M. (1992). Earthquake source nucleation: A physical model for short-term precursors. *Tectonophysics* 211.1-4, pp. 149–178.

Page, M. T., and Elst, N. J. van der (2018). Fault-tolerant b-values and aftershock productivity. *Journal of Geophysical Research: Solid Earth* 123.12, pp. 10–880.

Page, M., and Felzer, K. (2015). Southern San Andreas fault seismicity is consistent with the Gutenberg–Richter magnitude–frequency distribution. *Bulletin of the Seismological Society of America* 105.4, pp. 2070–2080.

Power, W. L., Tullis, T. E., and Weeks, J. D. (1988). Roughness and wear during brittle faulting. *Journal of Geophysical Research: Solid Earth* 93.B12, pp. 15268–15278.

Renard, F. et al. (2006). High resolution 3D laser scanner measurements of a strike-slip fault quantify its morphological anisotropy at all scales. *Geophysical Research Letters* 33.4.

Rice, J. R. (1992). Fault stress states, pore pressure distributions, and the weakness of the San Andreas fault. *International Geophysics*. Vol. 51. Elsevier, pp. 475–503.

Rice, J. R. (1993). Spatio-temporal complexity of slip on a fault. *Journal of Geophysical Research: Solid Earth* 98.B6, pp. 9885–9907.

Rice, J. R. (2006). Heating and weakening of faults during earthquake slip. *Journal of Geophysical Research: Solid Earth* 111.B5.

Rice, J. R., Lapusta, N., and Ranjith, K. (2001). Rate and state dependent friction and the stability of sliding between elastically deformable solids. *Journal of the Mechanics and Physics of Solids* 49.9, pp. 1865–1898.

Rubin, A. M., and Ampuero, J. P. (2005). Earthquake nucleation on (aging) rate and state faults. *Journal of Geophysical Research: Solid Earth* 110.B11.

Rubinstein, J. L. et al. (2012). Fixed recurrence and slip models better predict earthquake behavior than the time-and slip-predictable models: 1. Repeating earthquakes. *Journal of Geophysical Research: Solid Earth* 117.B2.

Ruina, A. (1983). Slip instability and state variable friction laws. *Journal of Geophysical Research: Solid Earth* 88.B12, pp. 10359–10370.

Sagy, A., Brodsky, E. E., and Axen, G. J. (2007). Evolution of fault-surface roughness with slip. *Geology* 35.3, pp. 283–286.

Sammis, C. G., and Rice, J. R. (2001). Repeating earthquakes as low-stress-drop events at a border between locked and creeping fault patches. *Bulletin of the Seismological Society of America* 91.3, pp. 532–537.

Schaal, N., and Lapusta, N. (2019). Microseismicity on patches of higher compression during larger-scale earthquake nucleation in a rate-and-state fault model. *Journal of Geophysical Research: Solid Earth* 124.2, pp. 1962–1990.

Schaff, D. P., and Beroza, G. C. (2004). Coseismic and postseismic velocity changes measured by repeating earthquakes. *Journal of Geophysical Research: Solid Earth* 109.B10.

Schaff, D. P., Beroza, G. C., and Shaw, B. E. (1998). Postseismic response of repeating aftershocks. *Geophysical Research Letters* 25.24, pp. 4549–4552.

Schorlemmer, D., and Wiemer, S. (2005). Microseismicity data forecast rupture area. *Nature* 434.7037, pp. 1086–1086.

Segall, P. et al. (2010). Dilatant strengthening as a mechanism for slow slip events. *Journal of Geophysical Research: Solid Earth* 115.B12.

Shimazaki, K., and Nakata, T. (1980). Time-predictable recurrence model for large earthquakes. *Geophysical Research Letters* 7.4, pp. 279–282.

Sieh, K. E. (1978). Central California foreshocks of the great 1857 earthquake. *Bulletin of the Seismological Society of America* 68.6, pp. 1731–1749.

Skarbek, R. M., Rempel, A. W., and Schmidt, D. A. (2012). Geologic heterogeneity can produce aseismic slip transients. *Geophysical Research Letters* 39.21.

Tal, Y., Hager, B. H., and Ampuero, J. P. (2018). The effects of fault roughness on the earthquake nucleation process. *Journal of Geophysical Research: Solid Earth* 123.1, pp. 437–456.

Tormann, T., Wiemer, S., and Mignan, A. (2014). Systematic survey of high-resolution b value imaging along Californian faults: Inference on asperities. *Journal of Geophysical Research: Solid Earth* 119.3, pp. 2029–2054.

Vidale, J. E. et al. (1994). Variations in rupture process with recurrence interval in a repeated small earthquake. *Nature* 368.6472, p. 624.

Voss, R. F. (1988). Fractals in nature: From characterization to simulation. *The Science of Fractal Images*. Springer, pp. 21–70.

Waldhauser, F., and Schaff, D. P. (2008). Large-scale relocation of two decades of northern California seismicity using cross-correlation and double-difference methods. *Journal of Geophysical Research: Solid Earth* 113.B8.

Wesnousky, S. G. (1994). The Gutenberg-Richter or characteristic earthquake distribution, which is it? *Bulletin of the Seismological Society of America* 84.6, pp. 1940–1959.

Yabe, S., and Ide, S. (2017). Slip-behavior transitions of a heterogeneous linear fault. *Journal of Geophysical Research: Solid Earth* 122.1, pp. 387–410.

Ye, L. et al. (2016). Rupture characteristics of major and great (Mw$\geq$ 7.0) megathrust earthquakes from 1990 to 2015: 1. Source parameter scaling relationships. *Journal of Geophysical Research: Solid Earth* 121.2, pp. 826–844.

Zanzerkia, E. E., Beroza, G. C., and Vidale, J. E. (2003). Waveform analysis of the 1999 Hector Mine foreshock sequence. *Geophysical Research Letters* 30.8.

Zoback, M., Hickman, S., and Ellsworth, W. (2010). Scientific drilling into the San Andreas fault zone. *Eos, Transactions American Geophysical Union* 91.22, pp. 197–199.

Zoback, M., Hickman, S., and Ellsworth, W. (2011). Scientific drilling into the San Andreas fault zone–an overview of SAFOD's first five years. *Scientific Drilling* 11, pp. 14–28.